

ISSUE: 30  
SCOPUS

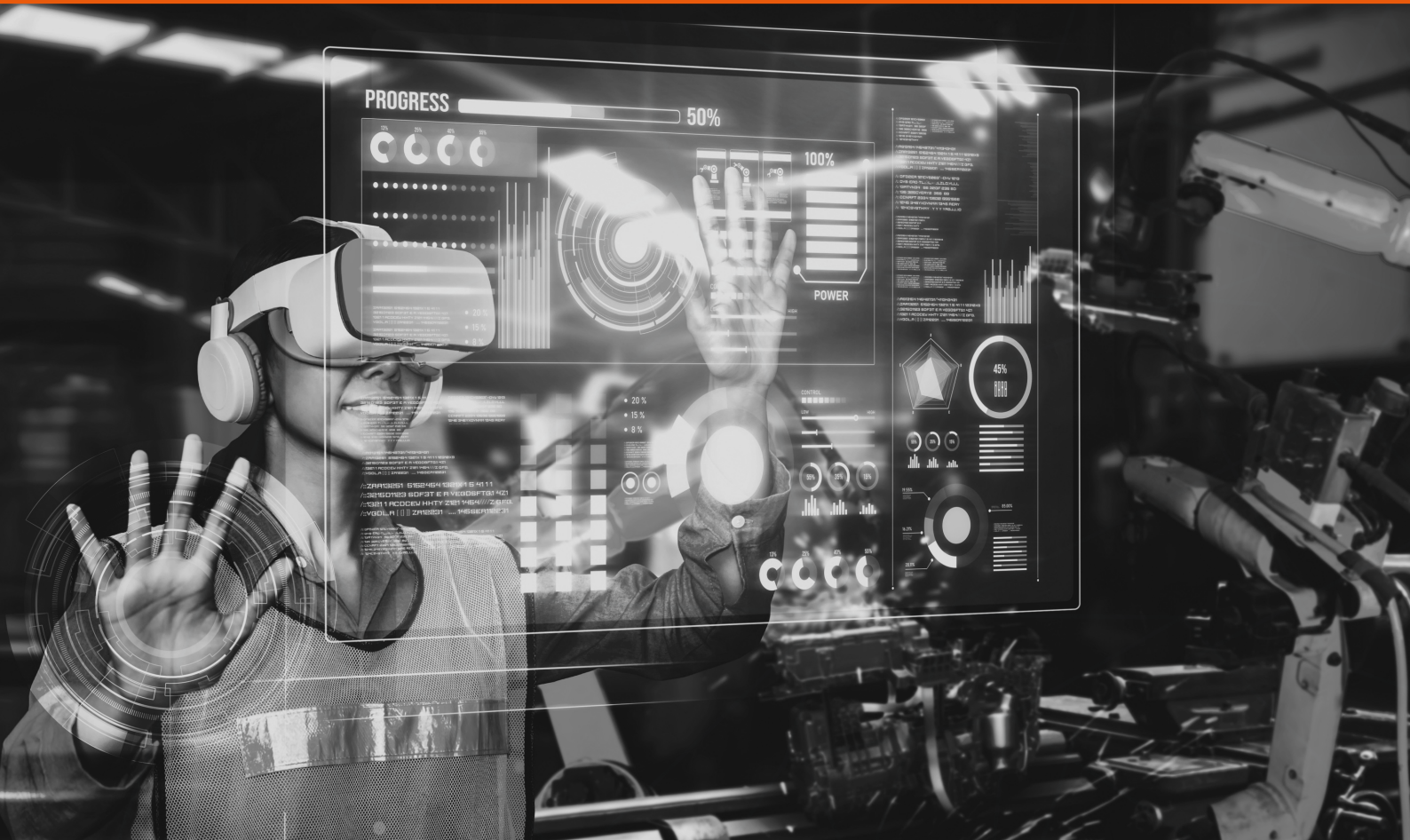
UNIVERSIDAD POLITÉCNICA SALESIANA ECUADOR

pISSN: 1390-650X  
eISSN: 1390-860X

july / december 2023

# INGENIUS

Revista de Ciencia y Tecnología



- Design and deployment of an IoT-based monitoring system for hydroponic crops.

Pag. 9

- Methodological Proposal for the Design and Analysis of a Formula sae monocoque.

Pag. 42

- Evolutionary artificial neural network for temperature control in a batch polymerization reactor.

Pag. 79

- Monte Carlo simulation of uncontrolled Electric Vehicle charging impact on distributed generation.

Pag. 120

Indexed in: **SCOPUS**

# INGENIUS

INGENIUS • Issue 30 • july/december 2023. Journal of Science and Tecnology of the Universidad Politécnica Salesiana of Ecuador. Publication dedicated to studies related to the Sciences of Mechanical Engineering, Electrical Engineering, Electronic Engineering, Mechatronic Engineering, Systems Engineering and Industrial Engineering.

## Editors Board

RAFAEL ANTONIO BALART GIMENO, PHD, Universidad Politécnica de Valencia, España – Editor-in-chief.

JOHN IGNACIO CALLE SIGÜENCIA, PHD, Universidad Politécnica Salesiana, Ecuador – Editor-in-chief.

ESTEBAN MAURICIO INGA ORTEGA, PHD, Universidad Politécnica Salesiana, Ecuador – Associate Editor.

MARLON XAVIER QUINDE ABRIL, MSC, Universidad Politécnica Salesiana, Ecuador – Associate Editor.

TEODIANO FREIRE BASTOS FILHO, PHD, (Universidade Federal do Espírito Santo, Brasil – Associate Editor.

## Scientific board

JUAN LÓPEZ MARTÍNEZ, PHD, Universidad Politécnica de Valencia, España.

ELENA FORTUNATI, PHD, Universidad de Perugia, Italia.

GUSTAVO ROVELO RUIZ, PHD, Hasselt University, Diepenbeek, Bélgica.

FRANKLIN GAVILANEZ ALVAREZ, PHD, American University, Estados Unidos.

PIEDAD GAÑAN ROJO, PHD, Universidad Pontificia Bolivariana, Colombia.

JOSÉ ALEX RESTREPO, PHD, Universidad Simón Bolívar, Venezuela.

SERGIO LUJAN MORA, PHD, Universidad de Alicante, España.

MARTHA ZEQUERA DÍAZ, PHD, Pontificia Universidad Javeriana, Colombia.

GROVER ZURITA, PHD, Universidad Privada Boliviana, Bolivia.

VLADIMIR ROBLES, PHD, Universidad Politécnica Salesiana, Ecuador.

GERMÁN ARÉVALO, PHD, Universidad Politécnica Salesiana, Ecuador.

WILBERT AGUILAR, PHD, Universidad de las Fuerzas Armadas, ESPE, Ecuador.

JACK BRAVO TORRES, PHD, Universidad Politécnica Salesiana, Ecuador.

WALTER OROZCO, PHD, Universidad Politécnica Salesiana, Ecuador.

MARIELA CERRADA, PHD, Universidad Politécnica Salesiana, Ecuador.

JULIO CÉSAR VIOLA, PHD, Universidad Politécnica Salesiana, Ecuador.

SERGIO GAMBOA SÁNCHEZ, PHD, Universidad Nacional Autónoma de México, México.

ROGER ABDÓN BUSTAMANTE PLAZA, PHD, Universidad de Chile, Chile.

CHRISTIAN BLUM, PHD, Consejo Superior de Investigaciones Científicas, España.

SILVIA NOEMI SCHIAFFINO, PHD, Universidad Nacional del Centro de la Provincia de Buenos Aires, Argentina.

ANALÍA ADRIANA AMANDI, PHD, Universidad Nacional del Centro de la Provincia de Buenos Aires, Argentina.

RUBÉN DE JESÚS MEDINA MOLINA, PHD,

Universidad de Los Andes, Venezuela.

JOHNNY JOSUÉ BULLÓN TORREALBA, PHD, Universidad de Los Andes, Venezuela.

RODRIGO PALMA HILLERNS, PHD, Universidad de Chile, Chile.

GERARDO ESPINOZA PÉREZ, PHD, Universidad Nacional Autónoma de México, México.

ALEXANDRE MENDES ABRÃO, PHD, Universidad Federal de Minas Gerais, Brasil.

KAMLA ABDEL RADI ISMAIL, PHD, Universidad Estatal de Campinas Unicamp, Brasil.

ARNALDO DA SILVA, PHD, Universidad Estatal de Campinas Unicamp, Brasil.

ÁLVARO ROCHA, PHD, Universidad de Coimbra, Portugal.

JOSÉ ANTENOR POMILIO, PHD, Universidad Estatal de Campinas Unicamp, Brasil.

LUIS PAULO REIS, PHD, Universidad de Minho, Portugal.

LUÍS FERNANDES, PHD, Escuela Superior Náutica Infante d. Henrique, Portugal.

ANÍBAL TRAÇA DE ALMEIDA, PHD, Universidad de Coimbra, Portugal.

JORGE SÁ SILVA, PHD, Universidad de Coimbra, Portugal.

PEDRO MANUEL SOARES MOURA, PHD, Universidad de Coimbra, Portugal.

SÉRGIO MANUEL RODRIGUES LOPES, PHD, Universidad de Coimbra, Portugal.

RICARDO MADEIRA SOARES BRANCO, PHD, Universidad de Coimbra, Portugal.

CARLOS ALEXANDRE BENTO CAPELA, PHD, Universidad de Coimbra, Portugal.

FILIFE ARAUJO, PHD, Universidad de Coimbra, Portugal.

LUIS MANUEL GUERRA SILVA ROSA, PHD, Universidad de Lisboa, Portugal.

HÉLDER DE JESUS FERNANDES, PUGA, PHD, Universidad de Minho, Portugal.

FILIFE SAMUEL, PEREIRA DA SILVA, PHD, Universidad de Minho, Portugal.

CÉSAR SEQUEIRA, PHD, Universidad de Lisboa, Portugal.

JOSÉ TEIXEIRA ESTÊVÃO FERREIRA, PHD,

Universidad de Coimbra, Portugal.

NUNO LARANJEIRO, PHD, Universidad de Coimbra, Portugal.

LUÍS AMARAL, PHD, Universidad de Lisboa, Portugal.

JORGE HENRIQUES, PHD, Universidad de Coimbra, Portugal.

WILLIAM IPANAQUE, PHD, Universidad de Piura, Perú.

LORENZO LEIJA SALAS, PHD, Centro de Investigación y Estudios Avanzados del Instituto Politécnico Nacional, México.

VALERI KONTOROVICH MAZOVER, PHD, Centro de Investigación y de Estudios Avanzados del Instituto Politécnico Nacional, México.

ALEJANDRO ÁVILA GARCÍA, PHD, Centro de Investigación y de Estudios Avanzados del Instituto Politécnico Nacional, México.

PAOLO BELLAVISTA, PHD, Universidad de Bologna, Italia.

CARLOS RUBIO, PhD, Centro de Ingeniería y Desarrollo Industrial, México.

FERNANDO HERNÁNDEZ SÁNCHEZ, PhD, Centro de Investigación Científica de Yucatán, México.

EMILIO MUÑOZ SANDOVAL, PhD, Instituto Potosino de Investigación Científica y Tecnológica, México.

YASUHIRO MATSUMOTO KUWABARA, PhD, Centro de Investigación y de Estudios Avanzados del Instituto Politécnico Nacional, México.

DAVID ZUMOFFEN, PhD, Centro Internacional Franco Argentino de Ciencias de la Información y de Sistemas, Argentina.

VICENTE RODRÍGUEZ GONZÁLEZ, PhD, Instituto Potosino de Investigación Científica y Tecnológica, México.

ALEJANDRO RODRÍGUEZ ÁNGELES, PhD, Centro de Investigación y de Estudios Avanzados del Instituto Politécnico Nacional, México.

ALISTAIR BORTHWICK, PhD, Universidad de Edimburgo, Reino Unido.

## Reviewers board

FEDERICO DOMINGUEZ, PHD, Escuela Superior Politécnica del Litoral, Ecuador.

ENRIQUE CARRERA, PHD, Universidad de las Fuerzas Armadas, ESPE, Ecuador.

ANDRÉS TELLO, MSc, Universidad de Cuenca, Ecuador.

CRISTIAN GARCÍA BAUZA, PHD, Universidad Nacional del Centro de la Provincia de Buenos Aires, Argentina.

OSVALDO AÑÓ, PHD, Universidad Nacional de San Juan, Argentina.

THALÍA SAN ANTONIO, PHD, Universidad Técnica de Ambato, Ecuador.

VICTOR SAQUICELA, PHD, Universidad de Cuenca, Ecuador.

GONZALO OLMEDO, PHD, Universidad de las Fuerzas Armadas, ESPE, Ecuador.

ROMÁN LARA, PHD, Universidad de las Fuerzas Armadas, ESPE, Ecuador.

GUILLERMO SORIANO, PHD, Escuela Superior Politécnica del Litoral, Ecuador.

MARÍA FERNANDA GRANDA, PHD, Universidad de Cuenca, Ecuador.

RICARDO CAYSSIALS, PHD, Universidad Tecnológica Nacional, Argentina.

LEONARDO SOLAQUE GUZMAN, PHD, Universidad Militar Nueva Granada, Colombia.

JOSÉ DI PAOLO, PHD, Universidad Nacional de Entre Ríos, Argentina.

ASTRID RUBIANO FONSECA, PHD, Universidad Militar Nueva Granada, Colombia.

ROBINSON JIMÉNEZ, PHD, Universidad Militar Nueva Granada, Colombia.

ALFONSO ZOZAYA, PHD, Universidad de Carabobo, Venezuela.

MAURICIO MAULEDOUX, PHD, Universidad Militar Nueva Granada, Colombia.

LUIS MEDINA, PHD, Universidad Simón Bolívar, Venezuela.

ERNESTO CUADROS-VARGAS, PHD, Universidad Católica San Pablo, Perú.

SAMUEL SEPÚLVEDA CUEVAS, PHD, Universidad de la Frontera, Chile.

CARLOS CARES, PHD, Universidad de la Frontera, Chile.

RAFAEL SOTELO, PHD, Universidad de Montevideo, Uruguay.

OMAR LOPEZ, PHD, Universidad de Los Andes, Colombia.

JOB FLORES-GODOY, PHD, Universidad Católica del Uruguay, Uruguay.

LUIS MARIO MATEUS, PHD, Universidad de los Andes, Colombia.

AMADEO ARGÜELLES CRUZ, PHD, Instituto Politécnico Nacional, México.

SANTIAGO BENTANCOURT PARRA, PHD, Universidad Pontificia Bolivariana, Colombia.

GERMÁN ZAPATA, PHD, Universidad Nacio-

nal de Colombia, Colombia.

PEDRO GARCÍA, PHD, Universidad Autónoma de Barcelona, España.

ARTURO CONDE ENRÍQUEZ, PHD, Universidad Autónoma de Nuevo León, México.

ALBERTO CAVAZOS GONZÁLEZ, PHD, Universidad Autónoma de Nuevo León, México.

ERNESTO VÁZQUEZ MARTÍNEZ, PHD, Universidad Autónoma de Nuevo León, México.

MIGUEL DÍAZ RODRIGUEZ, PHD, Universidad de Los Andes, Venezuela.

EFRAÍN ALCORTA GARCÍA, PHD, Universidad Autónoma de Nuevo León, México.

LUIS CHIRINOS GARCIA, PHD, Pontificia Universidad Católica de Perú, Perú.

OSCAR AVILÉS, PHD, Universidad Militar Nueva Granada, Colombia.

DORA MARTÍNEZ DELGADO, PHD, Universidad Autónoma de Nuevo León, México.

DAVID OJEDA, PHD, Universidad Técnica del Norte, Ecuador.

IRENE BEATRÍZ STEINMANN, PHD, Universidad Tecnológica Nacional, Argentina.

MARIO SERRANO, Universidad Nacional de San Juan, Argentina.

CORNELIO POSADAS CASTILLO, PHD, Universidad Autónoma Nuevo León, México.

MARIO ALBERTO RIOS MESIAS, PHD, Universidad de Los Andes, Colombia.

YUDITH CARDINALE VILLARREAL, PHD, Universidad Simón Bolívar, Venezuela.

EDUARDO MATALANAS, PHD, Universidad Politécnica de Madrid, España.

JOSE EDUARDO OCHOA LUNA, PHD, Universidad Católica San Pablo, Perú.

DANTE ANGEL ELIAS GIORDANO, PHD, Pontificia Universidad Católica de Perú, Perú.

MANUEL PELAEZ SAMANIEGO, PHD, Universidad de Cuenca, Ecuador.

JUAN ESPINOZA ABAD, PHD, Universidad de Cuenca, Ecuador.

PIETRO CODARA, PHD, Universidad de Milan, Italia.

ALBERTO SORIA, PHD, Centro de Investigación y de Estudios Avanzados del Instituto Politécnico Nacional, México.

JOSÉ M. ALLER, PHD, Universidad Politécnica Salesiana, Ecuador.

FERNEY AMAYA F., PHD, Universidad Pontificia Bolivariana, Medellín, Colombia.

SANTIAGO ARANGO ARAMBURO, PHD, Universidad Nacional de Colombia, Colombia.

DIEGO ARCOS-AVILÉS, PHD, Universidad de las Fuerzas Armadas, ESPE, Ecuador.

PABLO AREVALO, PHD, Universidad Politécnica Salesiana, Ecuador.

ROBERTO BELTRAN, MSc, Universidad de las Fuerzas Armadas, ESPE, Ecuador.

LEONARDO BETANCUR, PHD, Universidad Pontificia Bolivariana, Medellín, Colombia.

ROBERTO GAMBOA, PHD, Universidad de Lisboa, Portugal.

PAULO LOPES DOS SANTOS, PHD, Universidad do Porto, Portugal.

PEDRO ANDRÉ DIAS PRATES, PHD, Universidad de Coimbra, Portugal.

JOSÉ MANUEL TORRES FARINHA, PHD, Universidad de Coimbra, Portugal.

CELSO DE ALMEIDA, PHD, Universidad Estatal de Campinas Unicamp, Brasil.

RAMON MOLINA VALLE, PHD, Universidad Federal de Minas Gerais, Brasil.

CRISTINA NADER VASCONCELOS, PHD, Universidad Federal Fluminense, Brasil.

JOÃO M. FERREIRA CALADO, PHD, Universidad de Lisboa, Portugal.

GUILHERME LUZ TORTORELLA, PHD, Universidad Federal de Santa Catarina, Brasil.

MAURO E. BENEDET, PHD, Universidad Federal de Santa Catarina, Brasil.

ARTEMIS MARTI CESCHIN, PHD, Universidade de Brasilia, Brasil.

GILMAR BARRETO, PHD, Universidad Estatal de Campinas Unicamp, Brasil.

RICARDO EMILIO F. QUEVEDO NOGUEIRA, PHD, Universidad Federal de Ceará, Brasil.

WESLEY LUIZ DA SILVA ASSIS, PHD, Universidad Federal Fluminense, Brasil.

ANA P. MARTINAZZO, PHD, Universidad Federal Fluminense, Brasil.

JORGE BERNARDINO, PHD, Universidad de Coimbra, Portugal.

LUIS GERALDO PEDROSO MELONI, PHD, Universidad Estatal de Campinas Unicamp, Brasil.

FACUNDO ALMERAYA CALDERÓN, PHD, Universidad Autónoma de Nuevo León, México.

FREDDY VILLAO QUEZADA, PHD, Escuela Superior Politécnica del Litoral, Ecuador.

JOSE MANRIQUE SILUPU, MSc, Universidad de Piura, Perú.

GERMÁN ARIEL SALAZAR, PHD, Instituto de Investigaciones en Energía no Convencional, Argentina.

JOSÉ MAHOMAR JANANIÁS, PHD, Universidad del BIOBIO, Chile.

ARNALDO JÉLVEZ CAAMAÑO, PHD, Universidad del BIOBIO, Chile.

JORGE ANDRÉS URIBE, MSc, Centro de Ingeniería y Desarrollo Industrial, México.

RICARDO BELTRAN, PHD, Centro de Investigación en Materiales Avanzados, México.

ADI CORRALES, MSc, Centro de Ingeniería y Desarrollo Industrial, México.

JORGE URIBE CALDERÓN, PHD, Centro de Investigación Científica de Yucatán, México

JOSÉ TRINIDAD HOLGUÍN MOMACA, MSc, Centro de Investigación en Materiales Avanzados, México.

JUAN MANUEL ALVARADO OROZCO, PhD, Centro de Ingeniería y Desarrollo Industrial, México.

ARNALDO JÉLVEZ CAAMAÑO, PhD, Universidad del BIOBIO, Chile.

JAVIER MURILLO, PhD, Centro Internacional Franco Argentino de Ciencias de la Información y de Sistemas, Argentina.

LUCAS DANIEL TERISSI, PhD, Universidad Nacional de Rosario, Argentina.

RENE VINICIO SANCHEZ LOJA, MSc, Universidad Politécnica Salesiana, Ecuador.

FREDDY LEONARDO BUENO PALOMEQUE, MSc, Universidad Politécnica Salesiana, Ecuador.

DIEGO CABRERA MENDIETA, MSc, Universidad Politécnica Salesiana, Ecuador.

EDWUIN JESUS CARRASQUERO, PhD, Universidad Técnica de Machala, Ecuador.

CARLOS MAURICIO CARRILLO ROSERO, MSc, Universidad Técnica de Ambato, Ecuador.

DIEGO CARRION GALARZA, MSc, Universidad Politécnica Salesiana, Ecuador.

CARMEN CELI SANCHEZ, MSc, Universidad Politécnica Salesiana, Ecuador.

DIEGO CHACON TROYA, MSc, Universidad Politécnica Salesiana, Ecuador.

PAUL CHASI, MSc, Universidad Politécnica Salesiana, Ecuador.

JUAN CHICA, MSc, Universidad Politécnica Salesiana, Ecuador.

DIEGO MARCELO CORDERO GUZMÁN, MSc, Universidad Católica de Cuenca, Ecuador.

LUIS JAVIER CRUZ, PhD, Universidad Pontificia Bolivariana, Medellín, Colombia.

FABRICIO ESTEBAN ESPINOZA MOLINA, MSc, Universidad Politécnica Salesiana, Ecuador.

JORGE FAJARDO SEMINARIO, MSc, Universidad Politécnica Salesiana, Ecuador.

PATRICIA FERNANDEZ MORALES, PhD, Universidad Pontificia Bolivariana, Medellín, Colombia.

MARCELO FLORES VAZQUEZ, MSc, Universidad Politécnica Salesiana, Ecuador.

CARLOS FLORES VÁZQUEZ, MSc, Universidad Católica de Cuenca, Ecuador.

CARLOS FRANCO CARDONA, PhD, Universidad Nacional de Colombia, Colombia.

CRISTIAN GARCÍA GARCÍA, MSc, Universidad Politécnica Salesiana, Ecuador.

TEONILA GARCÍA ZAPATA, PhD, Universidad Nacional Mayor de San Marcos, Perú.

LUIS GARZÓN MÑOZ, PhD, Universidad Politécnica Salesiana, Ecuador.

NATALIA GONZALEZ ALVAREZ, MSc, Universidad Politécnica Salesiana, Ecuador.

ERNESTO GRANADO, PhD, Universidad Simón Bolívar, Venezuela.

ADRIANA DEL PILAR GUAMAN, MSc, Universidad Politécnica Salesiana, Ecuador.

JUAN INGA ORTEGA, MSc, Universidad Politécnica Salesiana, Ecuador.

ESTEBAN INGA ORTEGA, PhD, Universidad Politécnica Salesiana, Ecuador.

PAOLA INGAVÉLEZ, MSc, Universidad Politécnica Salesiana, Ecuador.

CESAR ISAZA ROLDAN, PhD, Universidad Pontificia Bolivariana.

NELSON JARA COBOS, MSc, Universidad Politécnica Salesiana, Ecuador.

RUBEN JERVES, MSc, Universidad Politécnica Salesiana, Ecuador.

VICTOR RAMON LEAL, PhD, Investigador de PDVSA, Venezuela

GABRIEL LEON, MSc, Universidad Politécnica Salesiana, Ecuador.

EDILBERTO LLANES, PhD, Universidad Internacional SEK, Ecuador.

LUIS LÓPEZ, MSc, Universidad Politécnica Salesiana, Ecuador.

CARLOS MAFLA YÉPEZ, MSc, Universidad Técnica del Norte, Ecuador.

HADER MARTÍNEZ, PhD, Universidad Pontificia Bolivariana, Medellín, Colombia

JAVIER MARTÍNEZ, PhD, Instituto Nacional de Eficiencia Energética y Energías Renovables, Ecuador.

ALEX MAYORGA, MSc, Universidad Técnica de Ambato, Ecuador.

JIMMY MOLINA, MSc, Universidad Técnica de Machala, Ecuador.

ANDRES MONTERO, PhD, Universidad de Cuenca, Ecuador.

VICENTE MORALES, MSc, Universidad Técnica de Ambato, Ecuador.

FABIÁN MORALES, MSc, Universidad Técnica de Ambato, Ecuador.

DIEGO MORALES, MSc, Ministerio de Electricidad y Energías Renovables del Ecuador.

YOANDRYS MORALES TAMAYO, PhD, Universidad Técnica de Cotopaxi, Cotopaxi

OLENA LEONIDIVNA NAIDIUK, MSc, Universidad Politécnica Salesiana, Ecuador.

OSCAR NARANJO, MSc, Universidad del Azuay, Ecuador.

PAUL NARVAEZ, MSc, Universidad Politécnica Salesiana, Ecuador.

HERNÁN NAVAS OLMEDO, MSc, Universidad Técnica de Cotopaxi, Ecuador.

CESAR NIETO, PhD, Universidad Pontificia Bolivariana, Medellín, Colombia

FABIO OBANDO, MSc, Universidad Politécnica Salesiana, Ecuador.

LUIS ORTIZ FERNANDEZ, MSc, Universidade Federal de Rio Grande del Norte, Brasil

PABLO PARRA, MSc, Universidad Politécnica Salesiana, Ecuador.

PAULO PEÑA TORO, PhD, Ministerio de Productividad, Ecuador.

PATSY PRIETO VELEZ, MSc, Universidad Politécnica Salesiana, Ecuador.

DIEGO QUINDE FALCONI, MSc, Universidad Politécnica Salesiana, Ecuador.

DIANA QUINTANA ESPINOZA, MSc, Universidad Politécnica Salesiana, Ecuador.

WILLIAM QUITIAQUEZ SARZOSA, MSc, Universidad Politécnica Salesiana, Ecuador.

FLAVIO QUIZHPI PALOMEQUE, MSc, Universidad Politécnica Salesiana, Ecuador.

WASHINGTON RAMIREZ MONTALVAN, MSc, Universidad Politécnica Salesiana, Ecuador.

FRAN REINOSO AVECILLAS, MSc, Universidad Politécnica Salesiana, Ecuador.

NÉSTOR RIVERA CAMPOVERDE, MSc, Universidad Politécnica Salesiana, Ecuador.

JORGE ROMERO CONTRERAS, MSc, Universidad de Carabobo, Venezuela

FABIAN SAENZ ENDERICA, MSc, Universidad de las Fuerzas Armadas, ESPE, Ecuador.

LUISA SALAZAR GIL, PhD, Universidad Simón Bolívar, Venezuela

GUSTAVO SALGADO ENRÍQUEZ, MSc, Universidad Central del Ecuador., Ecuador.

JUAN CARLOS SANTILLÁN LIMA, MSc, Universidad Nacional de Chimborazo

JONNATHAN SANTOS BENÍTEZ, MSc, Universidad Politécnica Salesiana, Ecuador.

ANDRÉS SARMIENTO CAJAMARCA, MSc, Universidad Federal de Santa Catarina, Brasil

LUIS SERPA ANDRADE, MSc, Universidad Politécnica Salesiana, Ecuador.

CRISTIAN TIMBI SISALIMA, MSc, Universidad Politécnica Salesiana, Ecuador.

MILTON TIPAN SIMBAÑA, MSc, Universidad Politécnica Salesiana, Ecuador.

PAUL TORRES JARA, MSc, Universidad Politécnica Salesiana, Ecuador.

RODRIGO TUFÍÑO CÁRDENAS, MSc, Universidad Politécnica Salesiana, Ecuador.

FERNANDO URGILES ORTÍZ, MSc, Universidad Politécnica Salesiana, Ecuador.

JUAN VALLADOLID QUITOISACA, MSc, Universidad Politécnica Salesiana, Ecuador.

EFRÉN VÁZQUEZ SILVA, PhD, Universidad Politécnica Salesiana, Ecuador.

JULIO VERDUGO, MSc, Universidad Politécnica Salesiana, Ecuador.

MARY VERGARA PAREDES, PhD, Universidad de los Andes, Merida, Venezuela

JENNIFER YEPEZ ALULEMA, MSc, Universidad Politécnica Salesiana, Ecuador.

JULIO ZAMBRANO ABAD, MSc, Universidad Politécnica Salesiana, Ecuador.

PATRICIA ZAPATA MOLINA, MSc, Universidad Politécnica Salesiana, Ecuador.

## **Publications board**

JUAN CÁRDENAS TAPIA, SDB, PHD  
JOSÉ JUNCOSA BLASCO, PHD  
JUAN PABLO SALGADO GUERRERO, PHD  
ANGLE TORRES TOUKOUMIDIS, PHD  
JAIME PADILLA VERDUGO, PHD  
SHEILA SERRANO VINCENTI, MSC  
JORGE CUEVA ESTRADA, MSC  
JOHN CALLE SIGÜENCIA, PHD  
FLORALBA AGUILAR GORDÓN, PHD  
BETTY RODAS SOTO, MSC  
MÓNICA RUIZ VÁSQUEZ, MSC  
JORGE ALTAMIRANO SÁNCHEZ, MSC  
DAVID ARMENDÁRIZ GONZÁLEZ, MSC

### **General Editor**

ANGEL TORRES TOUKOUMIDIS, PHD

## **Technical board**

DRA. MARCIA PEÑA, Style Reviewer,  
Centro Gráfico Salesiano - Editorial Don Bosco  
MSC. MARLON QUINDE ABRIL, Diagramming and layout  
BSC. ANDRES LOPEZ, Community Manager  
BSC. MARÍA JOSÉ CABRERA, Marcalyc Support  
BSC. CHRISTIAN ARPI, Community Managers Coordinator's team

## **Publications Service**

HERNÁN HERMOSA (General Coordination)  
MARCO GUTIÉRREZ (OJS Layout)  
PAULINA TORRES (Style Editing)  
RAYSA ANDRADE (Layout)  
MARTHA VINUEZA (Layout)  
ADRIANA CURIEL AVILA, (Translation)

## **Editorial**

Editorial Abya Yala (Quito-Ecuador),  
Av. 12 de octubre N422 y Wilson,  
Bloque A, UPS Quito, Ecuador.  
Casilla 17-12-719 Teléfonos: (593-2) 3962800 ext. 2638  
email: [editorial@abyayala.org](mailto:editorial@abyayala.org)

Printing: 800 copies

Typographic system used in the composition of this document  $\text{\LaTeX}$ .

# INGENIUS

REVISTA DE CIENCIA Y TECNOLOGIA

Issue 30

july – december 2023

ISSN impreso 1390-650X / ISSN electrónico 1390-860X

The administration of the journal is done through the following parameters:

The journal uses the academic anti-plagiarism system  

The articles have an identification code (Digital Object Identifier) 

The editorial process is managed through the Open Journal System 

It is an open access publication (Open Access) licensed Creative Commons



The politics copyright of use postprint, are published in the Self-Archive Policy Repository

Sherpa/Romeo. 

The articles of the present edition can be consulted in

<http://revistas.ups.edu.ec/index.php/ingenius>



UNIVERSIDAD POLITÉCNICA SALESIANA DEL ECUADOR

INGENIUS Journal, is indexed in the following Databases and scientific information systems:

### SELECTIVE DATABASES



Scopus



Google scholar



Scientific Indexing Services



### REVIEWS EVALUATION PLATFORMS



### SELECTIVE DIRECTORIES



Journal Seeker  
Research Bible



AcademicKeys  
UNLOCKING ACADEMIC CAREERS



ULRICHSWEB™  
GLOBAL SERIALS DIRECTORY

### SELECTIVE SERIAL LIBRARY



REDIB  
Red Iberoamericana  
de Innovación y Conocimiento Científico



### SCIENTIFIC LITERATURE SEARCHERS OPEN ACCESS



DIRECTORY OF  
OPEN ACCESS  
JOURNALS



Journals for Free

### OTHER BIBLIOGRAPHICAL DATABASES



Journal  
TOCs  
The latest Journal Tables of Contents

PKP|INDEX

# CATALOG OF INTERNATIONAL UNIVERSITY LIBRARIES



UNIVERSITÄT BAMBERG



## THE USE OF ARTIFICIAL INTELLIGENCE IN SCIENTIFIC ARTICLE WRITING

Dear readers:

Artificial intelligence (AI) has emerged as a powerful tool that can greatly assist in scientific research and writing, including the creation of high-quality scientific articles. The integration of AI technology in the writing process has the potential to revolutionize the way we produce and disseminate scientific knowledge. In this editorial, we explore the benefits and implications of using AI in scientific article writing.

One of the significant advantages of employing AI in scientific writing is its ability to analyze vast amounts of data efficiently. Machine learning algorithms can process and extract valuable insights from complex datasets, enabling researchers to identify patterns and relationships that may have otherwise gone unnoticed. This capability not only expedites the research process but also aids in generating hypotheses based on the analysis results.

Additionally, AI can assist in the automatic generation of article summaries and abstracts. By utilizing AI algorithms, researchers can quickly obtain concise and informative summaries of scientific papers, facilitating a rapid understanding of their content. This is particularly beneficial for scholars who need to review numerous articles within limited timeframes. Automatic summarization can condense essential information and provide an overview of the article's content.

AI also proves to be invaluable in terms of improving the style and grammar of scientific articles. Language models trained on vast amounts of text can identify and rectify common errors, such as grammatical mistakes, punctuation issues, or incorrect usage of scientific terminology. This not only enhances the overall quality of the writing but also enables authors to convey their ideas more effectively.

Moreover, AI can provide assistance in the structuring and organization of scientific articles. AI-

powered tools can analyze existing content and offer recommendations on how to best structure sections, improve coherence and cohesion, or express ideas more clearly and precisely. These tools serve as virtual writing assistants, supporting researchers in crafting well-organized and compelling scientific narratives.

AI technology can also play a role in plagiarism detection. Algorithms designed to detect similarities can compare the content of an article with an extensive database of existing publications, flagging potential matches or excessive similarities. This aids in upholding the integrity and originality of scientific work, ensuring that credit is given where it is due.

However, it is essential to acknowledge that despite the benefits AI brings to scientific article writing, human involvement remains crucial. AI should be viewed as a supportive tool rather than a replacement for human expertise and judgment. The knowledge, creativity, and experience of researchers are irreplaceable in the scientific writing process.

Furthermore, ethical considerations come into play when employing AI in scientific article writing. Transparency is of utmost importance. Researchers must disclose the use of AI tools or language models to ensure the integrity and accountability of their work. Proper attribution and acknowledgment of the contribution made by AI in the writing process are imperative.

In conclusion, the integration of AI in scientific article writing offers numerous advantages, including data analysis, automated summarization, grammar correction, writing assistance, and plagiarism detection. While AI enhances the efficiency and quality of scientific writing, it should always be accompanied by human oversight and critical thinking. Maintaining transparency and adhering to ethical guidelines are paramount in utilizing AI as a valuable tool in scientific research and writing.

John Calle-Sigüencia, PhD

Editor in Chief

# TABLE OF CONTENTS

<b>Design and deployment of an IoT-based monitoring system for hydroponic crops</b> . . . . .	9
Diseño y despliegue de un sistema de monitoreo basado en IoT para cultivos hidropónicos	
Manuel Montaña-Blacio, Jorge González-Escarabay, Óscar Jiménez-Sarango	
Leydi Mingo-Morocho, César Carrión-Aguirre	
<b>Methodology based on data science for the development of a forecast of the ower generation of a photovoltaic solar plant</b> . . . . .	19
Metodología basada en ciencia de datos para el desarrollo de pronóstico de la generación de energía de una planta solar fotovoltaica	
César A. Yajure-Ramírez	
<b>Polynomial cross-roots application for the exchange of radiant energy between two triangular geometries</b> . . . . .	29
Aplicación de raíces cruzadas polinomiales al intercambio de energía radiante entre dos geometrías triangulares	
Yanan Camaraza-Medina	
<b>Methodological Proposal for the Design and Analysis of a Formula SAE monocoque</b>	42
Propuesta metodológica para el diseño y análisis de un monocasco Formula Student	
Rafael Wilmer Contreras Urgilés, Carlos Ayrton Jaramillo Andrade, Erick Josué Pizarro Barrera	
<b>Correlation for the calculation of turbulent friction in pipes</b> . . . . .	54
Correlación para el cálculo de la fricción turbulenta en tuberías	
San Luis Tolentino, Omar González	
<b>Study for localization of fault in the electrical distribution systems</b> . . . . .	64
Estudio para la localización de fallas en sistemas de distribución eléctrica	
Roberto Gómez, Diego Cabrera, Pablo Robles	
<b>Evolutionary artificial neural network for temperature control in a batch polymerization reactor</b> . . . . .	79
Red neuronal artificial evolutiva para el control de temperatura en un reactor batch de polimerización	
Francisco Javier Sánchez-Ruiz, Elizabeth Argüelles Hernández, José Terrones-Salgado,	
Luz Judith Fernández Quiroz	
<b>Advances and strategies to improve the performance of biodiesel in diesel engine</b> . . . . .	90
Avances y estrategias para mejorar el desempeño del biodiésel en motor diésel	
Héctor-Hugo Riojas-González, Liborio-Jesús Bortoni-Anzures, Juan-Julián Martínez-Torres,	
Héctor A. Ruiz	
<b>Methodological Proposal for Distance Protection in Transmission Lines for Integration of Non-conventional Renewable Energies</b> . . . . .	106
Propuesta metodológica para la protección de distancia en líneas de transmisión ante la integración de energías renovables no convencionales	
M. F. Velasco, Génesis Maliza Paladines, Fernando Vaca-Urbano	
<b>Monte Carlo simulation of uncontrolled Electric Vehicle charging impact on distributed generation</b> . . . . .	120
Impacto de la simulación Montecarlo de carga no controlada de vehículos eléctricos en la generación distribuida	
Carlos W. Villanueva-Machado, Jaime E. Luyo, Alberto Ríos-Villacorta	
<b>Guidelines</b> . . . . .	135
Normas editoriales	



# DESIGN AND DEPLOYMENT OF AN IOT-BASED MONITORING SYSTEM FOR HYDROPONIC CROPS

## DISEÑO Y DESPLIEGUE DE UN SISTEMA DE MONITOREO BASADO EN IOT PARA CULTIVOS HIDROPONICOS

Manuel Montaña-Blacio<sup>1,\*</sup> , Jorge González-Escarabay<sup>2</sup> ,  
 Óscar Jiménez-Sarango<sup>3</sup> , Leydi Mingo-Morocho<sup>3</sup> , César Carrión-Aguirre<sup>3</sup> 

Received: 18-11-2022, Received after review: 15-12-2022, Accepted: 02-02-2023, Published: 01-07-2023

### Abstract

The IoT is a technological trend that enables the application of intelligent systems between connected things. IoT is being applied in different fields, including agriculture, where new techniques such as hydroponics are booming. As the increase in ambient temperature and climate changes caused by global warming have negatively affected agricultural production and the rapid growth of the world's population, which will reach approximately 9.6 billion by 2050, the industrial pace of agriculture needs to be even faster and more precise. This research presents a scalable IoT monitoring system based on Sigfox technology with 89.37% prediction capabilities through neural networks for agricultural applications. An effective four-layer architecture consisting of perception, network, middleware, and application is provided. The system was experimentally tested and validated for five months by monitoring temperature, humidity, and nutrient recirculation control in a hydroponic system in Loja, Ecuador. The developed system is smart enough to adequately control the hydroponic environment based on the multiple input parameters collected, facilitating effective management for farmers and improving production.

**Keywords:** Hydroponics, Sigfox, Neural Networks, Ufox, Internet of Things, Smart Agriculture

### Resumen

El IoT es tendencia tecnológica que hace posible sistemas inteligentes entre cosas conectadas. Su aplicación se encuentra en diferentes campos, uno de ellos es la agricultura, donde el uso de nuevas técnicas, como la hidroponía, está en auge. Es importante abordar esta área, porque la población mundial alcanzará un aproximado de 9600 millones de habitantes para el 2050, por ende, para satisfacer esta demanda se necesita que el ritmo industrial agrícola sea aún más rápido y preciso. Además, el aumento de la temperatura ambiente y los cambios climáticos por el calentamiento global también están afectando negativamente a la producción agraria. En esta investigación se presenta un sistema de monitoreo IoT escalable basado en la tecnología Sigfox con capacidades de predicción del 89,37 % a través de redes neuronales para aplicaciones agrícolas. Se proporciona una arquitectura efectiva de cuatro capas que consta de percepción, red, middleware y aplicación. Para la validación, el sistema fue construido, probado experimentalmente y validado mediante el monitoreo de la temperatura, humedad y control de la recirculación de nutrientes, en un sistema hidropónico de la ciudad de Loja en Ecuador, durante cinco meses. El sistema desarrollado es lo suficientemente inteligente para proporcionar la acción de control adecuada para el entorno hidropónico, en función de los múltiples parámetros de entrada recopilados, facilitando una gestión efectiva para los agricultores, por ende, mejorando su producción.

**Palabras clave:** hidroponía, Sigfox, redes neuronales, Ufox, Internet de las cosas, agricultura inteligente

<sup>1,\*</sup>Facultad de sistemas y telecomunicaciones, Universidad Estatal Península de Santa Elena, Ecuador.  
 Corresponding author ✉: mmontano@upse.edu.ec.

<sup>2</sup>Facultad de la educación el arte y la comunicación, Universidad Nacional de Loja, Ecuador.

<sup>3</sup>Tecnología Superior en Electrónica, Instituto Superior Tecnológico Sudamericano, Loja, Ecuador.

Suggested citation: Montaña-Blacio, M.; González-Escarabay, J.; Jiménez-Sarango, O.; Mingo-Morocho, L. and Carrión-Aguirre, C. "Design and deployment of an IoT-based monitoring system for hydroponic crops," *Ingenius, Revista de Ciencia y Tecnología*, N.º 30, pp. 9-18, 2023, DOI: <https://doi.org/10.17163/ings.n30.2023.01>.

## 1. Introduction

The Internet of Things (IoT) is a cutting-edge technology that has brought multiple benefits to the population and organizations in recent years. One of the main benefits of using this innovative technology is the ability to produce and consume services in real-time. IoT offers solutions in different scenarios such as traffic, healthcare, security, smart homes and cities, etc. [1–3]. IoT technology is also used in different areas and levels of industrial and agricultural production in agriculture [4]. The main contribution of IoT in agriculture is monitoring, which helps automation and information gathering to have precision-controlled crops and greenhouses [5]. Precision agriculture aims to provide a decision-support system that helps farmers implement efficient farming practices to increase profitability, reduce environmental risks, and preserve natural resources [6, 7].

Agricultural monitoring applications use sensors or devices to help farmers collect relevant data that benefit crop growth and production. Some IoT-based approaches analyze and process data remotely by applying cloud services [8–10], which helps researchers and farmers make better decisions. A case study of IoT management that monitors variables such as wind, soil, atmosphere, and water over a large area is proposed in [11]. This study identifies agricultural monitoring solutions considering sites or subdomains to monitor soil, air, temperature, water, diseases, location, environmental conditions, pests, and fertilization. It also explains how IoT enhances human interaction through electronic devices, low-cost communication protocols, and communication technologies.

Sigfox wireless communication technology is an emerging low power wide area (LPWAN) technology that offers secure data transmission and low power consumption [12]. It uses unlicensed radio spectrum in the industrial, scientific, and medical (ISM) bands and enables two-way communication between users and sensors on an individual or group level. Therefore, Sigfox is suitable for IoT applications that only require the transmission of small data packets and low power consumption. Hernández et al. [9] present a relevant case where they design a scalable IoT-based monitoring system with prediction capabilities for agricultural applications, provide an effective four-layer architecture, and implement the connectivity of greenhouse monitoring system devices over the Sigfox network.

Despite recent advances in IoT technologies, their implementation in agriculture remains challenging. One of the main problems is monitoring the variation of weather conditions in greenhouses or crop fields. It is necessary to efficiently place several measurement points within the crop fields to obtain more detailed information about the behavior of environmental conditions. This work aims to design and implement an

IoT-based monitoring system for hydroponic crops using a scalable, modular, and low-cost system architecture.

The system monitors weather conditions and risk factors affecting crop growth, considering temperature and humidity as relevant variables. For this, a customized IoT device was built using the Sigfox network to send the data to the Internet, and the ThingSpeak platform was used to visualize and analyze the data. A machine learning algorithm was created to predict temperature considering humidity and the data collected by the system to simulate future changes in climate variables. The system was validated in a hydroponic lettuce system in Loja. The main contribution of this research is to propose the application of a practical and scalable system to monitor and control climatic conditions in crops. The IoT structure consists of a four-layer architecture: a sensing layer to collect crop information, a network layer to facilitate Internet connections, a middleware layer to enable cloud services, and an application layer to deliver specific information to users.

The research is divided into sections: Section 1, introduction; Section 2, materials and methods; Section 3, architecture of the proposed IoT monitoring system; Section 4, design and implementation of the system components; Section 5, experimental validation of the implemented monitoring system; and Section 6, conclusions and future directions of the research.

## 2. Materials and methods

This research was conducted at the Marieta de Veintimilla School in Loja, with a quantitative experimental approach to develop and implement an IoT system for monitoring and predicting environmental variables such as temperature, humidity, and UV radiation. For this, a phased model was proposed according to the proposed architecture.

The first phase was to develop the IoT prototype using Sigfox technology and electronic components of free software and hardware. The second phase was to collect temperature and humidity data using DTH22 and ML8511 UV sensors to determine UV radiation. A Ufox controller synchronized to a real-time clock (RTC) unit was used as a central module, which activates and deactivates a water pump that provides liquid and nutrients to a hydroponic growing system. Sigfox technology transferred the real-time information to the ThingSpeak IoT platform.

The third phase focused on a data analysis method based on neural networks. The information collected by the sensors was the basis for the learning model to predict the variables related to the system and thus predict the environmental conditions that affect plant growth. The final phase was to present the data to the

user to monitor the status of the sensors and establish correlation. The inverse proportionality between the temperature and humidity variables, essential for determining cultivation parameters in the hydroponic system, was verified.

## 2.1. System architecture

The study of the Internet of Things (IoT) has resulted in extensive scientific literature. There are multiple architectures, frameworks, or conceptual models for IoT systems [13–17]. However, there is no single stan-

dard reference architecture that encompasses a variety of technologies. In [18, 19], the incorporation of IoT technologies for sustainable agriculture is discussed.

Figure 1 shows the proposed multi-layer architecture for the IoT-based hydroponic monitoring system. This design has four layers: sensing layer, network layer, middleware layer, and application layer, and streamlines production processes using a practical and scalable system. This means that the architecture allows monitoring several variables or an entire process at minimal cost, benefiting the cultivation process through hydroponic systems or smart farming.

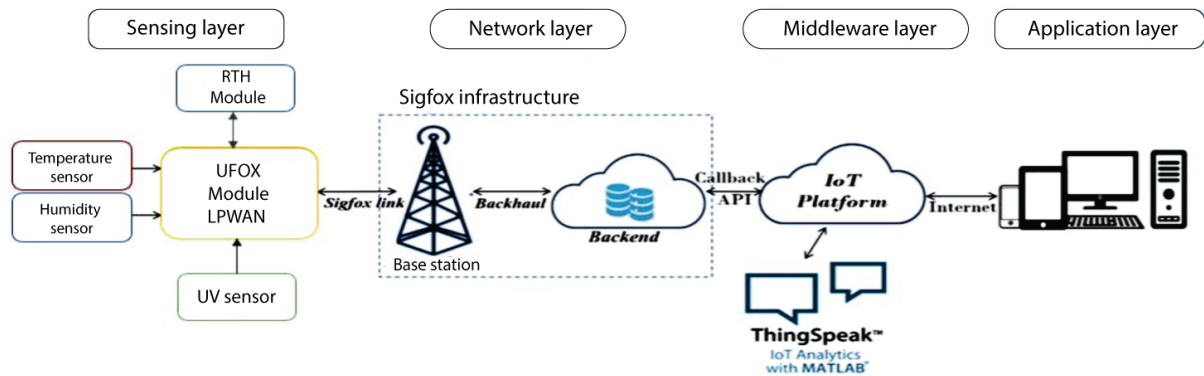


**Figure 1.** Proposed architecture for the monitoring system

Optimal plant growth conditions depend on the needs and requirements of each plant. Therefore, an environmental monitoring system is essential to maximize effective and sustainable crop production. Generally, the microclimatic parameters that determine crop productivity must be continuously monitored and controlled to create an optimal environment. However, climatic heterogeneity can cause significant differences in quantitative and qualitative plant characteristics, productivity, and the development of various diseases. The sensing layer shows the connected sensors and devices that enable remote climate monitoring.

Some environmental factors that affect plant growth are temperature, relative humidity, CO<sub>2</sub>, light, and water [20]. For this case study, the IoT device includes only temperature, relative humidity, UV radiation, and water and nutrient monitoring sensors. These sensors are connected to a digital, analog, and PWM input of a Ufox microcontroller with a Sigfox module integrator for communication. The RTC module connects using an I2C interface to the controller that controls the time for the recirculation of nutrients to the system. It has a real-time calendar that turns on a pump every four hours for ten minutes, sufficient time for adequate growth of the lettuce plants.

Communication technologies play an essential role in the implementation of IoT systems. There are sev-

eral standards for data transmission between sensors and IoT platforms. They can be classified as short-range wireless networks (e.g., Zigbee, Bluetooth, Z-Wave, Wifi, etc.) or long-range wireless networks (GPRS, 3G, 4G, and 5G). Short-range networks restrict the ability to provide global coverage, while conventional long-range networks are expensive and require much power. Consequently, IoT applications have driven a new type of wireless technology called low-power wide area network (LPWAN) [21]. These further wireless communications are better suited to machine-to-machine (M2M), and IoT devices; LoRaWAN, Sigfox, and NB-IoT are among the leading LPWAN technologies for IoT implementation. Each business activity has different requirements and specifications for IoT connectivity, such as coverage, performance, packet size, power consumption, cost, etc.

For hydroponic system monitoring applications, it is crucial to establish connections to use low-cost hardware with long-distance coverage and low power consumption, and scalability. This is why the connectivity of the proposed system to the IoT device over a Sigfox network was established. Once the data were collected at the IoT device, the LPWAN module sent the data to the Internet using the Sigfox network. The data communication followed the Sigfox protocol, where each device has a unique ID to route and sign



of fewer than  $\pm 0.5$  degrees Celsius at a resolution of 0.1 degrees. The sensing time was 2 seconds. The power supply range was 3 to 6 volts DC. Only one wire or conductor cable not exceeding 20 meters is required for connection to the microcontroller.

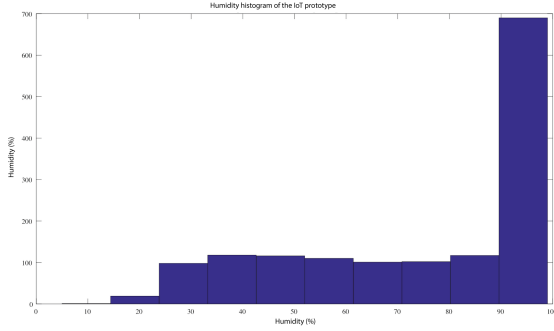


Figure 5. Humidity histogram of the created IoT device.

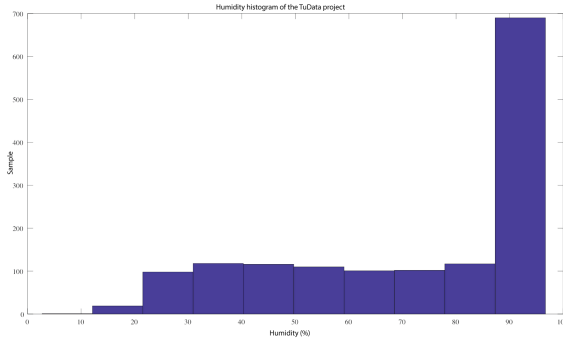


Figure 6. Relative humidity histogram of the TuData project.

### 2.3. Prediction

Artificial neural networks (ANNs) application for data analysis has increased considerably nowadays due to their multiple uses and advantages, such as adaptive learning, fault tolerance, and real-time operations [22]. ANNs predict climatic variables, greenhouse-type environments, and implicit variables, such as humidity, temperature, altitude, etc. ANN techniques are based on mathematical models that simulate the principles of biological neural networks, with the ability to learn from their environment [23]. They are generally distributed in layers and interconnected through a network architecture [24], where three layers can be distinguished: the input layer, the hidden layer, and the output layer. Other Machine Learning (ML) approaches, such as support vector machines, fuzzy logic, genetic models, etc., can be used in predicting weather variables. Still, the ANN model has an easy-to-implement structure and has shown better harmony between performance and complexity [25]. Based on a supervised analysis, an ML algorithm was defined using the R language to

analyze the patterns of a hydroponic system to predict temperature as a function of humidity following a three-layer model (input layer, hidden layer, and output layer) [23], because this structure is related to Kolmogorov's theory, which states that any continuous function can be approximated by a network with a hidden layer [26]. Figure 7 shows the implemented three-layer ANN

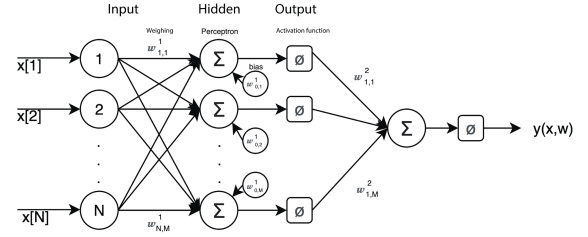


Figure 7. Structure of the proposed neural network.

The prediction of temperature ( $x$ ) over time ( $m$ ) is expressed as [26], using equation (1).

$$\hat{x}[m] = \sum_{j=0}^M w_{j,1}^{(2)} \phi(a_j) \quad (1)$$

With (2):

$$a_j = \begin{cases} 0 & \text{if } j = 0 \\ \sum_{i=0}^N \omega_{i,j}^{(1)} x[i] = X^T W_j^{(1)} & \text{otherwise} \end{cases} \quad (2)$$

Where  $\phi(a_j)$  is the output of the  $j$ -ésima neuron with activation function,  $\phi(a_j) = \text{tahn}(a_j)$ ,  $x = (1, x[1], \dots, x[N])^T$  the vector of input signals, and  $w = \{w_1^{(\iota)}, \dots, w_M^{(\iota)}\}$ , whit  $W_j^{(\iota)} = (W_{1,j}^{\iota}, \dots, W_{N,j}^{\iota})^T$  for  $\iota = 1, 2$ , the sets of all network weight and bias parameters. The transpose of a vector is denoted by  $()^T$ , and the identity activation function  $f(z) = z$  determines the total output of the neural network. Finally, the network is trained with a Resilient Back-propagation algorithm to calculate the error gradient.

### 3. Results and discussion

The proposed IoT monitoring system was implemented in a hydroponic system for growing lettuce in Loja, Ecuador. Soilless cultivation is becoming an effective technique for planting certain vegetables. Optimal temperatures for lettuce cultivation are cold climates ranging between 15 and 18 degrees Celsius, maximum temperatures between 18 and 24 degrees Celsius, and relative humidity of 70% [27]. The quantitative analysis of this study aims to provide information on the current understanding of new IoT technologies and their impact on existing production methods.

The size of the hydroponic system studied is approximately 400 plants, as shown in Figure 8. Ambient temperature and humidity measurements were taken every 10 minutes, totaling 144 samples daily for five months between January and May 2022. However, samples were missing due to some communication, power, or other failures. We estimated the missing samples using the nearest-neighbor imputation technique to solve this problem.

The ThingView application was used as a mobile user interface for real-time monitoring, interpretation, and visualization. This application functions as the interaction interface between the user and the system for precision crop control and monitoring. Figure 9 shows the measurement dataset from the web user

interface.



Figure 8. Case study hydroponic system

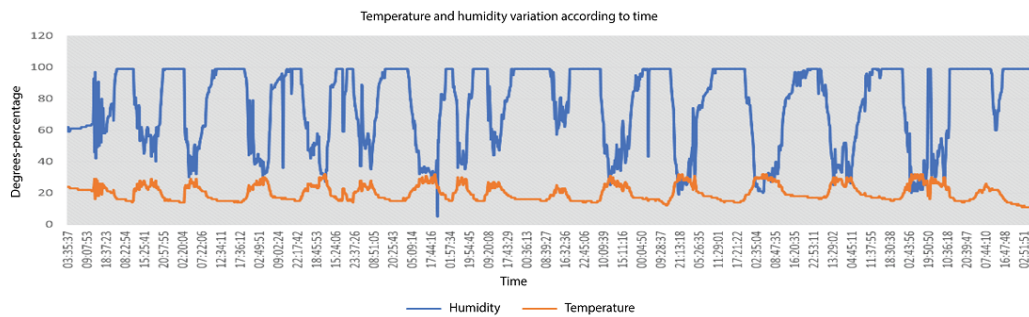


Figure 9. Temperature and humidity measurements

### 3.1. Training and testing of ANNs

Before the training and testing process for the adjustment of the prediction model, it was necessary to define the origin of the data taken from sensors with IoT technology. These data were transmitted and captured in real-time during January and May 2022, considering this time is the winter season according to the climatic zone. It was possible to collect 6000 records purified through a cleaning and validation process to obtain a total of 5063 base records for the experimentation that served as the primary input of the neural network.

The training data considered 70 % of the total validated records, while the remaining 30 % was used in testing. In the experimentation practice, a data normalization process was performed to achieve a better coupling between the model and the data, where  $d_{max}$  is the highest value in the data set and  $d_{min}$  is the lowest;  $r_{max} = 1$ , and  $r_{min} = -1$  represent the maximum and minimum values for the corresponding range mapping.

$$\bar{d}_s [kT] = \left[ \frac{d_s [kt] - d_{min}}{d_{max} - d_{min}} (r_{max} - r_{min}) \right] + r_{min} \quad (3)$$

After the training process, the optimized weights

and ANN biases were accurately calculated. The test data set was evaluated using the root mean square error (RMSE) and a confusion matrix to assess the accuracy of the predictions by performing a supervised analysis. The RMSE established the absolute level of fit that the model generated on the data by comparing the value predicted by the ML model with the actual value in the dataset [28] (equation (4)).

Where  $\hat{y}$  is a vector containing a data set of  $n$  predictions, and  $y$  is the vector of actual values to evaluate the denormalized prediction results compared to the simulated unscaled data.

$$RMSE = \frac{1}{n} \sum_{i=1}^n (\hat{y}_i - y_i)^2 \quad (4)$$

### 3.2. Prediction results

Implementing a design of homogeneous experiments was necessary to obtain the results. The primary variable analyzed was the number of neurons to be established in the network's hidden layer to determine the best scenario. The variables were also validated using correlation indexes, showing the association level between two quantitative random variables. A degree of correlation is considered to exist when the data of

one variable varies systematically with the values of the other [29].

Figure 10 shows a significant negative correlation index between the temperature and humidity variables corresponding to -0.95, which can be considered a strong negative correlation.

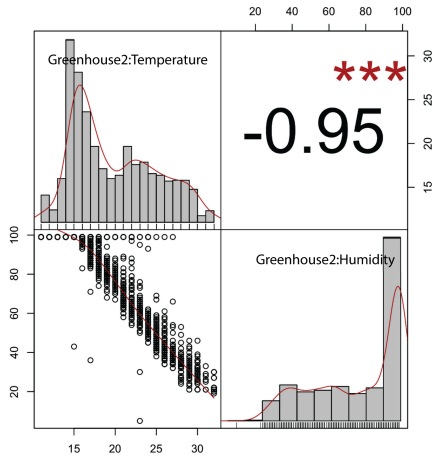


Figure 10. Correlation index.

The design of experiments emphasizes the number of neurons within the hidden layer of the network and

the interconnections generated by the relationships between them. The experiments were validated by randomized cross-validation. Table 1 shows the model, the number of neurons in the hidden layer, the RMSE value generated, and the prediction accuracy obtained.

The model that best fits this type of data is ANN 4, which consists of four neurons in the hidden layer and has a better performance, with an RMSE value of 0.11 and an accuracy of 89.37 %, according to the supervised data analysis. Figure 11 shows the structure of the neural network.

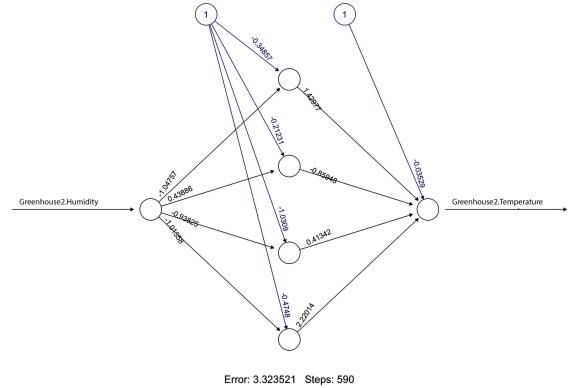


Figure 11. Neural network structure

Table 1. Model indications

Model	Neurons	Algorithm	Activation function	Learning rate	Threshold	RMSE	Accuracy
RNA 1	1	Resilient Backpropagation	Sigmoid	0.01	0.01	0.14	87.33%
RNA 2	2	Resilient Backpropagation	Sigmoid	0.01	0.01	0.13	88.01%
RNA 3	3	Resilient Backpropagation	Sigmoid	0.01	0.01	0.14	87.1%
RNA 4	4	Resilient Backpropagation	Sigmoid	0.01	0.01	0.11	89.37%
RNA 5	5	Resilient Backpropagation	Sigmoid	0.01	0.01	0.14	87.33%

Considering the variables analyzed, the experimental environment, and the data obtained, it can be stated that the temperature can be predicted with 89.37 % accuracy as a function of humidity, according

to the experiments performed and the ANN 4 model defined. Figure 12 shows the prediction results. The predicted values were compared with the actual temperature measured by the IoT system for one week

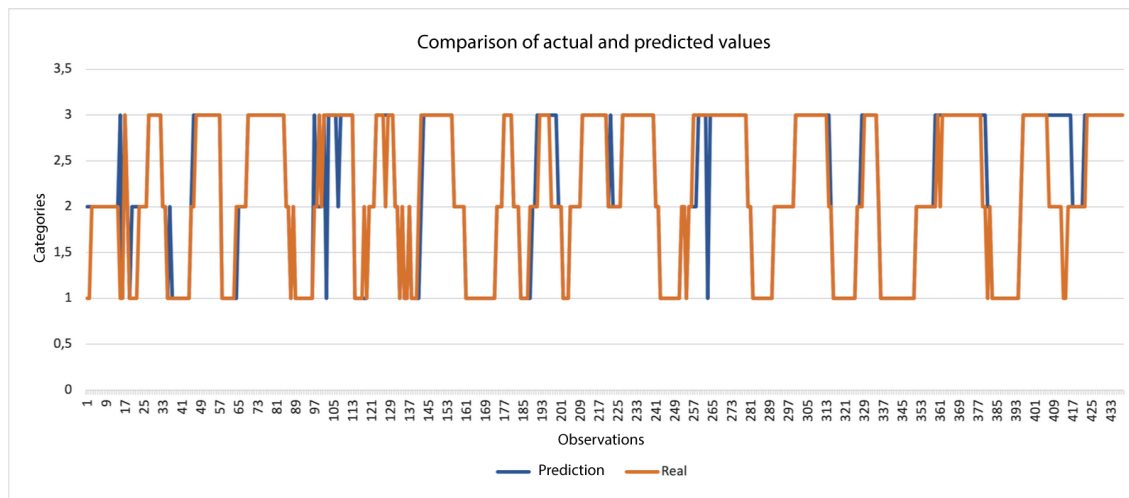


Figure 12. System temperature and expected temperature.

## 4. Conclusions

This research presented an IoT-based monitoring system for smart agriculture, designed and implemented to provide optimal conditions and cost-effective solutions for plant cultivation methods and life cycles of hydroponic systems. The system design, implementation, and machine learning application for environmental prediction were analyzed in detail. The IoT system was experimentally validated by monitoring temperature and humidity for five months. The system availability rate during this period was approximately 85 % due to human failures and packet loss. The case study demonstrated that 100% spatial coverage of the system could be achieved with only one IoT device for a hydroponic system with a capacity of 400 plants. Accurate automatic control for nutrient recirculation was conducted with 100 % functionality through the control of the RTC module.

A data-driven prediction model was implemented using an artificial neural network. The results showed that the ANN model could be used to predict temperature as a function of humidity; with a simple three-layer ANN and four neurons in the hidden layer, the prediction accuracy was 89.37 %. Compared to similar solutions, the proposed IoT framework is more flexible and meets the requirements for optimizing productivity and sustainability through emergent communication. Further studies will focus on experimental greenhouse validation using automatic control and long-term temperature and humidity predictions. Another relevant topic for future research could be implementing and evaluating specific operations and/or strategic decision-making using the proposed IoT system architecture.

## References

- [1] M. A. Montaña Blacio, J. E. Briceño Sarmiento, O. G. Jiménez Sarango, and E. E. González Malla, “Sistema integral de hogar inteligente basado en home assistant y raspberry PI,” *Tecnología e innovación frente a los desafíos de un siglo en curso*, pp. 101–126, 2021. [Online]. Available: <https://bit.ly/3IoQjYn>
- [2] S. Chen, H. Xu, D. Liu, B. Hu, and H. Wang, “A vision of IoT: Applications, challenges, and opportunities with china perspective,” *IEEE Internet of Things Journal*, vol. 1, no. 4, pp. 349–359, 2014. [Online]. Available: <https://doi.org/10.1109/JIOT.2014.2337336>
- [3] S. Singh, P. K. Sharma, B. Yoon, M. Shojafar, G. H. Cho, and I.-H. Ra, “Convergence of blockchain and artificial intelligence in IoT network for the sustainable smart city,” *Sustainable Cities and Society*, vol. 63, p. 102364, 2020. [Online]. Available: <https://doi.org/10.1016/j.scs.2020.102364>
- [4] A. Medela, B. Cendón, L. González, R. Crespo, and I. Nevaes, “IoT multiplatform networking to monitor and control wineries and vineyards,” in *2013 Future Network & Mobile Summit*, 2013, pp. 1–10. [Online]. Available: <https://bit.ly/3E6vwGx>
- [5] M. S. Farooq, S. Riaz, A. Abid, T. Umer, and Y. B. Zikria, “Role of IoT technology in agriculture: A systematic literature review,” *Electronics*, vol. 9, no. 2, p. 319, 2020. [Online]. Available: <https://doi.org/10.3390/electronics9020319>
- [6] L. García, L. Parra, J. M. Jimenez, J. Lloret, and P. Lorenz, “IoT-based smart irrigation systems: An overview on the recent trends on sensors and

- IoT systems for irrigation in precision agriculture,” *Sensors*, vol. 20, no. 4, p. 1042, 2020. [Online]. Available: <https://doi.org/10.3390/s20041042>
- [7] N. Zhang, M. Wang, and N. Wang, “Precision agriculture a worldwide overview,” *Computers and Electronics in Agriculture*, vol. 36, no. 2, pp. 113–132, 2002. [Online]. Available: [https://doi.org/10.1016/S0168-1699\(02\)00096-0](https://doi.org/10.1016/S0168-1699(02)00096-0)
- [8] M. Monica, B. Yeshika, G. S. Abhishek, H. A. Sanjay, and S. Dasiga, “IoT based control and automation of smart irrigation system: An automated irrigation system using sensors, GSM, bluetooth and cloud technology,” in *2017 International Conference on Recent Innovations in Signal processing and Embedded Systems (RISE)*, 2017, pp. 601–607. [Online]. Available: <https://bit.ly/3xlFgsv>
- [9] C. A. Hernández-Morales, J. M. Luna-Rivera, and R. Pérez-Jiménez, “Design and deployment of a practical IoT-based monitoring system for protected cultivations,” *Computer Communications*, vol. 186, pp. 51–64, 2022. [Online]. Available: <https://doi.org/10.1016/j.comcom.2022.01.009>
- [10] M. R. Ramli, P. T. Daely, D.-S. Kim, and J. M. Lee, “IoT-based adaptive network mechanism for reliable smart farm system,” *Computers and Electronics in Agriculture*, vol. 170, p. 105287, 2020. [Online]. Available: <https://doi.org/10.1016/j.compag.2020.105287>
- [11] R. Zheng, T. Zhang, Z. Liu, and H. Wang, “An EIoT system designed for ecological and environmental management of the xianghe segment of China’s Grand Canal,” *International Journal of Sustainable Development & World Ecology*, vol. 23, no. 4, pp. 372–380, 2016. [Online]. Available: <https://doi.org/10.1080/13504509.2015.1124470>
- [12] C. Gómez, J. C. Veras, R. Vidal, L. Casals, and J. Paradells, “A sigfox energy consumption model,” *Sensors*, vol. 19, no. 3, p. 681, 2019. [Online]. Available: <https://doi.org/10.3390/s19030681>
- [13] M. Montaño, R. Torres, P. Ludeña, and F. Sandoval, “IoT management analysis using SDN: Survey,” in *Applied Technologies*, M. Botto-Tobar, S. Montes León, O. Camacho, D. Chávez, P. Torres-Carrión, and M. Zambrano Vizuete, Eds. Springer International Publishing, 2021, pp. 574–589. [Online]. Available: [https://doi.org/10.1007/978-3-030-71503-8\\_45](https://doi.org/10.1007/978-3-030-71503-8_45)
- [14] R. K. Singh, R. Berkvens, and M. Weyn, “Agrifusion: An architecture for IoT and emerging technologies based on a precision agriculture survey,” *IEEE Access*, vol. 9, pp. 136 253–136 283, 2021. [Online]. Available: <https://doi.org/10.1109/ACCESS.2021.3116814>
- [15] G. Codeluppi, A. Cilfone, L. Davoli, and G. Ferrari, “Lorafarm: A lorawan-based smart farming modular iot architecture,” *Sensors*, vol. 20, no. 7, p. 2028, 2020. [Online]. Available: <https://doi.org/10.3390/s20072028>
- [16] V. P. Kour and S. Arora, “Recent developments of the internet of things in agriculture: A survey,” *IEEE Access*, vol. 8, pp. 129 924–129 957, 2020. [Online]. Available: <https://doi.org/10.1109/ACCESS.2020.3009298>
- [17] X. Shi, X. An, Q. Zhao, H. Liu, L. Xia, X. Sun, and Y. Guo, “State-of-the-art internet of things in protected agriculture,” *Sensors*, vol. 19, no. 8, p. 1833, 2019. [Online]. Available: <https://doi.org/10.3390/s19081833>
- [18] Y. Liu, X. Ma, L. Shu, G. P. Hancke, and A. M. Abu-Mahfouz, “From industry 4.0 to agriculture 4.0: Current status, enabling technologies, and research challenges,” *IEEE Transactions on Industrial Informatics*, vol. 17, no. 6, pp. 4322–4334, 2021. [Online]. Available: <https://doi.org/10.1109/TII.2020.3003910>
- [19] S. Santiteerakul, A. Sopadang, K. Yaiyuathet Tip-payawong, and K. Tamvimol, “The role of smart technology in sustainable agriculture: A case study of wangree plant factory,” *Sustainability*, vol. 12, no. 11, p. 4640, 2020. [Online]. Available: <https://doi.org/10.3390/su12114640>
- [20] R. Pertierra Lazo and J. Quispe Gonzabay, “Análisis económico de lechugas hidropónicas bajo sistema raíz flotante en clima semiárido,” *La Granja: Revista de Ciencias de la Vida*, vol. 31, no. 1, pp. 118–130, 2020. [Online]. Available: <http://doi.org/10.17163/lgr.n31.2020.09>
- [21] D. D. Olatinwo, A. Abu-Mahfouz, and G. Hancke, “A survey on LPWAN technologies in WBAN for remote health-care monitoring,” *Sensors*, vol. 19, no. 23, p. 5268, 2019. [Online]. Available: <https://doi.org/10.3390/s19235268>
- [22] C. A. Ruiz and D. J. Matich, *Redes neuronales: Conceptos básicos y aplicaciones*. Universidad Tecnológica Nacional, Facultad Regional Rosario, 2001. [Online]. Available: <https://bit.ly/418PqdY>
- [23] C. M. Bishop, *Pattern Recognition and Machine Learning*. Springer, 2006. [Online]. Available: <https://bit.ly/3k6Ct3o>
- [24] I. Ullah, M. Fayaz, N. Naveed, and D. Kim, “ANN based learning to kalman filter algorithm for indoor environment prediction

- in smart greenhouse,” *IEEE Access*, vol. 8, pp. 159 371–159 388, 2020. [Online]. Available: <https://doi.org/10.1109/ACCESS.2020.3016277>
- [25] D.-H. Jung, H. S. Kim, C. Jhin, H.-J. Kim, and S. H. Park, “Time-serial analysis of deep neural network models for prediction of climatic conditions inside a greenhouse,” *Computers and Electronics in Agriculture*, vol. 173, p. 105402, 2020. [Online]. Available: <https://doi.org/10.1016/j.compag.2020.105402>
- [26] R. O. Duda, P. E. Hart, and D. G. Stork, *Pattern Classification*. John Wiley & Sons, 2012. [Online]. Available: <https://bit.ly/3RZpY6g>
- [27] G. Saavedra, F. Corradini, A. Antúnez, S. Felmer, P. Estay, and P. Sepúlveda, *Manual de producción de lechuga*. Instituto de Investigaciones Agropecuarias (INIA)., 2017. [Online]. Available: <https://bit.ly/3RY6lf3>
- [28] E. L. Lehmann and G. Casella, *Theory of Point Estimation*. Springer Science & Business Media, 2006. [Online]. Available: <https://bit.ly/3jX6XFb>
- [29] S. van Dongen and A. J. Enright, “Metric distances derived from cosine similarity and Pearson and Spearman correlations,” 2012. [Online]. Available: <https://doi.org/10.48550/arXiv.1208.3145>



# METHODOLOGY BASED ON DATA SCIENCE FOR THE DEVELOPMENT OF A FORECAST OF THE POWER GENERATION OF A PHOTOVOLTAIC SOLAR PLANT

## METODOLOGÍA BASADA EN CIENCIA DE DATOS PARA EL DESARROLLO DE PRONÓSTICO DE LA GENERACIÓN DE ENERGÍA DE UNA PLANTA SOLAR FOTOVOLTAICA

César A. Yajure-Ramírez<sup>1,\*</sup>

Received: 03-03-2023, Received after review: 21-04-2023, Accepted: 26-04-2023, Published: 01-07-2023

### Abstract

The use of photovoltaic solar plants for the generation of electrical energy has been constantly increasing in recent years, and many of these plants are connected to the external electrical network, which makes it necessary to forecast the electrical energy generated by the solar plants to assist in the management of the network operator. This research presents a methodology based on data science to develop the forecast of electrical energy generated from photovoltaic solar plants, using three different techniques for comparison purposes: time series analysis, multiple linear regression, and artificial neural network. Historical data of peak power, solar irradiance, ambient temperature, wind speed, and soiling rate from an experimental NREL photovoltaic solar plant were used. To evaluate the performance of the models, the RMSE, MAE, and MAPE metrics are used, resulting in the ARIMA model of the time series analysis having the best performance with a MAE of 1.38 kWh, RMSE of 1.40 kWh, and MAPE of 6.35%. In the correlation analysis, it was determined that power generation was independent of the soiling rate, so this variable was discarded in the regression models.

**Keywords:** Machine learning, solar irradiance, artificial neural network, linear regression, time series, ambient temperature.

### Resumen

El uso de plantas solares fotovoltaicas para la generación de energía eléctrica ha ido en constante aumento en los últimos años. Muchas de estas se conectan a la red eléctrica externa, por lo que se hace necesario el pronóstico de la energía eléctrica generada por las plantas solares para coadyuvar en la gestión del operador de la red. En esta investigación se presenta una metodología basada en la ciencia de datos para desarrollar el pronóstico de energía eléctrica generada de plantas solares fotovoltaicas, utilizando, para efectos de comparación, tres técnicas diferentes: análisis de series de tiempo, regresión lineal múltiple, y red neuronal artificial. Se trabajó con los datos históricos de la potencia pico, la irradiancia solar, la temperatura ambiente, la velocidad del viento, y la tasa de suciedad, de una planta solar fotovoltaica experimental del NREL. Para evaluar el desempeño de los modelos se utilizan las métricas RMSE, MAE, y MAPE, resultando que el modelo ARIMA del análisis de series de tiempo fue el que mejor desempeño tuvo con un MAE de 1.38 kWh, RMSE de 1.40 kWh, y MAPE de 6.35%. En el análisis de correlación se determinó que la generación de energía era independiente de la tasa de suciedad, por lo que se descartó esta variable en los modelos de regresión.

**Palabras clave:** aprendizaje automático, irradiancia solar, red neuronal artificial, regresión lineal, serie de tiempo, temperatura ambiente

<sup>1,\*</sup>Posgrado en Investigación de Operaciones, Universidad Central de Venezuela, Venezuela.  
 Corresponding author ✉: cyajure@gmail.com.

Suggested citation: Yajure-Ramírez, C. A. "Methodology based on data science for the development of a forecast of the power generation of a photovoltaic solar plant," *Ingenius, Revista de Ciencia y Tecnología*, N.º 30, pp. 19-28, 2023, DOI: <https://doi.org/10.17163/ings.n30.2023.02>.

## 1. Introduction

The use of renewable energy sources for electricity production has increased in recent years due to public policies in some countries aimed at reducing environmental pollution caused by fossil fuel sources and bringing electricity to remote places where the traditional power grid does not reach. According to the 2022 Global Renewable Energy Status Report, in 2011, 20.4% of electricity came from renewable sources, mainly hydro, solar, wind, bioenergy, and geothermal. In 2021 this percentage increased to 28.3% (15% hydro, 10% solar and wind, and 3% bioenergy and geothermal). As for solar photovoltaic energy, in 2021, there were 942 GW of installed capacity for electricity generation worldwide, showing an increase of 23% compared to 2020 [1].

The use of solar energy for electricity production has been evolving technologically, so the use of solar photovoltaic plants connected to the external power grid has been increasing, reporting an increase of 20% worldwide by 2021 [1]. The energy coming from solar photovoltaic plants is subject to climatic variations, specifically solar irradiance, and temperature. To contribute to the stability and reliability of the electrical system, it is necessary to develop forecasts of the energy generated considering the historical data of these climatic variables. This forecast also contributes to improving the management of the operation and maintenance of these solar photovoltaic plants.

Therefore, this research aims to present a methodology based on data science to develop the forecast of electric power generation from solar photovoltaic plants and to present a comparative study of three different techniques to obtain the forecast models: ARIMA (Autoregressive Integrated Moving Average) model of time series analysis, multiple linear regression, and artificial neural network. For the evaluation of the models, the metrics mean absolute error (MAE), root mean square error (RMSE), mean absolute percentage error (MAPE), and the coefficient of determination  $R^2$  were used.

Several research studies on the proposed objectives were reviewed, and various publications were found. Mittal *et al.* [2] reviewed the use of machine learning for photovoltaic power forecasting, reaffirming that solar irradiance and temperature are essential for this forecast. They concluded that hybrid models are the best option for better predicting solar photovoltaic energy.

Sharkawy *et al.* [3] developed a study using a neural network to create a short-term solar plant power forecasting model. They considered five days of data to train the model and the remaining day of data to evaluate the model. The input variables were temperature and radiation. They concluded that the model obtained is adequate since, in training, the RMSE was

0.187 MWh, and in the forecasting phase, the absolute error was 0.08 MWh. Kasagani y Manickam [4] conducted a daily power forecasting study using artificial neural networks and the historical data of power, operating hours, daily global solar radiation, and ambient temperature of the solar photovoltaic plant. As a performance metric, they used the relative RMSE. They concluded that the forecast using an artificial neural network with three neurons in the hidden layer was the best performing, with a MAPE of 4.18% and a relative RMSE of 5.74%. Pattanaik *et al.* [5] performed a comparative analysis of different methods for power forecasting of a solar photovoltaic plant. They concluded that forecasting using genetic algorithms is more convenient and accurate than statistical analysis.

Akhter *et al.* [6] reviewed the methods for forecasting electric power generated by solar photovoltaic plants based on machine learning and metaheuristic techniques. They showed the advantages and disadvantages of each method and compared heuristic methods with machine learning methods. They concluded that hybrid techniques (composed of at least two methods) are the most accurate for all forecast horizons, with a reduction of about 15% in MAPE and RMSE. Alaraj *et al.* [7] developed a decision tree ensemble-based model for power forecasting of a solar photovoltaic plant, using meteorological data from Qassim in Saudi Arabia and comparing their results with other models. They considered the metrics RMSE, MAE, MAPE, and training time to evaluate the model. They concluded that the ENBG model is the best-performing model, with an MAE of 8.89 W in the training phase and 12.05 W in the test phase.

Anuradha *et al.* [8] analyzed the power forecasting of a solar photovoltaic plant by applying different machine-learning techniques and using historical data of climatic variables and generated power. The techniques used were support vector machine, random forests, and linear regression. They concluded that the random forest regression model was the most accurate in its results, with 94.01%. Borunda *et al.* [9] presented a fast methodology to evaluate the best location of a solar photovoltaic plant and to forecast the electric power it will generate, using historical data of climatic variables and machine learning algorithms. They validated the methodology by comparing it with real solar photovoltaic plants in Mexico.

This research consists of several sections; Section 2 explains the methodology and data used in the study; Section 3 shows the results obtained; and Section 4 shows the research conclusions. The bibliographic references used are also shown.

## 2. Materials and methods

The methodology consists of applying the stages of a data science project, applying its methodology in each stage. According to VanderPlas [10], data science is an interdisciplinary area that includes, in turn, three different areas: statistical skills to model and summarize data; computer skills to design and use algorithms to store, process and visualize these data efficiently; and expertise in the specific field or business of research, which in this work, is the generation of electric power from solar photovoltaic plants.

Cielen's work [11] presents the stages of a data science project. The first stage consists of establishing the objectives to be achieved, which requires knowledge of the field, i.e., generation from solar photovoltaic plants and meeting needs. The second stage consists of obtaining the data of interest, which, in this case, correspond to the regular measurements of the variables in a solar photovoltaic plant from its data acquisition system. The variables required to form the data set depend on the project objective(s). Once the dataset is available, the next step is to process the data, which consists of reviewing, cleaning, transforming, and combining these data to have the appropriate structure. Then, exploratory data analysis is performed using statistical and graphical techniques that can be univariate, bivariate, or multivariate. At this stage, knowledge of interest for the study may already be found, so some projects only reach this stage. If the knowledge from the previous step is insufficient, or if the idea is to move on, the data modeling stage is implemented, which consists of applying mathematical algorithms to obtain models that deepen the knowledge acquired. The number and type of algorithms depend on the objectives set in the first stage. Finally, the decision-making stage is reached, considering the results obtained.

One might think that the stages of a data science project are applied sequentially; however, there may be cases where this does not occur. Depending on the results obtained in the exploratory analysis stage and/or the modeling stage, it may be necessary to return to the data processing stage to improve the structure of the data, to the data collection stage to obtain some other variable, or even to the first stage to reformulate the project objectives.

The methodology is applied to data from a particular solar photovoltaic plant. This section presents the data collection and data processing stages. The exploratory data analysis and modeling stages are shown in the next section.

### 2.1. Data collection

The data used in this research come from the data acquisition system of a solar photovoltaic plant at the U.S. National Renewable Energy Laboratory (NREL)

in Golden, Colorado. They were collected from the public dataset web page of the NREL data acquisition system [12].

The plant comprises five Sanyo mono-silicon solar panels with 200 watts of peak power each [13]. These panels are installed in a fixed mounting, with a 40° tilt angle and an azimuth angle 180°. The data correspond to measurements taken and stored every minute of the plant's peak power output ("ac\_power") in watts, ambient temperature ("ambient\_temp") in degrees Celsius, irradiance ("poa\_irradiance") in watts per square meter, wind speed in meters per second ("wind\_speed"), and soiling rate ("soiling"). Data collection began on February 25, 2010, and ended on December 13, 2016, with 1.558.875 rows (records or instances).

### 2.2. Data processing

Data processing techniques are applied at this stage, such as detecting possible missing data or duplicate rows, outlier detection, data transformation, data column combination, and verifying the appropriate format for the different variables. The way to apply these and other techniques using the Python programming language is described in [14].

After an initial review, seven missing data were detected in the ambient temperature variable, and 17 362 missing data in the wind speed variable. The rows with missing temperature data correspond to less than 0.001% of the total rows, and the rows with missing wind speed data correspond to approximately 1.11% of the total rows. Although these percentages are low, it was decided to attribute them to the mean value of the three data closest to the missing data. It is worth mentioning that no duplicate rows were detected.

Considering the data in the original date column, columns corresponding to the data reading's year, month, week, day, and hour were created. Likewise, considering the column of peak electric power, the column of generated electric energy ("ac\_energy") in kilowatt hours (kWh) was created, which is used as the target variable in the forecast models. As for the ambient temperature, it was rescaled from Celsius to Kelvin units.

It was detected that there were no records for January, September, and October 2010, which could alter the results of the exploratory analysis. Consequently, this analysis was performed with existing data between 2011 and 2016.

## 3. Analysis and results

This section presents the stages of exploratory analysis, data modeling, and the discussion of results.

### 3.1. Exploratory data analysis

After processing the data in the previous stage, 1,429,678 rows or records were obtained corresponding to the minute values of the measurements of the variables and the other variables that were generated. Data sets with daily, weekly, monthly, and annual resolutions were obtained for analysis. This was achieved by grouping the original data with minute resolution in the corresponding period.

Table 1. shows the results of the descriptive analysis of the daily data using univariate statistics. It can be observed that, except for the (soiling) rate, the mean value of the variables is close to the median value. The range of the solar irradiance and wind speed variables is high, with the mean value closer to the minimum value than the maximum value.

**Table 1.** Descriptive statistical summary of the data.

Statistics	Variables				
	ac_energy	ambient_temp	poa_irradiance	soiling	wind_speed
Mean	4.19	286.96	465.02	95.87	1.76
Standard deviation	1.66	9.91	165.34	4.28	0.71
Minimum	0.00	252.21	33.34	75.89	0.00
First quartile	3.22	279.67	360.27	94.12	1.32
Median	4.57	287.30	490.45	97.40	1.60
Third quartile	5.48	295.28	595.11	99.00	1.99
Maximum	6.98	306.29	1,237.92	100.00	6.15

Next, a correlation analysis was performed considering the climatic variables, the soiling rate, and the AC electric generation, with data on a daily scale. According to Navlani *et al.* [15], Pearson's method is used when the data are symmetrically distributed (normal) to calculate the correlation coefficient. However, Spearman's method is recommended when the data has asymmetry and/or outliers. Kendall's method is used when the data is not required to follow some distribution. Because of this, all three methods were used to calculate the coefficients of all variables concerning AC electric power. The results are shown in Table 2.

**Table 2.** Correlation coefficients.

Variable	Method		
	Pearson	Spearman	Kendall
ac_energy	1.00	1.00	1.00
poa_irradiance	0.78	0.83	0.71
ambient_temp	0.43	0.32	0.21
wind_speed	0.27	0.30	0.20
soiling	0.01	0.02	0.02

To interpret the values shown in Table 2, it should be remembered that the correlation coefficient varies between "-1" and "1". When the value is positive, the direction of increase or decrease of the pair of variables is the same, and when the value is negative, the direction is the reverse. On the other hand, the absolute value "1" means that the magnitude of growth or

decrease is equal for both variables, while the value "0" means that the pair of variables is not related at all. For the values between "0" and "1", we consider Ratner [16], who states that "values between 0 and 0.3 (0 and -0.3) indicate a weak positive (negative) relationship. Values between 0.3 and 0.7 (-0.3 and -0.7) indicate a moderate positive (negative) relationship. Values between 0.7 and 1.0 (-0.7 and -1.0) indicate a strong positive (negative) relationship".

Considering the results in Table 2, solar irradiance has a strong and positive relationship with electric power. Ambient temperature has a positive and moderate relationship with electric power. The relationship of wind speed with electric power is positive, weak to moderate. While for this case, the relationship between soiling rate and electric power is practically independent.

Then, time curves were generated for the main variables of the data set. Figure 1 shows the behavior of the average solar irradiance (bars) vs. the electrical energy generated (line) for each of the years of the study period.

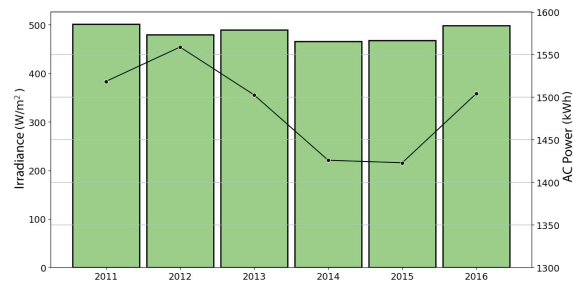


**Figure 1.** Solar irradiance vs. AC power

The average solar irradiance remained approximately constant during the study period. The energy generated reached its maximum value in 2012, decreased to minimum values during 2014 and 2015, and increased again in 2016.

Figure 2 shows the average monthly values of solar irradiance, electric power, and AC energy generated. The monthly energy production remained relatively constant during the whole period, and the behavior of the power almost perfectly followed the behavior of the solar irradiance.

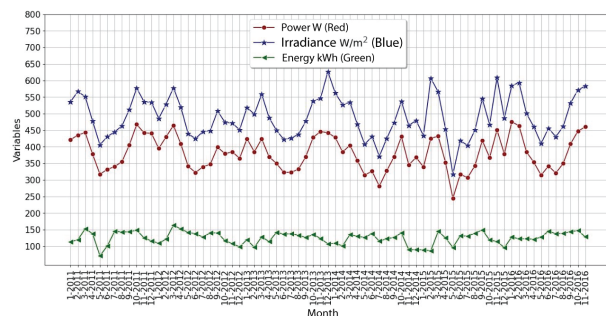


**Figure 2.** Monthly behavior of the variables

Figure 3 shows the weekly average values of solar irradiance and electric power, and the AC power generated per week of the year. The behavior of electric power and solar irradiance is almost identical. As for electric power, it reached its minimum value in the fifth week of the year and its maximum value in the thirteenth week. The energy generated decreased in the last five weeks of the year.

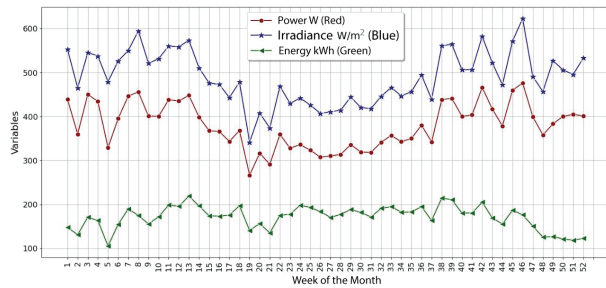


Figure 3. Weekly behavior of the variables

Figure 4 shows the daily average values of solar irradiance and electrical power, and the energy generated on each day of the month. Unlike the previous curves, in this case, the shapes of the three curves are approximately the same, with minimum values at the beginning and middle of the month. The curves do not have any defined trend (upward or downward).

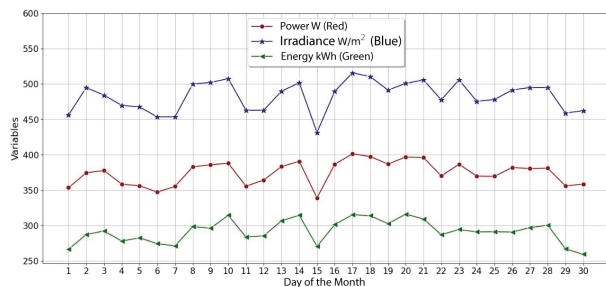


Figure 4. Daily behavior of the variables

To visualize the symmetry and dispersion of the data, Figure 5 shows the Box-Plot diagrams of each variable on a weekly scale. Previously, the values of each variable were scaled between zero and one for comparison.

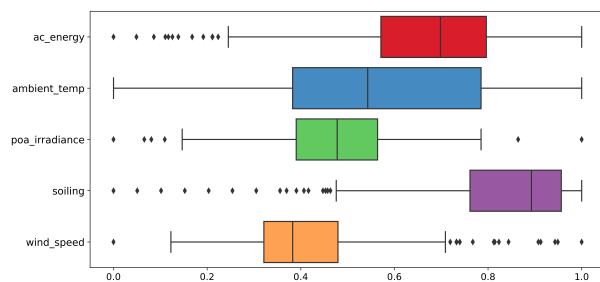


Figure 5. Box-Plot diagrams of the variables

According to Figure 5, it can be said that except ambient temperature, all the other variables present outliers. It is worth mentioning that they are slight outliers, according to Tukey's test [17], so they are not imputed. Solar irradiance is the most symmetrical variable, besides having few outliers. The soiling rate is the variable with the most outliers and the highest asymmetry. Ambient temperature is the variable with the highest dispersion in its data, and solar irradiance is the variable with the lowest dispersion.

### 3.2. Data modeling

Mathematical algorithms were applied to obtain forecasting models of the generated electric power. Specifically, a multiple linear regression model, an artificial neural network regression model, and a time series analysis model were obtained using weekly data. The data correspond to 310 weeks, from week 41, 2010, to week 47, 2016. The data from week 48 to week 50, 2016, were used to compare the forecast obtained from the three models mentioned above.

#### 3.2.1. Multiple Linear Regression Algorithm

The multiple linear regression algorithm (MLR) is a supervised machine learning algorithm. The model obtained from this algorithm is linear in the parameters (coefficients) and not necessarily in the explanatory or predictor variables. The target variable is AC electric energy in kWh, while the predictor variables are solar irradiance ("poa\_irradiance"), ambient temperature ("ambient\_temp"), and wind speed ("wind\_speed"). The soiling rate was not considered due to its null correlation with the target variable; moreover, in the first regression model, its coefficient in the regression equation was not statistically significant.

It was verified that there are no significant correlations between the predictor variables, as shown in Figure 6. All the absolute values of the correlation coefficient are less than 0.3, indicating weak relationships between the variables.

The data set, consisting of the objective and predictor variables, was randomly divided into two parts. The first part, composed of 80% of the data (256 records), was used to create and train the regression model. The second part, consisting of 20% (64 records), evaluated the model obtained in the training phase. The metrics used to assess the model were MAE and RMSE since, according to [18], they are statistical measures used to evaluate models. The  $R^2$  was used, which according to Hair *et al.* [19], is a "measure of the proportion of the variance of the dependent variable concerning its mean that is explained by the independent or predictor variables". Alaraj *et al.* [7] use the same metrics except for the  $R^2$ .

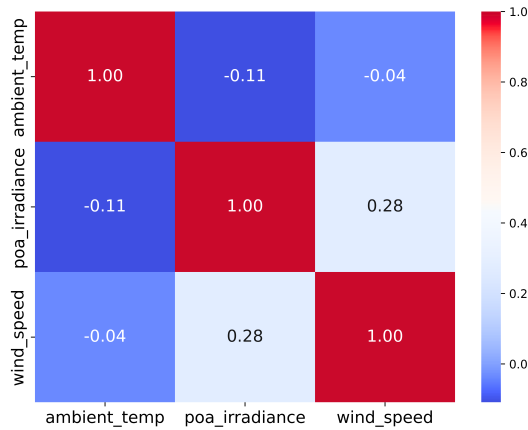


**Figure 6.** Correlation matrix of the predictor variables

After applying the algorithm, the coefficients 0.446, 0.043, and 4.002 were obtained for the predictor variables ambient temperature, solar irradiance, and wind speed, respectively. This indicates that a unit increase in the weekly average ambient temperature means an increase of 0.446 kWh; a unit increase in solar irradiance implies a rise of 0.043 kWh in power generation, and a unit increase in the weekly average of wind speed means an increase of about 4 kWh in weekly power generation. The value of the intercept is -125.98.

Table 3 shows the results of the performance metrics. The predictor variables explain about 81% of the variance of the objective variable, indicating that the model has a good fit quality. Since the average weekly generated electric power is 29 kWh, the obtained RMSE (2.87) corresponds to almost 10% of the mean, and the obtained MAE (2.30) is nearly 8%.

**Table 3.** RLM model indicators.

Indicator	Value Obtained
$R^2$	0.81
RMSE (kWh)	2.87
MAE (kWh)	2.30
<b>Shapiro-Wilk test to the residuals</b>	
Statistic	0.995
p-value	0.998

The Shapiro-Wilk test statistic was used to verify the statistical assumption of normality of the residuals required by this model, which has as its null hypothesis that the data are normally distributed. The test statistic varies between 0 and 1, indicating that the data are normally distributed when it is close to 1. To verify the rejection or not of the null hypothesis, the p-value is considered. Table 3 also shows that the value of 0.995 for the statistic and a p-value of 0.998 (greater than 5% statistical significance) suggest insufficient evidence to reject the null hypothesis that the residuals are normally distributed [20].

### 3.2.2. Artificial neural network algorithm

When applying the artificial neural network (ANN), the same data used for the multiple linear regression model, the same objective variable, and the same predictor variables were used. For cross-validation of the model, 80% of the data (256 records) were used for training, and 20% of the data (64 records) were used for evaluation.

According to Kapoor *et al.* [21], a "multilayer perceptron" model was used, composed of the input layer, the output layer, and a group of hidden layers between the input and output. Three layers were used for this study: an input layer, an output layer, and a hidden layer. All the layers are dense because, according to Moolayil [22], "a dense layer is a regular layer that connects all its neurons with all the neurons of the previous layer".

The activation functions were defined for each of the network layers. The rectified linear activation function (ReLU) was applied for the input and hidden layers, allowing only positive values to pass through. These two layers have a total of 256 neurons each. As for the output layer, this has a linear activation function so as not to limit the forecast values, and it has only one neuron, which is needed to forecast the electrical energy. According to Chollet [23], a loss function is required, which is used to control the deviation of the forecast from its expected value; so, for this study, MAE and MSE were used as loss functions. If the deviation is not adequate, its value is fed back to the input through an optimization function, which according to Chollet [23], updates the input weights and repeats the cycle. In this research, he used the root-mean-square propagation optimizer (RMSProp). Sharkawy *et al.* [3] also use an ANN with three layers but with a hyperbolic activation function.

Table 4 shows the results obtained by applying the ANN algorithm. The quality of the fit is around 88%, which is better than that obtained with the RLM model. Both RMSE and MAE are lower than those obtained with the MLR model. As for the analysis of the residuals, they are normally distributed since the test statistic is close to 1 and the p-value is higher than 5% of statistical significance.

**Table 4.** ANN model indicators.

Indicator	Value obtained
$R^2$	0.88
RMSE (kWh)	2.35
MAE (kWh)	1.85
<b>Shapiro-Wilk test to the residuals</b>	
Estadístico	0.967
p-valor	0.422

### 3.2.3. Time series analysis

When applying the analysis to the time series of the generated AC electric power, an ARIMA model is obtained, which requires three parameters: the order of the autoregressive part  $p$ , the order of integration  $d$ , and the order of the moving average  $q$ . If the series is seasonal, the three parameters for the seasonal part ( $P$ ,  $D$ ,  $Q$ ) must also be considered. The model is obtained by applying the Box-Jenkins methodology, presented in [24] and mentioned in more detail in [25].

The methodology starts with data preparation, including transformation to stabilize variance and/or differencing to make the series stationary (parameter  $d$  is defined). The potential initial models are selected using the autocorrelation and partial autocorrelation functions (parameters  $p$  and  $q$  are defined). The parameters of the possible models are estimated, and the best of them is selected using a performance criterion. This criterion is usually the AIC (Akaike Information Criteria), which, according to [26], is the most popular for selecting the best model. This is followed by the diagnostic stage, in which the residuals are analyzed to verify that they are equal or approximately equal to white noise. Finally, the model is used to forecast the time series.

Following the methodology, the extended Dickey-Fuller test is applied to verify the stationarity of the AC power series. According to Gujarati and Porter [27], this test is also known as the unit root test and is popular in determining the stationarity or non-stationarity of a time series. The test statistic was less than the three critical values (1%, 5%, 10%). The p-value is approximately equal to zero, so the null hypothesis of the existence of a unit root is rejected. Therefore, it can be said that the series in level is stationary. The latter implies that the parameter  $d$  is zero.

Figure 7 shows the graphs of the autocorrelation function (upper) and the partial autocorrelation function (lower) of the AC power series, considering up to 106 lags because the data present annual seasonality (52 weeks). There are at least two significant autocorrelation values. The series is confirmed to be seasonal, with the first seasonal value (week 52) significant for both graphs, which should be considered in the proposed model.

After performing the corresponding iterations minimizing the value of the AIC metric and checking the characteristics of the residuals obtained with each model, the model selected for forecasting is ARIMA(0,0,2)(1,1,1)52. The results obtained from forecasting with the ARIMA model and the other models are presented below.

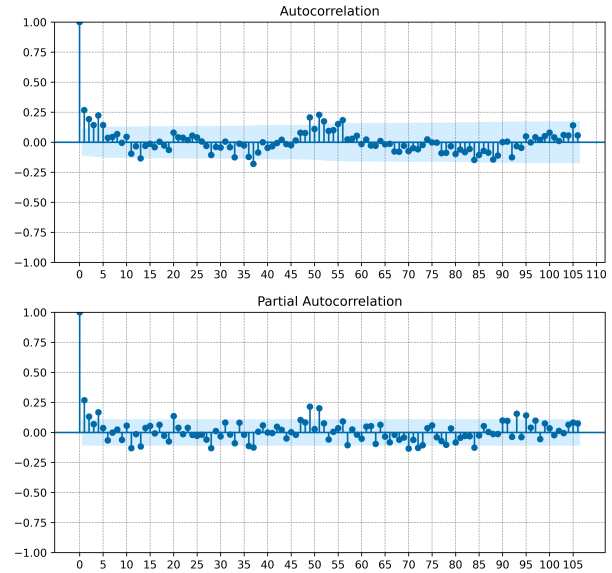


Figure 7. Autocorrelation and partial autocorrelation functions

### 3.2.4. Comparison of forecasts

Forecasts of electric power generated for weeks 48, 49, and 50 of 2016 were performed using each of the three models and were evaluated using RMSE, MAE, and MAPE metrics. Table 5, shows the results of the energy forecast in kWh, indicating that the ARIMA model forecast is the closest to the actual values of energy generated.

Table 5. Pronósticos de energía AC.

Week	Real Energy	MRL Forecast	ANN Forecast	ARIMA Forecast
48	23.63	28.15	30.13	25.04
49	20.20	23.68	22.48	18.54
50	21.92	27.36	26.02	22.97

Table 6 shows the performance metrics of the three models for the forecasts presented in Table 5. The ARIMA model is the best performer, with a MAPE of about 6% versus almost 20% for the other two models. The MAE and RSME are much lower for the ARIMA model.

Table 6. Performance of the models.

Metrics	Models		
	MLR	ANN	ARIMA
MAE (kWh)	4.48	4.29	1.38
RMSE (kWh)	4.55	4.63	1.40
MAPE (%)	20.39	19.16	6.35

The results in Table 6 agree with those reported by [25] since these authors state that moving average

methods are suitable for the short term and that regression methods are more appropriate for the medium and long term. For these authors, the "short term" is associated with periods of up to three months, while the "long term" refers to more than two years.

#### 4. Conclusions

The behavior of the electrical energy generated over time is similar to the behavior of the solar irradiance for data with a resolution close to the minute resolution of the measurements, i.e., daily resolution. This result agrees with the correlation analysis, which showed that solar irradiance correlates 0.78 with the electrical energy generated. Regarding ambient temperature and wind speed, the correlation coefficient with electric power is between moderate and weak, with 0.43 and 0.27, respectively.

The predictor variables of the multiple linear regression model explain 81% of the variability of the target variable. The analysis of the residuals derived from this model indicates that they follow a normal distribution. As for the artificial neural network model, the coefficient of determination was 88%; the MAE and RMSE indicators were lower compared to the regression model, and the residuals were normally distributed.

While finding the appropriate ARIMA model, it was determined that the AC electric power level series is stationary and has annual stationarity. The model obtained minimizes the AIC criterion; the residuals are independently distributed and are not serially correlated.

When forecasting with the models obtained, the ARIMA model performed best, with the lowest values of the three error indicators: MAE, RMSE, and MAPE, with 1.38 kWh, 1.40 kWh, and 6.35%, respectively. The neural network model showed lower MAPE and MAE indicators than those obtained with the multiple linear regression model, but its RMSE metric was the highest of the three models.

#### References

- [1] REN21, *Renewables 2022 - Global Status Report. Renewables Now - Paris 2022*, 2022. [Online]. Available: <https://bit.ly/3I09MhE>
- [2] A. Kumar Mittal, K. Mathur, and S. Mittal, "A review on forecasting the photovoltaic power using machine learning," *Journal of Physics: Conference Series*, vol. 2286, no. 1, p. 012010, jul 2022. [Online]. Available: <https://dx.doi.org/10.1088/1742-6596/2286/1/012010>
- [3] A.-N. Sharkawy, M. Ali, H. Mousa, A. Ali, and G. Abdel-Jaber, "Machine learning method for solar PV output power prediction," *SVU-International Journal of Engineering Sciences and Applications*, vol. 3, no. 2, pp. 123–130, 2022. [Online]. Available: <https://doi.org/10.21608/svusrc.2022.157039.1066>
- [4] D. V. S. Krishna Rao Kasagani and P. Manickam, "Modeling of solar photovoltaic power using a two-stage forecasting system with operation and weather parameters," *Energy Sources, Part A: Recovery, Utilization, and Environmental Effects*, vol. 0, no. 0, pp. 1–19, 2022. [Online]. Available: <https://doi.org/10.1080/15567036.2022.2032880>
- [5] D. Pattanaik, S. Mishra, G. P. Khuntia, R. Dash, and S. C. Swain, "An innovative learning approach for solar power forecasting using genetic algorithm and artificial neural network," *Open Engineering*, vol. 10, no. 1, pp. 630–641, 2020. [Online]. Available: <https://doi.org/10.1515/eng-2020-0073>
- [6] M. N. Akhter, S. Mekhilef, H. Mokhlis, and N. Mohamed Shah, "Review on forecasting of photovoltaic power generation based on machine learning and metaheuristic techniques," *IET Renewable Power Generation*, vol. 13, no. 7, pp. 1009–1023, 2019. [Online]. Available: <https://doi.org/10.1049/iet-rpg.2018.5649>
- [7] M. Alaraj, A. Kumar, I. Alsaïdan, M. Rizwan, and M. Jamil, "Energy production forecasting from solar photovoltaic plants based on meteorological parameters for qassim region, Saudi Arabia," *IEEE Access*, vol. 9, pp. 83 241–83 251, 2021. [Online]. Available: <https://doi.org/10.1109/ACCESS.2021.3087345>
- [8] K. Anuradha, D. Erlapally, G. Karuna, V. Sri-lakshmi, and K. Adilakshmi, "Analysis of solar power generation forecasting using machine learning techniques," *E3S Web Conf.*, vol. 309, p. 01163, 2021. [Online]. Available: <https://doi.org/10.1051/e3sconf/202130901163>
- [9] M. Borunda, A. Ramírez, R. Garduno, G. Ruiz, S. Hernández, and O. A. Jaramillo, "Photovoltaic power generation forecasting for regional assessment using machine learning," *Energies*, vol. 15, no. 23, p. 8895, 2022. [Online]. Available: <https://doi.org/10.3390/en15238895>
- [10] J. VanderPlas, *Python data science handbook: Essential tools for working with data*. O'Reilly Media, Inc., 2016. [Online]. Available: <https://bit.ly/3BkwSeM>
- [11] D. Cielen, A. Meysman, and M. Ali, *Introducing Data Science: Big Data, Machine Learning, and more, using Python tools*. Manning Publication, 2016. [Online]. Available: <https://bit.ly/42wWD80>

- [12] DuraMAT. (2023) PVDAQ time-series with soiling signal - Data and Resources. Durable Module Materials Consortium. [Online]. Available: <https://bit.ly/42NKc7t>
- [13] SolarDesignTool, *Sanyo HIP200BA3 (200W) Solar Panel*. SolarDesignTool, 2023. [Online]. Available: <https://bit.ly/3pu1dFk>
- [14] W. McKinney, *Python for Data AnalysisOreilly and Associate Series*. "O'Reilly Media, Inc.", 2013. [Online]. Available: <https://bit.ly/3HZnfGr>
- [15] A. Navlani, A. Fandango, and I. Idris, *Python Data Analysis: Perform data collection, data processing, wrangling, visualization, and model building using Python*. Packt Publishing Ltd, 2021. [Online]. Available: <https://bit.ly/42voHsb>
- [16] B. Ratner, *Statistical and Machine-Learning Data Mining:: Techniques for Better Predictive Modeling and Analysis of Big Data*. CRC Press, 2017. [Online]. Available: <https://bit.ly/3VPx933>
- [17] I. A. Uribe, "Guía metodológica para la selección de técnicas de depuración de datos," Master's thesis, Universidad Nacional de Colombia, Medellín, Colombia, 2010. [Online]. Available: <https://bit.ly/3VQ5n6t>
- [18] D. C. Montgomery, C. L. Jennings, and M. Kulahci, *Introduction to Time Series Analysis and Forecasting*. Wiley Series in Probability and Statistics, 2015. [Online]. Available: <https://bit.ly/3LTZiRS>
- [19] J. F. Hair, W. C. Black, B. J. Babin, and R. E. Anderson, *Multivariate Data Analysis*. Pearson Education Limited, 2013. [Online]. Available: <https://bit.ly/3LWEHMN>
- [20] V. Platas García, *Contrastes de normalidad*. Universidade de Santiago de Compostela. Faculdade de Matemáticas, 2021. [Online]. Available: <https://bit.ly/3MfxZ5Z>
- [21] A. Gulli, A. Kapoor, and S. Pal, *Deep Learning with TensorFlow 2 and Keras*. Packt Publishing, 2019. [Online]. Available: <https://bit.ly/42MPT5r>
- [22] J. Moolayil, *Learn Keras for Deep Neural Networks: A Fast-Track Approach to Modern Deep Learning with Python*. Apress, 2018. [Online]. Available: <https://bit.ly/3nMtrL4>
- [23] F. Chollet, *Deep Learning with Python*. Manning Publications Company, 2017. [Online]. Available: <https://bit.ly/3LV4a9w>
- [24] G. E. P. Box, G. M. Jenkins, and G. C. Reinsel, *Time Series Analysis: Forecasting and Control*. Wiley Series in Probability and Statistics, 2008. [Online]. Available: <https://bit.ly/44OEALU>
- [25] S. Makridakis, S. Wheelright, and R. Hyndman, *Manual of Forecasting: Methods and Applications*. Wiley-Interscience, 1998. [Online]. Available: <http://dx.doi.org/10.13140/RG.2.1.2528.4880>
- [26] T. C. Mills, *Applied Time Series Analysis: A Practical Guide to Modeling and Forecasting*. Elsevier, 2019. [Online]. Available: <https://bit.ly/42sM5Xd>
- [27] D. N. Gujarati and D. C. Porter, *Econometría*. McGraw-Hill Interamericana, 2010. [Online]. Available: <https://bit.ly/44Tq0mc>





# POLYNOMIAL CROSS-ROOTS APPLICATION FOR THE EXCHANGE OF RADIANT ENERGY BETWEEN TWO TRIANGULAR GEOMETRIES

## APLICACIÓN DE RAÍCES CRUZADAS POLINOMIALES AL INTERCAMBIO DE ENERGÍA RADIANTE ENTRE DOS GEOMETRÍAS TRIANGULARES

Yanan Camaraza-Medina<sup>1,\*</sup>

Received: 12-02-2023, Received after review: 21-04-2023, Accepted: 26-04-2023, Published: 01-07-2023

### Abstract

The view factor between surfaces is essential in radiative heat transfer. Currently, there are no analytical solutions to evaluate the view factors between triangular geometries with common edges and angle  $\theta$  due to the high mathematical complexity associated with their development. For these configurations, the literature only has Sauer's graphical solutions, which generate average errors of 12%. This study developed an approximate method that does not involve high mathematical complexity and guarantees a fit of less than 12%. For this purpose, 32 different geometric configurations were studied (8 basic and 24 derived), obtaining the solutions for each evaluated case. 42 different transmitter and receiver dimensions were used to validate the models obtained. The vision factors were computed in each case using the analytical solution (AS), the numerical solution obtained with Simpson's 1/3 multiple rules (SMR) with five intervals, and Bretzhtsov's cross-root (BCR). The results obtained in each of the eight base cases were compared. In all cases evaluated, the BCR showed the best fits with an error of  $\pm 6\%$  in more than 90% of the samples, while the SMR showed an average scatter of  $\pm 6\%$  in 65% of the data. The practical nature of the contribution and the reasonable fitting values obtained show that this proposal is a suitable tool for thermal engineering.

**Keywords:** triangular surfaces, Bretzhtsov cross-root, view factor

### Resumen

El factor de visión entre superficies es esencial en la transferencia de calor por radiación. En la actualidad, para evaluar los factores de visión entre geometrías triangulares con bordes comunes y ángulo  $\theta$  no se dispone de soluciones analíticas, debido a la elevada complejidad matemática asociada a su desarrollo. Para estas configuraciones, la literatura solo tiene las soluciones gráficas de Sauer, cuyo uso genera errores medios del 12%. En este trabajo se desarrolla un método aproximado que no genere una alta complejidad matemática y que garantice un ajuste inferior al 12%. Para este propósito fueron estudiadas 32 configuraciones geométricas diferentes (8 básicas y 24 derivadas), siendo obtenidas las soluciones para cada uno de los casos evaluados. Para la validación de los modelos obtenidos se usaron 42 dimensiones diferentes de emisor y receptor, siendo computados en cada caso los factores de visión mediante la solución analítica (SA), la solución numérica obtenida con la regla múltiple de Simpson 1/3 (RMS) con cinco intervalos y mediante la raíz cruzada de Bretzhtsov (RCB), comparándose finalmente los resultados obtenidos en cada uno los ocho casos básicos. En todos los casos evaluados, la RCB mostró los mejores ajustes, con un error de  $\pm 6\%$  en más del 90% de las muestras, mientras que la RMS mostró una dispersión media de  $\pm 6\%$  en el 65% de los datos. La naturaleza práctica de la contribución y los valores razonables de ajuste obtenidos, establecen a la propuesta como una herramienta adecuada para su uso en la ingeniería térmica.

**Palabras clave:** superficies triangulares, raíz cruzada de Bretzhtsov, factor de visión

<sup>1,\*</sup>Technical Sciences Faculty, University of Matanzas, Cuba. Corresponding author ✉: [yanan.camaraza@umcc.cu](mailto:yanan.camaraza@umcc.cu).

Suggested citation: Camaraza-Medina, Y. "Polynomial cross-roots application for the exchange of radiant energy between two triangular geometries," *Ingenius, Revista de Ciencia y Tecnología*, N.º 30, pp. 29-41, 2023, DOI: <https://doi.org/10.17163/ings.n30.2023.03>.

## 1. Introduction

It is required to evaluate the thermal radiation between surfaces in thermal engineering. The vision factor establishes what fraction of the radiant energy emitted by one surface is intercepted by another [1].

The geometrical relationship between two surfaces and its influence on the view factor has been studied for decades, obtaining numerical and analytical solutions for different geometrical configurations [2–5]. For example, Howell extensively compiled view factors with more than 320 different configurations [6].

The accelerated leap in using computational techniques has generalized the implementation of commercial programs based on the finite element method (FEM) to solve thermal radiation problems [7–10].

Three-dimensional edge problems are reduced to surfaces with common edges and angle  $\theta$  included. However, shape factor algebra is tedious for these geometries, so numerical solutions such as FEM are preferred [11–13].

In FEM, meshes generally use triangular elements and rarely use rectangles or squares unless the overall geometry is a perfect cube. Determining an analytical solution for the view factor between triangular geometries requires sums of multiple integrals due to changing integration contours. In many cases, the solutions are not elementary functions, requiring the manipulation of inverse trigonometric functions, polylogarithms, and sums of infinite series [14].

This makes direct integration extremely tedious for unshared or without common edges geometries, so numerical integration is preferred. For this reason, analytical solutions for these types of geometries are lacking [15].

Using SMR with five intervals, the view factors were plotted for several perpendicular triangular geometries with common edges [16]. However, their graphical interpretation generated mean errors of 12 %, demonstrating that they do not apply to FEM since they cannot be discretized. In the specialized technical literature, only this graphical solution is available to obtain the view factors between triangular geometries [6–13].

The BCR method provides a proper fit during the approximation of complex functions, so it can be used to create the expressions required in the FEM discretization. The BCR method is similar to the FEM because its mathematical conception is based on the formation of nodes, obtaining the polynomial fits from the interconnection of the nodes [17]. Considering the above, it is demonstrated that there is a lack of analytical solutions (exact or approximate) to estimate the view factors between triangular geometries with common edges and angle  $\theta$  included.

Therefore, this study aims to develop approximate solutions to calculate the view factors between triangular geometries with common edges and angle  $\theta$

included, without involving high mathematical complexity and guaranteeing a good fit concerning the SA. Thus, it is possible to establish a new analysis method for use in the FEM.

This research develops the exact analytical solutions for eight basic triangular geometries and their respective BCRs. For comparison, 42 examples with various aspect ratios were calculated for each geometry, using the AS, BCR, and SMR.

The practical nature of the contribution and the reasonable fitting values obtained demonstrate that this proposal is a suitable tool to be applied in thermal engineering and related practices that require thermal radiation calculations between triangular geometries.

## 2. Materials y methods

### 2.1. Definition of the view factor

The view factor  $F_{12}$  depends on the position and geometrical configuration of the emitting surface  $A_1$  and the receiving surface  $A_2$ , defined as the fraction of the radiation leaving the former and intercepted by the latter, which is expressed as [18], in equation (1).

$$F_{12} = \frac{1}{\pi A_1} \int_{A_1} \int_{A_2} \frac{\cos O_1 \cos O_2}{r^2} dA_2 dA_1 \quad (1)$$

Where:  $O_1, O_2$ – angles between the normal vector of the areas  $dA_1$  and  $dA_2$  and the line connecting the center of the surfaces  $A_1$  and  $A_2$ , respectively.  $r$ – distance between the centers of surfaces  $A_1$  and  $A_2$ , (see Figure 1).

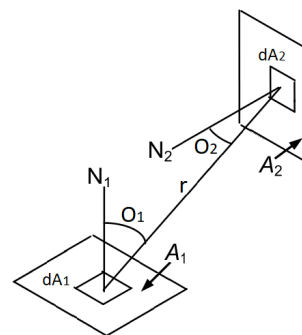


Figure 1. Basic geometry of the view factor

Equation (1) requires a double integration over the surfaces, which is complex and time-consuming since a large set of immediate integrals must be manipulated and subsequently factorized.

Numerical approximations can simplify the analysis because a suitable fit can be obtained with an appropriate set of intervals. For three-dimensional (3-D) configurations, various solution methods, such as contour integration, are available [19–24].

This work uses contour integration to obtain the view factor of the eight geometries analyzed. To approximate the special functions generated in the integration, the BCR method is used.

## 2.2. Mesh creation for surface elements

In modern engineering, triangular elements are widely used to generate meshes. In contrast, rectangular or

square elements are rarely used, except in cases where the overall geometry is a perfect cube. Formulating this type of geometry requires a complex mathematical treatment that includes sums of the quadruple integral equation (1) caused by the variation of the limits in the projection on each coordinate axis. The viewing factor between two rectangular surfaces of the same width, with common edge and angle  $\theta$  included, is given by equation (2) (see Figure 2).

$$f_{(1)} = F_{a-b} = \frac{\sin^2 \theta}{\pi A_1} \int_0^L dy_1 \int_0^D dx \int_0^W dz \int_0^D \frac{xz}{\{(y_1 - y_2)^2 + x^2 + z^2 - 2xz \cos \theta\}^2} dy_2 \quad (2)$$

The following substitutions are used to evaluate equation (2).

After evaluating equation (2), we obtain the following solution  $f_{(1)}$ , (equation (4)).

$$X = W/D; Y = L/D; R = \sqrt{X^2 + Y^2 - 2XY \cos \theta} \quad (3)$$

$$f_{(1)} = \frac{1}{\pi Y} \left\{ \begin{aligned} & -\frac{\sin 2\theta}{4} \left\{ Y^2 \tan^{-1} \left( \frac{X}{Y} \csc \theta - \cot \theta \right) + X^2 \tan^{-1} \left( \frac{Y}{X} \csc \theta - \cot \theta \right) + XY \sin \theta + \left( \frac{\pi}{2} - \theta \right) (X^2 + Y^2) \right\} + \\ & + \frac{1}{4} \ln \left\{ \left\{ \frac{X^2}{R^2} \left( \frac{1+X^2}{1+R^2} \right)^{\cos 2\theta} \right\}^{X^2 \sin^2 \theta} \left( \frac{Y^2 + Y^2 R^2}{R^2 + Y^2 R^2} \right)^{Y^2 \sin^2 2\theta} \left( \frac{(1+X^2)(1+Y^2)}{1+R^2} \right)^{\cos^2 \theta + 1} \right\} + \\ & + (\sin^3 \theta \cos \theta) \tan^{-1} \left( \frac{Y \sin \theta \sqrt{X^2 + \cot^2 \theta + 1}}{X^2 - Y X \cos \theta + 1} \right) \sqrt{X^4 + X^2 (\cot^2 \theta + 1)} + X \tan^{-1} \left( \frac{1}{X} \right) + \\ & + Y \tan^{-1} \left( \frac{1}{Y} \right) - R \cot^{-1}(R) + \frac{\sin 2\theta}{2} \int_0^Y \sqrt{Z^2 + \cot^2 \theta + 1} \tan^{-1} \left( \frac{X \sin \theta \sqrt{z^2 + \cot^2 \theta + 1}}{z^2 - z X \cos \theta} + 1 \right) dz \end{aligned} \right\} \quad (4)$$

In equations (2), (3) and (4), the angle  $\theta$  is given in radians. Equation (4) is very complex; for this reason, the last integral was not solved because its solution can be obtained numerically using Simpson's 1/3 rule (with at least eight intervals).

Drawing diagonal lines divides the emitting surface  $A_1$  and receiving surface  $A_2$  into eight triangular geometries. Applying the shape algebra for the geometry in Figure 3,  $\frac{1}{2}n^{n-1} = \frac{1}{2}4^{4-1} = 32$  combinations of view factors are obtained (see Figure 3). The analyzed geometry is symmetric; therefore, it is possible to define seven basic cases, as shown in Figure 4.

**Case 1:** Right triangle to rectangle, with common side and angle  $\theta$  between both surfaces.

**Case 2:** Right triangle to right triangle, with common side and angle  $\theta$  between both surfaces: vertices at a common point.

**Case 3:** Right triangle to right triangle, with common side and angle  $\theta$  between both surfaces: vertices at opposite ends.

**Case 4:** Isosceles triangle to rectangle, with common side and angle  $\theta$  between both surfaces.

**Case 5:** Right triangle to right triangle of different size, with angle  $\theta$  between both surfaces: vertices at a common point.

**Case 6:** Right triangle to right triangle of different size, with angle  $\theta$  between both surfaces: vertices at opposite ends.

**Case 7:** Perpendicular right triangles with an equal

edge and arranged in opposite directions.

The view factors for the remaining cases can be obtained using the sum rule.

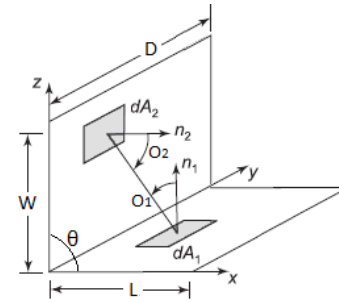


**Figure 2.** Rectangles of equal width, with common edge and angle  $\theta$  included

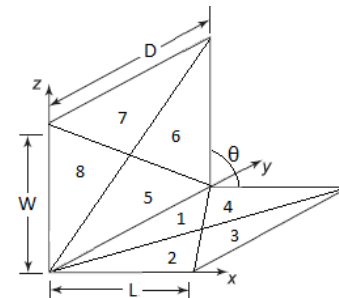


**Figure 3.** Division of rectangular surfaces into triangular elements

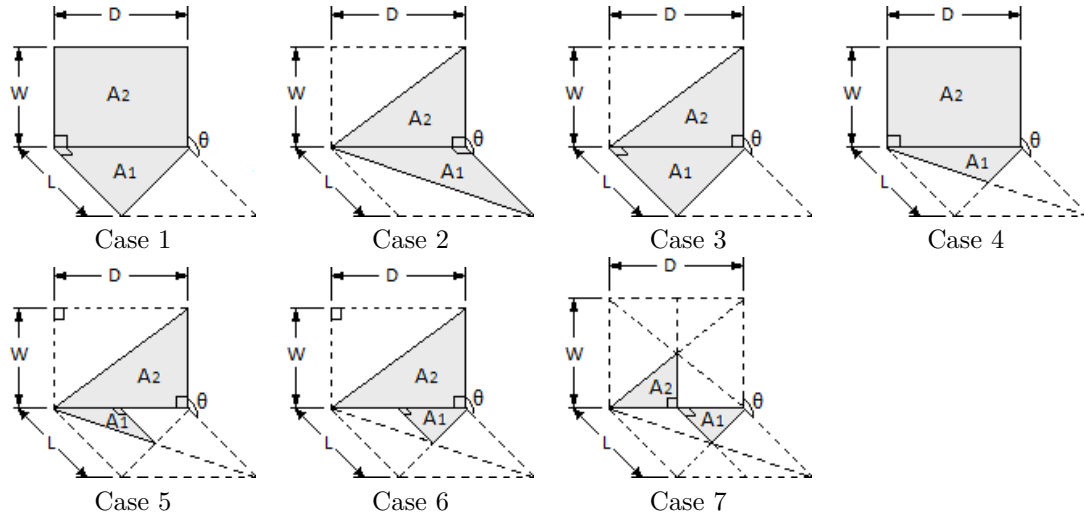


Figure 4. Basic configurations for triangular geometries

### 2.3. Modeling of the view factor. Case 1

In Case 1 (see Figure 5), it is satisfied that the equation (5).

$$\cos O_1 = \frac{z \sin \theta}{r}; \cos O_2 = \frac{x \sin \theta}{r} \quad (5)$$

$$r = (y_1 - y_1)^2 + x^2 + z^2 - 2xz \cos \theta$$

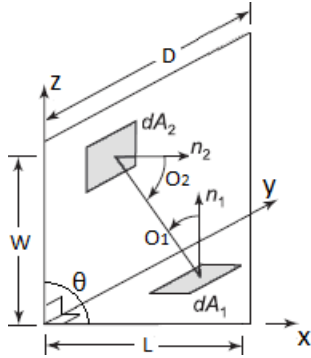


Figure 5. Basic Geometry for Case 1

$$f_2 = \frac{1}{\pi A_1} \int_0^b dy \int_0^c \left\{ \tan^{-1} \left( \frac{1}{z} \right) + \frac{z \sin^2 \theta}{2} \ln \left[ \frac{z^2 (z^2 - 2az \cos \theta + 1 + a^2)}{(1+z^2)(a^2 + z^2 - 2az \cos \theta)} \right] - z \sin \theta \cos \theta \left[ \frac{\pi}{2} - \theta + \tan^{-1} \left( \frac{a - z \cos \theta}{z \sin \theta} \right) \right] + \cos \theta \sqrt{1 + z^2 \sin^2 \theta} \left[ \tan^{-1} \left( \frac{a - z \cos \theta}{\sqrt{1 + z^2 \sin^2 \theta}} \right) + \tan^{-1} \left( \frac{z \cos \theta}{\sqrt{1 + z^2 \sin^2 \theta}} \right) \right] + \frac{a \cos \theta - z}{\sqrt{a^2 + z^2 - 2az \cos \theta}} \tan^{-1} \left( \frac{1}{\sqrt{a^2 + z^2 - 2az \cos \theta}} \right) \right\} dz \quad (8)$$

$$f_2 = 2f_1 \left\{ \frac{a^2 b^2}{8(a^2 + b^2)} \ln \left( \frac{b^2 + c^2}{(a^2 + c^2)^2} \right) + \frac{a^2 b^4}{4(a^2 + b^2)^2} \ln \left( \frac{b(a^2 + c^2)}{a(b^2 + c^2)} \right) + \frac{a^4 b^2}{4(a^2 + b^2)^2} \ln \left( \frac{b}{a} \right) + \frac{a^2 c^2}{8(a^2 + b^2)} \ln \left( \frac{(b^2 + c^2)(a^2 + b^2 + c^2)}{c^2(a^2 + c^2)} \right) + \frac{a^2}{8} \ln \left( \frac{a^4(a^2 + b^2 + c^2)^2}{(a^2 + b^2)^2(a^2 + c^2)} \right) + \frac{b^2}{8} \ln \left( \frac{(a^2 + b^2)(a^2 + c^2)}{b^2(a^2 + b^2 + c^2)} \right) + \frac{c^2}{8} \ln \left( \frac{c^2(a^2 + b^2 + c^2)}{(a^2 + b^2)(a^2 + c^2)} \right) + \frac{3}{4} ab \tan^{-1} \left( \frac{b}{a} \right) + \frac{1}{2} bc \tan^{-1} \left( \frac{b}{a} \right) - \frac{1}{2} b \sqrt{a^2 + c^2} \tan^{-1} \left( \frac{b}{\sqrt{a^2 + c^2}} \right) - \frac{a^4}{8(a^2 + b^2)} \ln (a^2 + c^2) + \frac{ab^2(2a - \pi b)}{8(a^2 + b^2)} + \frac{a^2 b^2 \left( \frac{b^4}{a^2 + b^2} - b^2 - c^2 \right)}{2(a^2 + b^2)^{\frac{3}{2}} \sqrt{b^2 + c^2 - \frac{b^4}{a^2 + b^2}}} \tan^{-1} \left( \frac{(a^2 + b^2)^{\frac{3}{2}} \sqrt{b^2 + c^2 - \frac{b^4}{a^2 + b^2}}}{(a^2 + b^2)^{\frac{3}{2}} (b^2 + c^2 - \frac{b^4}{a^2 + b^2} - b^2 \{ (a^2 + b^2) - b^2 \})} \right) - \frac{1}{2} \int_0^a \left[ \frac{bx^2}{a\sqrt{x^2 + c}} \tan^{-1} \left( \frac{a\sqrt{x^2 + c}}{x^2 + c^2 + \frac{b^2}{a^2}(x^2 - ax)} \right) + \frac{bx}{\sqrt{x^2 + c}} \tan^{-1} \left( \frac{\frac{b}{a}x - b}{\sqrt{x^2 + c}} \right) \right] dx \quad (9)$$

Substituting equation (5) in equation (1), the view factor  $F_{12}$  is given by equation (6).

$$f_2 = \frac{\sin^2 \theta}{\pi A_1} \int_0^L dy_1 \int_0^{y_1 D/L} dx \int_0^D dz \cdot \int_0^W \frac{xz}{\{(y_1 - y_2)^2 + x^2 + z^2 - 2xz \cos \theta\}^2} dy_2 \quad (6)$$

In equation (6), the change indicated in equation (7) was made to perform the integration.

$$W = a; D = b; L = c \quad (7)$$

Equation (6) is first integrated on the emitting surface  $A_1$ , obtaining a sum of integrals, which is given by equation (8).

After a complex process in which it was necessary to solve  $n^n = 4^4 = 256$  primitive functions, the sum of double integrals of equation (8) was solved, whose solution is given in equation (9).

In equation (9), the term  $f_{(1)}$  is obtained by equation (4). Due to the complexity of equation (9), the last integral is not solved, and its solution is obtained numerically using the SMR (twelve intervals are recommended). Equation (9) is transformed as the equation (10).

$$F_{12} = f_{(n)} = 2F_{(1)} \cdot \varphi_n \quad (10)$$

Equation (10) is then transformed by dividing each

dimensional variable by the length of the common edge  $b$ . The result is shown below the equation (11).

$$\begin{aligned} 1 &= b/b; X = a/b; Y = c/b \\ R &= \sqrt{X^2 + Y^2 - 2XY \cos \theta} \end{aligned} \quad (11)$$

Applying in equation (9) the change of variables of equation (11), the analytical solution for Case 1 is obtained, which is given by equation (12).

$$\begin{aligned} f_{(2)} = 2f_{(1)} &\left\{ \frac{X^2}{8(X^2+1)} \ln \left( \frac{Y^2+1}{R^4} \right) + \frac{X^2}{4(X^2+1)^2} \ln \left( \frac{R^2}{X(Y^2+1)} \right) + \frac{X^2 Y^2}{8(X^2+1)} \ln \left( \frac{(Y^2+1)(R^2+1)}{Y^2 R^2} \right) + \right. \\ &+ \frac{X^4}{4(X^2+1)^2} \ln \left( \frac{1}{X} \right) - \frac{X^4}{8(X^2+1)} \ln \left( R^2 \right) + \frac{3X}{4} \tan^{-1} \left( \frac{1}{X} \right) + \frac{Y}{2} \tan^{-1} \left( \frac{1}{Y} \right) - \frac{R}{2} \tan^{-1} \left( \frac{1}{R} \right) + \\ &+ \frac{1}{8} \ln \left\{ \left( \frac{X^4(R^2+1)^2}{R^2(X^2+1)^2} \right)^{X^2} \left( \frac{Y^2(R^2+1)}{R^2(X^2+1)} \right)^{Y^2} \left( \frac{R^2(X^2+1)}{R^2+1} \right) \right\} + \frac{2X^2 - \pi}{8(X^2+1)} - \\ &+ \frac{X^2 \left( Y^2 - \frac{X^2+2}{X^2+1} \right)}{2(X^2+1)^{\frac{3}{2}} \sqrt{Y^2 - \frac{X^2+2}{X^2+1}}} \tan^{-1} \left( \frac{(X^2+1)^{\frac{3}{2}} \sqrt{Y^2 - \frac{X^2+2}{X^2+1}}}{(X^2+1) \left( Y^2 - \frac{X^2+2}{X^2+1} \right) - X^2} \right) - \end{aligned} \quad (12)$$

Equation (12) is a combination of variables  $(Y; X)$ . Evaluating this equation may be difficult because it is necessary to solve polylogarithms, sums of infinite series, and inverse trigonometric functions. However, using Bretzhtsov's cross-root method, it is possible to obtain an approximate result, facilitating the calculation of the view factor.

To implement the cross-root method, nodes are constructed using prefixed values  $(Y; X)$ , which are joined using diagonal lines forming the families of curves  $a_n$  and  $b_n$ . In this study, the values  $Y = (0.1; 0.2; 0.5; 1; 3; 10)$  and  $X = (0.1; 0.3; 0.6; 1; 3; 6; 10)$  are used.

Tables 1 and 2 summarize the combination of variables  $(Y; X)$  for each node and the nodes that integrate each curve  $a_n$  and  $b_n$ , respectively. Figure 6 plots the families of curves  $a_n$  and  $b_n$ .

The next step is to compute the vision factor using equation (12) for each of the combinations of variables  $(Y; X)$  in Table 1, plotting them in a  $F_{12}; X$  diagram, as shown in Figure 7. The union of the nodes along the x-axis makes it possible to create a third family of curves  $c_n$ . A particularity is that all the nodes integrating the same curve  $c_n$  have the same value of the variable  $Y$ , as shown in Table 1. Table 3 summarizes the nodes integrating each  $c_n$  curve.

**Table 1.** Combinations of variables  $(Y; X)$  for each node

node	$(Y, X)$	node	$(Y, X)$	node	$(Y, X)$	node	$(Y, X)$
1	3 ; 0.1	12	1 ; 0.6	23	0.5 ; 1	34	0.5 ; 6
2	10 ; 0.3	13	3 ; 1	24	1 ; 3	35	1 ; 10
3	1 ; 0.1	14	10 ; 3	25	3 ; 6	36	0.1 ; 3
4	3 ; 0.3	15	0.1 ; 0.1	26	10 ; 10	37	0.2 ; 6
5	10 ; 0.6	16	0.2 ; 0.3	27	0.1 ; 0.6	38	0.5 ; 10
6	0.5 ; 0.1	17	0.5 ; 0.6	28	0.2 ; 1	39	0.1 ; 6
7	1 ; 0.3	18	1 ; 1	29	0.5 ; 3	40	0.2 ; 10
8	3 ; 0.6	19	3 ; 3	30	1 ; 6	41	10 ; 0.1
9	10 ; 1	20	10 ; 6	31	3 ; 10	42	0.1 ; 10
10	0.2 ; 0.1	21	0.1 ; 0.3	32	0.1 ; 1		
11	0.5 ; 0.3	22	0.2 ; 0.6	33	0.2 ; 3		

**Table 2.** Nodes integrating each curve  $a_n$  and  $b_n$

$a_n$	nodes	$b_n$	nodes
$a_1$	1-2	$b_1$	10-21
$a_2$	3-4-5	$b_2$	6-16-27
$a_3$	6-7-8-9	$b_3$	3-11-22-32
$a_4$	10-11-12-13-14	$b_4$	1-7-17-28-36
$a_5$	15-16-17-18-19-20	$b_5$	41-4-12-23-33-39
$a_6$	21-22-23-24-25-26	$b_6$	2-8-18-29-37-42
$a_7$	27-28-29-30-31	$b_7$	5-13-24-34-40
$a_8$	32-33-34-35	$b_8$	9-19-30-38
$a_9$	36-37-38	$b_9$	14-25-35
$a_{10}$	39-40	$b_{10}$	20-31

**Table 3.** Nodes integrating each  $c_n$  curve

$c_n$	nodes	$c_n$	nodes
$c_1$	15-21-27-32-36-39-42	$c_4$	3-7-12-18-24-30-35
$c_2$	10-16-22-28-33-37-40	$c_5$	1-4-8-13-19-25-31
$c_3$	6-11-17-23-29-34-38	$c_6$	41-2-5-6-14-20-26

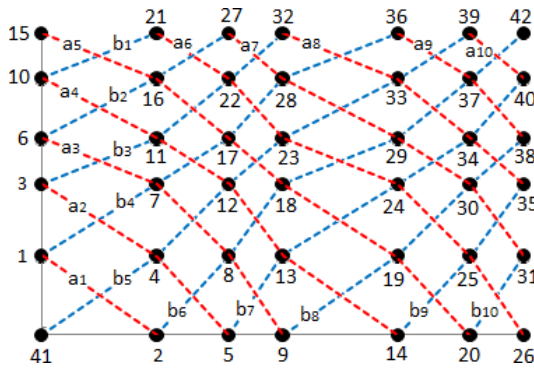


Figure 6. Families of curves  $a_n$  and  $b_n$

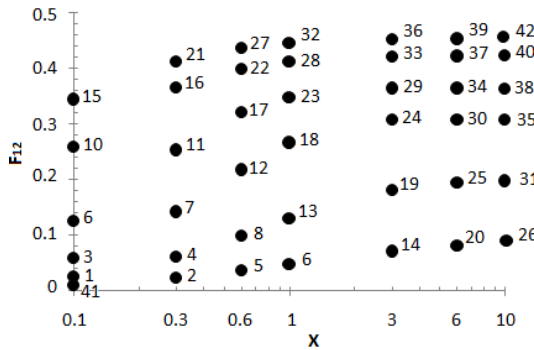


Figure 7. Scheme for applying cross-roots

Each curve of the families  $a_n$ ,  $b_n$ ,  $c_n$  is approximated individually by the Least Squares Method (LSM), using a third-degree polynomial in the form  $mX^3 + nX^2 + oX + p$ , thus establishing a dependence between the view factor  $F_{12}$  and the  $X$  variable. Figure 8 shows the application of the method for curves  $a_5$ ,  $b_5$ ,  $c_4$ .

Table 4 shows the values of the constants  $m$ ,  $n$ ,  $o$ ,  $p$  obtained by applying LMS to all the curves  $a_n$ ,  $b_n$ ,  $c_n$ . The  $m$ ,  $n$ ,  $o$ ,  $p$  values are averaged in each curve, thus obtaining the approximate functions  $A_n$ ,  $B_n$ ,  $C_n$ .

For each curve, the apparent angle of transmissibility (see Figure 8) is given by the equation (13)

$$\psi = \tan^{-1} \left( \frac{X}{Y} \right) \quad (13)$$

Therefore, Bretzhtsov's cross-root is given by the equation (14).

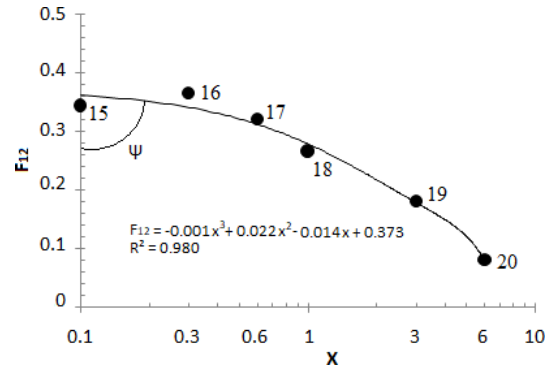
$$\varphi_n = A_n\psi^2 + B_n\psi + C_n \quad (14)$$

Table 4 shows the constants  $m$ ,  $n$ ,  $o$ ,  $p$  for the polynomials  $A_n$ ,  $B_n$ ,  $C_n$ . For the approximations, the  $X$  variables were used, keeping the  $Y$  variables constant; therefore, to apply the cross roots, the  $Y$  variables were alternated by  $X$ , obtaining the following equations (15) to (17) for the polynomials  $A_n$ ,  $B_n$ ,  $C_n$ .

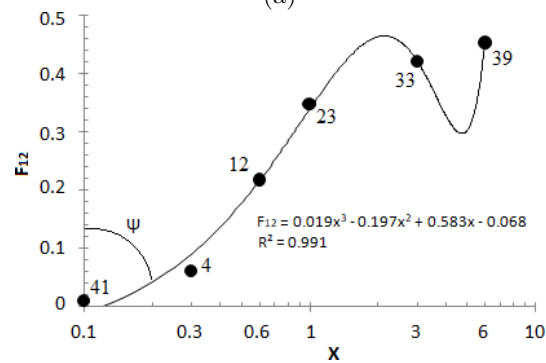
$$A_n = -0.022Y^3 + 0.316Y^2 - 0.89Y + 0.5 \quad (15)$$

$$B_n = 0.056Y^3 - 0.783Y^2 + 2.23Y - 1.43 \quad (16)$$

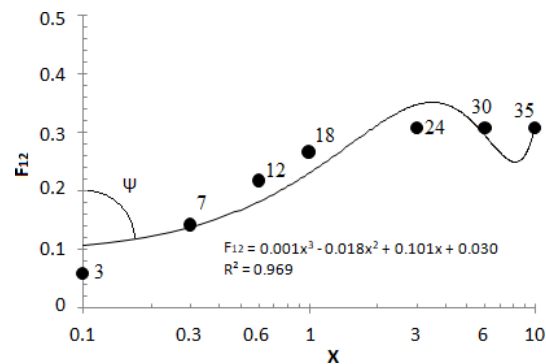
$$C_n = 0.03Y^3 + 0.407Y^2 - 1.07Y + 2.02 \quad (17)$$



(a)



(b)



(c)

Figure 8. Approximation by Least Squares (a), curve  $a_5$ , (b) curve  $b_5$ , (c) curve  $c_4$

Substituting equations (15) through (17) into equation (14), we obtain that Bretzhtsov's cross-root for Case 1 is given by equation (18).

$$\varphi_n = (-0.022Y^3 + 0.316Y^2 - 0.89Y + 0.5) \psi^2 + (0.056Y^3 - 0.783Y^2 + 2.23Y - 1.43) \psi - 0.03Y^3 + 0.407Y^2 - 1.07Y + 2.02 \quad (18)$$

**Table 4.** Constants  $m, n, o, p$  obtained by applying LMS

Curve	m	n	o	p
$a_2$	0	0.186	-1.023	0.51
$a_3$	0.549	0.32	-0.528	0.91
$a_4$	-0.278	0.28	-0.88	0.352
$a_5$	-0.337	0.52	-0.514	0.373
$a_6$	-0.11	0.64	-2.48	0.484
$a_7$	0	0.66	-0.95	0.456
$a_8$	0	-0.03	-0.713	0.447
$a_9$	0	-0.05	-0.03	0.468
average $A_n$	-0.022	0.316	-0.89	0.5
Curve	m	n	o	p
$b_1$	0	0	3.06	-1.181
$b_2$	0	-1.96	2.97	-1.53
$b_3$	0	-1.18	2.34	-1.44
$b_4$	0.424	-0.592	1.98	-1.67
$b_5$	0.019	-0.197	2.583	-1.068

$b_6$	0.106	-1.91	3.22	-2.99
$b_7$	0.011	-0.75	2.37	-1.07
$b_8$	0	-0.93	2.29	-1.123
$b_9$	0	-0.31	1.19	-1.285
$b_{10}$	0	0	0.29	-0.94
average $B_n$	0.056	-0.783	2.23	-1.43
Curve	m	n	o	p
$c_1$	0	0.16	-1.69	2.374
$c_2$	0.018	0.28	-1.103	2.307
$c_3$	0.02	0.34	-1.161	2.183
$c_4$	0.002	-0.035	-1.173	2.088
$c_5$	0.14	0.99	-0.92	2.16
$c_6$	0	0.71	-0.37	1.01
average $C_n$	0.03	0.407	-1.07	2.02

Substituting equation (18) in equation (10), the view factor for Case 1 is obtained, which is given by equation (19).

$$f_{(2)} = 2f_{(1)} \cdot \{ (-0.022Y^3 + 0.316Y^2 - 0.89Y + 0.5) \psi^2 + (0.056Y^3 - 0.783Y^2 + 2.23Y - 1.43) \psi - 0.03Y^3 + 0.407Y^2 - 1.07Y + 2.02 \} \quad (19)$$

### 3. Results and discussion

For practical engineering use, equation (19) is much simpler than the analytical solution (SA) of equation (12). The percentage deviation (error) is computed with respect to the analytical solution and is obtained by the following relation in equation (20) [25].

$$D_{\%} = 100 \cdot \frac{SA - Val}{SA} \quad (20)$$

Where:  $D_{\%}$  is the percentage of deviation.  $SA$  is the view factor obtained by the analytical solution.  $Val$  is the view factor obtained by approximate methods.

To calculate the  $D_{\%}$  values, the view factors are computed for the 42 combinations of variables ( $Y; X$ ) in Table 1, using the  $AS$ , the  $SMR$  with five intervals, and the view factors obtained with the  $BCR$ .

Figure 9 plots the  $D_{\%}$  values obtained with equation (18) for the view factors calculated by  $SMR$  and  $BCR$ , adjusted in error bands of  $\pm 3\%$  and  $\pm 6\%$ .

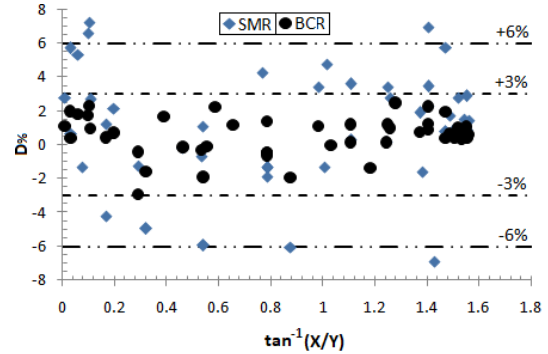


**Figure 9.**  $D_{\%}$  obtained with equation (18) for Case 1

For Case 1, Figure 9 shows that  $BCR$ s have a better fit with respect to  $SA$ , with a mean error of  $\pm 3\%$  for 100% of the ( $Y; X$ ) points analyzed. On the contrary, the view factors obtained with  $SMR$  have a lower fit with respect to the  $AS$ , with mean errors of  $\pm 3\%$  and  $\pm 6\%$  for 54,8% and 85,7% of the ( $Y; X$ ) points evaluated, respectively.

#### 3.1. Modeling and validation of Cases 2 to 7

For Cases 2 to 7 (see Figure 4), mathematically, the view factor  $F_{12}$  is given by equations (21) to (26).

$$Case\ 2 \quad f_{(3)} = \frac{\sin^2\theta}{\pi A_1} \int_0^L dy_1 \int_0^{y_1 D/L} dx \int_0^W dy_2 \int_0^{y_2 D/L} \frac{xz}{\{(y_1 - y_2)^2 + x^2 + z^2 - 2xz \cos\theta\}^2} dz \quad (21)$$

$$\text{Case 3 } f_{(4)} = \frac{\sin^2\theta}{\pi A_1} \int_0^L dy_1 \int_0^{y_1 D/L} dx \int_0^W dy_2 \int_0^{y_2 D/L} \frac{xz}{\{(y_1 - y_2)^2 + x^2 + z^2 - 2xz \cos\theta\}^2} dz \quad (22)$$

$$\text{Case 4 } f_{(5)} = \frac{\sin^2\theta}{\pi A_1} \int_0^{L/2} dy_1 \int_0^{y_1 D/L} dx \int_0^W dz \int_0^{y_2 D/L} \frac{xz}{\{(y_1 - y_2)^2 + x^2 + z^2 - 2xz \cos\theta\}^2} dy_2 \quad (23)$$

$$\text{Case 5 } f_{(6)} = \frac{\sin^2\theta}{\pi A_1} \int_0^{L/2} dy_1 \int_0^{y_1 D/L} dx \int_0^W dy_2 \int_0^{y_2 D/L} \frac{xz}{\{(y_1 - y_2)^2 + x^2 + z^2 - 2xz \cos\theta\}^2} dz \quad (24)$$

$$\text{Case 6 } f_{(7)} = \frac{\sin^2\theta}{\pi A_1} \int_0^{L/2} dy_1 \int_{y_1 D/L}^0 dx \int_0^W dy_2 \int_0^{y_2 D/L} \frac{xz}{\{(y_1 - y_2)^2 + x^2 + z^2 - 2xz \cos\theta\}^2} dz \quad (25)$$

$$\text{Case 7 } f_{(8)} = \frac{\sin^2\theta}{\pi A_1} \int_0^{L/2} dy_1 \int_{-y_1 D/L}^0 dx \int_0^{W/2} dy_2 \int_0^{y_2 D/L} \frac{xz}{\{(y_1 - y_2)^2 + x^2 + z^2 - 2xz \cos\theta\}^2} dz \quad (26)$$

The analytical solutions of equations (21) to (26) are long and complex because they require the handling of Spence functions, Gamma function, sums of polynomials, modified Bessel functions of first species and zero, one, and two orders; for this reason, they are

not presented in this study.

For the solution of equations (21) to (26), the same procedure for Case 1 is used, obtaining the following approximations to calculate the view factor for Cases 2 to 7.

$$\text{Case 2 } f_{(3)} = 2f_{(1)} \cdot \{(-0.001Y^3 + 0.033Y^2 - 0.14Y + 0.265)\psi^2 + (0.011Y^3 - 0.177Y^2 + 0.7Y - 0.615)\psi - 0.01Y^3 + 0.142Y^2 - 0.475Y + 1.29\} \quad (27)$$

$$\text{Case 3 } f_{(4)} = 2f_{(1)} \cdot \{(-0.031Y^3 + 0.424Y^2 - 1.257Y + 1.1)\psi^2 + (0.071Y^3 - 0.975Y^2 + 2.92Y - 2.06)\psi - 0.034Y^3 + 0.462Y^2 - 1.268Y + 1.6\} \quad (28)$$

$$\text{Case 4 } f_{(5)} = 2f_{(1)} \cdot \{(-0.01Y^2 + 0.24Y + 0.67)\psi^2 + (0.02Y^2 - 0.31Y - 2.2)\psi - 0.02Y^2 + 0.27Y + 3\} \quad (29)$$

$$\text{Case 5 } f_{(6)} = 2f_{(1)} \cdot \{(-0.02Y^3 + 0.29Y^2 - 1.1Y + 0.6)\psi^2 + (0.06Y^3 - 0.88Y^2 + 2.96Y - 4.41)\psi - 0.04Y^3 + 0.55Y^2 - 1.41Y + 1.87\} \quad (30)$$

$$\text{Case 6 } f_{(7)} = 2f_{(1)} \cdot \{(-0.011Y^3 + 0.12Y^2 - 0.025Y + 0.52)\psi^2 + (0.025Y^3 - 0.307Y^2 + 0.49Y - 1.64)\psi - 0.134Y^3 + 0.183Y^2 - 0.35Y + 2.47\} \quad (31)$$

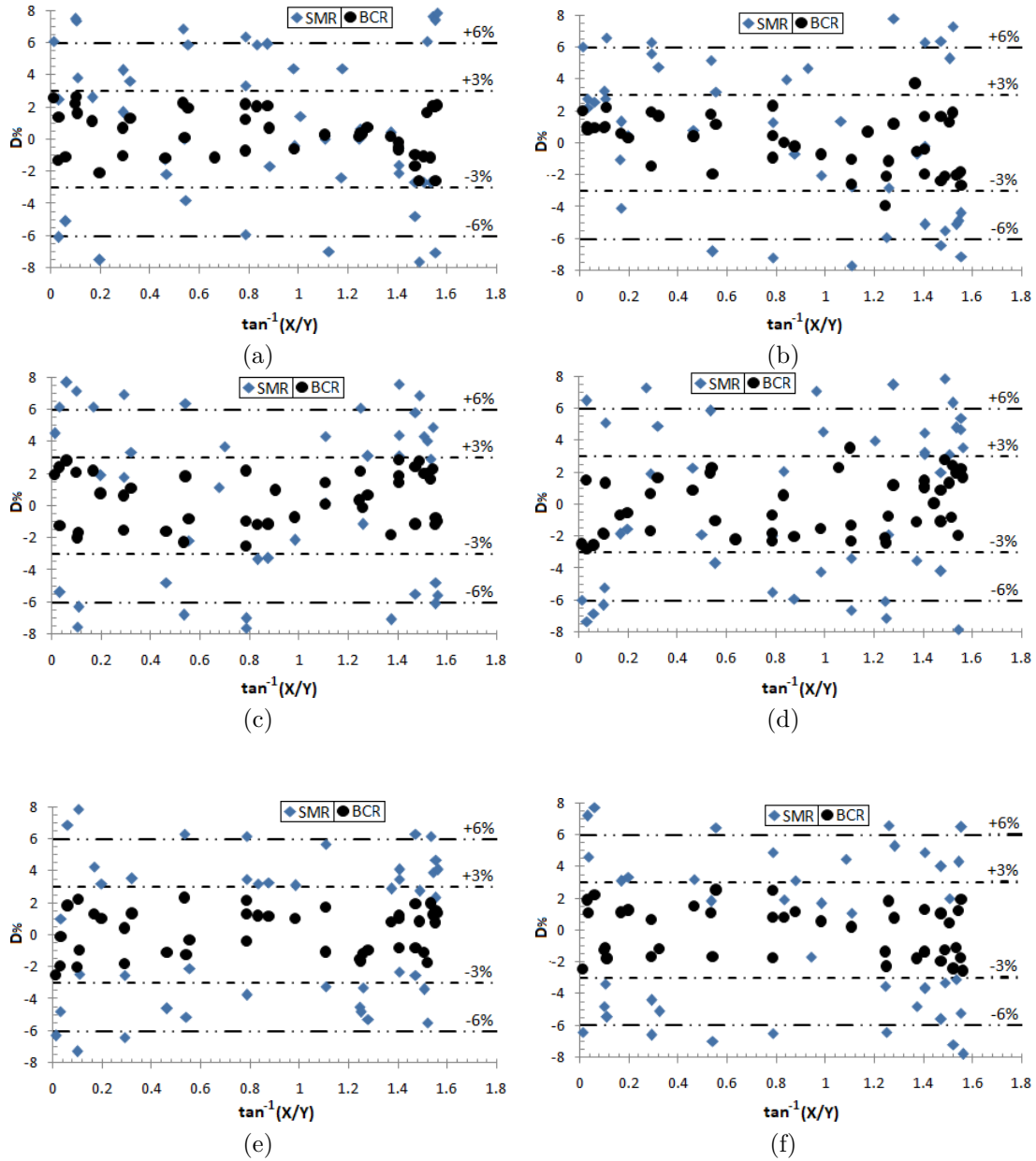
$$\text{Case 7 } f_{(8)} = 2f_{(1)} \cdot \{(0.015^2 - 0.108Y + 0.08)\psi^2 + (-0.015Y^2 + 0.096Y + 0.048)\psi - 0.001Y^2 + 0.04Y + 0.058\} \quad (32)$$

Figure 10 plots in  $\pm 3\%$  and  $\pm 6\%$  error band the  $D_{\%}$  obtained with equation (18) for the view factors calculated with SMR and BCR for Cases 2 to 7.

For Case 2, Figure 10 shows that BCRs have the best fit with respect to AS, with a mean error of  $\pm 3\%$  in 97.6% of the  $(Y; X)$  points analyzed. On the contrary, the view factors obtained with SMR have a lower fit with respect to AS, with mean errors of  $\pm 3\%$  and  $\pm 6\%$  in 28.5% and 64.3% of the  $(Y; X)$  points

evaluated, respectively.

For Case 3, Figure 10 shows that BCRs have a better fit with respect to AS, with mean errors of  $\pm 3\%$  and  $\pm 6\%$  in 92.9% and 100% of the  $(Y; X)$  points analyzed. The view factors obtained with SMR have a lower fit with respect to AS, computing mean errors of  $\pm 3\%$  and  $\pm 6\%$  in 38.1% and 69.0% of the  $(Y; X)$  points evaluated, respectively.



**Figure 10.**  $D\%$  values obtained with equation (18) for the cases analyzed. (a) Case 2; (b) Case 3; (c) Case 4; (d) Case 5; (e) Case 6; (f) Case 7

For Case 4, Figure 10 shows that BCRs have a better fit with respect to AS with mean errors of  $\pm 3\%$  and  $\pm 6\%$  in 90.5% and 100% of the  $(Y; X)$  points analyzed. In contrast, the view factors obtained with SMR have a lower fit with respect to AS, with mean errors of  $\pm 3\%$  and  $\pm 6\%$  in 21.4% and 61.9% of the  $(Y; X)$  points evaluated, respectively.

For Case 5, Figure 10 shows that BCRs have a better fit with respect to AS with mean errors of  $\pm 3\%$  and  $\pm 6\%$  in 95.2% and 100% of the  $(Y; X)$  points analyzed. The view factors obtained with SMR have a lower fit with respect to AS, computing mean errors of  $\pm 3\%$  and  $\pm 6\%$  in 26.2% and 71.4% of the  $(Y; X)$

points evaluated, respectively.

For Case 6, Figure 10 shows that BCRs have a better fit with respect to AS with mean errors of  $\pm 3\%$  in 100% of the  $(Y; X)$  points analyzed. On the contrary, the view factors obtained with SMR have a lower fit with respect to AS, with mean errors of  $\pm 3\%$  and  $\pm 6\%$  in 31.0% and 81.0% of the  $(Y; X)$  points evaluated, respectively.

For Case 7, Figure 10 shows that BCRs have a better fit with respect to AS with mean errors of  $\pm 3\%$  in 100% of the  $(Y; X)$  points analyzed. The view factors obtained with SMR have a lower fit with respect to AS, computing mean errors of  $\pm 3\%$  and  $\pm 6\%$  in 23.8%

and 73.8% of the  $(Y; X)$  points evaluated, respectively.

### 3.2. Other geometric configurations

In Figure 3, the emitting and receiving surfaces are divided into four triangular surfaces, resulting in  $0.5n^{n-1} = 0.5 \cdot 4^{4-1} = 32$  possible combinations (see

Figure 11). Using the view factors  $f_{(1)}$  to  $f_{(8)}$ , it is possible to obtain the view factors for the remaining configurations by applying the rule of sums and the algebra of form factors. Table 5 shows the relationships for computing the view factor for the configurations in Figure 11.

**Table 5.** View factor settings for triangular surfaces

Case	$\mathbf{F}_{(1-2)} \cdots \mathbf{f}_{(n)}$	Case	$\mathbf{F}_{(1-2)} \cdots \mathbf{f}_{(n)}$
Case 8	$f_{(9)} = f_{(5)}$	Case 20	$f_{(21)} = 3f_{(3)} + f_{(8)} - 2f_{(6)} - 2f_{(7)}$
Case 9	$f_{(10)} = f_{(5)}$	Case 21	$f_{(22)} = 4f_{(1)} + 3f_{(6)} + 3f_{(7)} - 3f_{(3)} - 2f_{(4)} - 4f_{(5)} - f_{(8)}$
Case 10	$f_{(11)} = 2f_{(1)} - f_{(2)}$	Case 22	$f_{(23)} = 4f_{(5)} + f_{(3)} + f_{(8)} - 2f_{(6)} - 2f_{(7)}$
Case 11	$f_{(12)} = f_{(6)} + f_{(7)}$	Case 23	$f_{(24)} = 5f_{(3)} + 4f_{(4)} + 5f_{(5)} + f_{(8)} - 4f_{(1)} - 4f_{(2)} - 4f_{(6)} - 4f_{(7)}$
Case 12	$f_{(13)} = 2f_{(2)} - f_{(5)}$	Case 24	$f_{(25)} = 2f_{(1)} + f_{(4)} - 2f_{(2)}$
Case 13	$f_{(14)} = 4f_{(1)} + f_{(5)} - 4f_{(2)}$	Case 25	$f_{(26)} = 2f_{(1)} + f_{(3)} - 2f_{(2)}$
Case 14	$f_{(15)} = 2f_{(4)} - f_{(6)} - f_{(7)}$	Case 26	$f_{(27)} = f_{(2)} - f_{(3)}$
Case 15	$f_{(16)} = 4f_{(1)} + f_{(6)} + f_{(7)} - 2f_{(3)} - 2f_{(4)}$	Case 27	$f_{(28)} = f_{(2)} - f_{(4)}$
Case 16	$f_{(17)} = 2f_{(3)} - f_{(6)} - f_{(7)}$	Case 28	$f_{(29)} = f_{(5)} - f_{(6)} - f_{(7)}$
Case 17	$f_{(18)} = f_{(3)} + f_{(8)}$	Case 29	$f_{(30)} = 2f_{(3)} + 2f_{(4)} + f_{(5)} - 4f_{(2)} - f_{(6)} - f_{(7)}$
Case 18	$f_{(19)} = f_{(6)} + f_{(7)} - f_{(3)} - f_{(8)}$	Case 30	$f_{(31)} = 2f_{(2)} + f_{(6)} + f_{(7)} - f_{(5)} - 2f_{(4)}$
Case 19	$f_{(20)} = 4f_{(5)} + f_{(3)} + f_{(8)} - 2f_{(6)} - 2f_{(7)}$	Case 31	$f_{(32)} = 2f_{(2)} + f_{(6)} + f_{(7)} - f_{(5)} - 2f_{(3)}$

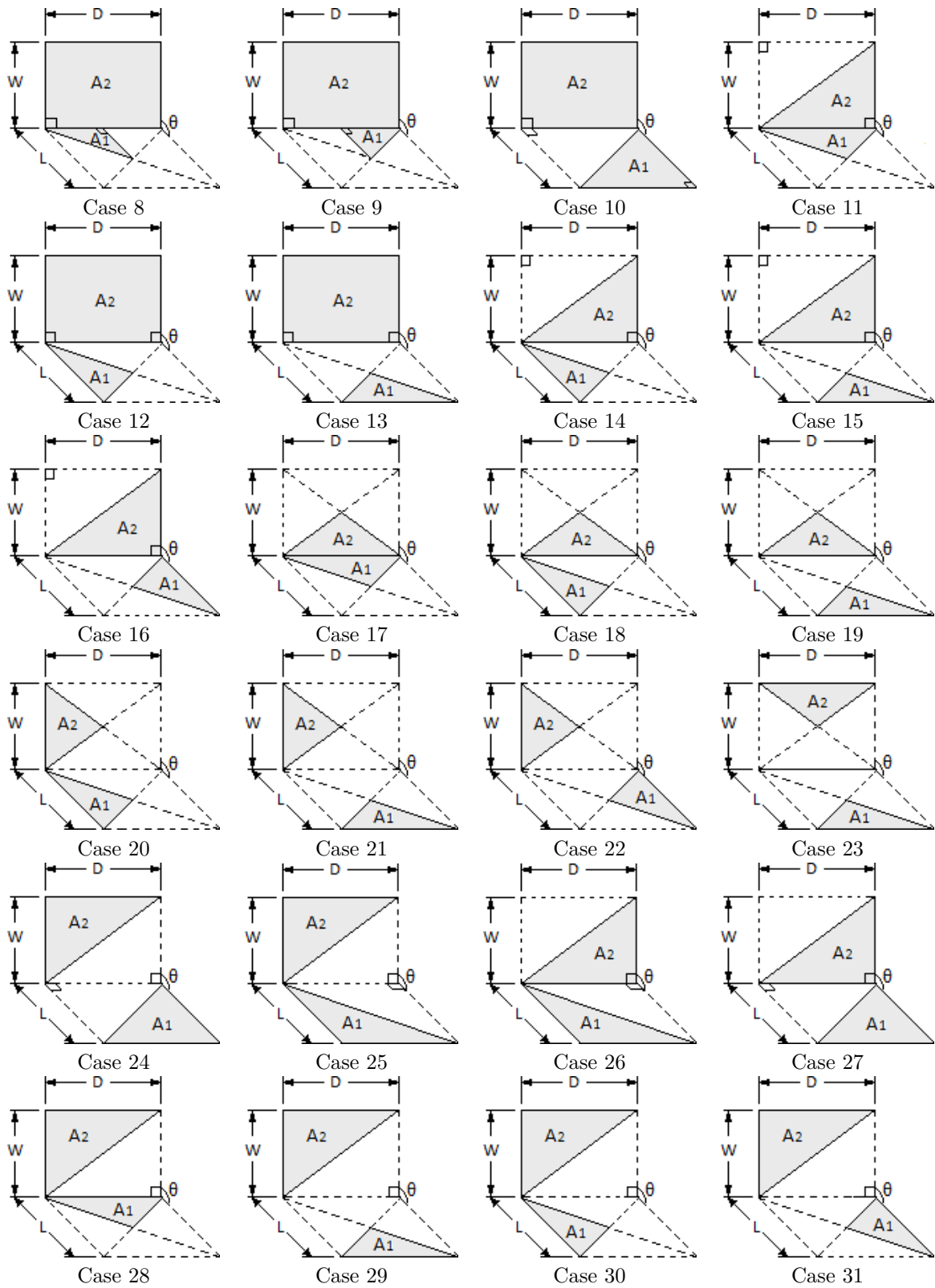


Figure 11. View factor settings for triangular surfaces

## 4. Conclusions

This study developed an approximate method to determine the view factor for 32 combinations of triangular geometries with common edges and angle  $\theta$  included, located in a 3-D space.

To validate the proposed models, 42 examples with various aspect ratios were evaluated for each geometry of the eight basic cases, comparing the results obtained by the AS with those of the SMR with five intervals and those computed by the proposed method with BCR.

In all the cases evaluated, the RCB showed the best fits with an error of  $\pm 6\%$  in more than 90% of the samples, and the SMR showed an average dispersion of  $\pm 6\%$  in 65% of the data, confirming the validity of the hypothesis on its use. For the remaining 24 geometric configurations studied, the basic relations for calculating the view factor from the expressions obtained for the eight basic cases were presented.

The practical nature of the contribution and the reasonable fitting values obtained demonstrate that this proposal is a suitable tool to be applied in thermal engineering and radiation heat transfer calculation tasks.

Due to the lack of similar precedents in the literature, the proposed method highlights this research's scientific and practical value. The solutions provided could be incorporated into the available catalogs for calculating view factors.

## Acknowledgments

The author gratefully acknowledges the assistance and recommendations from Professor Dr. John R. Howell, Department of Mechanical Engineering, University of Texas, Austin, and Professor Dr. Jack H. Lewis, Department of Mathematics, Massachusetts Institute of Technology, USA.

## References

- [1] J. R. Howell and M. P. Mengüç, "Radiative transfer configuration factor catalog: A listing of relations for common geometries," *Journal of Quantitative Spectroscopy and Radiative Transfer*, vol. 112, no. 5, pp. 910–912, 2011. [Online]. Available: <https://doi.org/10.1016/j.jqsrt.2010.10.002>
- [2] Y. F. Nassar, "Analytical-numerical computation of view factor for several arrangements of two rectangular surfaces with non-common edge," *International Journal of Heat and Mass Transfer*, vol. 159, p. 120130, 2020. [Online]. Available: <https://doi.org/10.1016/j.ijheatmasstransfer.2020.120130>
- [3] M. F. Modest and S. Mazumder, "Chapter 4 - View factors," in *Radiative Heat Transfer (Fourth Edition)*, fourth edition ed., M. F. Modest and S. Mazumder, Eds. Academic Press, 2022, pp. 127–159. [Online]. Available: <https://doi.org/10.1016/B978-0-12-818143-0.00012-2>
- [4] Y. Camaraza-Medina, A. Hernández-Guerrero, and J. L. Luviano-Ortiz, "Analytical view factor solution for radiant heat transfer between two arbitrary rectangular surfaces," *Journal of Thermal Analysis and Calorimetry*, vol. 147, pp. 14 999–15 016, 2022. [Online]. Available: <https://doi.org/10.1007/s10973-022-11646-4>
- [5] Y. Camaraza Medina, *Introducción a la termo-transferencia*. Editorial Universitaria (Cuba), 2020. [Online]. Available: <https://bit.ly/44PcgsO>
- [6] J. R. Howell, *A Catalog of Radiation Configuration Factors*. McGraw-Hill, 1982. [Online]. Available: <https://bit.ly/42qHzIJ>
- [7] J. R. Howell, M. Pinar Menguc, and R. Siegel, *Thermal Radiation Heat Transfer*. CRC Press, 2010. [Online]. Available: <https://bit.ly/42u9jfy>
- [8] M. K. Gupta, K. J. Bumtariya, H. Shukla, P. Patel, and Z. Khan, "Methods for evaluation of radiation view factor: A review," *Materials Today: Proceedings*, vol. 4, no. 2, Part A, pp. 1236–1243, 2017, 5th International Conference of Materials Processing and Characterization (ICMPC 2016). [Online]. Available: <https://doi.org/10.1016/j.matpr.2017.01.143>
- [9] A. Narayanaswamy, "An analytic expression for radiation view factor between two arbitrarily oriented planar polygons," *International Journal of Heat and Mass Transfer*, vol. 91, pp. 841–847, 2015. [Online]. Available: <https://doi.org/10.1016/j.ijheatmasstransfer.2015.07.131>
- [10] A. Narayanaswamy and P. Meyappan, "An analytic expression for radiation view factors between two planar triangles with arbitrary orientations," in *Proceedings of CHT-15. 6th International Symposium on ADVANCES IN COMPUTATIONAL HEAT TRANSFER*, 12 2015, pp. 1545–1550. [Online]. Available: <https://doi.org/10.1615/ICHMT.2015.IntSympAdvComputHeatTransf.1500>
- [11] R. Sudharshan Reddy, D. Arepally, and A. Datta, "View factor computation and radiation energy analysis in baking oven with obstructions: Analytical and numerical method," *Journal of Food Process Engineering*, vol. 46, p. e14270, 01 2023. [Online]. Available: <http://dx.doi.org/10.1111/jfpe.14270>

- [12] Y. Zhou, R. Duan, X. Zhu, J. Wu, J. Ma, X. Li, and Q. Wang, "An improved model to calculate radiative heat transfer in hot combustion gases," *Combustion Theory and Modelling*, vol. 24, no. 5, pp. 829–851, 2020. [Online]. Available: <https://doi.org/10.1080/13647830.2020.1769866> <https://doi.org/10.1080/13647830.2020.1769866>
- [13] X.-J. Yi, L.-Y. Zhong, T.-B. Wang, W.-X. Liu, D.-J. Zhang, T.-B. Yu, Q.-H. Liao, and N.-H. Liu, "Near-field radiative heat transfer between hyperbolic metasurfaces based on black phosphorus," *The European Physical Journal B*, vol. 92, no. 9, p. 217, Sep 2019. [Online]. Available: <https://doi.org/10.1140/epjb/e2019-100274-y>
- [14] J. R. Ehlert and T. F. Smith, "View factors for perpendicular and parallel rectangular plates," *Journal of Thermophysics and Heat Transfer*, vol. 7, no. 1, pp. 173–175, 1993. [Online]. Available: <https://doi.org/10.2514/3.11587>
- [15] C. K. Krishnaprakas, "View factor between inclined rectangles," *Journal of Thermophysics and Heat Transfer*, vol. 11, no. 3, pp. 480–481, 1997. [Online]. Available: <https://doi.org/10.2514/2.6267>
- [16] H. J. Sauer Jr., "Configuration factors for radiant energy interchange with triangular areas," *ASHRAE Transactions*, vol. 80, no. 2, pp. 268–279, 1974. [Online]. Available: <https://bit.ly/3I0jXm0>
- [17] Y. Camaraza-Medina, A. A. Sánchez Escalona, O. M. Cruz-Fonticiella, and O. F. García-Morales, "Method for heat transfer calculation on fluid flow in single-phase inside rough pipes," *Thermal Science and Engineering Progress*, vol. 14, p. 100436, 2019. [Online]. Available: <https://doi.org/10.1016/j.tsep.2019.100436>
- [18] W. Boeke and L. Wall, "Radiative exchange factors in rectangular spaces for the determination of mean radiant temperatures," *Building services engineering*, vol. 43, pp. 244–253, 1976.
- [19] F. F. Sönmez, H. Ziar, O. Isabella, and M. Zeman, "Fast and accurate ray-casting-based view factor estimation method for complex geometries," *Solar Energy Materials and Solar Cells*, vol. 200, p. 109934, 2019. [Online]. Available: <https://doi.org/10.1016/j.solmat.2019.109934>
- [20] S. Francisco, A. Raimundo, A. Gaspar, A. V. Oliveira, and D. Quintela, "Calculation of view factors for complex geometries using Stokes' theorem," *Journal of Building Performance Simulation*, vol. 7, pp. 203–216, 05 2014. [Online]. Available: <http://dx.doi.org/10.1080/19401493.2013.808266>
- [21] S.-A. Biehs, R. Messina, P. S. Venkataram, A. W. Rodríguez, J. C. Cuevas, and P. Ben-Abdallah, "Near-field radiative heat transfer in many-body systems," *Rev. Mod. Phys.*, vol. 93, p. 025009, Jun 2021. [Online]. Available: <https://doi.org/10.1103/RevModPhys.93.025009>
- [22] Y. Camaraza-Medina, A. Hernández-Guerrero, and J. L. Luviano-Ortiz, "Experimental study on influence of the temperature and composition in the steels thermo physical properties for heat transfer applications," *Journal of Thermal Analysis and Calorimetry*, vol. 147, no. 21, pp. 11 805–11 821, Nov 2022. [Online]. Available: <https://doi.org/10.1007/s10973-022-11410-8>
- [23] M. Lakhi and A. Safavinejad, "Numerical investigation of combined force convective-radiative heat transfer in a horizontal channel with Lattice Boltzmann method," *Journal of Thermal Analysis and Calorimetry*, vol. 146, no. 4, pp. 1911–1922, Nov 2021. [Online]. Available: <https://doi.org/10.1007/s10973-020-10136-9>
- [24] M. Bonnici, P. Mollicone, M. Fenech, and M. A. Azzopardi, "Analytical and numerical models for thermal related design of a new pico-satellite," *Applied Thermal Engineering*, vol. 159, p. 113908, 2019. [Online]. Available: <https://doi.org/10.1016/j.applthermaleng.2019.113908>
- [25] Y. Camaraza-Medina, "Methods for the determination of the heat transfer coefficient in air cooled condenser used at biomass power plants," *International Journal of Heat and Technology*, vol. 39, no. 5, pp. 1443–1450, 2021. [Online]. Available: <https://doi.org/10.18280/ijht.390505>



# METHODOLOGICAL PROPOSAL FOR THE DESIGN AND ANALYSIS OF A FORMULA SAE MONOCOQUE

## PROPUESTA METODOLÓGICA PARA EL DISEÑO Y ANÁLISIS DE UN MONOCASCO FORMULA STUDENT

Rafael Wilmer Contreras Urgilés<sup>1,\*</sup> , Carlos Ayrton Jaramillo Andrade<sup>1</sup> ,  
 Erick Josué Pizarro Barrera<sup>1</sup> 

Received: 11-04-2021, Received after review: 19-04-2023, Accepted: 05-05-2023, Published: 01-07-2023

### Abstract

This paper explains the methodology employed to design a Formula Student monocoque based on the regulations set forth in 2020. The values obtained from CAD (Computer Aided Design) modeling and FEM (Finite Element Method) analysis are the pillars of this study. The values of mass, center of gravity, and geometry have been specifically selected because they provide crucial information that aids in the identification of optimization points during the design process. The FEM analysis establishes the allowable stresses for the monocoque within the safety parameters, with a minimum admissible safety factor of 1.1. Two CFRP laminates (Carbon Fiber Laminate and Epoxy Resin Laminate) are developed from the model obtained. The first one yields a simulated weight of 38 kg, and the second one a weight of 20 kg. A stress analysis was performed on the lighter-weight model, obtaining results superior to those of a tubular chassis. A 2017 electric single-seater model is taken as a reference.

**Keywords:** Monocoque, FEM, FSAE, center of gravity, CFRP, AEF

### Resumen

En el presente documento se realiza la explicación de la metodología utilizada para el diseño de un monocoque Formula Student basado en el reglamento del año 2020. Los valores obtenidos del modelado mediante software CAD (diseño asistido por computador) y el análisis por MEF (método de elementos finitos) sirven de base para este estudio. Los valores de masa, centro de gravedad y la geometría son los seleccionados, ya que aportan una mayor información, lo que ayuda a determinar puntos de optimización en el proceso de diseño. En el análisis MEF se determina los esfuerzos admisibles por el monocoque y que se encuentran dentro de los parámetros de seguridad, siendo el factor de seguridad mínimo admisible de 1,1. Del modelo obtenido se desarrolla dos laminados CFRP (laminado de fibra de carbono y resina epoxi) de los cuales el primero da un resultado de peso simulado de 38 kg, y la segunda configuración de laminado un resultado de 20 kg. Se somete el modelo con menor peso al análisis de esfuerzos, los resultados obtenidos son superiores a un chasis tubular, se toma como referencia un modelo monoplaza eléctrico del 2017.

**Palabras clave:** monocoque, MEF, FSAE, centro de gravedad, CFRP, AEF

<sup>1,\*</sup>Ingeniería Mecánica Automotriz, Universidad Politécnica Salesiana, Cuenca, Ecuador.  
 Corresponding author ✉: rcontreras@ups.edu.ec.

Suggested citation: Contreras Urgilés, R. W.; Jaramillo Andrade, C. A. and Pizarro Barrera, E. J. "Methodological Proposal for the Design and Analysis of a Formula SAE Monocoque," *Ingenius, Revista de Ciencia y Tecnología*, N.º 30, pp. 42-53, 2023, DOI: <https://doi.org/10.17163/ings.n30.2023.04>.

## 1. Introduction

The monocoque is a structure that significantly reduces the weight of a vehicle. This chassis is used in elite automobile competitions, like Formula 1, and its subcategories, like Le Mans and Indycar. In Formula 3 tests, established by the International Automobile Federation (FIA), the monocoque is designed to pass static tests considered the desired standard of structural integrity for a monocoque [1].

The materials most commonly used in the manufacturing of monocoques are primarily composed of carbon fiber-reinforced polymer (CFRP) [2] and Honeycomb panels [3]. These materials exhibit high resistance to torsion and stresses and can be formed in almost any geometry. Ashby's research [4] presents a methodological proposal with a sandwich panel composed of three main elements: a core, a matrix, and carbon fiber. The carbon fiber has been studied in different orientations and combinations in the plane [5]. The combinations among degrees have allowed obtaining the desired mechanical properties in different directions and orientations. In the case of Honeycomb, as indicated in the study by Eurenus et al. [6], a symmetric hexagonal pattern of this structure exhibits relatively high properties in terms of compression and resistance to rupture while maintaining low density.

However, these materials have the disadvantage of being expensive and requiring complex manufacturing processes. In the design process, different geometries are considered. The Politécnico di Torino has analyzed different types of models [7, 8], as this parameter is crucial in optimizing the weight of the monocoque [9]. Based on this information, a CAD model that meets all the geometric requirements specified in the FSAE regulations was developed [10, 11]. Regarding chassis manufacturing, the study conducted by [12] has applied a methodology including design, analysis, and subsequent fabrication. The authors have confirmed the reliability of this methodology through dynamic tests.

In this work, geometry and aerodynamics are considered to take advantage of the shape of the monocoque to effectively minimize the need for additional elements that increase its weight [13]. Another significant parameter is the application of the CFRP laminate as an optimization point, as using different laminates can also reduce the overall weight of the vehicle. Additionally, the directions of the fibers help to reinforce some of the stresses to which the structure is subjected [14]. These cutting-edge materials and manufacturing processes optimize and improve performance in automobile competitions [15]. The results of proper lamination and optimal material selection enable the creation of a specific FEM model that, with reduced weight, can withstand the minimum stresses required by the competition [16].

Zhao [17] has studied a specific software used for FEM models, obtaining favorable results in predicting the overall behavior of the model's structure. Regarding the meshing of the model, a suitable element size was selected to create an accurate mathematical model for stress analysis. The most significant stresses applied to the structure are torsional rigidity, longitudinal rigidity, and lateral impact analysis [8]. Considering the design of the monocoque from Squadra Corse Polito [7] and the design from the University of Seville [18], an expected weight optimization of approximately 50% is anticipated. This will result in a more efficient model with reduced weight and a more resistant structure capable of withstanding the stresses applied to these vehicles.

## 2. Materials and Methods

This section presents aspects related to material selection, the main configuration of the panel, and the parameters for developing the design. Furthermore, it describes the results obtained from stress simulation.

### 2.1. Methodology

After analyzing the state of the art, a workflow was developed to determine the order and activities related to the design, structural analysis, and weight optimization of the model.

In the first stage, the FSAE regulations were reviewed to determine the most significant parameters regarding the design and restrictions of the monocoque [11].

In the second stage, the model was designed considering the restrictions previously analyzed [12].

Figure 1 illustrates the complete model. In the third stage, CFRP lamination was conducted to establish the thickness of the final model. The laminate varies depending on the section, as each requires a distinct thickness to withstand the stresses.

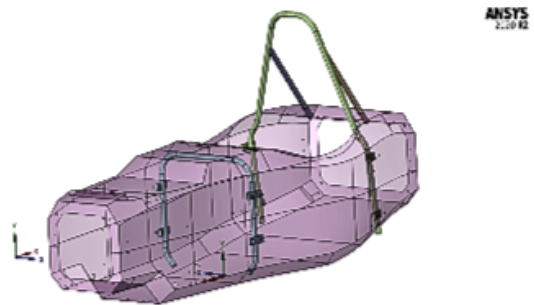


Figure 1. Final surface model

The analysis of the results is presented in detail in the section corresponding to the development of the proposed methodology.

## 2.2. Materials

The materials used in the analysis are carbon fiber fabric reinforcements in a sandwich structure (Figure 2) with Honeycomb. The combination of different materials is known as composite materials. These materials exhibit high mechanical resistance to withstand stresses and excellent stress dissipation capability throughout the structure. This sandwich panel comprises three main components: a core, a matrix, and carbon fibers [4].

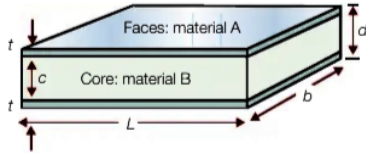


Figure 2. Typical sandwich structure [4]

### 2.2.1. Fibers

Elements made of fiber composite materials can be designed to suit each load case, allowing the material to be created based on specific static requirements. The directions of the fibers can also be customized. The material acquires the desired properties in all orientations by arranging carbon fiber sheets in various directions. The fiber orientations in the plane are  $0^\circ$ ,  $90^\circ$ , and  $\pm 45^\circ$  [5].

Figure 3 demonstrates that Kevlar fiber is the most resistant, whereas carbon fiber is the most rigid. Fiberglass is the least resistant and rigid but is the cheapest of the three.

These materials provide a considerable advantage in terms of overall weight. Their utilization is highly advantageous in constructing a structure with a rigidity comparable to that of a conventional metal structure while reducing its weight by half [5].

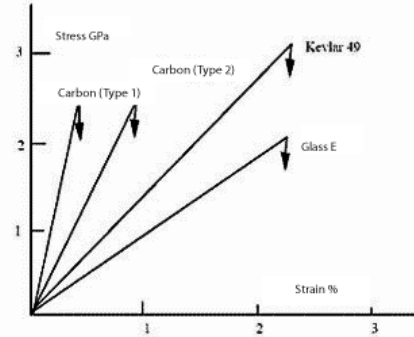


Figure 3. Fiber stress-strain diagram [5]

### 2.2.2. Matrix

The matrix is the material that supports and bonds all the fibers together. The fibers are impregnated into the matrix to form a single material.

Currently, two main types of resins are primarily used for the matrix: epoxy and polyester. Both resins are thermally stable, which means they do not melt under heat, although they may lose some rigidity properties. Additionally, they exhibit an isotropic structural behavior, indicating that their physical properties are similar in all directions. In this study, an epoxy resin was employed.

Table 1 lists some properties of the resins.

Table 1. Resin properties [5]

Property	Units	Epoxy resins	Polyester resins
Density	$Mg\ m^{-3}$	1.1-1.4	1.2-1.5
Young's modulus	GPa	3-6	2-4.5
Poisson Coefficient		0.38-0.4	0.37-0.39
Tensile resistance	MPa	35-100	40-90
Compression resistance	MPa	100-200	90-250
Elongation at break (tensile)	%	1-6	2
Thermal conductivity	$Wm^{-1}\ C^{-1}$	0.1	0.2
Expansion Coefficient	$10^{-6}\ C^{-1}$	60	100-200
Distortion temperature	$^\circ C$	50-300	50-110
Curing shrinkage	%	1-2	4-8
Water absorption (24 h a 20 $^\circ C$ )	%	0.1-0.4	0.1-0.3

### 2.2.3. Honeycomb Core

There are various types of Honeycomb cores, each with different properties depending on the material used for fabrication. The most common ones are made from aluminum, aramid paper (Nomex), steel, fiberglass, carbon, or ceramic [14]. The Honeycomb core is composed of a symmetrical hexagonal pattern, as depicted in Figure 4. This structure offers excellent compressive and tensile resistance properties and a low density [6].

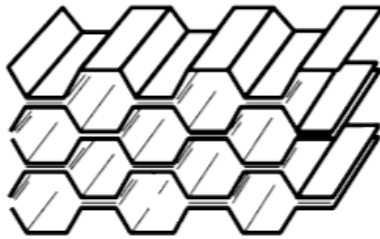


Figure 4. Structure with hexagonal cells [6]

In this study, an aluminum Honeycomb core was selected. This core has an excellent energy absorption capacity, and its thickness is 20 mm.

## 3. Results and discussion

In this section, weight and optimization objectives are established. To achieve a solid theoretical foundation, the flowchart presented in Figure 5 was considered to determine the final model [15].

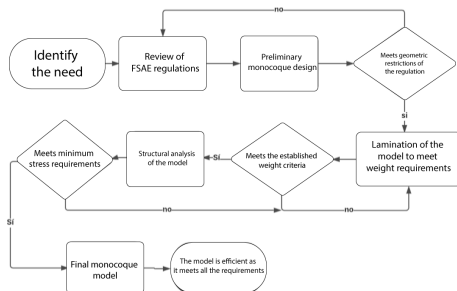


Figure 5. Monocoque design process

### 3.1. Determination of the CAD model

The model's design is based on the regulations for the 95th percentile male, as detailed below:

To maximize driver comfort, various factors are considered, including the vertical and horizontal position of the steering wheel, seat angle, pedal placement, and safety bars [9]. Figure 6 shows the template for the 95th percentile male. The specific distance values are detailed in the FSAE regulations [11]

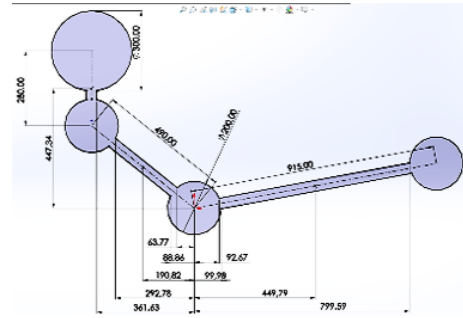


Figure 6. Template for the 95th percentile male [15]

After determining the percentiles and minimum dimensions of the cabin opening, and the minimum cross-sectional area, the first dimensioning is carried out to establish the foundation of the monocoque design. Figure 7 presents the cross-sectional and cabin openings.

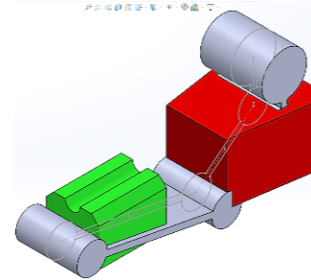


Figure 7. Isometric perspective view of the internal cross-sectional opening [15]

The dimensions of these sections are detailed below: Cabin opening (Figure 8)

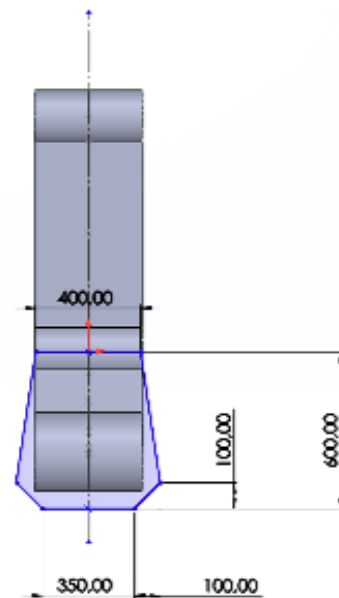
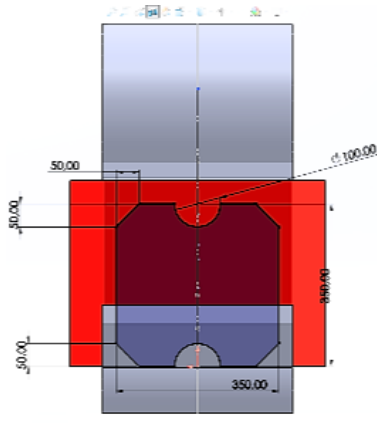


Figure 8. Cabin opening dimensions [15]

- 320 mm above the lowest point of the upper floor surface for monocoque design.
- 400 mm front width.
- 350 mm rear width.
- 600 mm minimum cabin length.

Internal cross-sectional area (Figure 9)



**Figure 9.** Dimensions of the internal cross-sectional area [15]

- An internal cross-sectional area must be kept clear to allow the passage of the template shown through the cabin.
- Minimum length and width of 350 mm.
- Radius of 50 mm at the top and bottom centers.

Using these measurements, a model is created incorporating the main components of the monocoque. These components include a battery located in the rear, an inverter positioned beneath the driver's legs, and a pair of firewalls. Figure 10 displays the primary side view sketch.

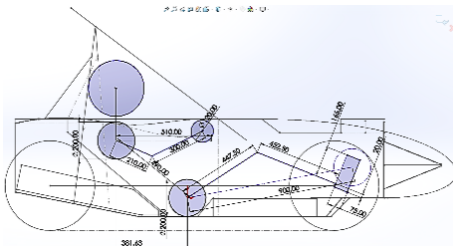


**Figure 10.** Arrangement of components and side sketch [15]

Based on this sketch, the CAD model is created, placing the attachment points of some elements on the monocoque. Figure [11] illustrates the final design.

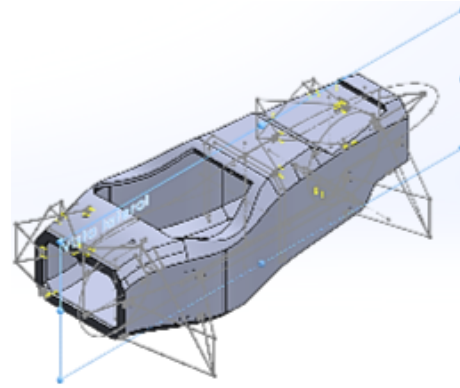


**Figure 11.** Final design of the monocoque [15]

With the final model, the center of gravity and the stresses are obtained, as detailed below:

### 3.2. Determination of the center of gravity

In this section, the weights are applied to the monocoque in the software. Subsequently, the main components selected for calculation are assembled, as shown in Table 2. Using the physical properties tool, the position of the center of gravity of the assembled prototype is determined, as shown in Figure 12.

**Table 2.** Approximate vehicle masses [10]

Components	Mass (kg)	%
Driver	70	42.85
Battery	36	20.57
Inverter	7	4
Pedal box	4.5	2.57
Steering	12.5	7.15
Monocoque	20	11.43
Other components	20	11.43
<b>Total</b>	<b>175</b>	<b>100</b>

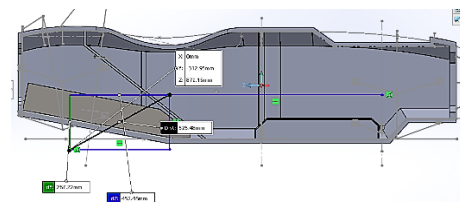


**Figure 12.** Center of gravity location [15]

### 3.3. Lateral mass transfer

To perform this calculation, it is considered that the vehicle follows a curve, acting on the center of gravity with a centrifugal acceleration of 4G. Figure 13 illustrates the free-body diagram defining the center of gravity and the direction of the loads.

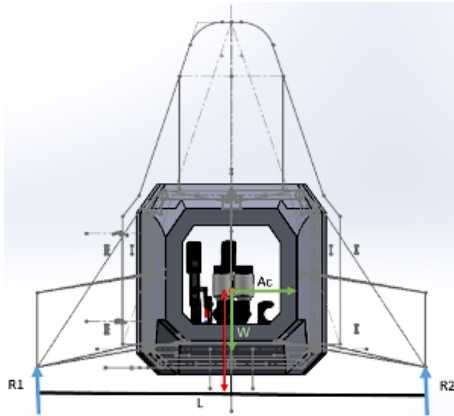


Figure 13. Free body diagram [15]

The R2 reaction is the load that influences torsional rigidity. This torque is applied in opposite directions on both sides of the front axle. A value of 6870 N was used to simulate a higher load on the monocoque and demonstrate the material's stiffness [11].

### 3.4. Longitudinal Mass Transfer and Braking

The longitudinal mass transfer in the direction of the front tires results from the braking forces. Figure 14 shows the free-body diagram for this stress.

The maximum speed, the coefficient of friction between the tires and the asphalt, the position of the center of gravity, the braking time, and the weight of the vehicle are determined as initial conditions.

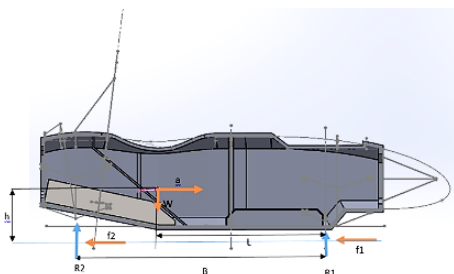


Figure 14. Longitudinal free-body diagram [15]

The calculated loads  $R1=1423.85$  N and  $f1=1181.79$  N involved in the longitudinal resistance and braking tests are taken as reference. However, in the simulation, all values are increased to further stress the model.

### 3.5. Side Impact Case

In the initial assessment, the vehicle's speed is assumed to be 40 km/h, considering the worst-case scenario, and applying a force of 4.5 G during the impact. A vehicle weight of 220 kg and a driver weight of 75 kg are used for the calculation [15]. By applying the formula for final velocity, considering a final velocity of 11.11 m/s corresponding to an initial velocity starting from rest, plus the multiplication of the acceleration (which is the value to be determined) by the time of 0.3 s, a value of 37.03 m/s<sup>2</sup> is obtained. Using this acceleration value, the resulting force is calculated by multiplying the acceleration by the mass of 290 kg, resulting in 10 739.66 N. This force is used for the simulation of the side impact [16].

### 3.6. Model Preparation in ANSYS ACP

The ANSYS software provides the Composite PrePost (ACP) tool to facilitate the creation of the finite element model and access the results.

Real models constructed with composite materials consist of multiple layers and various materials. Consequently, it is crucial to meticulously prepare the FEM model by ensuring accurate layer orientations and proper material stacking [17].

Figure 15 shows the final model with the layers in ANSYS ACP.

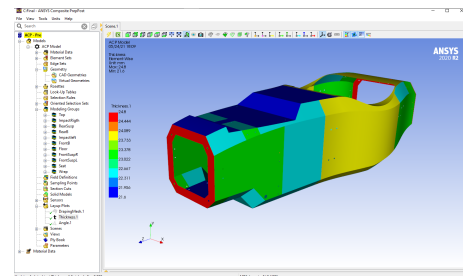


Figure 15. Final model in ANSYS ACP [15]

### 3.7. Analysis of the torsional rigidity of the model using FEM

Torsional rigidity is physically defined by the equation described below. Through FEM analysis, the total deformation is determined. Figure 16 shows how the values  $y1, x1$ . are measured [18].

$$k = \frac{M}{\theta}; \theta = \tan^{-1} \left( \frac{y1}{x1} \right)$$

Where:

M = Torsional moment (N\*m)

$\theta$  = Deformation angle (degrees)

$x1$  = Horizontal distance from the vehicle’s central plane to the point where the deformation  $y1$  is measured.

$y1$  = Vertical deformation

$K$  = torsional rigidity (N\*m/degrees)

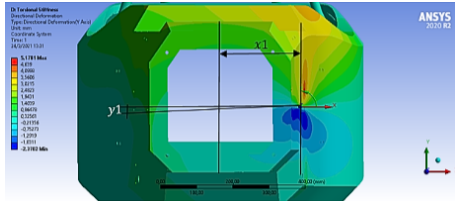


Figure 16. Distance  $x1$  and  $y1$  [15]

For this simulation, a force of 6870 N was applied, resulting in an average deformation of 1.001 mm and a maximum deformation of 4,2 mm as shown in Figure 17. A maximum deformation of 5,3 mm above the upper suspension point is observed where the stress is most concentrated.

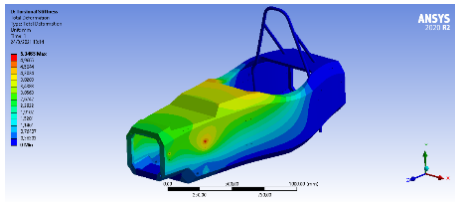


Figure 17. Torsional rigidity deformation [15]

### 3.8. Longitudinal rigidity analysis

To analyze this deformation, a load of 2500 N is applied to the front axle, resulting in a deformation of 1.99 mm, as shown in Figure 18.

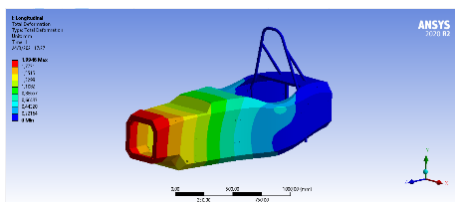


Figure 18. Longitudinal rigidity deformation [15]

Regarding the stress on the structure, the maximum value is 101.44 MPa, as shown in Figure 19. This stress is low because the structure exhibits a uniform distribution throughout its entirety.

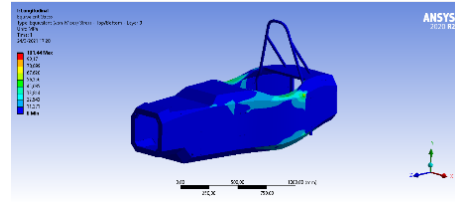


Figure 19. Longitudinal stresses [15]

### 3.9. Braking analysis

In this analysis, two loads are applied to the front axle with a value of 2500 N in the vertical direction and 2000 N in the longitudinal direction, resulting in a maximum deformation of 2.12 mm, as shown in Figure 20.

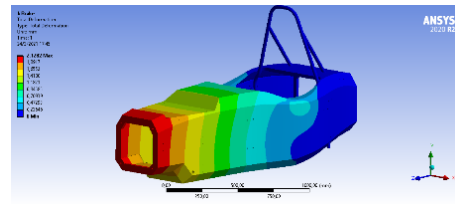


Figure 20. Braking deformation [15]

The maximum stress on the structure is 113.16 MPa, which does not cause material rupture, as shown in Figure 21.

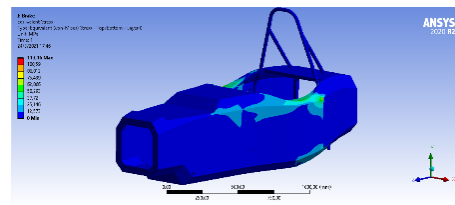


Figure 21. Braking stresses [15]

### 3.10. Side impact analysis

The value of this stress is 10,739.66 N, as detailed in section 3.53 [15]. The maximum deformation is 1.35 mm, as shown in Figure 22.

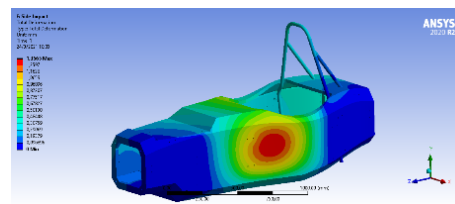


Figure 22. Side impact deformation [15]

The stress on the structure has a maximum value of 72.61 MPa, indicating a better distribution throughout the monocoque, as shown in Figure 23.

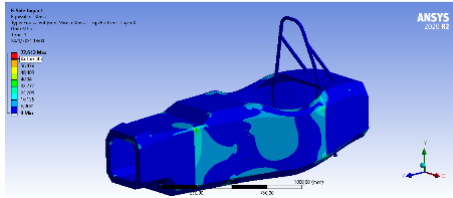


Figure 23. Side impact stresses [15]

### 3.11. Rollover simulation

In this simulation, three loads are applied: a longitudinal, a transverse, and a vertical load of 6 KN, 5 KN and 9 KN, respectively. The results show a maximum deformation value of 16.15 mm (Figure 24) and a maximum stress value of 426.52 MPa (Figure 25) [19].

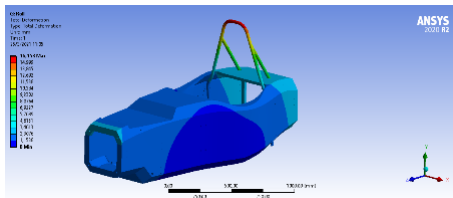


Figure 24. Main Hoop Deformation [15]

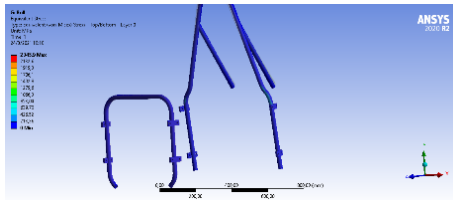


Figure 25. Main Hoop Stresses [15]

### 3.12. Weight simulation on the monocoque floor

In this simulation, the distributed weight of the elements is applied to the monocoque floor. Table 3 presents the weight of the elements and the corresponding forces exerted by them.

Table 3. Weight of the elements on the monocoque [15]

Component	Weight (kg)	Force (N)
Driver	75	735.75
Steering	12.5	122.62
Battery	36	353.16
Pedal box	4.5	44.15
Inverter	7	68.67

The results of this simulation show that the maximum deformation on the monocoque floor is 0.13 mm

(Figure 26), and the maximum stress is 15 MPa (Figure 27). This indicates that the material can perfectly withstand the weight of the elements.

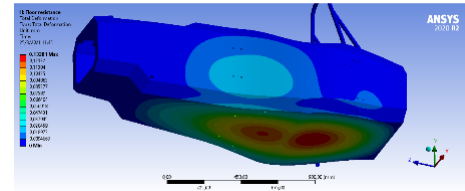


Figure 26. Floor deformation [15]

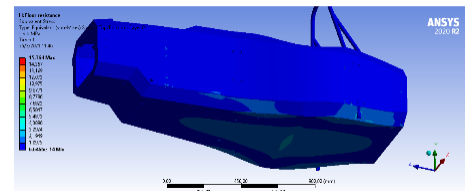


Figure 27. Floor stresses [15]

### 3.13. Data validation

#### 3.13.1. Design efficiency in terms of weight reduction

Considering the data obtained, an efficiency analysis was performed to assess the weight reduction of the prototype.

The EB17 model is used as a reference for comparison with the prototype design in this work [10].

Table 4 shows that the combined weight of the chassis and body is 55.31 kg, representing 23.54% of the total weight [15].

The material used in the Main and Front Hoop structures is "AISI 4130 steel normalized at 870 °C". The data were obtained from the EB17 simulation.

Figure 28 shows that using the software, a reduced weight of 0.0420 t (equivalent to 42 kg) was obtained without using the safety triangle in the ANSYS program. When adding the data from the safety triangle, the weight is 48.19 kg for the three combined elements [15]

Table 4. Approximate masses of EB17 [10]

Component	Mass (kg)	%
Driver	80	33.75
Engine	12	5.06
Powertrain	20	8.43
Steering system	10	4.21
Battery	80	33.75
Chassis	35	14.76
Total	237	100

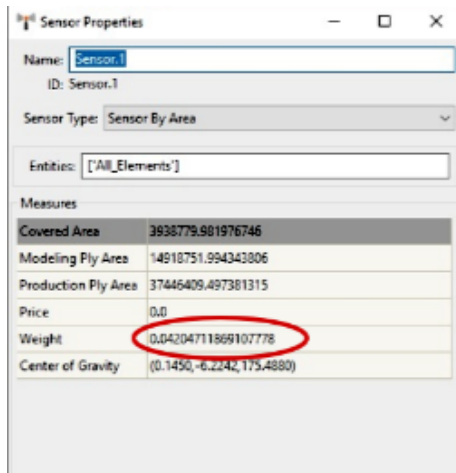


**Figure 28.** Preliminary weight of the monocoque obtained from ANSYS ACP [15]

For the final analysis, the weight of the monocoque was obtained by optimizing the layers of the model, as shown in Figure 29. Using its triangular structures, a weight of 0.0227 t (22.7 kg) was obtained, thus reducing nearly half of the initial weight.

Integrating safety elements increased security and reduced material layers, optimizing the weight. Along with its safety triangle, the final weight is 27.2 kg. The final weight optimization analysis shows a significant reduction compared to the EB17, which weighs 237 kg, with 55.31 kg resulting from the weight of the chassis and body. The monocoque has a final weight of 27.2 kg, indicating a 47.2% weight reduction optimization, which means 28.11 kg less for the theoretical single seater.

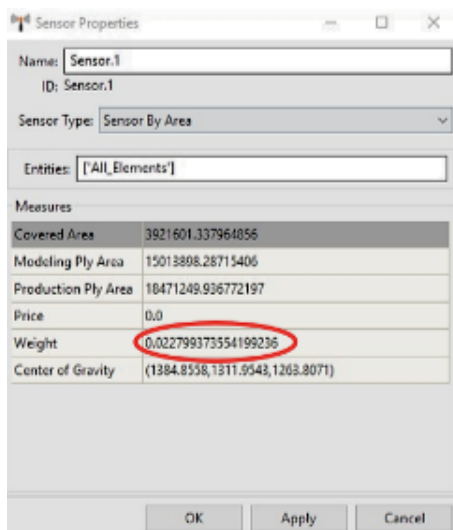


**Figure 29.** Final weight of the monocoque obtained from ANSYS ACP [15]

### 3.13.2. Torsional rigidity comparison

The monocoque demonstrates a superior stress dissipation capability, 2.1 times higher compared to the EB17 model, while also exhibiting a 17% reduction in stress concentration. Additionally, the monocoque boasts a 75% higher K value, which defines its torsional rigidity, in comparison to the EB17. This enhanced rigidity significantly contributes to the vehicle’s stability during cornering maneuvers. (Figure 30 and Table 5).

**Table 5.** Torsional rigidity of the models [15]

Model	Load (N)	Maximum stress	Maximum deformation	K (KNm/degree)
Monocoque	6780	306.22 MPa	4.2 mm	30
EB17	3133	370 MPa	3.8 mm	7.7

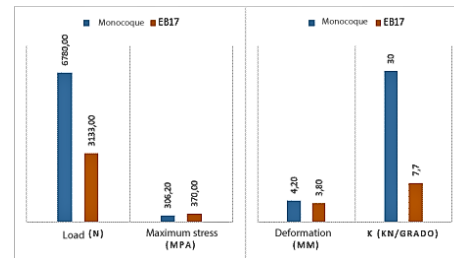


**Figure 30.** Torsional rigidity results [15]

### 3.13.3. Longitudinal rigidity comparison

The monocoque demonstrates an 11% reduction in applied load during the simulation, resulting in improved stress dissipation. This is attributed to a 45% decrease in stress concentration and a 50% reduction in deformation compared to the EB17 model. (Figure 31 and Table 6).

**Table 6.** Longitudinal rigidity comparison [15]

Model	Load (N)	Maximum stress	Maximum deformation
Monocoque	2500	101.44 MPa	1.99 mm
EB17	2782.68	182 MPa	4 mm

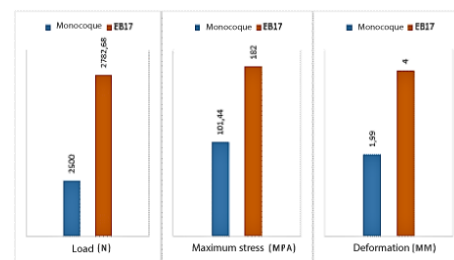


**Figure 31.** Longitudinal rigidity results [15]

### 3.13.4. Braking comparison

For this analysis, the loads acting on the front wheels are considered, including vertical and longitudinal loads on the vehicle. (Figure 32 and Table 7).

Table 7. Braking analysis [15]

Model	Vertical load	Longitudinal load	Maximum stress	Maximum deformation
Monocoque	2500 N	2000 N	113.16 MPa	2.12 mm
EB17	2782.68 N	2309.63 N	201 MPa	4.2 mm

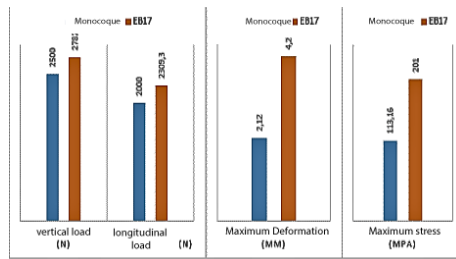


Figure 32. Braking results [15]

### 3.13.5. Side impact comparison

The monocoque experiences a reduction of 11% in vertical load and 14% in longitudinal load. This results in higher stress dissipation in the monocoque, as it exhibits a 44% reduction in stress concentration compared to the EB17. Additionally, the monocoque demonstrates a 44% decrease in deformation compared to the EB17 model. (Figure 33 and Table 8).

Table 8. Side impact analysis [15]

Model	Load (N)	Maximum stress	Maximum deformation
Monocoque	10740	72.61 MPa	1.35 mm
EB17	7000	361 MPa	3.32 mm

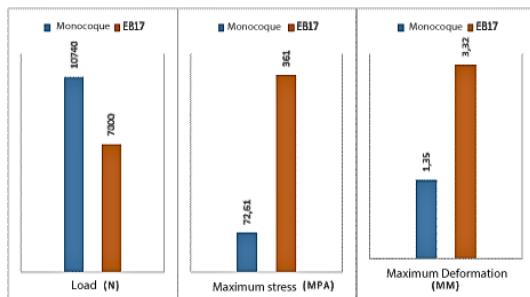


Figure 33. Side impact results [15]

The monocoque demonstrates superior stress dissipation within its structure, with a load 53% higher than that of the EB17 model and an 80% reduction

in stress accumulation. Furthermore, the monocoque exhibits a 60% decrease in deformation compared to its predecessor model.

## 4. Conclusions

Through the development of this article, the design proposal for a carbon fiber monocoque for a Formula Student single-seater has been determined. SolidWorks software has been used for modelling, and ANSYS software for simulation, allowing a thorough analysis of the performance and characteristics of the monocoque.

The proposal to use a monocoque chassis has achieved a weight reduction of 47.2% compared to its predecessor, the EB17, which had a tubular chassis. This demonstrates the superiority and relevance of implementing carbon fiber technology.

The proposed design implemented a sandwich structure utilizing ANSYS software. This structure enables the utilization of woven carbon fiber and aluminum Honeycomb. These materials have demonstrated excellent safety levels, and minimal deformations, and have successfully met safety standards.

## References

- [1] K. P. Hammer, *Design and Analysis of a Composite Monocoque for Structural Performance: A Comprehensive Approach*. Indiana University–Purdue University, 2019. [Online]. Available: <http://dx.doi.org/10.7912/C2/2703>
- [2] G. Davies, *Materials for automobile Bodies*. Elsevier, 2003. [Online]. Available: <https://bit.ly/42DnE9K>
- [3] Panel Systems. (2023) Larcore aluminium honeycomb panels. Panel Systems Ltda. [Online]. Available: <https://bit.ly/41F5dQs>
- [4] M. F. Ashby, *Materials Selection in Mechanical Design*. Butterworth-Heinemann, 2016. [Online]. Available: <https://bit.ly/41ETGAV>
- [5] F. P. Carballo, *Introducción al análisis y diseño con materiales compuestos*. Universidad de Sevilla, Escuela Técnica Superior de Ingenieros, 2008. [Online]. Available: <https://bit.ly/41z45hu>
- [6] C. A. Eurenus, N. Danielsson, A. Khokar, E. Krane, M. Olofsson, and J. Wass, *Analysis of Composite Chassis*. The Department of Applied Mechanics, Chalmers University of Technology, 2013. [Online]. Available: <https://bit.ly/3o38oE6>
- [7] F. Jourdan, *Degree Course in Automotive Engineering*. Politecnico di Torino, 2019. [Online]. Available: <https://bit.ly/3nZtHqB>

- [8] W. B. Riley and A. R. George, "Design, analysis and testing of a formula sae car chassis," in *Motorsports Engineering Conference & Exhibition*. SAE International, dec 2002. [Online]. Available: <https://doi.org/10.4271/2002-01-3300>
- [9] E. Tsirogiannis, G. Stavroulakis, and S. Makridis, "Design and modelling methodologies of an efficient and lightweight carbon-fiber reinforced epoxy monocoque chassis, suitable for an electric car," *Material Science and Engineering with Advanced Research*, vol. 2, pp. 5–12, 02 2017. [Online]. Available: <http://dx.doi.org/10.24218/msear.2017.21>
- [10] V. R. Álvarez Salazar, *Diseño y construcción de un chasis tubular de un vehículo de competencia Formula SAE eléctrico*. Universidad Politécnica Salesiana, 2018. [Online]. Available: <https://bit.ly/4324j1U>
- [11] SAE, *The 2020 Formula SAE Rules Version 1.0 are now published online under the Series Resources*. SAE International Privacy Policy, 2019. [Online]. Available: <https://bit.ly/4539Irb>
- [12] W. Contreras, P. Quezada, and L. Ortiz, *Propuesta metodológica para el diseño del chasis de un kart tipo KF4*. La ingeniería automotriz clave para el desarrollo sostenible de Ecuador, 2018, ch. Diseño Automotriz, pp. 55–77. [Online]. Available: <https://bit.ly/42EhUN2>
- [13] K. Egger, B. Ford, K. Nagao, N. Sharma, and D. Zusalim, *Formula SAE Monocoque Chassis Development*. Mechanical Engineering Department. California Polytechnic State University, San Luis Obispo, 2020. [Online]. Available: <https://bit.ly/42EiIl2>
- [14] J. Wu, O. Agyeman Badu, Y. Tai, and A. R. George, "Design, analysis, and simulation of an automotive carbon fiber monocoque chassis," *SAE International Journal of Passenger Cars - Mechanical Systems*, vol. 7, no. 2, pp. 838–861, apr 2014. [Online]. Available: <https://doi.org/10.4271/2014-01-1052>
- [15] C. A. Jaramillo Andrade and E. J. Pizarro Barrera, *Análisis y simulación de un monocoque de fibra de carbono para un monoplaza Formula Student*. Universidad Politécnica Salesiana, 2021. [Online]. Available: <https://bit.ly/3pFmc85>
- [16] R. Patil, "Fea analysis of fsae chassis," *International Journal of Engineering Research and*, vol. V9, 07 2020. [Online]. Available: <http://dx.doi.org/10.17577/IJERTV9IS070148>
- [17] B. Zhao, *Analysis of composite plates by using mechanics of structure genome and comparison with ANSYS*. Aeronautics and Astronautics. Purdue University Indianapolis, 2016. [Online]. Available: <https://bit.ly/3pQw8LW>
- [18] F. P. Ruiz and M. Solís Muñíz, *Diseño y cálculo del chasis monocoque de un monoplaza de competición tipo fórmula*. Tesis de Grado. Ingeniería Industrial. Escuela Técnica Superior de Ingeniería. Universidad de Sevilla. España, 2016. [Online]. Available: <https://bit.ly/3o8NT91>
- [19] M. Tamjidillah, R. Subagyo, H. Isworo, and H. Y. Nanlohy, "Modelling analysis of high effect of roll hoop main on the strength of student car formula chassis," *Journal of Achievements in Materials and Manufacturing Engineering*, vol. 1, pp. 26–40, 05 2020. [Online]. Available: <http://dx.doi.org/10.5604/01.3001.0014.1959>





# CORRELATION FOR THE CALCULATION OF TURBULENT FRICTION IN PIPES

## CORRELAÇÃO PARA EL CÁLCULO DE LA FRICCIÓN TURBULENTA EN TUBERÍAS

San Luis Tolentino<sup>1,\*</sup> , Omar González<sup>2</sup> 

Received: 25-01-2023, Received after review: 21-04-2023, Accepted: 18-05-2023, Published: 01-07-2023

### Abstract

One of the essential parameters in hydraulic systems of pipe networks is the friction factor  $\lambda$ . The friction factor is determined using the implicit Colebrook-White equation through iterative methods, which makes its application challenging. In this work, a correlation based on the recursive method is developed to calculate the friction factor using the Colebrook-White equation. Two empirical relationships are proposed to finalise the correlation, with coefficients and exponents calibrated in Excel 2019. The results of the two proposed relationships were compared with the Swamee-Jain and Haaland relationships for recursive increments. For the  $\lambda_8$  correlation, the maximum percentage error of the friction factor was 0,0000017%, for a relative roughness of 0,00001 and a Reynolds number of 4000. Additionally, the calculations yielded seven exact decimal digits for the friction factor. For Reynolds numbers greater than 4000, the percentage error decreases. As a result, it is concluded that the correlation based on the proposed explicit relationships satisfies the solution of the implicit Colebrook-White equation.

**Keywords:** Correlation, Colebrook-White equation, Percentage error, Friction factor, Recursive method

### Resumen

En los sistemas hidráulicos de redes de tuberías, uno de los parámetros fundamentales es el factor de fricción  $\lambda$ . El factor de fricción se determina con la ecuación implícita de Colebrook-White por medios iterativos, lo cual dificulta su aplicación. En el presente trabajo se construye una correlación basada en el método recursivo para el cálculo del factor de fricción, para lo cual se empleó la ecuación de Colebrook-White. Para el cierre de la correlación se proponen dos relaciones empíricas, donde sus coeficientes y exponentes fueron calibrados en Excel 2019. Se compararon los resultados de las dos relaciones que se proponen con las relaciones de Swamee-Jain y Haaland, para incrementos recursivos, donde para la correlación  $\lambda_8$  se obtuvo el error porcentual máximo del factor de fricción de 0,0000017 %, para la rugosidad relativa de 0,00001 y número de Reynolds 4000; así como, los decimales arrojaron siete dígitos decimales exactos para el factor de fricción. Para Reynolds mayores de 4000, el error porcentual disminuye. Se concluye que la correlación en función de las relaciones explícitas que se proponen satisface a la solución de la ecuación implícita de Colebrook-White.

**Palabras clave:** correlación, ecuación de Colebrook-White, error porcentual, factor de fricción, método recursivo

<sup>1,\*</sup>Group of Mathematical Modeling and Numerical Simulation (GMMNS), Universidad Nacional de Ingeniería, Lima, Perú. Corresponding author ✉: sanluist@gmail.com.

<sup>2</sup>Universidad Nacional Hermilio Valdizán, Huánuco, Perú.

Suggested citation: Tolentino, S. L. and González, O. "Correlation for the calculation of turbulent friction in pipes," *Ingenius, Revista de Ciencia y Tecnología*, N.º 30, pp. 54-63, 2023, DOI: <https://doi.org/10.17163/ings.n30.2023.05>.

## 1. Introduction

In pipe network systems in industrial processes, internal flow exhibits fluctuations in velocity, pressure, temperature, and other parameters. The flow is driven by pressure differentials, and flow friction is always present.

For a pipeline or measuring instrument, a gradient of pressure, velocity, and temperature occurs. The flow velocity is maximum in the central region, while at the wall, it is zero due to the no-slip condition. Therefore, a pressure decrease caused by viscous stresses represents an irreversible pressure loss known as pressure drop [1, 2]. There are abrupt pressure drops in the throat section in experimental flow measurement devices, such as the Venturi tube. In contrast, the pressure drops on the walls of the junctions between the throat section and the converging and diverging sections are lower compared to the central region of the flow [3].

The flow regime is classified into laminar, transitional, and turbulent. Smooth and parallel streamlines with orderly motion characterize the laminar flow. This flow is expected in fluids with high viscosity and low-speed motion. On the other hand, turbulent flow is characterized by random fluctuations of eddies at different scales.

These eddies transport mass, amount of motion, and energy to other flow regions, increasing the amount of motion, mass, and heat transfer in the affected areas. As a result, turbulent flow is associated with significant variations in the values of friction coefficients, mass transfer, and heat transfer [1, 2].

Osborne Reynolds [4] conducted experiments on pipe sections to study the flow and discovered that the flow regime is related to the ratio of inertial forces to viscous forces in the fluid. This ratio is known as the Reynolds number,  $R_e$ , and is calculated using the formula:  $R_e = Vd/\nu$ , where  $V$  is the average velocity,  $d$  is the internal diameter of the pipe,  $\nu = \mu/\rho$  is the kinematic viscosity,  $\mu$  is the dynamic viscosity, and  $\rho$  is the density of the fluid [1, 2].

The transition from laminar flow to turbulent flow is determined by the viscosity and velocity of the flow, as well as the pipe geometry, internal wall roughness, wall temperature, and other factors. In most practical conditions, flow is classified as follows: laminar flow for  $R_e \leq 2300$ , turbulent flow for  $R_e \geq 4000$ , and transitional flow in the range of  $2300 \leq R_e \leq 4000$  [1, 2].

Colebrook and White [5, 6] proposed an implicit equation to calculate the friction factor  $\lambda$ , in turbulent flow in pipes, based on the results of their experimental research. This equation is known as the Colebrook-White equation (1).

$$\frac{1}{\sqrt{\lambda}} = -2\log \left[ \frac{\varepsilon}{3,7} + \frac{2,51}{R_e\sqrt{\lambda}} \right] \quad (1)$$

The Colebrook-White equation combines data for transitional and turbulent flow in smooth and rough pipes. The parameter  $\varepsilon$  represents the relative roughness and is defined as  $\varepsilon = k/d$ , where  $k$  is the average height of the material's roughness and  $d$  is the pipe's internal diameter. The parameter  $R_e$  is the Reynolds number. The parameters  $\lambda$ ,  $\varepsilon$  and  $R_e$  are dimensionless.

The friction factor in the Colebrook-White equation cannot be solved accurately and explicitly using algebraic procedures. Therefore, the friction factor is determined using numerical methods through iterative procedures in computational codes, such as the Newton-Raphson method, bisection, fixed-point iteration, etc. This makes it challenging to obtain the friction factor in the design of pipeline networks due to the extensive and laborious calculations required by these iterative methods.

As an alternative solution to the implicit Colebrook-White equation, Moody [7] proposed using a graph that represents this equation. This graph is used in engineering to determine the friction factor. However, a numerical error is generated when determining the friction factor, which implies obtaining an approximate result.

The literature describes empirical correlations that provide an approximate solution for calculating the friction factor. These correlations are based on the Colebrook-White equation. Among the most well-known and widely used empirical correlations are the Swamee-Jain equation (2) [8], with a maximum estimated error of 3.2%, and the Haaland equation (3) [9], with a maximum estimated error of 2.1%.

$$\frac{1}{\sqrt{\lambda}} = -2\log \left[ \frac{\varepsilon}{3,7} + \frac{5,74}{R_e^{0,9}} \right] \quad (2)$$

$$\frac{1}{\sqrt{\lambda}} = -1,8\log \left[ \left( \frac{\varepsilon}{3,7} \right)^{1,11} + \frac{6,9}{R_e} \right] \quad (3)$$

Several authors have proposed various empirical and explicit relationships to decrease the numerical error associated with the friction factor in relation to  $\varepsilon$  and  $R_e$ . They have employed different methods to obtain a more accurate solution to achieve this.

Some authors, such as Mikata and Walczack [10], Rollmann and Spindler [11] and Biberg [12] apply the Lambert  $\omega$  function. Serghides [13], Vatankhah [14], and Azizi *et al.* [15] obtain correlations through combinations of algebraic procedures. Chen [16], Schorle *et al.* [17], Zigrang and Sylvester [18], Sousa *et al.* [19], Romeo *et al.* [20] and Offor and Alabi [21] obtain correlations using the recursive method with modifications of constants and exponents. Santos *et al.* [22] and Alfaro *et al.* [23] conduct experimental evaluations to calculate the friction factor.

In addition to the aforementioned authors, Pérez *et al.* [24] present a list of forty-nine (49) explicit relationships for calculating the friction factor. This list starts with the Moody equation [7] and ends with the one proposed by Azizi *et al.* [15].

It is worth mentioning that some recent studies have conducted reviews of the errors associated with the friction factor in correlations reported in the literature [25]. These studies reveal that the relationship proposed by Praks and Brkić [26] has a maximum percentage error of 0,001204%, the relationship proposed by Serghides [13] yields an error of 0,00256%, the relationship proposed by Vantakhak [14] has an error of 0,005952%, and the relationship proposed by Romeo *et al.* [20] presents an error of 0,007468%. Lamri and Easa [27] apply the Lagrange inversion theorem and obtain an error of 0,002% for four terms.

Based on the results obtained by the mentioned authors, it can be inferred that the error produced by each empirical equation is due to the structure of the equation with the algebraic terms it comprises and the coefficients and exponents used.

The numerical precision in the number of decimal digits of the friction factor is related to the percentage relative error. Therefore, it is essential to calibrate the coefficients and exponents to create a new empirical correlation that has a simple structure as a mathematical model.

This work develops an explicit correlation using the recursive method to calculate the friction factor for turbulent flow in pipes. Additionally, this correlation is evaluated for four explicit relationships that calculate the friction factor for the initial approximation. The methodology is described in Section 2, the results obtained for the friction factor and percentage errors are presented in Section 3, and finally, the conclusions of the analysis are discussed in Section 4.

## 2. Materials and methods

### 2.1. Graphical representation of the correlation curve fit

Figure 1 displays a generic scheme with three curve trajectories. It illustrates the curve of an implicit analytic function  $y = f(x, y)$ . Additionally, it shows the curve of an explicit empirical function  $y = h(x)$ , which is offset from the curve of the analytic function. The segmented curve corresponds to the correlation, which is the recursive function  $y_{n+1} = f(x, y_n)$ . This function approaches the curve of the analytic function.

At a local reference point  $(x_o, y_o)$  for the empirical function  $y_o = h(x_o)$ , the data  $x_o$  is within the range from  $x_a$  to  $x_b$  (x-axis), and the output data  $y_o$  is within the range from  $y_a$  to  $y_b$  (y-axis). For the analytic function, when  $x_o$ , the output data is  $y_m$ , establishing the reference point  $(x_o, y_m)$ . Similarly, for recursion, when

$x_o$ , is the input data, the result is  $y_{n+1}$ , defining the reference position  $(x_o, y_{n+1})$ . For a fixed point  $x_o$ , as the algebraic terms of the recursion  $y_{n+1}$  increase, starting from  $y_o$ , the dependent variable  $y_{n+1}$  approaches the fixed value  $y_m$ . This implies that the numerical error gradually decreases until achieving numerical convergence  $y_m = y_{n+1}$ . Therefore, for different input values  $x_o$ , the recursion curve would overlap the analytic curve in the range  $x_a \leq x_o \leq x_b$ , and the output data would fall within the range  $y_a \leq y_{n+1} \leq y_b$ .

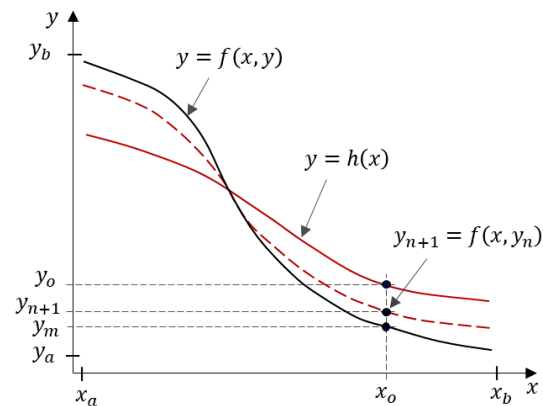


**Figure 1.** Basic schematic representation of the curves for the analytic, empirical, and recursive functions.

In Figure 1 the steps of the recursive method shown in equation (4).

$$\begin{aligned} y_1 &= f(x_o, y_o) \\ y_2 &= f(x_o, y_1) \\ y_3 &= f(x_o, y_2) \\ &\vdots \\ y_{n+1} &= f(x_o, y_n) \end{aligned} \quad (4)$$

Where the first approximation is  $y_1$ , the second is  $y_2$ , the third is  $y_3$ , and the last one  $y_{n+1}$ . The succession for  $y_{n+1}$ , increases progressively, starting from  $n = 0$ .

The function  $y_o = h(x_o)$  is an explicit mathematical expression that provides a representation of a closed initial calculation, where  $y_o$  is the first approximate solution.

### 2.2. Explicit relationship

To calculate the initial first approximation of the friction factor  $\lambda_o$ , it is necessary to establish a mathematical expression as an explicit relationship for this approximate solution.

To obtain the explicit relationship  $\lambda_o$ , equation (1) of Colebrook-White [5, 6] was considered.  $\sqrt{\lambda}$  was removed from the argument of the Colebrook-White equation, and the positions of the coefficients  $a_i$  and exponents  $n_i$  were adjusted. As a result, the explicit relationship  $\lambda_o$  for the initial friction factor calculation was structured as equation (5).

$$\frac{1}{\sqrt{\lambda_o}} = a_1 \log \left[ \left( \frac{\varepsilon}{a_2} \right)^{n_1} + \left( \frac{a_3}{R_e} \right)^{n_2} \right] \quad (5)$$

The input data consists of the independent parameters: the relative roughness  $\varepsilon$  and the Reynolds number  $R_e$ . These parameters are set in the range of  $1 \times 10^{-06} \leq \varepsilon \leq 0,05$  and  $4000 \leq R_e \leq 1 \times 10^{+08}$ . The output data is  $\lambda_o$ .

The coefficients  $a_1, a_2, a_3$  and the exponents  $n_1$  and  $n_2$  of equation (5) were iteratively calibrated in an Excel 2019 spreadsheet using equation (1) of Colebrook-White as a reference. The best results regarding the magnitudes of the coefficients and exponents were selected to establish two explicit relationships.

Table 1 displays the magnitudes of the coefficients and exponents for the two proposed explicit relationships, presented as equations (6) and (7).

**Table 1.** Calibrated values of coefficients and exponents

	Coefficient			Exponent	
	$a_1$	$a_2$	$a_3$	$n_1$	$n_2$
Eq. (6):	1,795	3,9	6,94	1,104	-
Eq. (7):	2	3,7	6,94	-	0,9

$$\frac{1}{\sqrt{\lambda_o}} = -a_1 \log \left[ \left( \frac{\varepsilon}{a_2} \right)^{n_1} + \frac{a_3}{R_e} \right] \quad (6)$$

$$\frac{1}{\sqrt{\lambda_o}} = -a_1 \log \left[ \frac{\varepsilon}{a_2} + \left( \frac{a_3}{R_e} \right)^{n_2} \right] \quad (7)$$

### 2.3. Correlation adjustment

Based on the recursive method, equation (1) of Colebrook-White [5,6] was adjusted to calculate the friction factor using  $\lambda_{n+1}$ , as the output data and  $\lambda_n$  as the input data. The modified equation (8) is expressed as follows.

$$\frac{1}{\sqrt{\lambda_{n+1}}} = a \log \left[ b + c \frac{1}{\sqrt{\lambda_n}} \right] \quad (8)$$

Where  $a = -2$ ,  $b = \varepsilon/3,7$  y  $c = 2,51/R_e$ .

Equation (8) is based on the base 10 logarithm. This equation is used to perform the calculations in this work. It can also be expressed in terms of the natural logarithm as follows:  $1/\sqrt{\lambda_{n+1}} = a_1 \ln [b + c/\sqrt{\lambda_n}]$ , where  $a_1 = a/\ln(10)$ .

Using equation (8), the correlation expressed as equation (9) was established to calculate the increment of the succession  $\lambda_{n+1} = \lambda_2, \lambda_4, \lambda_6, \lambda_8$ .

$$\begin{aligned} \frac{1}{\sqrt{\lambda_8}} &= a \log [b + ac \log [b + cD]] \\ D &= a \log [b + ac \log [b + cC]] \\ C &= a \log [b + ac \log [b + cB]] \\ B &= a \log [b + ac \log [b + cA]] \end{aligned} \quad (9)$$

Where  $D = \frac{1}{\sqrt{\lambda_6}}$ ,  $C = \frac{1}{\sqrt{\lambda_4}}$ ,  $B = \frac{1}{\sqrt{\lambda_2}}$  and  $A = \frac{1}{\sqrt{\lambda_o}}$ .

Equation (9) was extended by adding terms to evaluate up to  $\lambda_{n+1} = \lambda_{20}$ , although the mathematical expression for  $\lambda_{20}$  is not presented because the procedure is similar. The same principle as in equation (8) is applied.

The purpose of evaluating the correlation in a segmented manner was to determine the decrease in the percentage error of the friction factor for different values of the Reynolds number and relative roughness.

As input value of  $\lambda_o$  for  $A = 1/\sqrt{\lambda_o}$  en in equation (9), four explicit relationships were considered: the Swamee-Jain relationship [8] (equation (2)), the Haaland relationship [9] (equation (3)), and the equations (6) and (7) proposed in this work. Each relationship was evaluated separately in equation (9).

The percentage error of the friction factor  $\lambda(\%)$  was calculated using the following the equation (10).

$$\lambda(\%) = 100 \left| \frac{\lambda_m - \lambda_{n+1}}{\lambda_m} \right| \quad (10)$$

Where  $\lambda_m$  represents the friction factor of the exact solution of the Colebrook-White equation, and  $\lambda_{n+1}$  represents the friction factor obtained from equation (9).

It is worth mentioning that all numerical calculations and graphs were performed in an Excel 2019 spreadsheet.

## 3. Results and discussion

### 3.1. Correlation and explicit relationships for friction factor calculation

The correlation created using the recursive method is expressed by equation (9), where the parameter values are  $a = -2$ ,  $b = \varepsilon/3,7$ , and  $c = 2,51/R_e$ . This correlation is a mathematical expression that models the trajectory of the friction factor curve,  $\lambda$ , in relation to the relative roughness,  $\varepsilon$ , and the Reynolds number,  $R_e$ . Considering the term  $A = 1/\sqrt{\lambda_o}$ , in which the explicit relationships of  $1/\sqrt{\lambda_o}$  are substituted, acting as the correlation's finalizing factor.

The two explicit relationships proposed in this work to close equation (9) are equations (6) and (7), and they are expressed as follows.

It is worth mentioning that equation (9) has a simple structure for direct calculations, which improves the precision in reducing the error of the friction factor with each additional term in the recursion. Therefore, the exact decimal digits of the friction factor increase.

Below, we present the percentage errors of the friction factor yielded by equation (9) for the explicit relationships that serve as a closure for  $A = 1/\sqrt{\lambda_o}$ ,

equation (2) by Swamee-Jain, equation (3) by Haaland, and the proposed equations (6) and (7).

### 3.2. Percentage errors of the friction factor

Figure 2 shows the plots of the curve trajectories of the percentage errors of the friction factor  $\lambda_o$ , calculated by the initial first approximation for equations (2), (3), (6) and (7). These curve trajectories are essential to understand the effect of the coefficients and exponents on variable values of the relative roughness,  $\varepsilon$ , and the Reynolds number,  $R_e$ .

For the Reynolds number range of  $4000 \leq R_e \leq 1 \times 10^8$  and the relative roughness range of  $1 \times 10^{-06} \leq \varepsilon \leq 0,05$ , equation (6) exhibits an estimated maximum percentage error of 2.1%, while equation (7) has an error of 3.1%. Swamee-Jain's equation (2) shows an estimated maximum error of 3.2%, and Haaland's equation (3) has an error of 2.1%. In certain areas, equations (2), (3), (6), and (7) exhibit errors of around 0.1% (Figure 2). It is worth mentioning that the figures only depict curve trajectories for the relative roughness range of  $0,00001 \leq \varepsilon \leq 0,05$ .

For  $\varepsilon = 0,05$  (Figure 2a), equations (3) and (6) exhibit trajectories with a horizontal trend starting from the local position  $R_e = 1 \times 10^5$ . The curve of equation (7) overlaps with the curve of equation (2) and shows a straight-line trend with a negative slope. For  $\varepsilon = 0,00001$  (Figure 2d), the fluctuations in the friction factor curves are greater compared to the other curves illustrated in Figure 2.

For hydraulically rough pipes ( $\varepsilon = 0,05$ ), the trends differ much more from each other than in hydraulically smooth pipes ( $\varepsilon = 0,00001$ ), especially in the case of equations (2) and (7) for the curve in Figure 2a.

The curves show that the coefficients and exponents of each relationship have a dominant effect that defines their own trajectory behavior.

It is worth mentioning that, in Figure 2 and other figures shown below, there are inflection points in the curves during the descending peaks for specific Reynolds numbers, which are not visible because the error output data ( $y$ -axis) are absolute values according to equation (10). Additionally, it is essential to note that the vertical axis is on a logarithmic scale base 10 to facilitate the analysis of the curve trajectories.

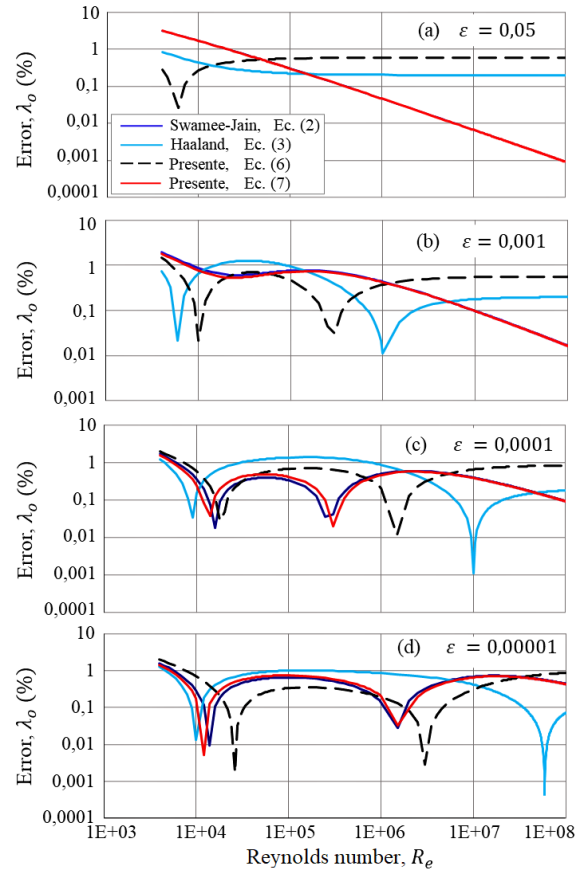


**Figure 2.** Percentage errors of the friction factor for  $\lambda_o$ , as the calculation of the first approximation of Equations (2), (3), (6) and (7)

Figures 3, 4, 5 and 6 show the trajectories of the curves for the percentage errors of the friction factor for  $\lambda_2$ ,  $\lambda_4$ ,  $\lambda_6$  and  $\lambda_8$ . As the terms increase, equations (2), (3), (6) and (7) define their own curve trajectories. The curve trajectories exhibit the highest percentage relative error of the friction factor for each value of  $\varepsilon$ , at the position  $R_e = 4000$ , for  $\lambda_2$ ,  $\lambda_4$ ,  $\lambda_6$  and  $\lambda_8$ .

The regions with the highest errors of the friction factor are found at the local positions  $\varepsilon = 0,00001$  and  $R_e = 4000$ , as illustrated in Figures 3d, 4d, 5d and 6d.

The equations (2), (3), (6) and (7) for  $\lambda_8$  (Figure 6d) have errors less than 0,000002%. For  $\lambda_6$  (Figure 5d), the maximum errors are 0,00006%. For  $\lambda_4$  (Figure 4d), the errors are 0,002%, and for  $\lambda_2$  (Figure 3d), the errors are 0,061%.

The magnitudes of the coefficients and exponents in each explicit relationship exhibit a specific behavior, which influences the evolution of the curve trajectories as the relative roughness increases within the same range of Reynolds numbers, as illustrated in Figures 2 to 6. For future work, it is recommended to perform comparisons with other explicit relationships by substituting them into equation (9) to determine which one yields the lowest percentage errors.

It is worth mentioning that something similar to

what is observed in Figure 2a also occurs in Figure 3a. For  $\lambda_2$  and  $\varepsilon = 0,05$ , equations (2) and (7) show a more significant difference in hydraulically rough pipes, with a trend of straight lines with a negative slope. Similarly, equations (3) and (6) also exhibit straight trajectories and intersect in the region around  $Re = 1 \times 10^{05}$ . This phenomenon is also observed in Figures 4a, 5a, and 6a, where the trajectories show a trend of straight lines for rough pipes ( $\varepsilon = 0,05$ ), respectively.

Table 2 displays the maximum errors of the friction factor for  $\varepsilon = 0,00001$  and the local Reynolds numbers  $4 \times 10^{03}$ ,  $1 \times 10^{04}$ ,  $1 \times 10^{05}$ ,  $1 \times 10^{06}$ ,  $1 \times 10^{07}$  and  $1 \times 10^{08}$ . These values correspond to  $\lambda_0$ ,  $\lambda_2$ ,  $\lambda_4$ ,  $\lambda_6$  and  $\lambda_8$ , which are related to Figures 2, 3, 4, 5 and 6. For equation (6) for  $\lambda_8$ , considering the conditions  $\varepsilon = 0,00001$  and  $Re = 4 \times 10^{03}$ , a maximum percentage error of  $1,7 \times 10^{-06}\%$  is obtained. For equations (2), (3) and (7), the errors are below  $1,7 \times 10^{-06} \%$ .

It is worth mentioning that as the recursion increases, the percentage errors decrease. Consequently, the friction factors for  $\lambda_8$  exhibit seven exact decimal digits for  $\varepsilon = 0,001$ , eight exact decimal digits for  $\varepsilon = 0,00001$  and nine exact decimal digits for  $\varepsilon = 0,05$  and  $\varepsilon = 0,0001$ , compared to the friction factor of Colebrook-White equation (1), as shown in Table 3. For recursion values lower than  $\lambda_8$ , the exact decimal digits decrease. For  $\lambda_6$  there are six exact decimal digits, for  $\lambda_4$  there are five exact decimal digits, and for  $\lambda_2$  there are four exact decimal digits.

In equation (9) for  $\lambda_8$ , the maximum percentage error of the friction factor was obtained, with a value of  $0.0000017\%$ , which is significantly lower than other reported percentage errors. Brkić and Stajić [25], obtained errors around  $0.001204\%$ , Praks and Brkić [26] obtained an error of  $0.002560\%$ , and Serghides [13] obtained an error of  $0.002560\%$ . It is worth mentioning that the percentage errors reported by Brkić and Stajić [25] have not been verified by the authors of this study through numerical calculations. Therefore, they are presented solely for comparative purposes.

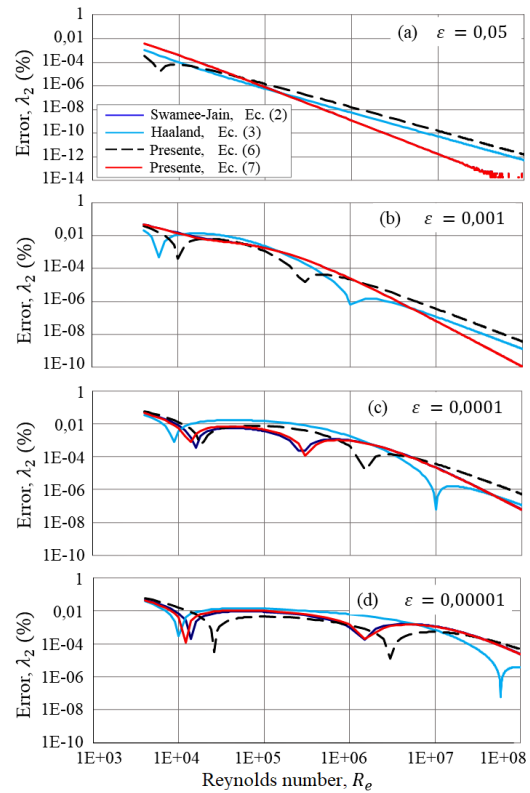


Figure 3. Percentage errors of the friction factor for  $\lambda_2$

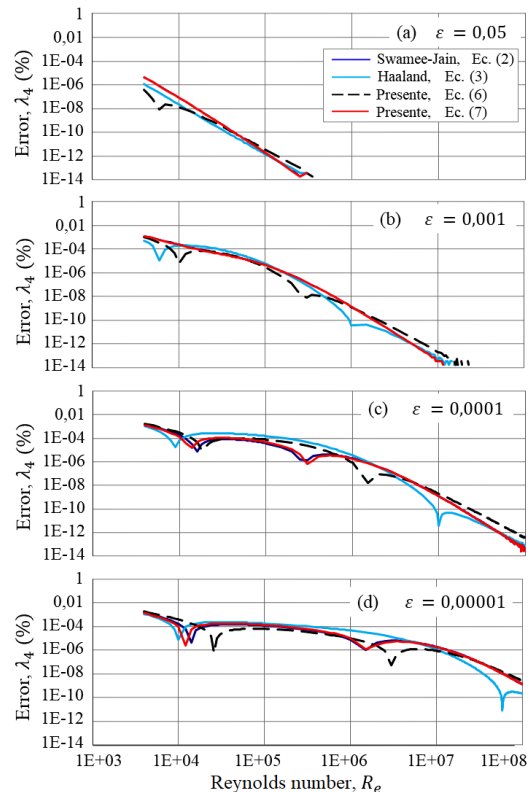


Figure 4. Percentage errors of the friction factor for  $\lambda_4$

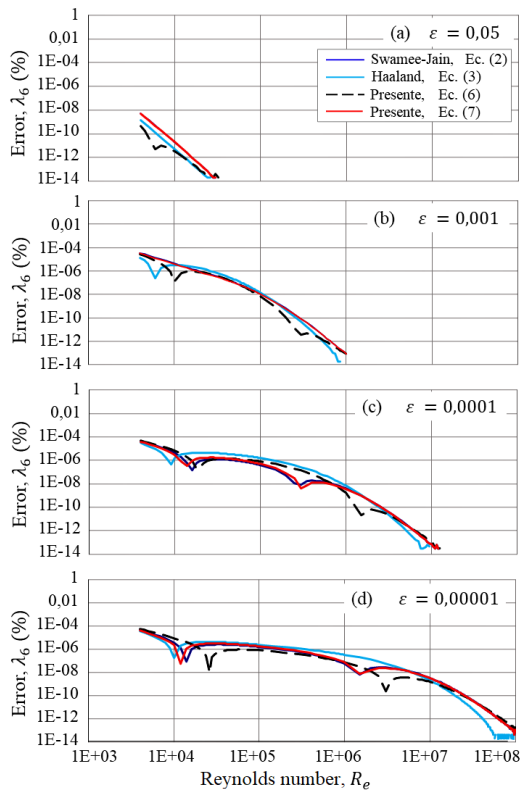


Figure 5. Percentage errors of the friction factor for  $\lambda_6$

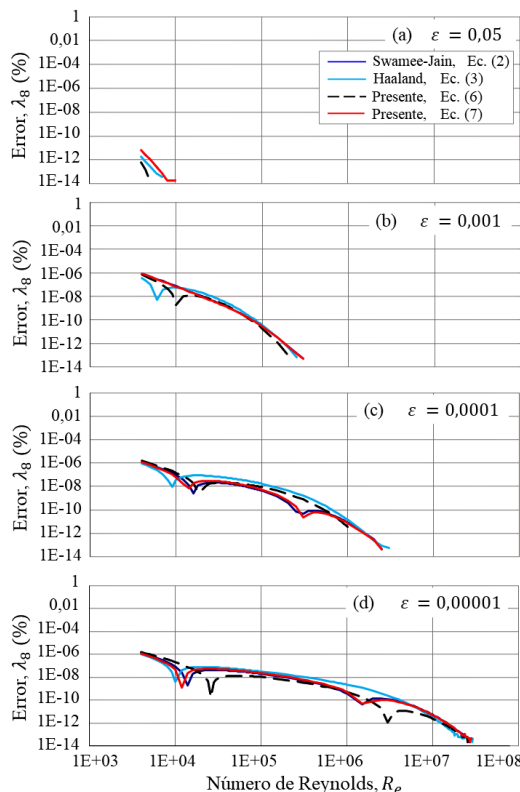


Figure 6. Percentage errors of the friction factor for  $\lambda_8$

Table 2. Percentage errors,  $\lambda$  (%), of the friction factor for the recursions, for  $\varepsilon = 0,00001$  and local  $R_e$

Error	Eq (2)	Eq (3)	Eq (6)	Eq (7)
$\lambda$ (%)	$R_e = 4E + 03$			
$\lambda_0$	1,6182	1,2790	2,0294	1,4803
$\lambda_2$	0,0482	0,0381	0,0610	0,0441
$\lambda_4$	0,0014	0,0011	0,0018	0,0013
$\lambda_6$	4,4E-05	3,5E-05	5,0E-05	4,0E-05
$\lambda_8$	1,4E-06	1,1E-06	1,7E-06	1,2E-06
$\lambda$ (%)	$R_e = 1E + 04$			
$\lambda_0$	0,2958	0,0132	0,7047	0,1769
$\lambda_2$	0,0068	0,0003	0,0163	0,0041
$\lambda_4$	1,6E-04	7,2E-06	3,8E-04	9,6E-05
$\lambda_6$	3,7E-06	1,7E-07	8,8E-06	2,3E-06
$\lambda_8$	8,6E-08	3,9E-09	2,1E-07	5,2E-08
$\lambda$ (%)	$R_e = 1E + 05$			
$\lambda_0$	0,6637	1,0164	0,3413	0,7522
$\lambda_2$	0,0088	0,0135	0,0045	0,0099
$\lambda_4$	1,2E-04	1,8E-04	6,0E-05	1,4E-04
$\lambda_6$	1,6E-06	2,4E-06	7,9E-07	1,8E-06
$\lambda_8$	2,1E-08	3,2E-08	1,1E-08	2,3E-08
$\lambda$ (%)	$R_e = 1E + 06$			
$\lambda_0$	0,1380	0,8650	0,1948	0,2036
$\lambda_2$	0,0010	0,0062	0,0013	0,0014
$\lambda_4$	7,1E-06	4,5E-05	1,0E-05	1,1E-05
$\lambda_6$	5,1E-08	3,2E-07	7,2E-08	7,6E-08
$\lambda_8$	3,7E-10	2,3E-09	5,2E-10	5,4E-10
$\lambda$ (%)	$R_e = 1E + 07$			
$\lambda_0$	0,6984	0,4194	0,3166	0,6651
$\lambda_2$	0,0011	7,0E-04	5,3E-04	0,0011
$\lambda_4$	2,0E-06	1,2E-06	8,8E-07	1,80E-06
$\lambda_6$	3,2E-09	1,9E-09	1,5E-09	3,1E-09
$\lambda_8$	5,3E-12	3,3E-12	2,4E-12	5,1E-12
$\lambda$ (%)	$R_e = 1E + 08$			
$\lambda_0$	0,4423	0,0732	0,8823	0,4351
$\lambda_2$	2,4E-05	3,9E-06	4,7E-05	2,3E-05
$\lambda_4$	1,3E-09	2,1E-10	2,5E-09	1,3E-09
$\lambda_6$	6,4E-14	0	1,3E-13	6,4E-14
$\lambda_8$	0	0	0	0

Figure 7 displays the decrease in the percentage error of the friction factor as recursion increases for  $\lambda_2, \lambda_4, \lambda_6, \lambda_8$ , up to  $\lambda_{20}$ .

For equations (2), (3) (6) and (7), with  $\varepsilon = 0,00001$  and a local position of  $R_e = 4E + 03$ , the following percentage errors are obtained:  $\lambda_9, 2,85E - 07\%$ ,  $\lambda_{10}, 4,95E - 08\%$ ,  $\lambda_{11}, 8,55E - 09\%$ ;  $\lambda_{12}, 1,5E - 09\%$ ,  $\lambda_{14}, 4,5E - 11\%$ ,  $\lambda_{16}, 1,5E - 12\%$ ,  $\lambda_{18}, 5,5E - 14\%$ , and  $\lambda_{20} 0,0\%$ .

For other values of relative roughness and Reynolds numbers, the percentage errors of the friction factor are lower. This indicates that as the Reynolds number increases, fewer terms in the recursion are required to achieve numerical convergence.

**Table 3.** Comparison of numerical values of friction factors for the recursions considering the Colebrook-White equation  $R_e = 4E + 03$  and local  $\varepsilon$

	Eq (2)	Eq (3)	Eq (6)	Eq (7)
$\lambda$	Eq (1): $\lambda = 0,076986834$ ; $\varepsilon = 0,05$			
$\lambda_0$	0,0793827	0,0776348	0,0772007	0,0793531
$\lambda_2$	0,0769896	0,0769876	0,0769870	0,0769895
$\lambda_4$	0,0769868	0,0769868	0,0769868	0,0769868
$\lambda_6$	0,0769868	0,0769868	0,0769868	0,0769868
$\lambda_8$	0,0769868	0,0769868	0,0769868	0,0769868
$\lambda$	Ec. (1): $\lambda = 0,040910389$ ; $\varepsilon = 0,001$			
$\lambda_0$	0,0416954	0,0412161	0,0415108	0,0416423
$\lambda_2$	0,0409306	0,0409183	0,0409259	0,0409293
$\lambda_4$	0,0409109	0,0409105	0,0409107	0,0409108
$\lambda_6$	0,0409104	0,0409103	0,0409104	0,0409104
$\lambda_8$	0,0409103	0,0409103	0,0409103	0,0409103
$\lambda$	Ec. (1): $\lambda = 0,040008431$ ; $\varepsilon = 0,0001$			
$\lambda_0$	0,0406678	0,0404853	0,0407853	0,0406129
$\lambda_2$	0,0400278	0,0400224	0,0400312	0,0400262
$\lambda_4$	0,0400090	0,0400088	0,0400091	0,0400089
$\lambda_6$	0,0400084	0,0400084	0,0400084	0,0400084
$\lambda_8$	0,0400084	0,0400084	0,0400084	0,0400084
$\lambda$	Ec. (1): $\lambda = 0,039917166$ ; $\varepsilon = 0,00001$			
$\lambda_0$	0,0405631	0,0404277	0,0407272	0,0405080
$\lambda_2$	0,0399364	0,0399324	0,0399412	0,0399347
$\lambda_4$	0,0399177	0,0399176	0,0399178	0,0399176
$\lambda_6$	0,0399171	0,0399171	0,0399171	0,0399171
$\lambda_8$	0,0399171	0,0399171	0,0399171	0,0399171

Equation (9) is applicable for hydraulic pipes with values lower than  $\varepsilon = 0,00001$ , and even for  $\varepsilon = 0$ . When  $\varepsilon = 0$ , equation (9) simplifies, and numerically, the error curves of the friction factor resemble the trajectories shown in Figure 7c. The results from the graphs and tables are not presented due to their similarity. For  $\lambda_8$ , and the range  $4000 \leq R_e \leq 1E + 08$ , the percentage error is lower than  $1,5E-06\%$ .

The Swamee-Jain and Haaland equations were evaluated in equation (9), starting from  $\lambda_2$ , and yielded similar results to the evaluations of the proposed equations (6) and (7).

Any equation that has structures different from equations (6) and (7) and that is used in equation (9) can reduce the percentage error of the friction factor.

The advantage of equation (9) lies in its simple structure and ease of use for directly calculating the friction factor as an approximate solution.

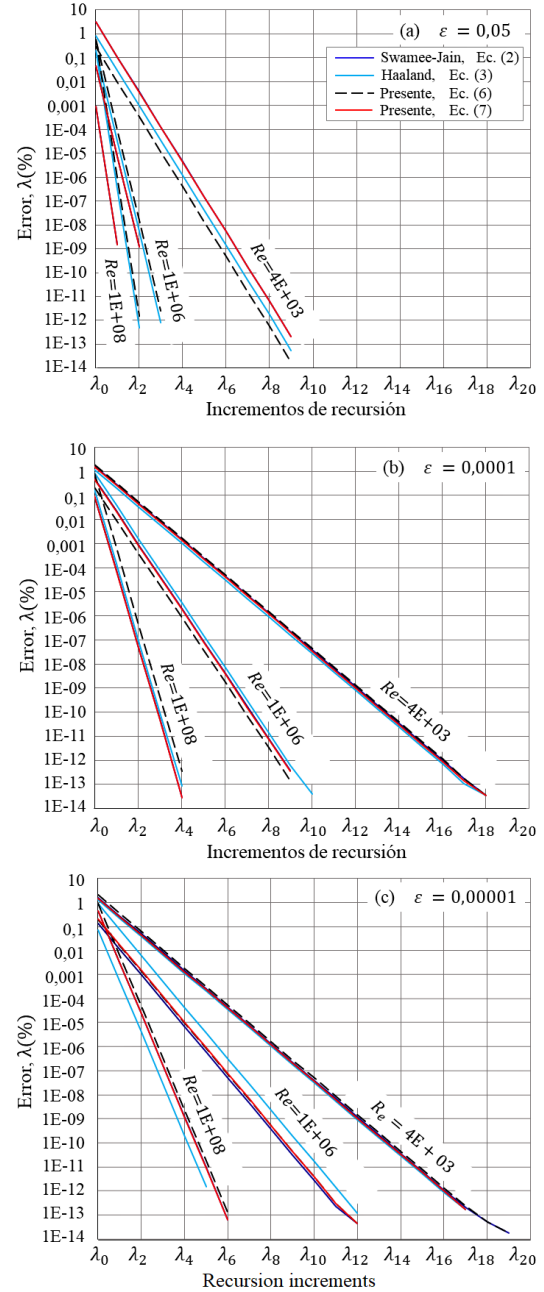


**Figure 7.** Percentage errors of the friction factor for equations (2), (3), (6) and (7)

### 4. Conclusions

The correlation expressed in equation (9) for  $\lambda_8$ , and the explicit relationships represented by equations (6) and (7) for calculating  $\lambda_0$  as an initial approximation provide an approximate solution for the implicit Colebrook-White equation (1). Equation (9) is applicable for turbulent flows within the Reynolds number range of  $4000 \leq R_e \leq 1E + 08$  and the relative roughness range of  $0,05 \geq \varepsilon \geq 0,00001$ . It can also be applied to smooth pipes within the same Reynolds

number range. However, equation (9) is not applicable for  $R_e < 4000$ .

Within the relative roughness range of,  $0,05 \geq \varepsilon \geq 0,00001$ , and Reynolds number range of  $4 \times 10^{03} \leq R_e \leq 1 \times 10^{08}$ , the estimated value of the maximum percentage error of the friction factor is  $1,7 \times 10^{-06} \%$ , for  $\varepsilon = 0,00001$  and  $R_e = 4 \times 10^{03}$ . In this case, the friction factor has seven exact decimal digits. For other values of relative roughness and Reynolds numbers, the numerical magnitudes of the friction factor exhibit more than seven exact decimal digits.

For recursions beyond  $\lambda_8$ , the exact decimal digits increase. For  $\varepsilon = 0,00001$  and  $R_e = 4 \times 10^{03}$ ,  $\lambda_{10}$  exhibits an error of  $4,95 \times 10^{-08} \%$ ,  $\lambda_{14}$  yields an error of  $4,5 \times 10^{-11} \%$ , and  $\lambda_{20}$  exhibits an error of 0,0%.

## References

- [1] F. M. White, *Fluid Mechanics*. McGraw Hill, 2011. [Online]. Available: <https://bit.ly/3ICSyXO>
- [2] Y. A. Cengel and J. M. Cimbala, *Fluid Mechanics: Fundamentals and Applications*. McGraw-Hill Higher Education, 2011. [Online]. Available: <https://bit.ly/43sCUX3>
- [3] S. L. B. Tolentino Masgo, "Estudio experimental y numérico de la presión del flujo de agua en un tubo Venturi," *Ingenius, Revista de Ciencia y Tecnología*, no. 23, pp. 9–22, 2020. [Online]. Available: <https://doi.org/10.17163/ings.n23.2020.01>
- [4] O. Reynolds, "An experimental investigation of the circumstances which determine whether the motion of water shall be direct or sinuous, and of the law of resistance in parallel channels," *Philosophical Transactions of the Royal Society of London*, vol. 174, pp. 935–982, 1883. [Online]. Available: <https://doi.org/10.1098/rstl.1883.0029>
- [5] C. F. Colebrook, C. M. White, and G. I. Taylor, "Experiments with fluid friction in roughened pipes," *Proceedings of the Royal Society of London. Series A - Mathematical and Physical Sciences*, vol. 161, no. 906, pp. 367–381, 1937. [Online]. Available: <https://doi.org/10.1098/rspa.1937.0150>
- [6] C. F. Colebrook, "Turbulent flow in pipes, with particular reference to the transition region between the smooth and rough pipe laws," *Journal of the Institution of Civil Engineers*, vol. 11, no. 4, pp. 133–156, 1939. [Online]. Available: <https://doi.org/10.1680/ijoti.1939.13150>
- [7] L. F. Moody and N. J. Princeton, "Friction factor for pipe flow," *Transaction of ASME*, vol. 66, pp. 671–684, 1944. [Online]. Available: <https://bit.ly/3BRgxyL>
- [8] P. K. Swamee and A. K. Jain, "Explicit equations for pipe-flow problems," *Journal of the Hydraulics Division*, vol. 102, no. 5, pp. 657–664, 1976. [Online]. Available: <https://doi.org/10.1061/JYCEAJ.0004542>
- [9] S. E. Haaland, "Simple and explicit formulas for the friction factor in turbulent pipe flow," *Journal of Fluids Engineering*, vol. 105, no. 1, pp. 89–90, Mar 1983. [Online]. Available: <https://doi.org/10.1115/1.3240948>
- [10] Y. Mikata and W. S. Walczak, "Exact analytical solutions of the Colebrook–White equation," *Journal of Hydraulic Engineering*, vol. 142, no. 2, p. 04015050, 2016. [Online]. Available: [https://doi.org/10.1061/\(ASCE\)HY.1943-7900.0001074](https://doi.org/10.1061/(ASCE)HY.1943-7900.0001074)
- [11] P. Rollmann and K. Spindler, "Explicit representation of the implicit Colebrook–White equation," *Case Studies in Thermal Engineering*, vol. 5, pp. 41–47, 2015. [Online]. Available: <https://doi.org/10.1016/j.csite.2014.12.001>
- [12] D. Biberg, "Fast and accurate approximations for the Colebrook equation," *Journal of Fluids Engineering*, vol. 139, no. 3, Dec 2016, 031401. [Online]. Available: <https://doi.org/10.1115/1.4034950>
- [13] T. K. Seguides, "Estimate friction factor accurately," *Chemical Engineering Journal*, vol. 91, pp. 63–64, 1984. [Online]. Available: <https://bit.ly/3oqUTyd>
- [14] A. R. Vatankhah, "Approximate analytical solutions for the Colebrook equation," *Journal of Hydraulic Engineering*, vol. 144, no. 5, p. 06018007, 2018. [Online]. Available: [https://doi.org/10.1061/\(ASCE\)HY.1943-7900.0001454](https://doi.org/10.1061/(ASCE)HY.1943-7900.0001454)
- [15] N. Azizi, R. Homayoon, and M. R. Hojjati, "Predicting the Colebrook–White friction factor in the pipe flow by new explicit correlations," *Journal of Fluids Engineering*, vol. 141, no. 5, Nov 2018, 051201. [Online]. Available: <https://doi.org/10.1115/1.4041232>
- [16] N. H. Chen, "An explicit equation for friction factor in pipe," *Industrial & Engineering Chemistry Fundamentals*, vol. 18, no. 3, pp. 296–297, 1979. [Online]. Available: <https://doi.org/10.1021/i160071a019>
- [17] B. J. Schorle, S. W. Churchill, and M. Shacham, "Comments on: "An explicit equation for friction factor in pipe"," *Industrial & Engineering Chemistry Fundamentals*, vol. 19, no. 2, pp. 228–228, 1980. [Online]. Available: <https://doi.org/10.1021/i160074a019>

- [18] D. J. Zigrang and N. D. Sylvester, "A review of explicit friction factor equations," *Journal of Energy Resources Technology*, vol. 107, no. 2, pp. 280–283, 1985. [Online]. Available: <https://doi.org/10.1115/1.3231190>
- [19] J. Sousa, M. d. C. Cunha, and A. S. Marques, "An explicit solution of the Colebrook–White equation through simulated annealing," *Water Industry Systems: Modelling and Optimization Applications*, vol. 2, pp. 347–355, 1999.
- [20] E. Romeo, C. Royo, and A. Monzon, "Improved explicit equations for estimation of the friction factor in rough and smooth pipes," *Chemical Engineering Journal*, vol. 86, pp. 369–374, 04 2002. [Online]. Available: [http://dx.doi.org/10.1016/S1385-8947\(01\)00254-6](http://dx.doi.org/10.1016/S1385-8947(01)00254-6)
- [21] U. Offor and S. Alabi, "An accurate and computationally efficient explicit friction factor model," *Advances in Chemical Engineering and Science*, no. 6, pp. 237–245, 2016. [Online]. Available: <http://dx.doi.org/10.4236/aces.2016.63024>
- [22] I. Santos-Ruiz, J. R. Bermúdez, F. R. López-Estrada, V. Puig, and L. Torres, "Estimación experimental de la rugosidad y del factor de fricción en una tubería," in *Memorias del Congreso Nacional de Control Automático, San Luis Potosí, México*, 2018, pp. 489–494. [Online]. Available: <https://bit.ly/3oubv8g>
- [23] A. P. Olivares-Gallardo, R. A. Guerra-Rojas, and M. A. Alfaro-Guerra, "Evaluación experimental de la solución analítica exacta de la ecuación de Colebrook–White," *Ingeniería Investigación y Tecnología*, vol. 2, pp. 1–11, 2019. [Online]. Available: <https://doi.org/10.22201/fi.25940732e.2019.20n2.021>
- [24] J. R. Pérez Pupo, J. N. Guerrero, and M. Batista Zaldívar, "On the explicit expressions for the determination of the friction factor in turbulent regime," *Revista mexicana de ingeniería química*, vol. 19, pp. 313–334, 01 2020. [Online]. Available: <https://bit.ly/3BUtqrD>
- [25] D. Brkić and Z. Stajić, "Excel VBA-based user defined functions for highly precise Colebrook's pipe flow friction approximations: a comparative overview," *FACTA UNIVERSITATIS Series: Mechanical Engineering*, vol. 19, no. 2, pp. 253–269, 2021. [Online]. Available: <https://doi.org/10.22190/FUME210111044B>
- [26] P. Praks and D. Brkić, "Advanced iterative procedures for solving the implicit Colebrook equation for fluid flow friction," *Advances in Civil Engineering*, 2018. [Online]. Available: <https://doi.org/10.1155/2018/5451034>
- [27] A. A. Lamri and S. M. Easa, "Computationally efficient and accurate solution for Colebrook equation based on Lagrange theorem," *Journal of Fluids Engineering*, vol. 144, p. 014504, 2022. [Online]. Available: <https://doi.org/10.1115/1.4051731>



# STUDY FOR LOCALIZATION OF FAULT IN THE ELECTRICAL DISTRIBUTION SYSTEMS.

## ESTUDIO PARA LA LOCALIZACIÓN DE FALLAS EN SISTEMAS DE DISTRIBUCIÓN ELÉCTRICA.

Roberto Gomez<sup>1</sup> , Diego Cabrera<sup>1</sup> , Pablo Robles<sup>2,\*</sup>

Received: 01-02-2023, Received after review: 21-04-2023, Accepted: 22-05-2023, Published: 01-07-2023

### Abstract

This article studies the location of faults in the electrical distribution system based on processing short-circuit signals. For this analysis, the simulation of cases using the CYME software is proposed, using the Wavelet transform to study the signal obtained and decomposed. The minimum spanning tree method is proposed so that fault location is optimal and reconnection time is minimal. This analysis considers the reclosers' location in the distribution system that will serve as information repositories. In this investigation, a fault location algorithm was developed to analyse transient phenomena, achieving good precision in time frequency. Applying the proposed method, the signal is broken down into different levels, obtaining the necessary parameters to determine the distance of the fault.

**Keywords:** Fault detector, Short-circuit impedance, Wavelet transform, Fault location, Fault distance.

### Resumen

En este artículo se estudia la localización de fallas en el sistema de distribución eléctrica, basándose en el procesamiento de las señales de cortocircuito. Para este análisis se propone la simulación de casos mediante el software CYME, empleando la transformada wavelet para el estudio de la señal obtenida y descompuesta. Se propone el método del árbol mínimo en expansión para que la localización de las faltas sea óptima y el tiempo de reconexión sea mínimo. Este análisis toma en cuenta la ubicación de los reconectores en el sistema de distribución que servirán como almacenadores de información. En esta investigación se desarrolló un algoritmo de localización de fallas mediante el análisis de fenómenos transitorios, lográndose buena precisión en tiempo-frecuencia. Aplicando el método propuesto se descompone la señal en diferentes niveles obteniéndose los parámetros necesarios para determinar la distancia de la falla.

**Palabras clave:** Detector de fallas, Impedancia de cortocircuito, Transformada Wavelet, Localización de fallas, Distancia de fallas.

<sup>1,\*</sup>Faculty of Electrical Engineering, Salesian Polytechnic University, Ecuador.

<sup>2</sup>Smart Grid Research Group, Salesian Polytechnic University, Quito, Ecuador.  
Corresponding author ✉: [probles@ups.edu.ec](mailto:probles@ups.edu.ec).

Suggested citation: Gomez, R.; Cabrera, D. and Robles, P. "Study for localization of fault in the electrical distribution systems.," *Ingenius, Revista de Ciencia y Tecnología*, N.º 30, pp. 64-78, 2023, DOI: <https://doi.org/10.17163/ings.n30.2023.06>.

## 1. Introduction

Distribution networks are responsible for supplying electric power to consumers using a set of electrical elements such as conductors, transformer equipment, protection, and structures for their fastening. In distribution networks, there are problems due to the location of faults. The faults can interrupt the electricity supply to the end consumer and make the network unstable, thus reducing the electric system's reliability. All these problems can impose economic losses on consumers, power plants, and distributors [1].

According to the study, [2], more than 80 percent of power system outages are due to failures that occur in distribution systems due to various reasons, such as lightning strikes, power system component failures due to aging equipment, and human error [3]. Therefore, distributors try to use efficient technologies, maintenance actions, and corrective procedures to reduce the failure rate and its destructive effects.

Fault location is one of the most critical issues in the electrical power distribution system, so proper location is essential to help electrical maintenance personnel directly locate the correct location and fix the problem quickly. This minimizes outage time, restores power, and reduces operating costs [4].

Despite technological advances and the need to improve performance, today's troubleshooting process still relies on trouble calls from affected customers. When a permanent fault occurs, managers in the operation center identify the feeder and the possible area of occurrence. Maintenance personnel are then sent to patrol that area to identify and isolate. This procedure is ineffective in certain circumstances because the area is sizeable [5].

Generally, methods based on impedance and fundamental frequency components, traveling waves, and knowledge [6] are used to diagnose and locate faults in distribution systems. The first method requires voltage and current measurement data at fundamental frequency to determine the impedance and estimate the fault location using one or several measurement points. This method has the advantage of being implemented at a low cost. Still, it has the disadvantage of estimating multiple fault locations due to the large number of branches that a distribution network may have [7]. The knowledge method encompasses methods based on analysis and statistics, distribution devices, artificial intelligence, and hybrid methods. The application of the knowledge method requires measurements of voltage and current on the feeder, the operating status of the substation and feeder breaker, and data provided by intelligent electronic devices (IED) and protection devices installed on the feeders [8]. The traveling wave method for fault location in distribution systems, which will be used for this work, is based on the transmission and reflection of traveling waves

between the line terminals and the fault point. This method requires IED and protection devices capable of storing current and voltage information of the network operation to obtain the transient waveform for the location of the fault occurring in the distribution system [9].

## 2. Materials and methods

Several methods have been proposed for fault location but are not readily applicable to distribution systems. This is mainly due to short and heterogeneous lines, lateral branches, load taps, and a lower degree of instrumentation in distribution systems.

Currently, the primary methods used to locate the location of single-phase ground faults in distribution networks are impedance, S-injection, traveling wave, and port diagnostic methods [10].

In addition to all the methods mentioned above, employing a FI is the most practical and affordable way for distribution systems, thus providing the best probable fault location [11]. FI in a system does not require sophisticated infrastructures, making it a suitable method in most distribution systems. The assignment of an FI to the networks could restrict the fault area identified by the supervisory control center, so the time required to locate it would decrease substantially. This leads to improved restoration time and service reliability indices. However, using FI in all candidate locations is unnecessary and costly, so cost-effective analysis is needed to determine how many and where FI should be located to get the most out of them [12].

HIF detection may be a protection function in intelligent electronic devices in power distribution networks [13]. HIF can be defined as a fault that draws low currents for conventional protective devices such as overcurrent relays or fuses to trip. Due to the low magnitude of the fault current, HIF does not damage system components but is a public safety hazard because it often involves an electrical arc that increases the fire risk of fire [4].

Several methods have emerged to detect faults in a distribution system over the years. In [14], an algorithm is presented to detect high-impedance faults by feature extraction based on the WT and a Neural Network. The extraction of the most relevant signal features is obtained from WT classification such as Haar, Symlet, Daubechies, Coiflet, and Biorthogonal; for each wavelet mentioned, a decomposition of different levels is performed, which allows the analysis to detect a fault.

Different types of short-circuit faults are generated in distribution networks, so in [15] suggests using the software package CYME that allows the construction of a distribution network and the simulation of several short-circuit faults. Matlab - Simulink uses the wavelet

transform that allows decomposing and reconstruction of original signals by decomposing the signal into different levels to improve the speed of fault detection.

Figure 1 represents the structure for this investigation; it sees the scenario when designing the distribution network system, as well as the dynamic analysis when existing a fault in one or more nodes; here is necessary to obtain the short-circuit profile; it is interesting to look at the Wavelet transform process, that allows analyzing what happens in the system and localized the distances and the original node when the system has a fault of various, therefore the result data allow build the metric with the critical information about ubication and system behavior.

Transient state analysis requires techniques that exploit the relationship between system parameters, transient frequency, and wave speed. For this reason, it [20] it is suggested to use the Wavelet transform since high frequencies have a better resolution in time.

A high-frequency component can be located with less relative error than a low-frequency component. Conversely, low frequencies have better resolution in the frequency domain than high-frequency components [21]. There are various methods for the location and calculation of the fault distance in electrical power systems, including the traveling wave method, which is applied in most cases for the location of faults in transmission systems.

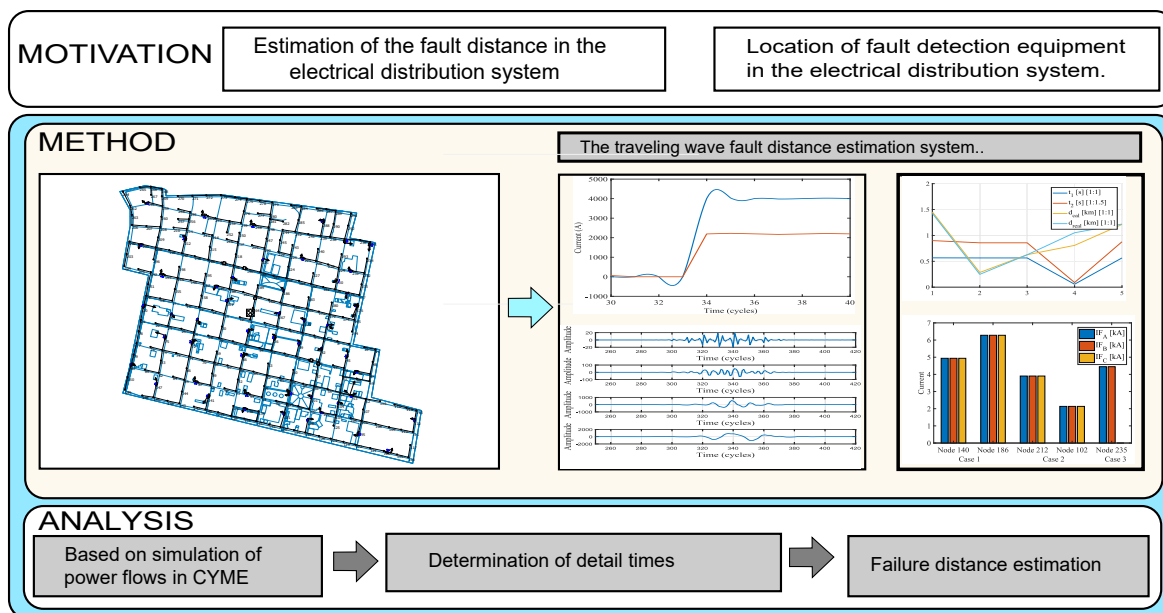


Figure 1. Figure Conceptual & Authors.

The flow diagram, see Figure 2, for obtaining fail signals is necessary to generate a profile obtained of CYME on dynamic analysis; here depends on the original data; if this information is not correct is mandatory interpol; therefore, the analysis Wavelet transform allows through a Daubechies and filter of fault to determine the time and the propagation velocity that is a possible estimation of fault distance from the nearest recloser.

In distribution systems, the traveling wave method is implemented, which has low accuracy when the configuration of the lines changes in impedance, so [19] proposes an accurate method of fault location in the distribution network based on the traveling wave with multiple measurement points. To obtain multiple metering points in [17], [22] distribution networks use digital relays at substations, IED along the primary feeders, SCADA sensors on the feeder circuit, and

smart meters at customers, all of which have the property of storing information about the operation of the distribution network, thus obtaining multiple metering points.

Table 1 exposes the nomenclature as well as the description of abbreviations that are being used in this investigation; for everything, research is mandatory in creating the state art; this is an excellent tool for the investigator can obtain information about the topic and develop the fundamental structure that through which is the possible analysis and evaluate the mathematics model exposes, see table 2.

There are various methods for the location and calculation of the fault distance in electrical power systems, including the traveling wave method, which is applied in most cases for the location of faults in transmission systems. In distribution systems, the traveling wave method is implemented, which has low accuracy

when the configuration of the lines changes impedance, so in [19] proposes an accurate method of fault location in the distribution network based on the traveling wave with multiple measurement points.

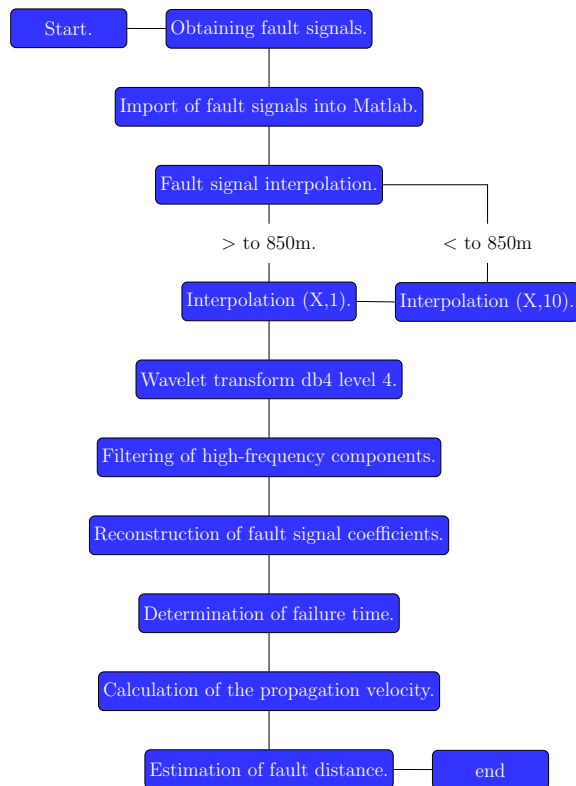


Figure 2. Flow Diagram & Authors.

There are various methods for the location and calculation of the fault distance in electrical power systems, including the traveling wave method, which is applied in most cases for the location of faults in transmission systems. In distribution systems, the traveling wave method is implemented, which has low accuracy when the configuration of the lines changes impedance, so in [19] proposes an accurate method of fault location in the distribution network based on the traveling wave with multiple measurement points.

In addition, an algorithm for fault distance estimation in distribution networks using the transient traveling wave and the Wavelet transform propose in [18], using the current traveling wave signals from the substation bus with the first arrival times of the

aerial difference component and zero sequences to calculate the estimated fault distance and the same can be analyzed with the mother wavelet db6 and level 1. However, this is possible only when there are symmetrical faults [23].

Nowadays, GIS geoprocessing computational tools are used to design an electrical distribution network, obtaining a geo-referenced database in which the minimum-spanning algorithm (MST), one of the practical mathematical theories used in electrical network simulation problems, is applied, which can optimize the electrical network [24], [25]. A geo-referenced database also allows applying algorithms such as K-Means and Elbow for a more accurate location of protective devices [26], [27].

In this scenery have been designed an electrical network system and the energy elements how, reclosers, substations, load, and others, ensuring the correct operation of the system is mandatory to execute the power flow and guarantee the voltage profile for the customer in figure 3, observed a short representation in the electrical distribution network, here observing the drop voltage and reclosers load, substation load, among others, this design system is a tool for fault analysis and a priority search the node location, everything is geolocated which allows having a strategy as realistic as possible.

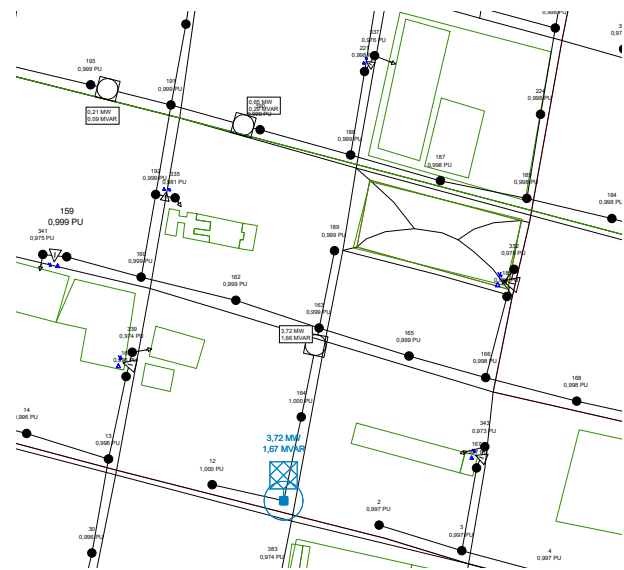


**Table 1.** Nomenclature & Description of Abbreviations & Authors

Nomenclature Description		Nomenclature	Description
$f(t)$	Analysis signal	$d_{real}$	Actual distance measured from the substation to the fault node.
$C$	Capacitance	$Wf(\mu, s)$	Continuous-time wavelet transform.
$IF$	Fault current	$d_f$	Fault distance measured from the distribution substation to the fault node.
$HIF$	High impedance faults	$FI$	Fault indicator.
$GIS$	Geographic information system	$L$	Inductance
$IEDs$	Intelligent electronic devices	$MST$	Minimum spanning tree.
$VLN$	Phase voltage.		
$\Delta_F$	Sampling frequency	$Z1$	Positive frequency impedance.
$s$	Scale	$I$	Rated current.
$STPC$	Simultaneous three-phase short-circuit	$S/E$	Substation.
$SWT$	The stationary wavelet transform	$TPSCNS$	Three-phase short-circuit near the substation.
$\mu$	Translation of the wavelet function in the analysis signal domain	$WT$	Wavelet transform.
$TPSCFS$	Three-phase short-circuit far from substation	$\psi^*\left(\frac{t-\mu}{s}\right)$	Wavelet transform function or wavelet function.
$\Delta_V$	Voltage drop	$t$	Time.
$v$	Wave propagation velocity	$t_d$	Wavelet detail time of the signal.
$Z0$	Zero frequency impedance	$TPSC$	Two-phase short circuit

**Table 2.** Summary of articles related to flaw detection equipment

Author, year	Objectives	Parameters considered				Thematic			
		Voltage	Current	Impedance	Fault Distance	Distribution Network	Short Circuit	Wavelet	Fault Location
[2], 2020	Increased accuracy in fault detection	✘	✘	✘	-	-	-	-	✘
[4], 2019	Fault finding in different locations	✘	✘	✘	✘	-	-	-	✘
[7], 2022	Troubleshooting for four-wire systems	✘	✘	-	✘	✘	-	-	✘
[9], 2020	Short-circuit fault detection	✘	✘	✘	✘	-	-	-	✘
[10], 2020	Line - ground fault location	✘	✘	✘	✘	-	-	-	✘
[12], 2020	Single-phase fault location	✘	✘	✘	✘	-	-	-	✘
[16], 2019	Minimize distance error	✘	✘	✘	✘	✘	✘	-	✘
[17], 2020	Combining devices in the network	✘	✘	-	✘	✘	-	-	-
[18], 2019	Parameterize short circuit	✘	✘	✘	✘	-	-	✘	✘
[19], 2020	Fault location method	✘	✘	✘	✘	-	-	-	✘
<b>Present work</b>	Fault location	-	✘	✘	✘	✘	✘	✘	✘

## 2.1. Problem Formulation and Methodology

Case studies are presented on faults in the electrical distribution system, which are identified by the Wavelet transform method; the acquisition of a database describing the operation of the system in a dynamic state is performed in the CYME software, allows simulating transient stability with their respective characteristics acquired by the identification method successively, so the data must contain as a fundamental variable the information of the current fault behavior, which must be interpolated if the distance is less than 850 meters, which is the threshold to have a better sampling of the signal. The traveling wave method calculates the fault distance, considering a system without a change of positive homopolar impedance. Distribution networks are subject to faults due to different types of origin or nature, which affect the electrical network components, generating disturbances in their correct operation and transients in the current and voltage signals. Therefore,

it is necessary to identify when a fault occurs using the WT.

The WT is an effective tool for fault identification due to its functionality for processing and analyzing transient signals. WT can be used to obtain simultaneous information about the time and frequency of a signal [14].

The electrical distribution system contains transformers of three phases on medium voltage; its power varies between 30 kVA and 200 kVA, the conductors configuration is 1/0 from phase and 2 for the neutral type ACSR for an overhead line, the reclosers location depends on the system characteristics, but for this investigation was used the failure indicators, other parameter import is the conductors capacity this ensures its changeability; everything scenery is geolocated with the optimal conditions for executed a power flow, see figure 4, the results are exposed in table 3, where the reader can observe the most relevant parameters.

**Table 3.** System characteristics in normal state

S/E Capacity	5 MVA
Total Load	
Real Power	3.686 MW
Reactive Power	2.325 MVAR
Apparent Power	4.358 MVA
Load Used	
Real Power	3.614 MW
Reactive Power	1,534 MVAR
Apparent Power	3,926 MVA
Total losses	0,823 MVA
Max. $\Delta V$	2,85 %
Length	15899 m

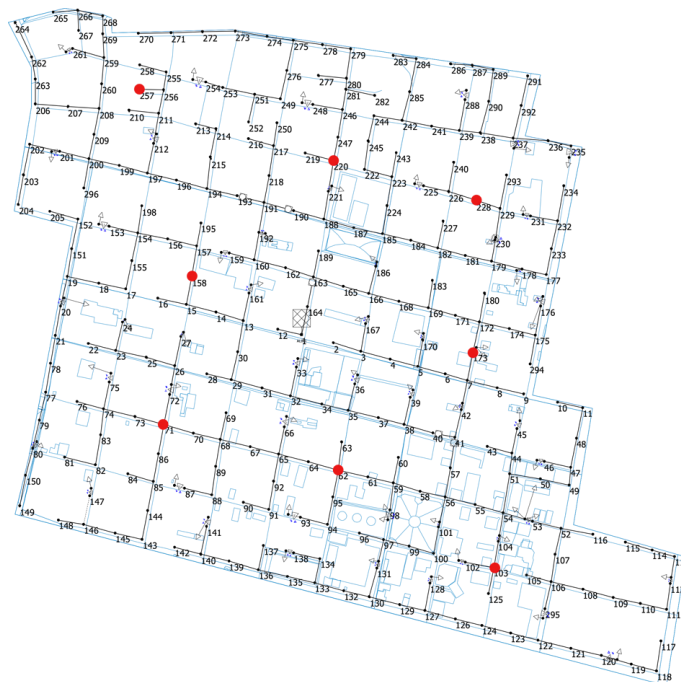


**Figure 4.** Scenario & Authors.

Signal analysis using WT is based on the dilation and translation of a mother wavelet on the signal. The scaling operation dilates and compresses the mother wavelet, resulting in low and high-frequency signals, respectively [14].

$$W_{f(\mu,s)} = \int_{-\infty}^{\infty} f(t) * \psi_{\mu,s}(t) dt \quad (1)$$

Can define  $\psi_{\mu,s}$  as the original Wavelet signal:

$$\psi_{\mu,s}(t) = \frac{1}{\sqrt{s}} \psi\left(\frac{t-\mu}{s}\right) \quad (2)$$

Where:

- $s$  - Scale
- $\mu$  - Translation of the wavelet function in the analysis signal domain.
- $t$  - Time.

Different mother wavelets are associated with the family: Daubechies, Coiflets, and Symmlet; for the case studies presented here, we used the Daubechies wavelet level 4 [db4] for the case studies presented.

It is proposed to locate the fault using the traveling wave method, which calculates the wave propagation. It depends on the inductive and capacitive parameters in equation 3 obtained from the positive sequence zero sequence impedance.

$$v = \frac{1}{\sqrt{L * C}} \quad (3)$$

$L$  represents the inductance of the distribution line per unit length. In contrast,  $C$  represents the capacitance of the distribution line per unit length. For either case, the parameters can be expressed in kilometers or meters; thus, the calculated velocity will be described in  $km/s$  or  $m/s$ . The distribution line configurations affect how the traveling waves travel through the network; see table 4.

**Table 4.** Line Parameters & Authors

Line	L (H/km)	C (F/km)	v (km/s)
Line 139-140	0,0011796	1,0242E-08	287705,1614
Line 166-186	0,0011796	1,0242E-08	287705,1614
Line 102-103	0,0011796	1,0242E-08	287705,1614
Line 197-212	0,0011796	1,0242E-08	287705,1614
Line 235-236	0,0011796	1,0242E-08	287705,1614

To calculate the fault distance, in addition to the velocity, it is necessary to determine the time of the

signal utilizing the wavelength and the sampling frequency, which is equal to  $3.3kHz$ .

$$d_f = \frac{t_d * \Delta F}{2} * v \quad (4)$$

$$error(\%) = \frac{|d_f - d_{real}|}{d_{real}} * 100 \quad (5)$$

In the location of fault-detecting equipment called FI, the jambu elbow method is implemented to estimate the number of clusters needed. The k-means algorithm allows for a better cluster of the fault indicators within the distribution network presented in the case study (Table 5).

To test the effectiveness of the proposed algorithm, a 22 kV distribution network georeferenced with QGIS, see table 1, is designed. These coordinates are imported to Matlab. The graph is conformed, in which the MST is applied, starting from a root vertex and finding all its linked nodes and the relations that allow connecting them, being the weight considered the smallest distance [28]. A minimum weight spanning tree is an edge-weighted digraph connected to all vertices without the presence of loops [29], [30].

The proposed feeder has 295 nodes, 48 three-phase transformers with two windings whose power in kVA are 30, 50, 75, 112.5, 150, and 200, a single-phase transformer of 75 kVA, 54 concentrated loads, and five reclosers. three-phase resulting in a feeder of 5 MVA installed load; see figure 4, table 3 shows its general data and in table 6 the cases to be studied.

**Table 5.** Algorithm information

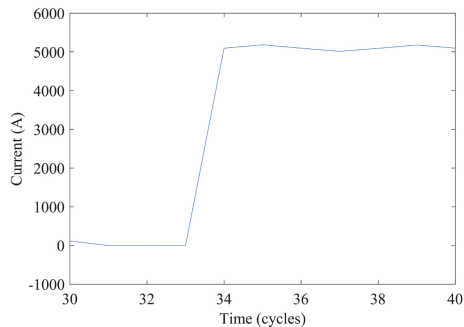
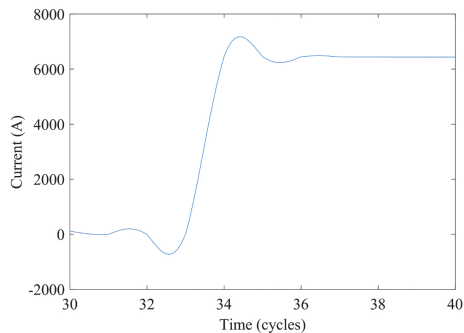
I: Current
T: Time
C, L, Fo: Auxiliary variable
$t_d$ : Wavelet detail time of the signal
v: Velocity
$d_f$ : Fault distance
Steps of the algorithm:
<b>Step 0:</b> Short-circuit current data entry
<b>Step 1:</b> Initialization of variables
<b>Step 2:</b> Data for the calculation of the failure node
$C_s$ = Capacitance [F/km]
$L_s$ = Inductance [H/km]
<b>Step 3:</b> Decomposition and reconstruction of the signal with the Wavelet transform
[C,L] = wavedec(I,4,db4)
Save max(C)
Fo = wrcoef('d',C,L,'db4')
<b>Step 4:</b> Find the two maximum peaks after the failure
Print $t_d$
<b>Step 5:</b> Calculate v
<b>Step 6:</b> Estimate distance and location of the fault node
<b>Step 7:</b> Estimation of the error percentage
<b>Step 8:</b> Graph the results
<b>Step 9:</b> End

**Table 6.** Study cases & Authors

Case	Fault Type	Fault Node
Three-phase short-circuit far and near substation	Three-phase	140 - 186
Simultaneous three-phase short-circuit	Three-phase	212 - 102
Two-phase short circuit	Two-phase	235

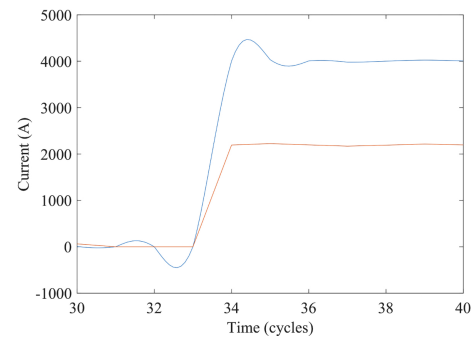
According to the exposed case study, the starting point is a three-phase short-circuit fault in node 140, 1427 meters from the medium voltage substation. The short-circuit data is generated from the storage of events by the protection and switching device, which is the 41-57 re-closer with a sampling frequency of 3.3 kHz; from the data originates the operation waveform of the distribution system under fault, see figure 5.

Starting from the same case, a three-phase short-circuit fault occurs near the substation at a distance of 274.6 meters. The fault signal is obtained from the storage of events by the protection and switching device, recloser 163-164. As the fault is lower than the threshold, we proceed to interpolate for better sampling; see figure 6.

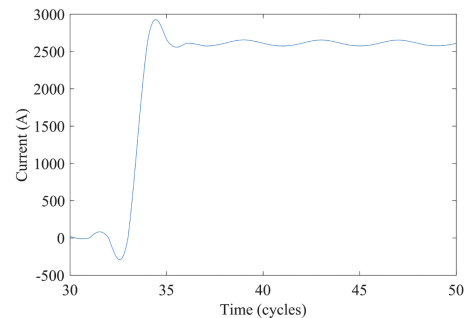
**Figure 5.** Three-phase short-circuit far from the substation & Authors.**Figure 6.** Three-phase short-circuit near the substation & CYME.

A second case is that of a simultaneous three-phase short circuit. Therefore, we have two distances, the first at 625.8 meters, lower than the threshold we must

interpolate, and the second at 1051.7 meters, taken from the substation. The signals are obtained from reclosers 41-57 and 191-193; see figure 7.

**Figure 7.** Simultaneous three-phase short-circuit in two nodes of electrical distribution system & CYME.

A two-phase fault occurs within the 190-191 recloser zone 1219 meters from the substation. In this case, the fault currents are symmetrical because there is no impedance change in the distribution lines; see figure 8.

**Figure 8.** Two-phase short circuit & CYME.

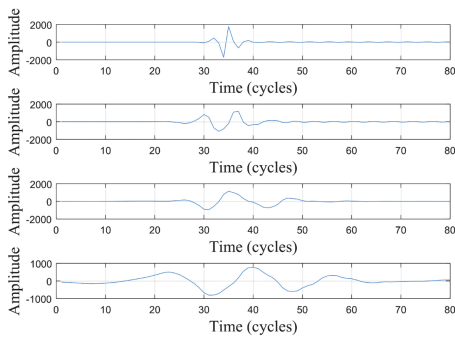
### 3. Results and discussion

A WT of family Db4 and order 4 is used from the fault signals obtained from each case. The signal is reconstructed using the maximum level based on the wavelet decomposition structure.

The detail signals for all cases are similar with the variation in their amplitude due to the number of calculated coefficients. One of the essential variables to

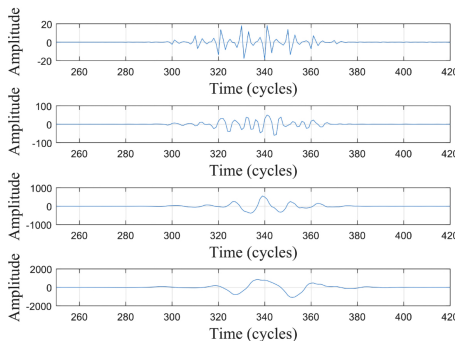
apply the traveling wave method and subsequent location of the fault is the exact time ( $t_d$ ), which results from the difference between the two consecutive peaks called rms value at the instant of the fault, which is calculated for each case.

For the application of the fault location and identification algorithm, it is necessary to determine the time TD for each case, which will be similar for each type of fault and can be obtained from the signal presented in Figure 9, which corresponds to the analysis of the identification of the distant fault of the substation located at node 140.



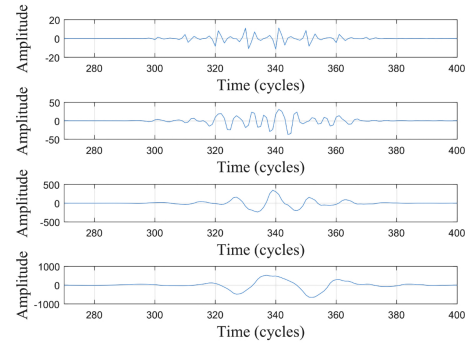
**Figure 9.** Wavelet detail signal to calculate the fault detail time away from the substation, amplitude on amperes vs WT of the order 4.

Now, as the fault occurs at node 186, located near the substation, the information from the database obtained by the recloser is interpolated due to the small amount of data. This allows a better signal for fault identification and determination of time  $t_d$ , figure 10.

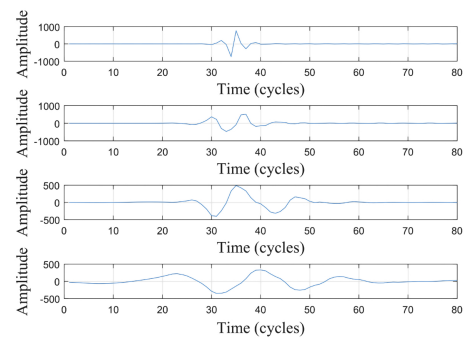


**Figure 10.** Wavelet detail signal to calculate fault detail time near the substation, amplitude on amperes vs WT of the order 4.

When two simultaneous faults occur, one located at node 212 and the second at node 102, which belong to recloser zone 41-57 and 191-193, respectively, two different databases were obtained in which an independent analysis of each signal was performed to identify the fault occurred and determine the  $t_d$  times of each fault signal, which are presented in Figure 11 and 12.

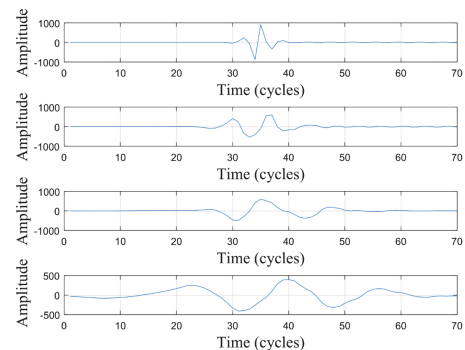


**Figure 11.** Wavelet detail signal for fault detail time calculation 1, amplitude on amperes vs. WT of the order 4.



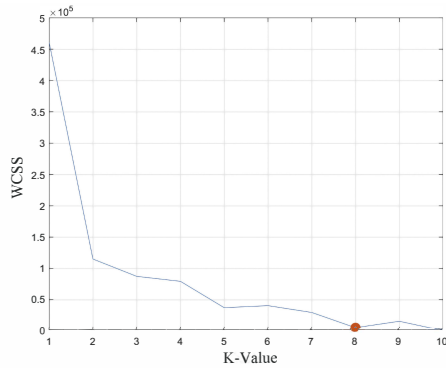
**Figure 12.** Wavelet detail signal for fault detail time calculation 2, amplitude on amperes vs. WT of the order 4.

Figure 13 shows the wavelet detail signal to obtain the time  $t_d$  for calculating the distance of the two-phase fault case occurring in the recloser 190-191 zone.



**Figure 13.** Wavelet detail signal for calculating the detailed time for the two-phase short circuit, amplitude on amperes vs. WT of the order 4.

Once the fault occurrence and the estimated distance from its origin are identified, the jambu elbow method is implemented to determine the required number of IF installed in the distribution network. The result of the elbow method is presented in Figure 14.



**Figure 14.** Elbow method for locating fault detection equipment.

The k-means method obtains the optimum location where each fault indicator should be installed, Figure 5 the optimum location of the 8 fault indicators, represented by red dots.

To verify that the developed algorithm estimates the fault distance correctly, Table 7 shows the results

**Table 7.** Results obtained after the occurrence of the failure.

Cases	Type of fault	$t_1$ (s)	$t_2$ (s)	$d_{cal}$ (km)	$d_{real}$ (km)	error(%)	Node
Case 1	TPSCFS	0,5667	0,6	1,4531	1,427	1,8626	140
	TPSCNS	0,5649	0,5715	0,28413	0,2476	3,4701	186
Case 2	STPC	0,5649	0, 0,5715	0,62706	0,6258	0,2	212
	STPC	0,0567	0,06	0,80768	1,0517	23,202	102
Case 3	TPSC	0,5649	0,5849	1,2117	1,219	0,5963	235

For each node where the fault occurs, the rated current and short-circuit current, Table 9, are shown in the fault current in Figure 14 and the rated current in Figure 17.

In figure 16, node 212, distant from the substation, presents the maximum rated current of the system due to a more significant amount of connected load. In contrast, node 102 presents the minimum rated current within the system and is connected to a small load. For the case of figure 15, it is observed that the maximum fault current occurs at node 186 near the substation due to a large amount of connected load, while node 102 again presents the minimum fault current for the same reason of having a smaller load.

The voltages at the nodes of the electrical distribution system vary depending on the distance at which they are located because the greater the distance, the more significant the voltage drop (Table 8), where the nominal and fault voltage values are shown.

obtained in the tests of each case, in which it can be seen that the calculated values of fault distance are satisfactory with a margin of error of less than 30%.

The distance calculation depends directly on the exact time, Figure 15, i.e., the calculated distance curve also varies by varying the time curves  $t_1$  and  $t_2$ . The same graph shows that the calculated distance curve is similar to the actual distance curve, i.e., satisfactory results.

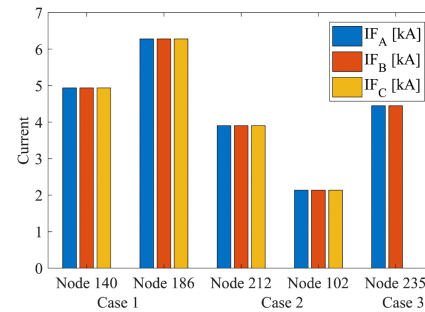


**Figure 15.** Node fault current.

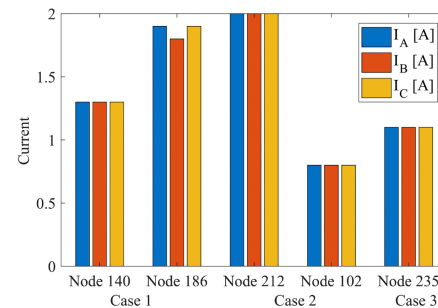


**Figure 16.** Nominal current of the node.

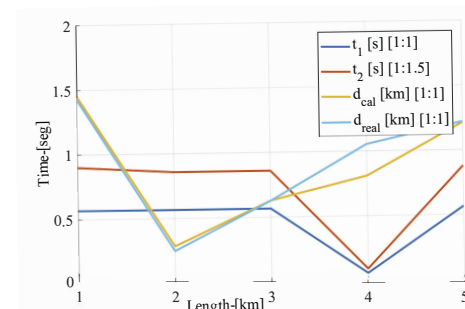


**Figure 17.** Detail time and actual and calculated distance.

**Table 8.** Nominal voltage and fault voltage.

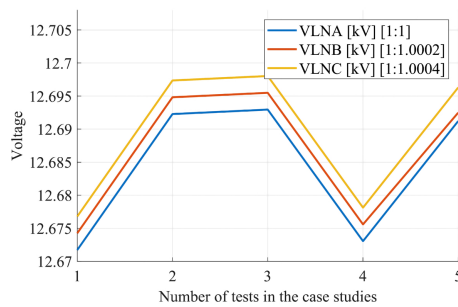
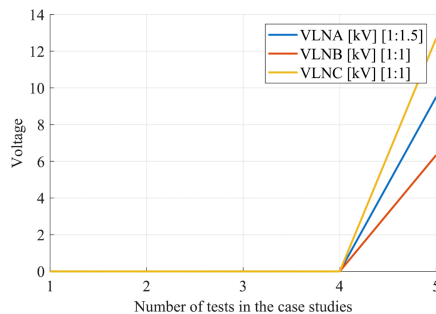
	Nominal phase voltage			Fault phase voltage		
	$VLNA$ (kV)	$VLNB$ (kV)	$VLNC$ (kV)	$VLNA$ (kV)	$VLNB$ (kV)	$VLNC$ (kV)
Case 1	140	12.671717	12.671717	12.671717	0.0017369	0.0017369
	186	12.692277	12.692277	12.692277	0.0002725	0.0002725
Case 2	212	12.692948	12.692948	12.692948	0.0016125	0.0016125
	102	12.673058	12.673058	12.673058	0.0007874	0.0007874
Case 3	235	12.691229	12.691229	12.691229	6.3432678	6.3432678

Figure 18 analyzes the phase voltage values that vary depending on the distance at which any node belonging to the distribution system is located, far or

near the substation. Figure 19 shows that each phase varies according to the fault type for the fault voltages (Table 9).

**Table 9.** Fault and rated current.

Cases	Nodes	$IF_A$ (kA)	$IF_B$ (kA)	$IF_C$ (kA)	$I_A$ (A)	$I_B$ (A)	$I_C$ (A)
Case 1	140	4,9372	4,9372	4,9372	1,3	1,3	1,3
	186	6,2784	6,2784	6,2784	1,9	1,8	1,9
Case 2	212	3,9035	3,9035	3,9035	2	2	2
	102	2,1351	2,1351	2,1351	0,8	0,8	0,8
Case 3	235	4,4482	4,4482	0	1,1	1,1	1,1

**Figure 18.** Nominal voltage of the node.**Figure 19.** Node fault voltage.

### 3.1. Discussion

The performance of the fault location algorithm based on WT and traveling wave propagation speed depends

on the configuration of the distribution system lines and the fault location. When the design of the lines does not present impedance change, the algorithm shows excellent performance in calculating the fault distance, so the location of the fault point is more accurate. When the configuration of the lines presents impedance changes, it is necessary that the feeder has IED and protection equipment installed in multiple topics to have more information about the occurrence of faults, which allows the algorithm to present a high performance.

Several simulations were performed far and near the substation; faults greater than 850 m should not interpolate the data, and more minor faults should be interpolated. Given this hypothesis, it was determined that the interpolation threshold is 850m.

The precise location analysis is necessary because there may be equal distances in the distribution network; it performs based on the protection and switching equipment, such as reclosers, which allows zoning and reduces the fault location error. Although the analysis is performed by recloser zone, there are still equal distances to the point of failure. The location of FI is proposed to achieve a precise fault location. They can visually indicate which section of the distribution line is at fault.

## 4. Conclusions

Fault location in electrical distribution systems is essential to improve their reliability and reduce the interruption time of electrical service; in this article, the wavelet transform is related to the traveling wave to propose a fault location method.

The distribution system characterization shows that the line parameters' variation influences the velocity calculation through the traveling wave and the different protection equipment installed in the feeder, whose sampling frequency varies depending on the make and model.

For the calculation of the fault distance, it is necessary to correctly choose the mother wavelet, which will allow identifying in a better way the two maximum peaks after the fault being this approximate, which can have up to 30% of permissible error.

The fault signal obtained by the network's protection equipment can be acquired from equipment far or near the substation. It should be noted that if the data for constructing the fault signal are insufficient to obtain a smoothed signal, they should be interpolated to have a broader database and better approximate the fault; tests have been conducted showing in this work that the optimal distance is 850 m.

The methodology implemented in this case study was able to locate the faults in the distribution system through the short circuit current signals visualized by the reclosers near the fault. Finding the correct detail coefficients since these coefficients directly influence the distance calculation. This being the duration time of the fault, it should be noted that the proposed methodology can only be used in scenarios where there is no impedance change in the distribution lines.

For the quantification of the fault-detecting equipment, the jambu elbow method was used, which is used to implement within the k means algorithm that will place the fault-detecting equipment at strategic nodes.

## References

- [1] R. Dashti, M. Daisy, H. R. Shaker, and M. Tahavori, "Impedance-based fault location method for four-wire power distribution networks," *IEEE Access*, vol. 6, pp. 1342–1349, 11 2017. [Online]. Available: <https://doi.org/10.1109/ACCESS.2017.2778427>
- [2] M. Gholami, A. Abbaspour, M. Moeini-Aghtaie, M. Fotuhi-Firuzabad, and M. Lehtonen, "Detecting the location of short-circuit faults in active distribution network using pmu-based state estimation," *IEEE Transactions on Smart Grid*, vol. 11, pp. 1396–1406, 3 2020. [Online]. Available: <https://doi.org/10.1109/TSG.2019.2937944>
- [3] S. Gururajapathy, H. Mokhlis, and H. Illias, "Fault location and detection techniques in power distribution systems with distributed generation: A review," *Renewable and Sustainable Energy Reviews*, vol. 74, pp. 949–958, 2017. [Online]. Available: <https://doi.org/10.1016/j.rser.2017.03.021>
- [4] S. H. Mortazavi, Z. Moravej, and S. M. Shahrtash, "A searching based method for locating high impedance arcing fault in distribution networks," *IEEE Transactions on Power Delivery*, vol. 34, pp. 438–447, 4 2019. [Online]. Available: <https://doi.org/10.1109/TPWRD.2018.2874879>
- [5] R. Dashti, M. Daisy, H. Mirshekali, H. R. Shaker, and M. Hosseini Aliabadi, "A survey of fault prediction and location methods in electrical energy distribution networks," *Measurement*, vol. 184, p. 109947, 2021. [Online]. Available: <https://doi.org/10.1016/j.measurement.2021.109947>
- [6] M. Dashtdar, "Fault location in distribution network based on fault current analysis using artificial neural network," *International Journal of Electrical and Computer Sciences (IJECS)*, vol. 1, pp. 18–32, 10 2018. [Online]. Available: <https://doi.org/10.33544/MJECE.V1I2.75>
- [7] J. Tavoosi, M. Shirkhani, A. Azizi, S. Ud Din, A. Mohammadzadeh, and S. Mobayen, "A hybrid approach for fault location in power distributed networks: Impedance-based and machine learning technique," *Electric Power Systems Research*, vol. 210, p. 108073, 2022. [Online]. Available: <https://doi.org/10.1016/j.epsr.2022.108073>
- [8] M. Azeroual, Y. Boujoudar, K. Bhagat, L. El Iysaouy, A. Aljarbouh, A. Knyazkov, M. Fayaz, M. S. Qureshi, F. Rabbi, and H. EL Markhi, "Fault location and detection techniques in power distribution systems with distributed generation: Kenitra city (morocco) as a case study," *Electric Power Systems Research*, vol. 209, p. 108026, 2022. [Online]. Available: <https://doi.org/10.1016/j.epsr.2022.108026>
- [9] Z. Jianwen, H. Hui, G. Yu, H. Yongping, G. Shuping, and L. Jianan, "Single-phase ground fault location method for distribution network based on traveling wave time-frequency characteristics," *Electric Power Systems Research*, vol. 186, p. 106401, 2020. [Online]. Available: <https://doi.org/10.1016/j.epsr.2020.106401>
- [10] J. Liang, T. Jing, H. Niu, and J. Wang, "Two-terminal fault location method of distribution network based on adaptive convolution neural network," *IEEE Access*, vol. 8, pp. 54 035–54 043, 2020. [Online]. Available: <https://doi.org/10.1109/ACCESS.2020.2980573>

- [11] P. Mršić, v. Zeljković, D. Lekić, B. Erceg, P. Matić, S. Zubić, and P. Balcerak, “Minimization of power interruption time in mv distribution networks with fault locators based on optimal placement of fault passage indicators,” in *2018 International Symposium on Industrial Electronics (INDEL)*, Nov 2018, pp. 1–7. [Online]. Available: <https://doi.org/10.1109/INDEL.2018.8637620>
- [12] X. Wang, H. Zhang, F. Shi, Q. Wu, V. Terzija, W. Xie, and C. Fang, “Location of single phase to ground faults in distribution networks based on synchronous transients energy analysis,” *IEEE Transactions on Smart Grid*, vol. 11, pp. 774–785, 1 2020. [Online]. Available: <https://doi.org/10.1109/TSG.2019.2938667>
- [13] W. C. Santos, F. V. Lopes, N. S. Brito, and B. A. Souza, “High-impedance fault identification on distribution networks,” *IEEE Transactions on Power Delivery*, vol. 32, pp. 23–32, 2 2017. [Online]. Available: <https://doi.org/10.1109/TPWRD.2016.2548942>
- [14] S. Silva, P. Costa, M. Gouvea, A. Lacerda, F. Alves, and D. Leite, “High impedance fault detection in power distribution systems using wavelet transform and evolving neural network,” *Electric Power Systems Research*, vol. 154, pp. 474–483, 1 2018. [Online]. Available: <https://doi.org/10.1016/J.EPSR.2017.08.039>
- [15] M. F. Guo, N. C. Yang, and L. X. You, “Wavelet-transform based early detection method for short-circuit faults in power distribution networks,” *International Journal of Electrical Power & Energy Systems*, vol. 99, pp. 706–721, 7 2018. [Online]. Available: <https://doi.org/10.1016/J.IJEPES.2018.01.013>
- [16] F. M. Aboshady, D. W. Thomas, and M. Sumner, “A new single end wideband impedance based fault location scheme for distribution systems,” *Electric Power Systems Research*, vol. 173, pp. 263–270, 8 2019. [Online]. Available: <https://doi.org/10.1016/J.EPSR.2019.04.034>
- [17] A. Silos-Sanchez, R. Villafafila-Robles, and P. Lloret-Gallego, “Novel fault location algorithm for meshed distribution networks with ders,” *Electric Power Systems Research*, vol. 181, p. 106182, 4 2020. [Online]. Available: <https://doi.org/10.1016/J.EPSR.2019.106182>
- [18] S. Myint and W. Wichakool, “A traveling wave-based fault section and fault distance estimation algorithm for grounded distribution systems,” *2019 IEEE PES GTD Grand International Conference and Exposition Asia, GTD Asia 2019*, pp. 472–477, 5 2019. [Online]. Available: <https://doi.org/10.1109/GTDASIA.2019.8715933>
- [19] P. Li, X. Liu, Z. Yuan, W. Chen, L. Yu, Q. Xu, and Y. Lin, “Precise fault location method of traveling wave in distribution grid based on multiple measuring point,” *2020 IEEE 4th Conference on Energy Internet and Energy System Integration: Connecting the Grids Towards a Low-Carbon High-Efficiency Energy System, EI2 2020*, pp. 1867–1872, 10 2020. [Online]. Available: <https://doi.org/10.1109/EI250167.2020.9346873>
- [20] X. G. Magagula, Y. Hamam, J. A. Jordaan, and A. A. Yusuff, “A fault classification and localization method in a power distribution network,” *2017 IEEE AFRICON: Science, Technology and Innovation for Africa, AFRICON 2017*, pp. 1337–1343, 11 2017. [Online]. Available: <https://doi.org/10.1109/AFRCON.2017.8095676>
- [21] Z. Jianwen and D. Jiaxin, “Traveling wave fault location for lines combined with overhead-lines and cables based on empirical wavelet transform,” *2019 IEEE 2nd International Conference on Electronics and Communication Engineering, ICECE 2019*, pp. 285–289, 12 2019. [Online]. Available: <https://doi.org/10.1109/ICECE48499.2019.9058522>
- [22] Y. Jiang, “Data-driven probabilistic fault location of electric power distribution systems incorporating data uncertainties,” *IEEE Transactions on Smart Grid*, vol. 12, pp. 4522–4534, 9 2021. [Online]. Available: <https://doi.org/10.1109/TSG.2021.3070550>
- [23] C. Zhang, G. Song, T. Wang, and L. Yang, “Single-ended traveling wave fault location method in dc transmission line based on wave front information,” *IEEE Transactions on Power Delivery*, vol. 34, pp. 2028–2038, 10 2019. [Online]. Available: <https://doi.org/10.1109/TPWRD.2019.2922654>
- [24] W. Pavón, E. Inga, and S. Simani, “Optimal routing an ungrounded electrical distribution system based on heuristic method with micro grids integration,” *Sustainability*, vol. 11, no. 6, 2019. [Online]. Available: <https://doi.org/10.3390/su11061607>
- [25] M. A. Alotaibi and M. M. A. Salama, “An incentive-based multistage expansion planning model for smart distribution systems,” *IEEE Transactions on Power Systems*, vol. 33, no. 5, pp. 5469–5485, Sep. 2018. [Online]. Available: <https://doi.org/10.1109/TPWRS.2018.2805322>
- [26] A. Valenzuela, E. Inga, and S. Simani, “Planning of a resilient underground distribution

- network using georeferenced data,” *Energies*, vol. 12, p. 644, 2 2019. [Online]. Available: <https://doi.org/10.3390/EN12040644>
- [27] M. A. Syakur, B. K. Khotimah, E. M. S. Rochman, and B. D. Satoto, “Integration k-means clustering method and elbow method for identification of the best customer profile cluster,” *IOP Conference Series: Materials Science and Engineering*, vol. 336, p. 012017, apr 2018. [Online]. Available: <https://doi.org/10.1088/1757-899x/336/1/012017>
- [28] M. Mosbah, S. Arif, R. D. Mohammedi, and A. Hellal, “Optimum dynamic distribution network reconfiguration using minimum spanning tree algorithm,” in *2017 5th International Conference on Electrical Engineering - Boumerdes (ICEE-B)*, Oct 2017, pp. 1–6. [Online]. Available: <https://doi.org/10.1109/ICEE-B.2017.8192170>
- [29] A. Guamán and A. Valenzuela, “Distribution network reconfiguration applied to multiple faulty branches based on spanning tree and genetic algorithms,” *Energies*, vol. 14, no. 20, 2021. [Online]. Available: <https://doi.org/10.3390/en14206699>
- [30] G. Michau, N. Pustelnik, P. Borgnat, P. Abry, A. Nantes, A. Bhaskar, and E. Chung, “A primal-dual algorithm for link dependent origin destination matrix estimation,” *IEEE Transactions on Signal and Information Processing over Networks*, vol. 3, no. 1, pp. 104–113, March 2017. [Online]. Available: <https://doi.org/10.1109/TSIPN.2016.2623094>





# EVOLUTIONARY ARTIFICIAL NEURAL NETWORK FOR TEMPERATURE CONTROL IN A BATCH POLYMERIZATION REACTOR.

## RED NEURONAL ARTIFICIAL EVOLUTIVA PARA EL CONTROL DE TEMPERATURA EN UN REACTOR BATCH DE POLIMERIZACIÓN.

Francisco Javier Sanchez-Ruiz<sup>1,\*</sup> , Elizabeth Argüelles Hernández<sup>1</sup> ,  
 José Terrones-Salgado<sup>1</sup> , Luz Judith Fernández Quíroz<sup>1</sup> 

Received: 06-03-2023, Received after review: 08-05-2023, Accepted: 29-05-2023, Published: 01-07-2023

### Abstract

The integration of artificial intelligence techniques introduces fresh perspectives in the implementation of these methods. This paper presents the combination of neural networks and evolutionary strategies to create what is known as evolutionary artificial neural networks (EANNs). In the process, the excitation function of neurons was modified to allow asexual reproduction. As a result, neurons evolved and developed significantly. The technique of a batch polymerization reactor temperature controller to produce polymethylmethacrylate (PMMA) by free radicals was compared with two different controls, such as PID and GMC, demonstrating that artificial intelligence-based controllers can be applied. These controllers provide better results than conventional controllers without creating transfer functions to the control process represented.

**Keywords:** ANNs, Evolved Neural Networks, Reactor Batch, Function Excitation, PMMA

### Resumen

La integración de técnicas de inteligencia artificial introduce nuevas perspectivas en la aplicación de estos métodos. Este trabajo presenta la combinación de redes neuronales y estrategias evolutivas para crear lo que se conoce como redes neuronales artificiales evolutivas (RNAE). Durante el proceso, se modificó la función de excitación de las neuronas para permitir su reproducción asexual. Como resultado, las neuronas evolucionaron y se desarrollaron significativamente. La técnica del controlador de temperatura de un reactor de polimerización por lotes para producir polimetilmetacrilato (PMMA) mediante radicales libres se comparó con dos controles diferentes (PID y GMC), demostrando así la aplicabilidad de los controladores basados en inteligencia artificial. Estos controladores ofrecen mejores resultados que los controladores convencionales sin crear funciones de transferencia al proceso de control representado.

**Palabras clave:** RNA, redes neuronales evolucionadas, lote de reactores, excitación de funciones, PMMA

<sup>1,\*</sup>Laboratorio de Investigación Biotecnológica, Grupo de Investigación de Bioenergía e Inteligencia Artificial, Universidad Popular Autónoma del Estado de Puebla, México.  
 Corresponding author ✉: franciscojavier.sanchez@upaep.mx.

Suggested citation: Sanchez-Ruiz, F.; Argüelles Hernández, E.; Terrones-Salgado, J. y Fernández Quíroz, L. "Evolutionary artificial neural network for temperature control in a batch polymerization reactor.," *Ingenius, Revista de Ciencia y Tecnología*, N.º 30, pp. 79-89, 2023, DOI: <https://doi.org/10.17163/ings.n30.2023.07>.

## 1. Introduction

Artificial neural networks are systems based on the cognitive and problem-solving capacity of the human brain, with the difference of greater robustness of the artificial neural network compared to the human brain. Who can establish that the systems based on artificial intelligence and artificial neural networks (ANNs) can submit an overlearning of the dynamics of the process, this being a feature of adjustment similar to the human brain [1–4].

Neural networks can be of different types, and the selection of the same depends on the characteristics required of the network and of the process, which means that the more robust network tends to be the most appropriate setting. However, as happens in the human brain [5–9], artificial neural networks can also present a learning non-adjustable, which is called (overlearning); this means that the neural network used as part of its adjustment calculated values not representative of the system, this being that the important part of research on artificial neural networks. The search for a neural network that avoids the presence of overlearning, this feature will cause that emit different types of neural networks artificial; these new types of neural networks combine other artificial intelligence techniques, such as fuzzy logic, evolutionary algorithms, and optimization techniques (stochastic methods) for improvement of the response of the neural network [10–14].

Who can use a neural network for the recognition of patterns and images, or as a controller, in this work is used an artificial neural network is combined with a technique of evolution, resulting in an evolutionary artificial neural network, known as neuroevolutionary control [15].

This study compares the functions of excitation applied to neuroevolutionary controllers and conventional controls such as PID and GMC and shows that systems based on artificial intelligence and neural networks evolutionary systems provide a better fit compared with traditional control systems the PID and not conventional GMC systems. This study raises a new aspect of applying intelligent systems in process control with unpredictable dynamics [16–18].

## 2. Materials and Methods

The characteristics of an evolutionary neural network controller are based on an artificial neural network, which consists of a function of neuronal representation that is based on the weights (values  $x_i$ ) of entry and a function of excitation  $\sigma$ ; the latter has the feature to propagate the pesos toward maximum and minimum [19–22].

Where  $w_0$  represents the value of the initial weight, what can replace the role of excitation ( $\sigma$ ) to minimize

the error, avoiding in this way the overlearning, Figure 1 shows the main structure of an artificial neural network schematically. Equation (1)

$$y = \sigma \left( w_0 + \sum_{i=1}^n w_i x_i \right) \quad (1)$$

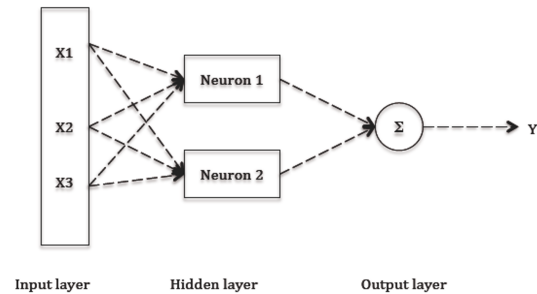


**Figure 1.** Basic structure of Artificial Neural Networks (ANNs)

As the neural network controller does not require to linearize the model according to a mathematical law of control given, this is mainly because the artificial neural network first linearized the evolutionary model in such a way that adequately represents the dynamics of the process, in Figure 2 shows how the use of a neural network controller [23].

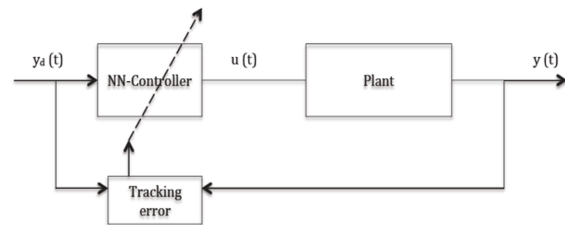


**Figure 2.** As Neural Network Controller

The response of the control based on evolutionary neural networks makes use of evolutionary algorithms, an algorithm that establishes the foundation of the evolution of the neural network and modifies the basic neural network.

When using the three methods of evolution in a neural network must be clear that the neural network works dynamically; for this case are only used. The first two techniques of evolution, this mainly due to the use of a neural network static; the neural network does not modify your static weights neural and interconnections, but if you evolve, generating new neurons information storage [24].

Implementing the techniques in an evolutionary neural network is done by implementing an evolution algorithm with a series of established steps. Figure 3

shows each of the sequential stages to obtain a structure of an evolutionary artificial neural network; the first stage of the structuring depends on getting synaptic weights, which can be obtained through a supervised or unsupervised process. For non-linear models such as fermentation reactors, gets values through an unsupervised algorithm, which is based on the variables of the mathematical model (T, P, yeast growth, concentration, Etc.), that is, those that are obtained from the solution. From the mathematical model, the weights are used in the neural network training process, which is combined with the evolution algorithm. The cycle is repeated until the most suitable structure is found (phenotype of the evolved neural network), which implies that there is still the possibility of evolution of the system; that is, if the control variables present disturbances, there will be adjusting according to the evolutionary process of the same structure of the evolutionary artificial neural network, this is done by the evolution method which is a thread where an analysis of the values of the trained weights is carried out, this is to generate a new generation of evolved neurons that adjust to the dynamics of the system [25]

Set up a system of control through evolutionary neural networks start arises as an architecture of a

primary neural network, which consists of a neuron of entry, a neuron in the hidden layer, and one neuron in the output layer; this architecture is set in such a way due to the prior knowledge of the variable will be only to check the temperature of reactor polymerization [26].

Once established, the basic architecture is set as a progenitor for each neuron: Equation (2).

$$P_A = (\nabla \cdot \sigma_i w_i + y_t) - E_i \quad (2)$$

Where  $\sigma_i$  is the function of excitation,  $w_i$  are synaptic weights (input),  $y_t$  is temporal series of synaptic weights propagated, and  $e_i$  is the error of training.

The expansions of weight and the excitation function are shown in the following equations, which show who can expand the weights in three dimensions, this is when the neural network can propagate information in three dimensions very similar to what happens in the human brain [14]. Equation (3) and (4)

The progenitor is as follows: Equation (5).

$$\nabla \cdot \sigma_i w_i = \frac{\partial(\sigma_i w_i)}{\partial x} + \frac{\partial(\sigma_i w_i)}{\partial y} + \frac{\partial(\sigma_i w_i)}{\partial z} \quad (3)$$

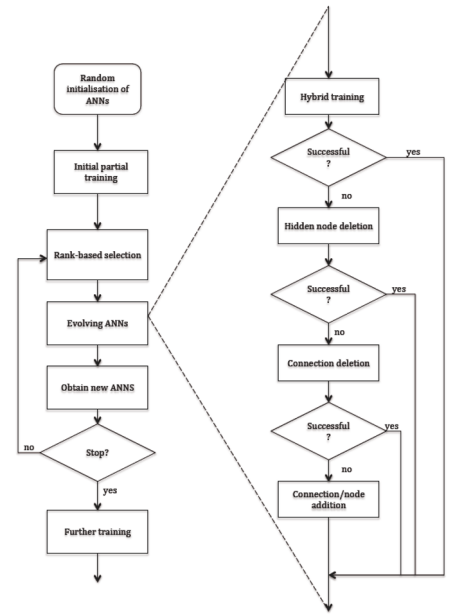


Figure 3. Flow diagram of the main structure of the EANN

$$\nabla \cdot \sigma_i w_i = \sigma_i \left( \sum_{i=1}^n \frac{\partial w_i}{\partial x} + \sum_{i=1}^n \frac{\partial w_i}{\partial y} + \sum_{i=1}^n \frac{\partial w_i}{\partial y} \right) + w_i \left( \sum_{i=1}^n \frac{\partial \sigma_i}{\partial x} \sum_{i=1}^n \frac{\partial \sigma_i}{\partial y} + \sum_{i=1}^n \frac{\partial \sigma_i}{\partial y} \right) \quad (4)$$

$$P_A = \left[ \left( \sigma_i \left( \sum_{i=1}^n \frac{\partial w_i}{\partial x} + \sum_{i=1}^n \frac{\partial w_i}{\partial y} + \sum_{i=1}^n \frac{\partial w_i}{\partial y} \right) + w_i \left( \sum_{i=1}^n \frac{\partial \sigma_i}{\partial x} \sum_{i=1}^n \frac{\partial \sigma_i}{\partial y} + \sum_{i=1}^n \frac{\partial \sigma_i}{\partial y} \right) \right) \right] + y_t P_A = \left[ \left( \sigma_i \left( \sum_{i=1}^n \frac{\partial w_i}{\partial x} + \sum_{i=1}^n \frac{\partial w_i}{\partial y} + \sum_{i=1}^n \frac{\partial w_i}{\partial y} \right) + w_i \left( \sum_{i=1}^n \frac{\partial \sigma_i}{\partial x} + \sum_{i=1}^n \frac{\partial \sigma_i}{\partial y} + \sum_{i=1}^n \frac{\partial \sigma_i}{\partial y} \right) \right) + y_t \right] - E_i \quad (5)$$

Who used the system to study three different excitation functions tangential function, equation (6), logarithmic, equation (7), and radial basis, equation (8).

$$\sigma_i = \frac{\exp(-\phi \cdot w_i) + \phi \exp(\phi \cdot w_i)}{\exp(-\phi \cdot w_i) - \exp(\phi \cdot w_i)} \quad (6)$$

$$\sigma_i = \frac{1}{1 + \exp(-\phi \cdot w_i)} \quad (7)$$

$$\sigma_i = \sum_{i=1}^n w_i \phi(\|w - w_{ci}\|) \quad (8)$$

Where  $\sum_{i=1}^n w_i$  represents the slope of the function of excitation and  $w_i$  weights of entry of the neural network, generally, these weights of entry to the artificial neural network can be obtained from a reference model or through the experimental data from the system to check.

The evolution of the neural network is performed using the equation of reproduction of progenitor; this evolutionary through the states and technique to evolved, equation (9).

$$P_{A_{n+i}} = P_{A_{S,i}} + \eta_i \nabla \times (P_{A_{T,i}} - P_{A_{S,i}}) \quad (9)$$

Where  $S$  and  $T$  represent each of the selected progenitors and  $\eta_i$  represents a uniform random number between zero and the unit [15].

The Levenberg performs the training of the neural network - Marquart (LM), an accelerated type of training that can simultaneously function as a gradient descent training as the Quasi-Newton (BFGS). The training of LM implements the Newton, based expansion second-order Taylor series method, thus obtaining a Hessian matrix of the weights of the network; after obtaining the Hessian matrix approximates a Jacobian matrix that involves different steps of training [26] Now who can express the LM method with the scaling factor  $\mu_k$ , equation (10).

$$W_{k+1} = W_k - \left[ \begin{array}{c} J^T(W_k) \cdot J(W_k) + \mu_k \cdot I \\ J^T(W_k) \cdot e(w_k) \end{array} \right]^{-1} \cdot \quad (10)$$

Where  $J(w_k)$  is a Jacobian matrix,  $I$  is the identity matrix, and  $e(w_k)$  is the error weight synaptic.

The neural network model is applied to the evolutionary model of a polymerization reactor using free radicals of methyl-methacrylate (MMA) for obtaining poly-methyl-methacrylate (PMMA). The mathematical model consists of mass balances, energy, and kinetic equations, this model is a direct way to implement control with neural networks, and the same applies to the rules necessary to obtain the control laws for drivers of type GMC and PID [27].

Mass Balance: equation (11) and (12).

$$\frac{dC_m}{dt} = -(K_{p0} + k_{fm}) C_m \xi_0 \quad (11)$$

$$\frac{dC_i}{dt} = -k_d C_i \quad (12)$$

Energy Balance: equation (13) and (14).

$$\frac{dT}{dt} = \frac{(-\Delta H_r) R_p}{C_p \rho_{mix}} - \frac{UA(T - T_J)}{C_p V \rho_{mix}} \quad (13)$$

$$\frac{dT_J}{dt} = \frac{(T_{JSP} - T_J)}{\tau_J} + \frac{UA(T - T_J)}{C_{pJ} V_J \rho_J} \quad (14)$$

Kinetic Equations: ((15) to (25)).

$$k_d = 1.58 \times 10^{15} \exp\left(\frac{-1.2874 \times 10^5}{RT}\right) \quad (15)$$

$$k_{p0} = 7.0 \times 10^6 \exp\left(\frac{-2.6334 \times 10^4}{RT}\right) \quad (16)$$

$$k_{fm} = 4.661 \times 10^9 \exp\left(\frac{-7.4479 \times 10^4}{RT}\right) \quad (17)$$

$$k_{fs} = 1.49 \times 10^9 \exp\left(\frac{-6.6197 \times 10^4}{RT}\right) \quad (18)$$

$$k_{\theta p} = 3.0233 \times 10^{13} \exp\left(\frac{-1.1700 \times 10^5}{RT}\right) \quad (19)$$

$$k_{\theta t} = 1.4540 \times 10^{20} c_{i,0} \exp\left(\frac{-1.4584 \times 10^5}{RT}\right) \quad (20)$$

$$k_p = \frac{k_{p0}}{\left(1 + \frac{k_{p0}}{Dk_{\theta p}}\right)} \quad (21)$$

$$k_t = \frac{k_{t0}}{\left(1 + \frac{k_{t0}}{Dk_{\theta t}}\right)} \quad (22)$$

$$D = \exp\left[\frac{2.303(1 - \phi_p)}{0.168 - 8.21 \times 10^{-6}(T - 387)^2 + 0.03(T - \phi_p)}\right] \quad (23)$$

$$\phi_p = \frac{\mu_1 M W_m}{\rho_p} \quad (24)$$

$$k_{fm} = Z_{fm} \exp\left(\frac{-E_{fm}}{RT}\right) \quad (25)$$

The implementation of a control system based on artificial intelligence (AI), such as evolutionary artificial neural networks, unlike other conventional control systems, only require training and knowledge of the behaviour of the process variables to be controlled,

in the case of a fermentation reactor, the following must be considered: temperature, growth kinetics of microorganisms, and concentration of the final fermentation product, for this very reason it breaks with the conventional tuning paradigms of a traditional system of control, although it must be taken into consideration that overlearning does not occur recurrently, which can be minimized by the self-adjusting training algorithm to the dynamics of the fermentative process itself.

The following equations give the control laws for the two types of controllers, such as the conventional PID and the other not-so-conventional GMC [18]. The classic tuning methods or heuristics to determine the PID control parameters were presented by Ziegler and Nichols (1942); they have significantly impacted practice and are still used today, not so much in the application but as a base and reference. Comparison, since they do not give a good tuning, these methods are based on the characterization of the process dynamics using two parameters with which the parameters of the PID controller are determined.

The frequency response method was implemented to characterize the system dynamics in a closed loop using only the proportional control action. Once this is done,  $K_p$  must be increased, starting from zero, until the system presents sustained oscillations at the output. This takes the approach to the limit of its stability. The parameters that characterize the system dynamics are  $K_u$  and  $T_u$ , where  $K_u$  is the proportional gain that makes the system oscillate sustainably, with oscillation period  $T_u$ . Once determined these parameters are, the PID parameters are obtained with Table 1 [19].

**Table 1.** ISE and States of Evolution

Neuronal Architecture (1,1,1)	Excitation Function (FT, FL, FBR)	ISE $10^{-2}$	States of Evolution
Four outputs	Tangential slope 1.5	0.3191	$1.0737 \times 10^9$
Four outputs	Logarithmic slope 1.5	0.2966	$1.0737 \times 10^9$
Three outputs	Gaussian Radial Basis slope 0.5	0.1887	27

PID control: equation (26).

$$\frac{dx}{dt} = K \left( (x_{sp} - x) + \frac{1}{T_i} \int_0^t (x_{sp} - x) dt + T_d \frac{d(x_{sp} - x)}{dt} \right) \quad (26)$$

Control GMC: equation (27).

$$\frac{dx}{dt} = k_1 (x_{sp} - x) + k_2 \int_0^t (x_{sp} - x) dt \quad (27)$$

### 3. Results and discussion

The reason to train a neural network is to establish the parameters of linearization of the mathematical model, to the polymerization reactor shows that Figure 4 shows the linearization of the mathematical model by training the evolutionary neural network, first training generates the parameter sequentially to establish the evolution of the same network.

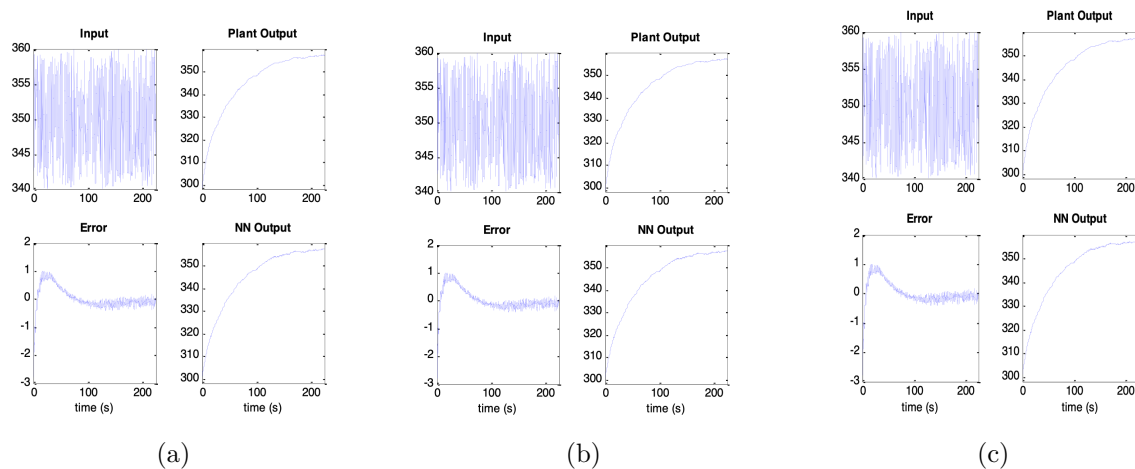


**Figure 4.** Responses of Plant and EANN (a) Logarithmic function, (b) Gaussian Radial Basis, (c) Tangential function.

The graphics training, validation, and testing provide the main trends of how evolutionary neural network (Figure 5), shows that the function of tangential type (Figure 5a) training has a setting similar to the function 0.79274 type logarithmic (Figure 5d). The

function of the Gaussian radial type training base setting is at a value of 0.99957, indicating that the radial basis function has less tendency to over-learning (Figure 5g). The graphics of validation and testing has similar behaviour for the three functions.

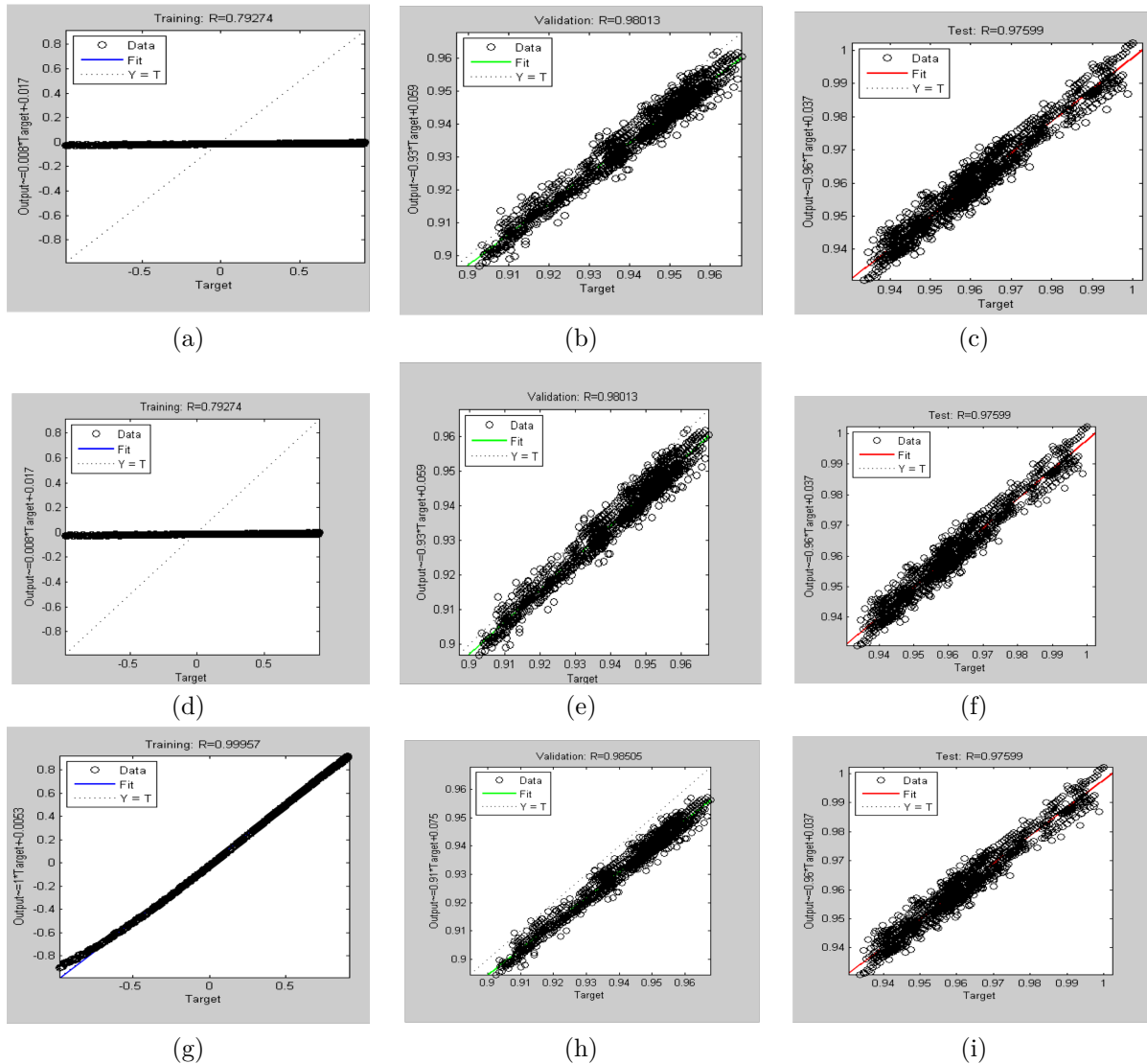


**Figure 5.** Training, Validation, and Testing of EANN

The results obtained by the evolutionary neural network are shown in Table 1, in the same observing the architecture of the artificial neural network and the evolutionary status of evolution, which has the same for different excitation functions. It should mention that simulations were conducted in Matlab, changing the number of outputs of the neural network from a range of 2 outputs of each neuron up to 4 outputs, which are obtained from evolutionary states. The states of evolution provide the total number of neurons evolved for the control system.

One of the advantages of implementing a control system with evolutionary artificial neural networks lies mainly in obtaining simple neural structures, which evolve according to the dynamics of the process itself, that is, with a basic design (neuronal phenotype). It is possible to have a capacity of adaptability to dynamics and non-linearities without requiring constant training,

presenting a closed or open loop self-learning system, as required by the process itself to be controlled. This is not possible for a conventional control system such as the PID that needs to be tuned in a closed loop, which can take time and not adjust to the dynamics of the process to be controlled.

We analyzed the three functions of excitation with different slopes and their influence developments in states; similarly, Integral Square Error (ISE) is calculated to determine which neural network is adjusted to the dynamics of the process.

Similarly, who performed analysis for integral square error (ISE) for two controllers used in the comparison (Table 2), the PID control and GMC, this error provides the information necessary to establish the setting of same to the dynamics process.

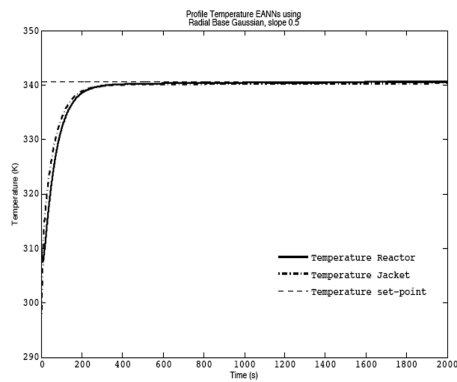
**Table 2.** ISE PID control and GMC

Type of Control	ISE
PID	0.3662
GMC	0.0198

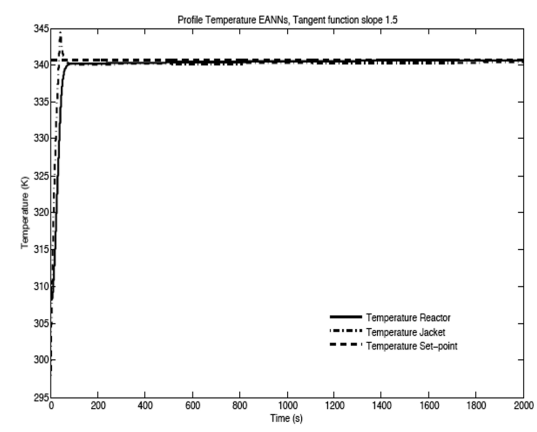
The selected structure of the neural network presents minor errors. Consequently, the smallest number of states of evolution is the evolutionary neural network with a function of type Gaussian radial basis with a value of  $\alpha=0.5$ , resulting in a total of 27 states of evolution. These states of evolution, to be minimum, indicate that those who added neural networks do not present overlearning, that part of the error spread toward the weights of forward and take as part of training itself. The number of outputs the neural network selected is 3 outputs; this number of outputs can also be a good selection of a neural network because it mainly to not be formed new neurons that may cause the about learning.

Figure 6 shows the response of neural control with the evolutionary function of Gaussian radial basis with three neural network outputs; what will note that it is adequately the set-point in a short period of time without portraying a shot in response to a controller.

Figures 7 - 8 shows the response of the controller for the other two excitation functions with different slope and number of outputs (see Table 1), the reaction of the control function tangential (Figure 7) with four outputs is presented on a shot for the temperature of the jacket. However, the control is set values set-point; in contrast, the driver's response with the logarithmic type function with a slope of 1.5 with the same number of outputs; for this profile was noted that the control response is adjusted to the set-point. Without that present over tire, the control response is very similar to the response given by the function of base type radial with a slope of 0.5. The limitation of the control function with the logarithmic type is that it presents too many states of evolution, which cause the evolutionary neural network shop to submit about learning.



**Figure 6.** Profile Temperature of EANNs Control using a radial basis function.



**Figure 7.** Profile Temperature of EANNs control using a tangential function.

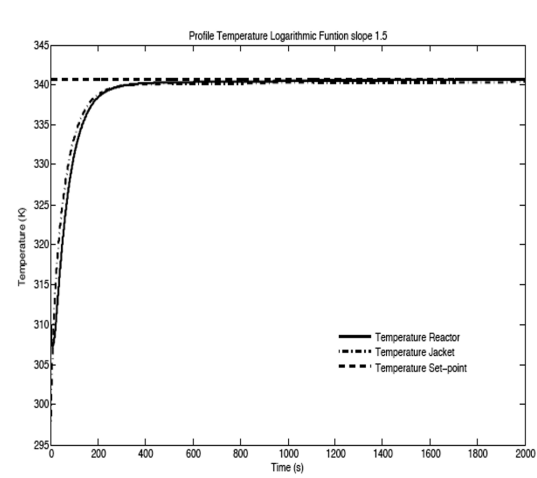


**Figure 8.** Profile Temperature of EANNs control using a logarithmic function.

The response of the PID control is shown in Figure 9 ; it is worth mentioning that tuning of PID control was performed using the technique of Zeigler-Nichols [19] for each of the constants of the controller; this response is observed on the drawbar that presents this driver is large compared with the control with neural networks, this is mainly attributable to the technique of tuning which causes the over tire tends to increase. The GMC also requires control of tuning because this control depends on a constant of the controller, which uses the technique used by Lee-Sullivan [18] for tuning of the same; the response of control GMC is shown in Figure 10, in comparison with the PID control the GMC does not have control over tire in its control response, which reaffirms that the technique of tuning of the controller is sensitive to the response of the same.

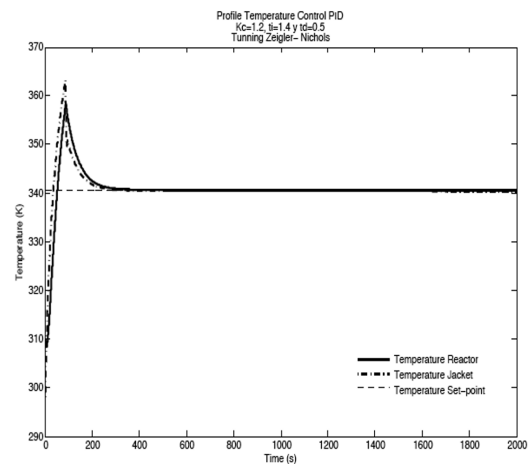


Figure 9. Profile Temperature using a PID controller

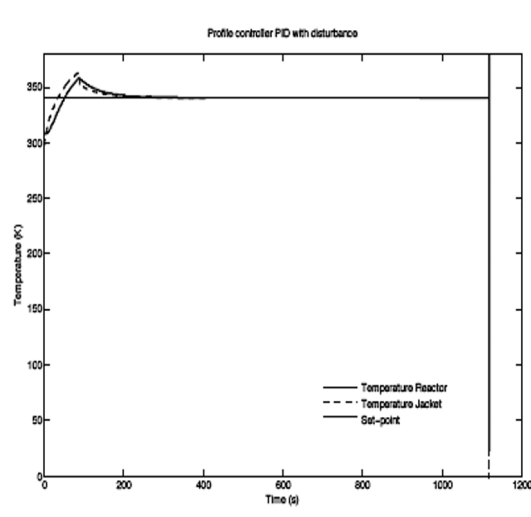


Figure 11. Controller PID with disturbance.

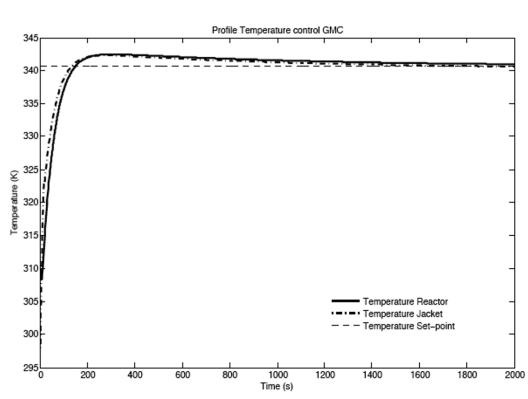


Figure 10. Profile Temperature using a controller GMC

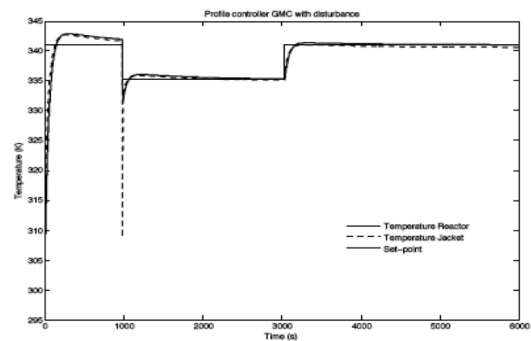


Figure 12. Controller GMC with disturbance.

In addition to the minimization of the ISE in control, the disturbances that can occur in the system are essential to measuring the response capacity of the control system; for the process studied. In this work, they were subjected to two disturbances and measured the ability. Adjustment with the lowest dead time ( $T_d$ ) and with a minimum frequency, the disturbance applied was a negative step change for the three control systems PID, GMC, and EANN. The PID controller fails to return to the set-point (Figure 11), causing control instability, GMC the trajectory of change in the set-point, variations in its sequence (Figure 12), and evolutionary neural network system change. The set point is followed sequentially without presenting any variation (Figure 13). The introduction of perturbations shows the robustness of the control system, indicating that evolutionary neural networks with radial Gaussian function are an option that offers better results compared to PID and GMC control.

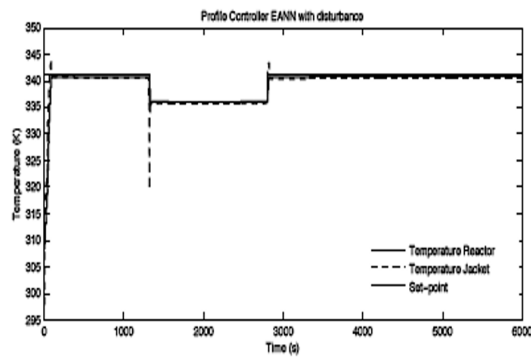


Figure 13. Controller EANN with disturbance.

## 4. Conclusion

This work presented a new alternative control based on evolutionary artificial neural networks through the use of different excitation functions and the modification

of the number of outputs of the neural network; using these two variables noted the trend in the evolution of the neural network. In the case study, the polymerization reactor for the obtaining of poly-methyl-methacrylate (PMMA) is a system that features a dynamic little predictable what conventional systems of control such as the PID and other not so traditional as GMC can produce good results but with the limitation of being restricted to the tuning of the controller, which was not the case with the control based on evolutionary neural networks, this type of control is properly adjusted to very dynamics of the process without having the need for a constant tuning, in addition to the control that is based on evolutionary neural networks also decreases the overshoot on the controls that are of a conventional type such as PID and GMC.

Concerning the different types of excitation functions, it is noted that the more complex function, as it is the type of radial basis, generates a better response from the controller based on evolutionary neural networks. When compared with the control of function logarithmic type, the difference lies in the minimization of the states of evolution, for the radial basis function of the number of outputs is minor, in addition to presenting a minimum of states of evolution, which indicates the probability of the network not to show a tendency to overlearning and so not getting a good response of the control.

Another option for training the evolutionary artificial neural network is Deep Learning, which can generally use under the supervised neural network training scheme; it can be an alternative for this type of system, if there are enough weights to carry out the projection of the dynamics of the process, all under a supervised training process, with simple neural structures or architectures. Another alternative to deep learning is a neural network evolution algorithm, which can be a new field of study for controlling nonlinear processes.

## References

- [1] J. Narkiewicz, M. Sochacki, and B. Zakrzewski, "Generic model of a satellite attitude control system," *International Journal of Aerospace Engineering*, vol. 2020, p. 5352019, Jul 2020. [Online]. Available: <https://doi.org/10.1155/2020/5352019>
- [2] N. F. Salahuddin, A. Shamiri, M. A. Hussain, and N. Mostoufi, "Hybrid fuzzy-GMC control of gas-phase propylene copolymerization in fluidized bed reactors," *Chemical Engineering Journal Advances*, vol. 8, p. 100161, 2021. [Online]. Available: <https://doi.org/10.1016/j.cej.2021.100161>
- [3] M. S. Mahmoud, M. Maaruf, and S. El-Ferik, "Neuro-adaptive fast terminal sliding mode control of the continuous polymerization reactor in the presence of unknown disturbances," *International Journal of Dynamics and Control*, vol. 9, no. 3, pp. 1167–1176, Sep 2021. [Online]. Available: <https://doi.org/10.1007/s40435-020-00731-x>
- [4] E. S. Yadav, P. Shettigar J, S. Poojary, S. Chokkadi, G. Jeppu, and T. Indiran, "Data-driven modeling of a pilot plant batch reactor and validation of a nonlinear model predictive controller for dynamic temperature profile tracking," *ACS Omega*, vol. 6, no. 26, pp. 16 714–16 721, 2021, pMID: 34250331. [Online]. Available: <https://doi.org/10.1021/acsomega.1c00087>
- [5] M. Maaruf, M. M. Ali, and F. M. Al-Sunni, "Artificial intelligence-based control of continuous polymerization reactor with input dead-zone," *International Journal of Dynamics and Control*, vol. 11, no. 3, pp. 1153–1165, Jun 2023. [Online]. Available: <https://doi.org/10.1007/s40435-022-01038-9>
- [6] P. Shettigar J, K. Lochan, G. Jeppu, S. Palanki, and T. Indiran, "Development and validation of advanced nonlinear predictive control algorithms for trajectory tracking in batch polymerization," *ACS Omega*, vol. 6, no. 35, pp. 22 857–22 865, 2021. [Online]. Available: <https://doi.org/10.1021/acsomega.1c03386>
- [7] H. Wang and Y. Chen, "Application of artificial neural networks in chemical process control," *Asian Journal of Research in Computer Science*, vol. 14, no. 1, pp. 22–37, 2022. [Online]. Available: <https://doi.org/10.9734/ajrcos/2022/v14i130325>
- [8] M. L. Dietrich, A. Brandolin, C. Sarmoria, and M. Asteasuain, "Mathematical modelling of rheological properties of low-density polyethylene produced in high-pressure tubular reactors," *IFAC-PapersOnLine*, vol. 54, no. 3, pp. 378–382, 2021, 16th IFAC Symposium on Advanced Control of Chemical Processes ADCHEM 2021. [Online]. Available: <https://doi.org/10.1016/j.ifacol.2021.08.271>
- [9] P. Shettigar J, J. Kumbhare, E. S. Yadav, and T. Indiran, "Wiener-neural-network-based modeling and validation of generalized predictive control on a laboratory-scale batch reactor," *ACS Omega*, vol. 7, no. 19, pp. 16 341–16 351, 2022. [Online]. Available: <https://doi.org/10.1021/acsomega.1c07149>
- [10] D. Q. Gbadago, J. Moon, M. Kim, and S. Hwang, "A unified framework for the mathematical modelling, predictive analysis, and optimization of reaction systems using computational fluid dynamics, deep neural network

- and genetic algorithm: A case of butadiene synthesis,” *Chemical Engineering Journal*, vol. 409, p. 128163, 2021. [Online]. Available: <https://doi.org/10.1016/j.cej.2020.128163>
- [11] M. García-Carrillo, A. B. Espinoza-Martínez, L. F. Ramos-de Valle, and S. Sánchez-Valdés, “Simultaneous optimization of thermal and electrical conductivity of high density polyethylene-carbon particle composites by artificial neural networks and multi-objective genetic algorithm,” *Computational Materials Science*, vol. 201, p. 110956, 2022. [Online]. Available: <https://doi.org/10.1016/j.commatsci.2021.110956>
- [12] L. Ghiba, E. N. Drăgoi, and S. Curteanu, “Neural network-based hybrid models developed for free radical polymerization of styrene,” *Polymer Engineering & Science*, vol. 61, no. 3, pp. 716–730, 2021. [Online]. Available: <https://doi.org/10.1002/pen.25611>
- [13] K. Bi, S. Zhang, C. Zhang, H. Li, X. Huang, H. Liu, and T. Qiu, “Knowledge expression, numerical modeling and optimization application of ethylene thermal cracking: From the perspective of intelligent manufacturing,” *Chinese Journal of Chemical Engineering*, vol. 38, pp. 1–17, 2021. [Online]. Available: <https://doi.org/10.1016/j.cjche.2021.03.033>
- [14] K. Ahmad, H. R. Ghatak, and S. M. Ahuja, “Response surface methodology (RSM) and artificial neural network (ANN) approach to optimize the photocatalytic conversion of rice straw hydrolysis residue (RSHR) into vanillin and 4-hydroxybenzaldehyde,” *Chemical Product and Process Modeling*, 2022. [Online]. Available: <https://doi.org/10.1515/cppm-2022-0003>
- [15] E. M. de Medeiros, H. Noorman, R. Maciel Filho, and J. A. Posada, “Production of ethanol fuel via syngas fermentation: Optimization of economic performance and energy efficiency,” *Chemical Engineering Science: X*, vol. 5, p. 100056, 2020. [Online]. Available: <https://doi.org/10.1016/j.cesx.2020.100056>
- [16] S. Greydanus, M. Dzamba, and J. Yosinski, “Hamiltonian neural networks,” in *Advances in Neural Information Processing Systems*, H. Wallach, H. Larochelle, A. Beygelzimer, F. d'Alché-Buc, E. Fox, and R. Garnett, Eds., vol. 32. Curran Associates, Inc., 2019. [Online]. Available: <https://bit.ly/3qhXPxB>
- [17] J. Zeng, L. Cao, M. Xu, T. Zhu, and J. Z. H. Zhang, “Complex reaction processes in combustion unraveled by neural network-based molecular dynamics simulation,” *Nature Communications*, vol. 11, no. 1, p. 5713, Nov 2020. [Online]. Available: <https://doi.org/10.1038/s41467-020-19497-z>
- [18] H. Wang and R. Mo, “Review of neural network algorithm and its application in reactive distillation,” *Asian Journal of Chemical Sciences*, vol. 9, no. 3, pp. 20–29, 2021. [Online]. Available: <https://doi.org/10.9734/ajocs/2021/v9i319073>
- [19] I. Moreno and J. Serracín, “Dr. Santiago Ramón y Caja,” *Prisma Tecnológico*, vol. 12, no. 1, pp. 86–87, 2021. [Online]. Available: <https://doi.org/10.33412/pri.v12.1.2985>
- [20] V. Buhrmester, D. Münch, and M. Arens, “Analysis of explainers of black box deep neural networks for computer vision: A survey,” *Machine Learning and Knowledge Extraction*, vol. 3, no. 4, pp. 966–989, 2021. [Online]. Available: <https://doi.org/10.3390/make3040048>
- [21] H. Chen, C. Fu, J. Zhao, and F. Koushanfar, “Deepinspect: A black-box trojan detection and mitigation framework for deep neural networks,” in *Proceedings of the Twenty-Eighth International Joint Conference on Artificial Intelligence, IJCAI-19*. International Joint Conferences on Artificial Intelligence Organization, 7 2019, pp. 4658–4664. [Online]. Available: <https://doi.org/10.24963/ijcai.2019/647>
- [22] E. Zihni, V. I. Madai, M. Livne, I. Galinovic, A. A. Khalil, J. B. Fiebach, and D. Frey, “Opening the black box of artificial intelligence for clinical decision support: A study predicting stroke outcome,” *PLOS ONE*, vol. 15, no. 4, pp. 1–15, 04 2020. [Online]. Available: <https://doi.org/10.1371/journal.pone.0231166>
- [23] R. Miikkulainen, J. Liang, E. Meyerson, A. Rawal, D. Fink, O. Francon, B. Raju, H. Shahrzad, A. Navruzyan, N. Duffy, and B. Hodjat, “Chapter 15 - evolving deep neural networks,” in *Artificial Intelligence in the Age of Neural Networks and Brain Computing*, R. Kozma, C. Alippi, Y. Choe, and F. C. Morabito, Eds. Academic Press, 2019, pp. 293–312. [Online]. Available: <https://doi.org/10.1016/B978-0-12-815480-9.00015-3>
- [24] Bilal, M. Pant, H. Zaheer, L. García-Hernández, and A. Abraham, “Differential evolution: A review of more than two decades of research,” *Engineering Applications of Artificial Intelligence*, vol. 90, p. 103479, 2020. [Online]. Available: <https://doi.org/10.1016/j.engappai.2020.103479>
- [25] A. Bashar, “Survey on evolving deep learning neural network architectures,” *Journal of Artificial Intelligence*, vol. 1, no. 2,

- pp. 73–82, 2019. [Online]. Available: <https://doi.org/10.36548/jaicn.2019.2.003>
- [26] Y. Sun, B. Xue, M. Zhang, and G. G. Yen, “Evolving deep convolutional neural networks for image classification,” *IEEE Transactions on Evolutionary Computation*, vol. 24, no. 2, pp. 394–407, 2020. [Online]. Available: <https://doi.org/10.1109/TEVC.2019.2916183>
- [27] E. Ekpo and I. Mujtaba, “Evaluation of neural networks-based controllers in batch polymerisation of methyl methacrylate,” *Neurocomputing*, vol. 71, no. 7, pp. 1401–1412, 2008, progress in Modeling, Theory, and Application of Computational Intelligenc. [Online]. Available: <https://doi.org/10.1016/j.neucom.2007.05.013>



# ADVANCES AND STRATEGIES TO IMPROVE THE PERFORMANCE OF BIODIESEL IN DIESEL ENGINE

## AVANCES Y ESTRATEGIAS PARA MEJORAR EL DESEMPEÑO DEL BIODIESEL EN MOTOR DIESEL

Héctor-Hugo Riojas-González<sup>1,\*</sup> , Liborio-Jesús Bortoni-Anzures<sup>1</sup> ,  
 Juan-Julián Martínez-Torres<sup>1</sup> , Héctor A. Ruiz<sup>2</sup> 

Received: 19-04-2023, Received after review: 11-05-2023, Accepted: 29-05-2023, Published: 01-07-2023

### Abstract

The demand for diesel utilization in heavy-duty vehicles continues to increase worldwide. However, the potential use of alternative fuels such as biodiesel has disadvantages, such as lower calorific value and higher viscosity. For this reason, it is necessary to improve its properties to optimize combustion in the engine and reduce emissions. This research explores the various blends that can improve biodiesel utilisation through strategies and advancements that optimize diesel engine performance. Among the various strategies to improve biodiesel, we find the mixtures of different bio-oils (vegetable oils, pyrolysis oils, and used cooking oils), blends of biodiesel with alcohol and hydrogen, the use of biodiesel as a pilot fuel, emulsions of biodiesel with water, and the application of antioxidants, nanotubes, and nanoparticles to biodiesel. It is concluded that currently, biodiesel can be used through the dual combustion technique, where it acts as a pilot fuel representing 10% or 20% of the total fuel in the engine. This strategy allows for the promotion of other fuels (liquids and gases) in dual combustion to find the optimal blend that is the best option for the diesel engine.

**Keywords:** Biodiesel, engines, mixtures, oils, dual combustion, emulsions

### Resumen

La demanda de diésel en vehículos pesados se incrementa cada año en el mundo. El posible uso de combustibles alternativos como el biodiésel tiene algunas desventajas como el menor valor calorífico y su mayor viscosidad, por esta razón se requiere mejorar sus propiedades, optimizando el comportamiento de la combustión en el motor y en la reducción de las emisiones. El objetivo del trabajo de investigación es explorar las diferentes mezclas que puedan ayudar a mejorar el uso del biodiésel a través de las estrategias y avances que se han generado con el propósito de beneficiar el desempeño del motor diésel. Entre las distintas estrategias de mejoramiento del biodiésel están las mezclas de distintos bioaceites (aceites vegetales, de pirólisis y usado de cocina), mezclas del biodiésel con alcohol, con hidrógeno, el biodiésel como combustible piloto, las emulsiones del biodiésel con agua y la aplicación del biodiésel con antioxidantes, nanotubos y nanopartículas. Se concluye que para poder usar actualmente el biodiésel se lo haría con la combustión dual, en donde este representaría el combustible piloto (10 % o 20 % del combustible total del motor). Con esta estrategia se puede impulsar a otros combustibles (líquidos y gaseosos) en la combustión dual, para que con el paso del tiempo se encuentre la mezcla óptima que sea la mejor opción para el motor diésel.

**Palabras clave:** biodiésel, motores, mezclas, aceites, combustión dual, emulsiones

<sup>1,\*</sup>Universidad Politécnica de Victoria, Ciudad Victoria, Tamaulipas, México.

Corresponding author ✉: [hriojasg@upv.edu.mx](mailto:hriojasg@upv.edu.mx)

<sup>2</sup>Grupo de Biorrefinería, Departamento de Investigación en Alimentos, Facultad de Ciencias Químicas, Universidad Autónoma de Coahuila, Saltillo, Coahuila, México.

Suggested citation: Riojas-González, H. H.; Bortoni-Anzures, L. J.; Martínez-Torres, J. J. and Ruiz, H. A. "Advances and strategies to improve the performance of biodiesel in diesel engine," *Ingenius, Revista de Ciencia y Tecnología*, N.º 30, pp. 90-105, 2023, DOI: <https://doi.org/10.17163/ings.n30.2023.08>.

## 1. Introduction

From 2010 to 2040, the demand for the most used fuel in heavy-duty vehicles, diesel, is expected to increase by 85%, while the gasoline demand will decrease by approximately 10% [1]. As a result, the growing demand for energy in transportation focuses on diesel engines [2]. Unfortunately, the transportation sector worldwide is one of the main contributors to environmental pollution, generating 26% of greenhouse gas emissions [3]. Biofuels are considered carbon-neutral fuels, as plant crops easily absorb the CO<sub>2</sub> they produce through photosynthesis. Among the biofuels is biodiesel, which has a lower energy content than diesel. This is due to biodiesel's higher density, viscosity, specific fuel consumption, and NO<sub>x</sub> emissions. These are some limitations that affect biodiesel.

However, the properties of biodiesel can be improved by applying metal-based additives, oxygenated additives, antioxidants, cetane improvers, lubricants, and cold flow property optimizers. The addition of al-

cohol [4] and the blend of diesel-alcohol with biodiesel result in the formation of diesterol. In the quest to improve the properties of biodiesel, many researchers have employed various methods, such as transesterification (Figure 1), oil heating, alcohol blending, and mixing with diesel or other alternative fuels [5]. Furthermore, renewable diesel has been obtained, which, unlike biodiesel, can be derived from lipids (oil or fat) as a raw material through a hydrodeoxygenation reaction with a catalyst at high temperatures and pressure [6]. This research aims to explore different blends that enhance the use of biodiesel through strategies and advancements that optimize diesel engine performance. The most critical factor for biodiesel production is the raw material used.

## 2. Blends with different oils

Several authors recommend blends of different oils (Tabla ).

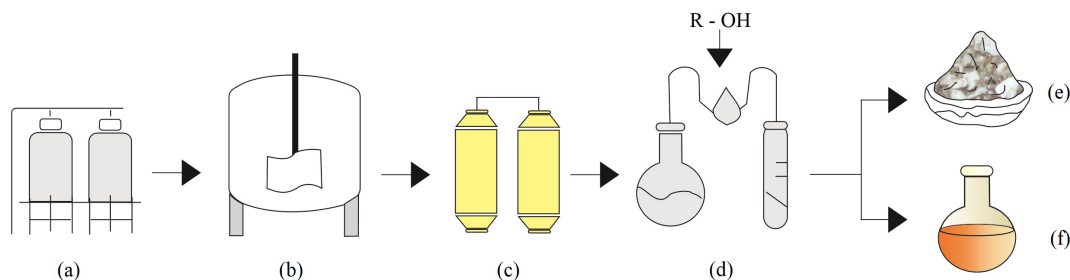


**Figure 1.** Transesterification process: (a) catalyst, (b) reactor with oil, (c) conditioning, (d) purification, (e) salts, and (f) biodiesel

**Table 1.** Evaluation of diesel engine performance using different bio-oils compared to conventional diesel

Type of bio-oil	Performance	Comments	Ref.
Soy methyl ester (SME) and yellow grease methyl ester (YGME)	Increase BSFC and YGME (12.2%) and GME (12.9%).	Both have a lower calorific value but exhibit good oxygenation, resulting in more efficient combustion.	[7]
Pithecellobium seed oil	BSFC increased.	There was a decrease in cylinder pressure, heat release rate, and exhaust temperature.	[8]
Orange peel oil	BTE improved at full load.	Reductions caused by low oil viscosity improve the complete combustion process.	[9]
PODE oil	BTE improved due to the type of oil used.	Due to the high oil-to-diesel blending ratio.	[10]

Type of bio-oil	Performance	Comments	Ref.
Palm oil	The output power decreased, and BSFC increased.	The use of oil with EGR caused a decrease in the release rate and generated fewer chemical reactions between the fuel and oxygen.	[11]
JOME	BTE increased, and BSFC decreased.	With the increase of EGR, the overall performance of the engine improved.	[12]
Mahua Oil	BSFC increased, and BTE decreased.	The engine efficiency decreased as the blending ratio of biodiesel increased.	[13]

Vallinayagam *et al.* [14] determined that a blend of 50% Kapok Methyl Ester (KME) and 50% pine oil was optimal in terms of performance and emissions. They observed a reduction in HC, smoke, and CO. However, the BTE of the blend was lower than diesel at low loads, although it was very similar to diesel at high loads. Singh *et al.* [15] determined that a blend of 70% Aamla oil and 30% eucalyptus oil reduces CO, HC, and smoke emissions, while NO<sub>x</sub> is equivalent to diesel.

Kasiraman *et al.* [16] recommend a blend of 70%

cashew shell oil and 30% camphor oil, which yields promising results, although it is still inferior to diesel. Dubey and Gupta [17] recommend a blend of 50% jatropha oil and 50% turpentine oil. This blend yielded the best results, significantly reducing NO<sub>x</sub>, CO, HC, and smoke compared to diesel, especially under full-load conditions. Sharma and Murugan [18] recommend a blend of 20% tire pyrolysis oil and 80% jatropha oil. Table 2 shows the physicochemical properties of the biodiesel.

**Table 2.** Technical properties of various biodiesel types

Type of biodiesel	Density (kg/m <sup>3</sup> )	Viscosity at 40 °C, cSt	Flashpoint (°C)	Cetane number	Calorific value (MJ/k)	Ref.
Pine oil	875,1	1,3	52	11	42,8	[14]
Pyrolysis oil	–	3,35	58	28	38,1	[18]
Orange oil	816	3,52	74	47	34,6	[9]
Mahua oil	960	24,58	232	–	36,1	[13]
Soybean oil	885	4,11	–	47,1	38,4	[19]
Used cooking oil	871	5,28	–	51	37,5	[20]
Rapeseed oil	886	6,18	–	59,3	40,8	[21]
Pongamia oil	870	6,79	–	> 48	38,8	[22]
Ceiba pentandra oil	880	1,9-6,0	–	47	–	[23]
Jatropha oil	874,3	4,34	130	52,7	42,67	[24]
Sunflower oil	880	4,3	148	54	40,76	[25]
Rice bran oil	880	–	–	56,3	39,54	[26]
Palm oil	870	–	–	56,5	38,84	[26]

### 3. Biodiesel-alcohol blend

Biodiesel's high viscosity, low volatility, and poor cold flow properties negatively affect combustion quality [19]. However, these characteristics can be improved by adding alcohol [27]. Fuel blends known as diesel (composed of diesel, biodiesel, and ethanol) have demonstrated greater efficiency, improved performance, and lower emissions. This is because ethanol, with its high calorific value and low density compared to biodiesel, compensates for its deficiencies [28].

Additionally, ethanol has low viscosity and optimal

cold flow properties, so when mixed with biodiesel, it helps reduce viscosity, increase volatility, and improve cold flow properties at low temperatures [29]. Table 3 presents the blend of ethanol and biodiesel and their emissions. The high oxygen content of ethanol can further reduce PM emissions in the mix with biodiesel [20]. The high cetane number of biodiesel compensates for the low cetane number of ethanol, thereby improving engine combustion [21].

The presence of biodiesel in the ethanol-diesel blend increases the cetane content and enhances the autoigni-

tion quality of the mixture [30]. Adding ethanol to the biodiesel-diesel blend improves overall physical properties such as evaporation and droplet size of the fuel mixture [22]. Tables 4 and 5 depict biodiesel blends with alcohols and their impact on engine performance.

**Table 3.** Emissions generation in the blend of biodiesel and ethanol

<b>Emission reduction</b>	<b>Comments</b>	<b>Ref.</b>
NO <sub>x</sub>	Emissions can be reduced with the biodiesel-ethanol blend.	[31]
CO, NO <sub>x</sub> and smoke	The reduction was due to the blend compared to pure biodiesel.	[32]
PM and NO <sub>x</sub>	The blend exhibits a higher maximum heat release rate and maximum cylinder pressure than pure biodiesel.	[20]
HC, CO and soot	Diesterol reduces BSFC, and ethanol acts as an oxidant for soot.	[33]
NO <sub>x</sub>	Diesterol exhibits a high heat of vaporization and reduces NO <sub>x</sub> emissions.	[34]

**Table 4.** Emission generation in the blend of biodiesel with alcohols

<b>Emission reduction</b>	<b>Type of alcohol</b>	<b>The reason</b>	<b>Ref.</b>
PM	Butanol	BTE was increased by adding 20 % butanol to the biodiesel.	[35]
CO and HC	Butanol and Pentanol	Pentanol blended with biodiesel showed better engine performance.	[23]
NO <sub>x</sub> and soot	n-Butanol	Applying higher injection pressure to the blend of butanol and biodiesel is a viable technique.	[36]
NO <sub>x</sub>	DME	The maximum heat release rate decreases when blending biodiesel with DME.	[37]
PM	n-Pentanol	Blending pentanol with biodiesel significantly reduces particle emissions.	[38]
NO <sub>x</sub> , HC and CO	1-Pentanol	The blend reduces emissions with a slight loss of BTE.	[39]
CO and HC	1-Octanol	Adding n-octanol improves BTE but increases NO <sub>x</sub> .	[40]

**Table 5.** Impact of bio-oil and alcohol blends on engine performance and emissions

Composition of the blend	Emission reduction	Engine performance	Ref.
70% diesel, 20% Jatropha oil, and 10% ethanol, with an addition of 25 ppm of Al <sub>2</sub> O <sub>3</sub> nanoparticles	HC, CO, NO <sub>x</sub> and smoke	The maximum cylinder pressure and the maximum rate of heat release were reached closer to TDC.	[24]
40% diesel, 40% biodiesel, 10% vegetable oil, and 10% propanol.	NO <sub>x</sub>	The blend exhibited the highest BSFC and lower NO <sub>x</sub> , emissions, but it led to an increase in levels of CO and HC.	[41]
A blend of diesel, residual sunflower biodiesel, n-pentanol and n-hexanol	Various	By adding n-heptanol, both BTE and BSFC values improved.	[42]
A blend of 5% DEE and the remaining portion of soybean oil biodiesel and diesel.	CO	There was an improvement in BSFC. However, it is essential to note that adding more than 40% of DEE could lead to engine detonation.	[43]
20% ethanol and 80% sunflower oil biodiesel de girasol	CO and NO <sub>x</sub>	With the blend, a higher thermal efficiency was achieved. However, when used at low speed, there is an increase in NO <sub>x</sub> emissions.	[25]

Another option for biodiesel blending is using longer-chain higher alcohols, such as butanol and pentanol. These alcohols can be blended with biodiesel at proportions of up to 20% and with diesel in diesel engines without any alterations [44]. Babu *et al.* [44], determined that up to 29% of butanol blended with biodiesel can be added without causing any modifications to the engine, thereby improving the properties of biodiesel and optimizing the combustion of the blends.

#### 4. Biogas and biodiesel blend

Biogas can be used in dual combustion as the primary fuel, with biodiesel serving as the pilot fuel. Sahoo [45] investigated the performance of dual combustion using biogas, obtaining a BTE of 16.8% and 16.1% for diesel and Jatropha biodiesel, respectively, compared to 20.9% for conventional diesel. Luijten and Kerkhof [46] analyzed synthetic biogas with a CO<sub>2</sub> variation from 30% to 60%, using a single-cylinder naturally aspirated diesel engine fueled with Jatropha biodiesel as the pilot fuel. They reported a slight variation in the engine's BTE when increasing the biogas energy proportion at high loads, while a significant BTE

decrease was observed at low loads. Table 6 displays the engine performance with the blend of biodiesel, alcohol, and biogas.

#### 5. Application of bio-oil with water

Using water-emulsified fuel in biodiesel (Figure 2) could reduce NO<sub>x</sub> and PM emissions [47]. Additionally, a decrease in smoke has been observed, but there is an increase in fuel consumption, CO, and HC emissions [48]. Fuel emulsion also reduces wear and friction, and this decrease could be related to the presence of water, which results in lower temperatures and, therefore, less combustion wear [49]. Water emulsion increases BTE (brake thermal efficiency) by improving fuel atomization and evaporation, creating a microexplosion that forms a fine aerosol and enhances fuel vaporization. The continuous braking of water droplets in the emulsification process increases the evaporation surface area and ensures precise mixing, resulting in improved reaction and combustion efficiency [50]. Table 7 presents the results obtained in the application of biodiesel emulsions.

**Table 6.** Dual fuel blending with bio-oil and alcohol with biogas

Type of blend	Emission reduction	Engine performance	Ref.
Soybean biodiesel as the pilot fuel, and biogas	Soot	Biogas combustion with biodiesel shows good performance and a reduction in soot.	[51]
Methyl ester of rice bran oil with biogas	CO and HC	Rice bran oil biodiesel improved performance with biogas at a higher compression ratio.	[26]
Biodiesel was used as a pilot fuel with a 6% DEE supplement, while biogas was the primary fuel.	CO, HC and smoke	The blend improved the engine performance and reduced BSFC, but an increase in NO <sub>x</sub> was observed.	[43]

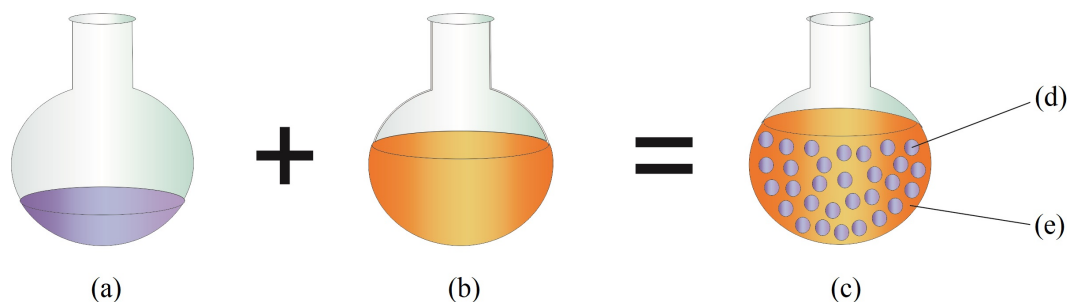


**Figure 2.** Emulsification phenomenon: (a) 30% water, (b) 70% fuel, (c) emulsion, (d) dispersed phase, (e) continuous phase.

**Table 7.** Application of bio-oils in emulsions

Emission reduction	Increasing emission	Engine performance characteristics	Ref.
CO and smoke	CO <sub>2</sub>	The BSFC and BSEC increased with the emulsion, while the BTE remained unchanged.	[52]
NO <sub>x</sub> and smoke	CO, CO <sub>2</sub> and HC	The use of diestrol-water microemulsions resulted in an increase in BSFC and a reduction in BTE.	[53]
NO <sub>x</sub> and soot	CO	A biodiesel nanoemulsion was used, resulting in increased fuel consumption.	[54]
NO <sub>x</sub>	HC, CO and smoke	The injection of 3 kg/h of water reduces NO <sub>x</sub> emissions by 50% without any deterioration in engine performance.	[55]
Smoke	-	The BTE increased to 7.4% with the bio-oil emulsion from wood waste pyrolysis.	[56]
HC and smoke	-	The BTE increased to 7.3% with the emulsion of wood pyrolysis oil and Jatropha methyl ester.	[57]

## 6. Biodiesel blend with natural gas

Natural gas can be used in dual-fuel combustion as the primary fuel, while biodiesel is used as the pilot fuel. Paul *et al.* [58] utilized pongamia pinnata methyl ester (PPME) as the pilot fuel in a dual-fuel CI engine by adding natural gas. Biodiesel showed an improvement in BTE and a reduction in BSFC. The combustion was more complete, reducing CO and HC emissions, although there was an increase in NO<sub>x</sub> emissions.

Tarabet *et al.* [59] determined that enriching natural gas with H<sub>2</sub> in a dual-fuel mode, using eucalyptus biodiesel as the pilot fuel improves engine performance and reduces emissions. On the other hand, the study conducted by Ryu [60] using vegetable oil (used cooking oil) as the pilot fuel in a DI Common Rail engine with natural gas, resulted in a power loss attributed to biodiesel due to its higher kinematic viscosity compared to diesel. Senthilraja *et al.* [61] conducted a

study on combining seed methyl ester blends with diesel-ethanol enriched with CNG. They reported an increase in BSFC when increasing the concentration of the biodiesel-ethanol combination.

On the other hand, in the experimental studies conducted by Kalsi *et al.* [62], an RCCI engine was fueled with biodiesel using compressed natural gas mixed with hydrogen, resulting in significant improvements in BTE and reduction of smoke, HC, and CO.

## 7. Biodiesel and hydrogen blend

Since hydrogen is a carbon-free energy carrier, all carbon-based emissions such as HC, CO, H<sub>2</sub>O, PM, and smoke decrease significantly in dual-fuel diesel engines under all loads [63]. The engine performance, as well as the engine behavior and its emissions with the blend of biodiesel and hydrogen, are presented in Tables 8 and 9, respectively.

**Table 8.** Engine performance with biodiesel and hydrogen blend

Type of blend	Engine performance	Ref.
Blending biodiesel with H <sub>2</sub> gas.	The blend reduces engine vibration and exhaust emissions, but biodiesel tends to generate noise.	[64]
Dual fuel with hydrogen and biodiesel.	With the blend, engine power was reduced from 190 g/Kwh to 104 g/Kwh, when switching from diesel to biodiesel.	[65]
A blend of diesel with Jatropha oil as biodiesel and 7% H <sub>2</sub> as pilot fuel.	With a 7% H <sub>2</sub> in the diesel/biodiesel blend, an increase in BTE was observed under full load conditions.	[66]
A blend of H <sub>2</sub> with jojoba oil methyl ester biodiesel as pilot fuel.	The thermal efficiency improved significantly, and the SFC was reduced.	[67]

**Table 9.** Engine performance and emissions with biodiesel and hydrogen blend

Emission reduction	Increasing emission	Engine performance	Ref.
CO and HC	NO <sub>x</sub>	With a blend of palm oil biodiesel and 20% hydroxyl gas, fuel consumption is reduced compared to conventional biodiesel.	[68]
CO, HC and smoke	NO <sub>x</sub>	With the blend of diesel and Jatropha oil as biodiesel, an increase in BTE was observed when adding 10% hydrogen H <sub>2</sub> to the blend.	[66]
NO <sub>x</sub>	-	Stable engine performance was achieved with a blend of 20% biodiesel and 80% diesel, along with an additional 10% hydrogen H <sub>2</sub> .	[69]
CO, HC and smoke	-	With the blend of waste cooking oil (WCO) emulsified with H <sub>2</sub> as the primary fuel, superior thermal efficiency is achieved even at high power levels.	[70]
CH <sub>4</sub>	-	Emissions were reduced by blending 20% H <sub>2</sub> with biodiesel.	[71]

### 8. Biodiesel and antioxidants blend

Several studies have indicated that the addition of antioxidants reduces emissions. Among the phenolic antioxidants, TBHQ, BHA, and BHT are commonly used to control fuel degradation and improve biodiesel storage. These antioxidants help reduce NO<sub>x</sub> emissions but may increase smoke, CO, and HC emissions [72].

Rashedul *et al.* [73] analyzed the effect of the antioxidant BHT in combination with Callophyllum biodiesel and found that BHT improves fuel stability, reducing NO<sub>x</sub> emissions. Additionally, it increased braking power, achieved higher thermal efficiency (BTE), and reduced specific fuel consumption (BSFC). On the other hand, Ryu [74] conducted a comparative study of antioxidants using soybean oil biodiesel. It concluded that the effectiveness of antioxidants follows the order TBHQ > PrG > BHA > BHT > alpha-tocopherol. The study also revealed that using these antioxidants leads to a decrease in specific fuel consumption. However, commercial antioxidant additives are often expensive and produced from non-renewable materials, which has motivated the search for new low-cost alternative additives obtained from biomass or waste sources [75].

### 9. Nanoparticles in biodiesel

Adding nanoparticles to biodiesel improves its thermophysical properties, such as conductivity, mass dif-

fusivity, surface-to-volume ratio, and physicochemical properties like kinematic viscosity, flash point, and pour point, among others [76].

Table 10 presents the engine performance with the mixture of nanoparticles and biodiesel. Carbon nanotubes (CNTs) have the potential to be used as additives in dual combustion to enhance the fuel and achieve improved results in terms of BSFC, BTE, and NO<sub>x</sub> emissions. However, the issue of the lack of stability in the CNT mixture can be addressed by applying a fuel stabilizer or surfactant [77]. Table 11 shows the engine behavior with the blend of biodiesel and CNTs.

Mirzajanzadeh *et al.* [78] provide a detailed explanation of the use of nanoparticles. They synthesized a soluble hybrid nanocatalyst to improve engine performance. They added a compound of cerium oxide and multi-walled carbon nanotubes functionalized with amide groups to the blend of diesel and biodiesel. The results showed a reduction in CO, HC, NO<sub>x</sub>, and soot emissions. Additionally, an improvement in engine performance and a decrease in fuel consumption were observed. However, caution must be exercised in using cerium oxide nanoparticles due to health risks such as cytotoxicity induction, oxidative stress, and lung inflammation [79]. Therefore, their use should be controlled. Replacing metal-based nanoparticles with non-metallic nanoparticles may be necessary as they are less toxic [80].

**Table 10.** Analysis of nanoparticles applied in biodiesel

Emission reduction	Type of nanoparticles	Engine performance	Ref.
CO and HC	TiO <sub>2</sub>	In the blend of biodiesel (20%) and the remaining diesel with TiO <sub>2</sub> , a decrease in BSFC and an improvement in BTE were observed. However, an increase in CO <sub>2</sub> and NO <sub>x</sub> emissions was also observed.	[81]
CO, CO <sub>2</sub> and NO <sub>x</sub>	Titanium nanoparticles	Adding titanium nanoparticles to the biodiesel blend reduces the BSFC, improves combustion and increases the BTE.	[82]
CO and HC	Nanometallic oxides	The blend of mahua oil biodiesel with nanoparticles in a CRDI engine reduces emissions.	[83]
NO <sub>x</sub> , HC and smoke	Cerium oxides	The blend of 70% diesel, 10% castor oil biodiesel, and 20% ethanol, along with an addition of 25 ppm of cerium oxide, reduced the heat release rate and, consequently, the emissions.	[84]
CO and HC	Alumina nanoparticles	The blend of biodiesel with ethanol and alumina increased exhaust gas temperature and BTE, but it also caused an increase in NO <sub>x</sub> emissions.	[85]
CO and NO <sub>x</sub>	MgO and SiO <sub>2</sub>	With the addition of nanoparticles to biodiesel, an improvement in engine performance and a reduction in emissions were observed.	[86]
HC, CO and NO <sub>x</sub>	Cobalt oxide Co <sub>3</sub> O <sub>4</sub>	The addition of CoO <sub>4</sub> to Jatropha oil biodiesel improved combustion and reduced emissions by 75% during an engine load operation.	[87]
-	Copper oxide	Blending copper oxide (50 ppm) with 20% Mahua oil biodiesel and the rest diesel reduced incomplete combustion, improved BTE, and facilitated cold starting.	[88]

**Table 11.** Engine performance and emissions with the blend of biodiesel and applied carbon nanotubes (CNTs)

Emission reduction	Engine performance	Ref.
CO, HC and NO <sub>x</sub>	A CNT blend was applied with a Jatropha methyl ester emulsion, resulting in an increase in BTE compared to pure biodiesel.	[89]
NO <sub>x</sub>	The blend of biodiesel and CNTs increased the BTE.	[90]
CO, HC and soot	The blend of biodiesel and CNT (5% and 20%, respectively) improved the BTE and reduced the BSFC.	[76]
NO <sub>x</sub>	The blend of biodiesel (neem oil methyl ester) with CNT increased the BTE, and due to the higher cetane number, the ignition delay was reduced, thereby improving combustion.	[91]
Soot	The combination of CNT, cerium oxide nanoparticles, and diesterol resulted in a highly efficient blend for combustion and a significant increase in engine performance.	[92]

A new alternative consists of using organic nanoparticles, such as coconut shells, which can be mixed with biodiesel and applied in diesel engines [93]. Table 12

presents the technical characteristics of the biodiesel ratio.

**Table 12.** Technical characteristics of biodiesel with nanoparticles

Properties	Biodiesel + nanoparticles				
	Algae oil + TiO <sub>2</sub> -SiO <sub>2</sub> 50	Mahua oil + ANP50	Soybean oil + alumina	Neem oil + CNT100	Jatropha oil + 100 CNT
Density (kg/m <sup>3</sup> )	817	827.5	-	889	899.4
Kinematic viscosity at a 40 °C (cSt)	3.03	3.37	3.37	4.28	5.76
Flashpoint °C	62.45	-	-	181	125
Cetane number	48	49.5	52	53	55
Calorific value (kJ/kg)	42,600	41,665	42,590	40,920	37,350
Reference	[81]	[83]	[85]	[91]	[89]

## 10. Conclusions

Due to the high production cost of biodiesel and some unfavorable properties, such as its low calorific value, high viscosity, and density compared to conventional diesel, it is crucial to implement strategies to increase its attractiveness. We have concluded that there are two promising alternatives for its future application. The first one is to find an appropriate blend that justifies the commercial use of biodiesel by optimizing its properties and performance. The second option is to use biodiesel as a component in fuel blends, using a proportion of 10% to 20% relative to the total fuel in the engine. This would allow for the application and promotion of other types of biofuels, such as gaseous fuels in dual-fuel diesel engines, opening new possibilities and contributing to greater sustainability in the transportation sector.

## References

- [1] G. T. Kalghatgi, "The outlook for fuels for internal combustion engines," *International Journal of Engine Research*, vol. 15, no. 4, pp. 383–398, 2014. [Online]. Available: <https://doi.org/10.1177/1468087414526189>
- [2] G. Kalghatgi, "Developments in internal combustion engines and implications for combustion science and future transport fuels," *Proceedings of the Combustion Institute*, vol. 35, no. 1, pp. 101–115, 2015. [Online]. Available: <https://doi.org/10.1016/j.proci.2014.10.002>
- [3] F. Barraaj and Y. Attalah, "Composite sustainable indicators framework for cost assessment of land transport mode in lebanon cities," *Journal of Transportation Technologies*, vol. 8, pp. 232–253, 2018. [Online]. Available: <https://doi.org/10.4236/jtts.2018.83013>
- [4] H. Rashedul, H. Masjuki, M. Kalam, A. Ashraful, S. Ashrafur Rahman, and S. Shahir, "The effect of additives on properties, performance and emission of biodiesel fuelled compression ignition engine," *Energy Conversion and Management*, vol. 88, pp. 348–364, 2014. [Online]. Available: <https://doi.org/10.1016/j.enconman.2014.08.034>
- [5] O. M. Ali, R. Mamat, N. R. Abdullah, and A. A. Abdullah, "Analysis of blended fuel properties and engine performance with palm biodiesel–diesel blended fuel," *Renewable Energy*, vol. 86, pp. 59–67, 2016. [Online]. Available: <https://doi.org/10.1016/j.renene.2015.07.103>
- [6] G. Knothe, "Biodiesel and renewable diesel: A comparison," *Progress in Energy and Combustion Science*, vol. 36, no. 3, pp. 364–373, 2010. [Online]. Available: <https://doi.org/10.1016/j.peccs.2009.11.004>
- [7] M. Canakci and M. Hosoz, "Energy and exergy analyses of a diesel engine fuelled with various biodiesels," *Energy Sources, Part B: Economics, Planning, and Policy*, vol. 1, no. 4, pp. 379–394, 2006. [Online]. Available: <https://doi.org/10.1080/15567240500400796>

- [8] S. Chandra Sekhar, K. Karuppasamy, N. Vedaraman, A. Kabeel, R. Sathyamurthy, M. Elkelawy, and H. Alm ELDin Bastawissi, "Biodiesel production process optimization from pithecellobium dulce seed oil: Performance, combustion, and emission analysis on compression ignition engine fuelled with diesel/biodiesel blends," *Energy Conversion and Management*, vol. 161, pp. 141–154, 2018. [Online]. Available: <https://doi.org/10.1016/j.enconman.2018.01.074>
- [9] K. Purushothaman and G. Nagarajan, "Performance, emission and combustion characteristics of a compression ignition engine operating on neat orange oil," *Renewable Energy*, vol. 34, no. 1, pp. 242–245, 2009. [Online]. Available: <https://doi.org/10.1016/j.renene.2008.03.012>
- [10] M. Xie, Z. J. Ma, Q. H. Wang, and J. Liu, "Investigation of engine combustion and emission performance fuelled with neat ponde and ponde/diesel blend," *Journal of Xi'an Jiaotong University*, vol. 51, no. 3, pp. 32–37, 2017. [Online]. Available: <https://doi.org/10.7652/xjtuxb201703006>
- [11] M. H. M. Yasin, R. Mamat, A. F. Yusop, P. Paruka, T. Yusaf, and G. Najafi, "Effects of exhaust gas recirculation (EGR) on a diesel engine fuelled with palm-biodiesel," *Energy Procedia*, vol. 75, pp. 30–36, 2015, clean, Efficient and Affordable Energy for a Sustainable Future: The 7th International Conference on Applied Energy (ICAE2015). [Online]. Available: <https://doi.org/10.1016/j.egypro.2015.07.131>
- [12] K. Venkateswarlu, K. V. Kumar, B. S. R. Murthy, and V. V. Subbarao, "Effect of exhaust gas recirculation and ethyl hexyl nitrate additive on biodiesel fuelled diesel engine for the reduction of noxemissions," *Frontiers in Energy*, vol. 6, no. 3, pp. 304–310, Sep 2012. [Online]. Available: <https://doi.org/10.1007/s11708-012-0195-9>
- [13] H. Raheman and S. Ghadge, "Performance of compression ignition engine with mahua (*madhuca indica*) biodiesel," *Fuel*, vol. 86, no. 16, pp. 2568–2573, 2007. [Online]. Available: <https://doi.org/10.1016/j.fuel.2007.02.019>
- [14] R. Vallinayagam, S. Vedharaj, W. Yang, P. Lee, K. Chua, and S. Chou, "Pine oil-biodiesel blends: A double biofuel strategy to completely eliminate the use of diesel in a diesel engine," *Applied Energy*, vol. 130, pp. 466–473, 2014. [Online]. Available: <https://doi.org/10.1016/j.apenergy.2013.11.025>
- [15] P. Singh, S. Chauhan, and V. Goel, "Assessment of diesel engine combustion, performance and emission characteristics fuelled with dual fuel blends," *Renewable Energy*, vol. 125, pp. 501–510, 2018. [Online]. Available: <https://doi.org/10.1016/j.renene.2018.02.105>
- [16] G. Kasiraman, B. Nagalingam, and M. Balakrishnan, "Performance, emission and combustion improvements in a direct injection diesel engine using cashew nut shell oil as fuel with camphor oil blending," *Energy*, vol. 47, no. 1, pp. 116–124, 2012, Asia-Pacific Forum on Renewable Energy 2011. [Online]. Available: <https://doi.org/10.1016/j.energy.2012.09.022>
- [17] P. Dubey and R. Gupta, "Effects of dual bio-fuel (jatropha biodiesel and turpentine oil) on a single cylinder naturally aspirated diesel engine without egr," *Applied Thermal Engineering*, vol. 115, pp. 1137–1147, 2017. [Online]. Available: <https://doi.org/10.1016/j.applthermaleng.2016.12.125>
- [18] A. Sharma and S. Murugan, "Potential for using a tyre pyrolysis oil-biodiesel blend in a diesel engine at different compression ratios," *Energy Conversion and Management*, vol. 93, pp. 289–297, 2015. [Online]. Available: <https://doi.org/10.1016/j.enconman.2015.01.023>
- [19] Y. Liu, J. Li, and C. Jin, "Fuel spray and combustion characteristics of butanol blends in a constant volume combustion chamber," *Energy Conversion and Management*, vol. 105, pp. 1059–1069, 2015. [Online]. Available: <https://doi.org/10.1016/j.enconman.2015.08.047>
- [20] L. Zhu, C. Cheung, W. Zhang, and Z. Huang, "Combustion, performance and emission characteristics of a DI diesel engine fueled with ethanol-biodiesel blends," *Fuel*, vol. 90, no. 5, pp. 1743–1750, 2011. [Online]. Available: <https://doi.org/10.1016/j.fuel.2011.01.024>
- [21] G. Khoobakht, M. Karimi, and K. Kheiralipour, "Effects of biodiesel-ethanol-diesel blends on the performance indicators of a diesel engine: A study by response surface modeling," *Applied Thermal Engineering*, vol. 148, pp. 1385–1394, 2019. [Online]. Available: <https://doi.org/10.1016/j.applthermaleng.2018.08.025>
- [22] C. Zhan, Z. Feng, W. Ma, M. Zhang, C. Tang, and Z. Huang, "Experimental investigation on effect of ethanol and di-ethyl ether addition on the spray characteristics of diesel/biodiesel blends under high injection pressure," *Fuel*, vol. 218, pp. 1–11, 2018. [Online]. Available: <https://doi.org/10.1016/j.fuel.2017.12.038>
- [23] H. Imdadul, H. Masjuki, M. Kalam, N. Zulkifli, A. Alabdulkarem, M. Kamruzzaman, and M. Rashed, "A comparative study of C4 and C5 alcohol treated diesel-biodiesel blends in terms of

- diesel engine performance and exhaust emission,” *Fuel*, vol. 179, pp. 281–288, 2016. [Online]. Available: <https://doi.org/10.1016/j.fuel.2016.04.003>
- [24] H. Venu and V. Madhavan, “Effect of  $Al_2O_3$  nanoparticles in biodiesel-diesel-ethanol blends at various injection strategies: Performance, combustion and emission characteristics,” *Fuel*, vol. 186, pp. 176–189, 2016. [Online]. Available: <https://doi.org/10.1016/j.fuel.2016.08.046>
- [25] H. Aydin and C. İlkılıç, “Effect of ethanol blending with biodiesel on engine performance and exhaust emissions in a CI engine,” *Applied Thermal Engineering*, vol. 30, no. 10, pp. 1199–1204, 2010. [Online]. Available: <https://doi.org/10.1016/j.applthermaleng.2010.01.037>
- [26] B. J. Bora and U. K. Saha, “Comparative assessment of a biogas run dual fuel diesel engine with rice bran oil methyl ester, pongamia oil methyl ester and palm oil methyl ester as pilot fuels,” *Renewable Energy*, vol. 81, pp. 490–498, 2015. [Online]. Available: <https://doi.org/10.1016/j.renene.2015.03.019>
- [27] M. Zaharin, N. Abdullah, G. Najafi, H. Sharudin, and T. Yusaf, “Effects of physicochemical properties of biodiesel fuel blends with alcohol on diesel engine performance and exhaust emissions: A review,” *Renewable and Sustainable Energy Reviews*, vol. 79, pp. 475–493, 2017. [Online]. Available: <https://doi.org/10.1016/j.rser.2017.05.035>
- [28] Y. Noorollahi, M. Azadbakht, and B. Ghobadian, “The effect of different diesterol (diesel–biodiesel–ethanol) blends on small air-cooled diesel engine performance and its exhaust gases,” *Energy*, vol. 142, pp. 196–200, 2018. [Online]. Available: <https://doi.org/10.1016/j.energy.2017.10.024>
- [29] L. Wei, C. Cheung, and Z. Ning, “Effects of biodiesel-ethanol and biodiesel-butanol blends on the combustion, performance and emissions of a diesel engine,” *Energy*, vol. 155, pp. 957–970, 2018. [Online]. Available: <https://doi.org/10.1016/j.energy.2018.05.049>
- [30] F. Aydın and H. Ögüt, “Effects of using ethanol-biodiesel-diesel fuel in single cylinder diesel engine to engine performance and emissions,” *Renewable Energy*, vol. 103, pp. 688–694, 2017. [Online]. Available: <https://doi.org/10.1016/j.renene.2016.10.083>
- [31] M. Parthasarathy, J. Isaac Joshua Ramesh Lalvani, B. Dhinesh, and K. Annamalai, “Effect of hydrogen on ethanol–biodiesel blend on performance and emission characteristics of a direct injection diesel engine,” *Ecotoxicology and Environmental Safety*, vol. 134, pp. 433–439, 2016, Green Technologies for Environmental Pollution Control and Prevention (Part 2). [Online]. Available: <https://doi.org/10.1016/j.ecoenv.2015.11.005>
- [32] T. Shudo, A. Fujibe, M. Kazahaya, Y. Aoyagi, I. Hajime, Y. Goto, and A. Noda, “The cold flow performance and the combustion characteristics with ethanol blended biodiesel fuel,” in *Powertrain & Fluid Systems Conference & Exhibition*. SAE International, oct 2005. [Online]. Available: <https://doi.org/10.4271/2005-01-3707>
- [33] A. Paul, R. Panua, and D. Debroy, “An experimental study of combustion, performance, exergy and emission characteristics of a ci engine fueled by diesel-ethanol-biodiesel blends,” *Energy*, vol. 141, pp. 839–852, 2017. [Online]. Available: <https://doi.org/10.1016/j.energy.2017.09.137>
- [34] D. B. Hulwan and S. V. Joshi, “Performance, emission and combustion characteristic of a multicylinder DI diesel engine running on diesel–ethanol–biodiesel blends of high ethanol content,” *Applied Energy*, vol. 88, no. 12, pp. 5042–5055, 2011. [Online]. Available: <https://doi.org/10.1016/j.apenergy.2011.07.008>
- [35] Z.-H. Zhang and R. Balasubramanian, “Investigation of particulate emission characteristics of a diesel engine fueled with higher alcohols/biodiesel blends,” *Applied Energy*, vol. 163, pp. 71–80, 2016. [Online]. Available: <https://doi.org/10.1016/j.apenergy.2015.10.173>
- [36] V. Soloiu, M. Duggan, H. Ochieng, S. Harp, J. Weaver, C. Jenkins, and B. Vlcek, “Premixed charge of n-butanol coupled with direct injection of biodiesel for an advantageous Soot- $NO_x$  trade-off,” in *SAE 2013 World Congress & Exhibition*. SAE International, apr 2013. [Online]. Available: <https://doi.org/10.4271/2013-01-0916>
- [37] J. Hou, Z. Wen, Z. Jiang, and X. Qiao, “Study on combustion and emissions of a turbocharged compression ignition engine fueled with dimethyl ether and biodiesel blends,” *Journal of the Energy Institute*, vol. 87, no. 2, pp. 102–113, 2014. [Online]. Available: <https://doi.org/10.1016/j.joei.2014.03.021>
- [38] K. Yang, L. Wei, C. Cheung, C. Tang, and Z. Huang, “The effect of pentanol addition on the particulate emission characteristics of a biodiesel operated diesel engine,” *Fuel*, vol. 209, pp. 132–140, 2017. [Online]. Available: <https://doi.org/10.1016/j.fuel.2017.07.093>

- [39] R. Sridhar, J. Jeevahan, and M. Chandrasekaran, "Effect of the addition of 1-pentanol on engine performance and emission characteristics of diesel and biodiesel fuelled single cylinder diesel engine," *International Journal of Ambient Energy*, vol. 41, no. 1, pp. 58–63, 2020. [Online]. Available: <https://doi.org/10.1080/01430750.2018.1443505>
- [40] V. Sriram, J. Jeevahan, G. Mageshwaran, G. B. Joseph, and R. B. Durairaj, "Engine performance and emission characteristics of 1-octanol blended bio-diesel in a single cylinder diesel engine," *International Journal of Mechanical and Production*, vol. 7, no. 6, pp. 623–630, 2017. [Online]. Available: <https://doi.org/10.24247/ijmperddc201770>
- [41] N. Yilmaz, A. Atmanli, and F. M. Vigil, "Quaternary blends of diesel, biodiesel, higher alcohols and vegetable oil in a compression ignition engine," *Fuel*, vol. 212, pp. 462–469, 2018. [Online]. Available: <https://doi.org/10.1016/j.fuel.2017.10.050>
- [42] D. Babu and R. Anand, "Effect of biodiesel-diesel-n-pentanol and biodiesel-diesel-n-hexanol blends on diesel engine emission and combustion characteristics," *Energy*, vol. 133, pp. 761–776, 2017. [Online]. Available: <https://doi.org/10.1016/j.energy.2017.05.103>
- [43] D. Barik and S. Murugan, "Effects of diethyl ether (DEE) injection on combustion performance and emission characteristics of karanja methyl ester (kme)–biogas fueled dual fuel diesel engine," *Fuel*, vol. 164, pp. 286–296, 2016. [Online]. Available: <https://doi.org/10.1016/j.fuel.2015.09.094>
- [44] M. Vinod Babu, K. Madhu Murthy, and R. G. Amba Prasad, "Butanol and pentanol: The promising biofuels for CI engines – a review," *Renewable and Sustainable Energy Reviews*, vol. 78, pp. 1068–1088, 2017. [Online]. Available: <https://doi.org/10.1016/j.rser.2017.05.038>
- [45] B. Sahoo, "Clean development mechanism potential of compression ignition diesel engines using gaseous fuels in dual fuel mode," Ph.D. dissertation, Indian Institute of Technology Guwahati, 2011. [Online]. Available: <https://bit.ly/3oGiWJA>
- [46] C. Luijten and E. Kerkhof, "Jatropha oil and biogas in a dual fuel CI engine for rural electrification," *Energy Conversion and Management*, vol. 52, no. 2, pp. 1426–1438, 2011. [Online]. Available: <https://doi.org/10.1016/j.enconman.2010.10.005>
- [47] A. Hasannuddin, J. Wira, S. Sarah, M. Ahmad, S. Aizam, M. Aiman, S. Watanabe, N. Hirofumi, and M. Azrin, "Durability studies of single cylinder diesel engine running on emulsion fuel," *Energy*, vol. 94, pp. 557–568, 2016. [Online]. Available: <https://doi.org/10.1016/j.energy.2015.10.144>
- [48] K. Ramalingam, A. Kandasamy, L. Subramani, D. Balasubramanian, and J. Paul James Thadhani, "An assessment of combustion, performance characteristics and emission control strategy by adding anti-oxidant additive in emulsified fuel," *Atmospheric Pollution Research*, vol. 9, no. 5, pp. 959–967, 2018. [Online]. Available: <https://doi.org/10.1016/j.apr.2018.02.007>
- [49] A. Hasannuddin, J. Wira, S. Sarah, W. Wan Syaidatul Aqma, A. Abdul Hadi, N. Hirofumi, S. Aizam, M. Aiman, S. Watanabe, M. Ahmad, and M. Azrin, "Performance, emissions and lubricant oil analysis of diesel engine running on emulsion fuel," *Energy Conversion and Management*, vol. 117, pp. 548–557, 2016. [Online]. Available: <https://doi.org/10.1016/j.enconman.2016.03.057>
- [50] M. Abedin, A. Imran, H. Masjuki, M. Kalam, S. Shahir, M. Varman, and A. Ruhul, "An overview on comparative engine performance and emission characteristics of different techniques involved in diesel engine as dual-fuel engine operation," *Renewable and Sustainable Energy Reviews*, vol. 60, pp. 306–316, 2016. [Online]. Available: <https://doi.org/10.1016/j.rser.2016.01.118>
- [51] S. H. Yoon and C. S. Lee, "Experimental investigation on the combustion and exhaust emission characteristics of bio-gas–biodiesel dual-fuel combustion in a ci engine," *Fuel Processing Technology*, vol. 92, no. 5, pp. 992–1000, 2011. [Online]. Available: <https://doi.org/10.1016/j.fuproc.2010.12.021>
- [52] X. Yuan, X. Ding, L. Leng, H. Li, J. Shao, Y. Qian, H. Huang, X. Chen, and G. Zeng, "Applications of bio-oil-based emulsions in a DI diesel engine: The effects of bio-oil compositions on engine performance and emissions," *Energy*, vol. 154, pp. 110–118, 2018. [Online]. Available: <https://doi.org/10.1016/j.energy.2018.04.118>
- [53] G. Kannan and R. Anand, "Experimental investigation on diesel engine with diesel–water micro emulsions," *Energy*, vol. 36, no. 3, pp. 1680–1687, 2011. [Online]. Available: <https://doi.org/10.1016/j.energy.2010.12.062>
- [54] A. B. Koc and M. Abdullah, "Performance and NOx emissions of a diesel engine fueled with biodiesel-diesel-water nanoemulsions," *Fuel Processing Technology*, vol. 109, pp. 70–77, may 2013. [Online]. Available: <https://doi.org/10.1016/j.fuproc.2012.09.039>

- [55] A. Sarvi, C.-J. Fogelholm, and R. Zevenhoven, "Emissions from large-scale medium-speed diesel engines: 1. influence of engine operation mode and turbocharger," *Fuel Processing Technology*, vol. 89, no. 5, pp. 510–519, 2008. [Online]. Available: <https://doi.org/10.1016/j.fuproc.2007.10.006>
- [56] R. Prakash, R. Singh, and S. Murugan, "Experimental investigation on a diesel engine fueled with bio-oil derived from waste wood–biodiesel emulsions," *Energy*, vol. 55, pp. 610–618, 2013. [Online]. Available: <https://doi.org/10.1016/j.energy.2013.03.085>
- [57] —, "Experimental studies on combustion, performance and emission characteristics of diesel engine using different biodiesel bio oil emulsions," *Journal of the Energy Institute*, vol. 88, no. 1, pp. 64–75, 2015. [Online]. Available: <https://doi.org/10.1016/j.joei.2014.04.005>
- [58] A. Paul, R. S. Panua, D. Debroy, and P. K. Bose, "Effect of compressed natural gas dual fuel operation with diesel and pongamia pin-nata methyl ester (PPME) as pilot fuels on performance and emission characteristics of a CI (compression ignition) engine," *Energy*, vol. 68, pp. 495–509, 2014. [Online]. Available: <https://doi.org/10.1016/j.energy.2014.03.026>
- [59] L. Tarabet, M. Lounici, K. Loubar, K. Khiari, R. Bouguessa, and M. Tazerout, "Hydrogen supplemented natural gas effect on a DI diesel engine operating under dual fuel mode with a biodiesel pilot fuel," *International Journal of Hydrogen Energy*, vol. 43, no. 11, pp. 5961–5971, 2018. [Online]. Available: <https://doi.org/10.1016/j.ijhydene.2017.09.045>
- [60] K. Ryu, "Effects of pilot injection pressure on the combustion and emissions characteristics in a diesel engine using biodiesel–CNG dual fuel," *Energy Conversion and Management*, vol. 76, pp. 506–516, 2013. [Online]. Available: <https://doi.org/10.1016/j.enconman.2013.07.085>
- [61] R. Senthilraja, V. Sivakumar, K. Thirugnanasambandham, and N. Nedunchezian, "Performance, emission and combustion characteristics of a dual fuel engine with diesel–ethanol – cotton seed oil methyl ester blends and compressed natural gas (CNG) as fuel," *Energy*, vol. 112, pp. 899–907, 2016. [Online]. Available: <https://doi.org/10.1016/j.energy.2016.06.114>
- [62] S. S. Kalsi and K. Subramanian, "Experimental investigations of effects of hydrogen blended CNG on performance, combustion and emissions characteristics of a biodiesel fueled reactivity controlled compression ignition engine (RCCI)," *International Journal of Hydrogen Energy*, vol. 42, no. 7, pp. 4548–4560, 2017. [Online]. Available: <https://doi.org/10.1016/j.ijhydene.2016.12.147>
- [63] V. Chintala and K. Subramanian, "A comprehensive review on utilization of hydrogen in a compression ignition engine under dual fuel mode," *Renewable and Sustainable Energy Reviews*, vol. 70, pp. 472–491, 2017. [Online]. Available: <https://doi.org/10.1016/j.rser.2016.11.24788>
- [64] E. Uludamar, Şafak Yıldızhan, K. Aydın, and M. Özcanlı, "Vibration, noise and exhaust emissions analyses of an unmodified compression ignition engine fuelled with low sulphur diesel and biodiesel blends with hydrogen addition," *International Journal of Hydrogen Energy*, vol. 41, no. 26, pp. 11 481–11 490, 2016. [Online]. Available: <https://doi.org/10.1016/j.ijhydene.2016.03.179>
- [65] T. Korakianitis, A. Namasivayam, and R. Crookes, "Hydrogen dual-fuelling of compression ignition engines with emulsified biodiesel as pilot fuel," *International Journal of Hydrogen Energy*, vol. 35, no. 24, pp. 13 329–13 344, 2010, 3rd Asian Bio Hydrogen Symposium. [Online]. Available: <https://doi.org/10.1016/j.ijhydene.2010.08.007>
- [66] M. Senthil Kumar, A. Ramesh, and B. Nagalingam, "Use of hydrogen to enhance the performance of a vegetable oil fuelled compression ignition engine," *International Journal of Hydrogen Energy*, vol. 28, no. 10, pp. 1143–1154, 2003. [Online]. Available: [https://doi.org/10.1016/S0360-3199\(02\)00234-3](https://doi.org/10.1016/S0360-3199(02)00234-3)
- [67] M. O. Hamdan and M. Y. Selim, "Performance of CI engine operating with hydrogen supplement co-combustion with jojoba methyl ester," *International Journal of Hydrogen Energy*, vol. 41, no. 24, pp. 10 255–10 264, 2016. [Online]. Available: <https://doi.org/10.1016/j.ijhydene.2016.04.168>
- [68] H. Masjuki, A. Ruhul, N. N. Mustafi, M. Kalam, M. Arbab, and I. Rizwanul Fattah, "Study of production optimization and effect of hydroxyl gas on a CI engine performance and emission fueled with biodiesel blends," *International Journal of Hydrogen Energy*, vol. 41, no. 33, pp. 14 519–14 528, 2016. [Online]. Available: <https://doi.org/10.1016/j.ijhydene.2016.05.273>
- [69] M. G. Shirk, T. P. McGuire, G. L. Neal, and D. C. Haworth, "Investigation of a hydrogen-assisted combustion system for a light-duty diesel vehicle," *International Journal of Hydrogen Energy*, vol. 33, no. 23, pp. 7237–7244, 2008. [Online]. Available: <https://doi.org/10.1016/j.ijhydene.2008.07.128>

- [70] M. Senthil Kumar and M. Jaikummar, "Studies on the effect of hydrogen induction on performance, emission and combustion behaviour of a WCO emulsion based dual fuel engine," *International Journal of Hydrogen Energy*, vol. 39, no. 32, pp. 18 440–18 450, 2014. [Online]. Available: <https://doi.org/10.1016/j.ijhydene.2014.08.124>
- [71] K. A. Subramanian and V. Chintala, "Reduction of GHGs emissions in a biodiesel fueled diesel engine using hydrogen," Oct 2013, volume 2: Fuels; Numerical Simulation; Engine Design, Lubrication, and Applications. [Online]. Available: <https://doi.org/10.1115/ICEF2013-19133>
- [72] K. Varatharajan and M. Cheralathan, "Effect of aromatic amine antioxidants on NO<sub>x</sub> emissions from a soybean biodiesel powered DI diesel engine," *Fuel Processing Technology*, vol. 106, pp. 526–532, 2013. [Online]. Available: <https://doi.org/10.1016/j.fuproc.2012.09.023>
- [73] H. Rashedul, H. Masjuki, M. Kalam, Y. Teoh, H. How, and I. Rizwanul Fattah, "Effect of antioxidant on the oxidation stability and combustion–performance–emission characteristics of a diesel engine fuelled with diesel–biodiesel blend," *Energy Conversion and Management*, vol. 106, pp. 849–858, 2015. [Online]. Available: <https://doi.org/10.1016/j.enconman.2015.10.024>
- [74] K. Ryu, "The characteristics of performance and exhaust emissions of a diesel engine using a biodiesel with antioxidants," *Biore-source Technology*, vol. 101, no. 1, Supplement, pp. S78–S82, 2010, Supplement Issue on Recent Developments of Biomass Conversion Technologies. [Online]. Available: <https://doi.org/10.1016/j.biortech.2009.05.034>
- [75] C. Dueso, M. Muñoz, F. Moreno, J. Arroyo, N. Gil-Lalaguna, A. Bautista, A. Gonzalo, and J. L. Sánchez, "Performance and emissions of a diesel engine using sunflower biodiesel with a renewable antioxidant additive from bio-oil," *Fuel*, vol. 234, pp. 276–285, 2018. [Online]. Available: <https://doi.org/10.1016/j.fuel.2018.07.013>
- [76] S. H. Hosseini, A. Taghizadeh-Alisaraei, B. Ghobadian, and A. Abbaszadeh-Mayvan, "Performance and emission characteristics of a ci engine fuelled with carbon nanotubes and diesel-biodiesel blends," *Renewable Energy*, vol. 111, pp. 201–213, 2017. [Online]. Available: <https://doi.org/10.1016/j.renene.2017.04.013>
- [77] A. F. Chen, M. Akmal Adzmi, A. Adam, M. F. Othman, M. K. Kamaruzzaman, and A. G. Mrwan, "Combustion characteristics, engine performances and emissions of a diesel engine using nanoparticle-diesel fuel blends with aluminium oxide, carbon nanotubes and silicon oxide," *Energy Conversion and Management*, vol. 171, pp. 461–477, 2018. [Online]. Available: <https://doi.org/10.1016/j.enconman.2018.06.004>
- [78] M. Mirzajanzadeh, M. Tabatabaei, M. Ardjmand, A. Rashidi, B. Ghobadian, M. Barkhi, and M. Pazouki, "A novel soluble nano-catalysts in diesel–biodiesel fuel blends to improve diesel engines performance and reduce exhaust emissions," *Fuel*, vol. 139, pp. 374–382, 2015. [Online]. Available: <https://doi.org/10.1016/j.fuel.2014.09.008>
- [79] A. Srinivas, P. J. Rao, G. Selvam, P. B. Murthy, and P. N. Reddy, "Acute inhalation toxicity of cerium oxide nanoparticles in rats," *Toxicology Letters*, vol. 205, no. 2, pp. 105–115, 2011. [Online]. Available: <https://doi.org/10.1016/j.toxlet.2011.05.1027>
- [80] S. Hoseini, G. Najafi, B. Ghobadian, R. Mamat, M. Ebadi, and T. Yusaf, "Novel environmentally friendly fuel: The effects of nanographene oxide additives on the performance and emission characteristics of diesel engines fuelled with ailanthus altissima biodiesel," *Renewable Energy*, vol. 125, pp. 283–294, 2018. [Online]. Available: <https://doi.org/10.1016/j.renene.2018.02.104>
- [81] S. Karthikeyan and A. Prathima, "Environmental effect of ci engine using microalgae methyl ester with doped nano additives," *Transportation Research Part D: Transport and Environment*, vol. 50, pp. 385–396, 2017. [Online]. Available: <https://doi.org/10.1016/j.trd.2016.11.028>
- [82] R. D'Silva, K. Binu, and T. Bhat, "Performance and emission characteristics of a C.I. engine fuelled with diesel and TiO<sub>2</sub> nanoparticles as fuel additive," *Materials Today: Proceedings*, vol. 2, no. 4, pp. 3728–3735, 2015, 4th International Conference on Materials Processing and Characterization. [Online]. Available: <https://doi.org/10.1016/j.matpr.2015.07.162>
- [83] C. S. Aalam and C. Saravanan, "Effects of nano metal oxide blended mahua biodiesel on CRDI diesel engine," *Ain Shams Engineering Journal*, vol. 8, no. 4, pp. 689–696, 2017. [Online]. Available: <https://doi.org/10.1016/j.asej.2015.09.013>
- [84] V. Arul, A. Selvan V, A. r b, and M. Udayakumar, "Effects of cerium oxide nanoparticle addition in diesel and diesel-biodiesel-ethanol blends on the performance and emission characteristics of a CI engine," *Journal of Engineering and Applied Sciences*, vol. 4, 09 2009. [Online]. Available: <https://bit.ly/3qgUUoW>

- [85] T. Shaafi and R. Velraj, "Influence of alumina nanoparticles, ethanol and isopropanol blend as additive with diesel-soybean biodiesel blend fuel: Combustion, engine performance and emissions," *Renewable Energy*, vol. 80, pp. 655–663, 2015. [Online]. Available: <https://doi.org/10.1016/j.renene.2015.02.042>
- [86] T. Özgür, M. Özcanli, and K. Aydin, "Investigation of nanoparticle additives to biodiesel for improvement of the performance and exhaust emissions in a compression ignition engine," *International Journal of Green Energy*, vol. 12, no. 1, pp. 51–56, 2015. [Online]. Available: <https://doi.org/10.1080/15435075.2014.889011>
- [87] D. Ganesh and G. Gowrishankar, "Effect of nano-fuel additive on emission reduction in a biodiesel fuelled CI engine," in *2011 International Conference on Electrical and Control Engineering*, 2011, pp. 3453–3459. [Online]. Available: <https://doi.org/10.1109/ICECENG.2011.6058240>
- [88] S. Senthur Prabu, M. Asokan, R. Roy, S. Francis, and M. Sreelekh, "Performance, combustion and emission characteristics of diesel engine fuelled with waste cooking oil biodiesel/diesel blends with additives," *Energy*, vol. 122, pp. 638–648, 2017. [Online]. Available: <https://doi.org/10.1016/j.energy.2017.01.119>
- [89] J. Sadhik Basha and R. Anand, "Performance, emission and combustion characteristics of a diesel engine using carbon nanotubes blended jatropha methyl ester emulsions," *Alexandria Engineering Journal*, vol. 53, no. 2, pp. 259–273, 2014. [Online]. Available: <https://doi.org/10.1016/j.aej.2014.04.001>
- [90] P. Tewari, E. Doijode, N. Banapurmath, and V. Yaliwal, "Experimental investigations on a diesel engine fuelled with multi-walled carbon nanotubes blended biodiesel fuels," *International Journal of Automotive Engineering and Technologies*, vol. 4, pp. 129–138, 2014. [Online]. Available: <https://doi.org/10.18245/ijaet.59113>
- [91] B. Gnanasikamani, "Effect of cnt as additive with biodiesel on the performance and emission characteristics of a DI diesel engine," *International Journal of ChemTech Research*, vol. 7, pp. 1230–1236, 02 2015. [Online]. Available: <https://bit.ly/43dFnF9>
- [92] V. Arul Mozhi Selvan, R. Anand, and M. Udayakumar, "Effect of cerium oxide nanoparticles and carbon nanotubes as fuel-borne additives in diesterol blends on the performance, combustion and emission characteristics of a variable compression ratio engine," *Fuel*, vol. 130, pp. 160–167, 2014. [Online]. Available: <https://doi.org/10.1016/j.fuel.2014.04.034>
- [93] K. Vinukumar, A. Azhagurajan, S. Vettivel, N. Vedaraman, and A. Haiter Lenin, "Biodiesel with nano additives from coconut shell for decreasing emissions in diesel engines," *Fuel*, vol. 222, pp. 180–184, 2018. [Online]. Available: <https://doi.org/10.1016/j.fuel.2018.02.129>



# METHODOLOGICAL PROPOSAL FOR DISTANCE PROTECTION IN TRANSMISSION LINES FOR INTEGRATION OF NON-CONVENTIONAL RENEWABLE ENERGIES

## PROPUESTA METODOLÓGICA PARA LA PROTECCIÓN DE DISTANCIA EN LÍNEAS DE TRANSMISIÓN ANTE LA INTEGRACIÓN DE ENERGÍAS RENOVABLES NO CONVENCIONALES

M. F. Velasco<sup>1,\*</sup> , Génesis Maliza Paladines<sup>1</sup> , Fernando Vaca-Urbano<sup>1</sup> 

Received: 25-01-2023, Received after review: 21-04-2023, Accepted: 18-05-2023, Published: 01-07-2023

### Abstract

This paper presents a methodology to set the distance protection (ANSI-21) in power systems that integrate nonconventional renewable energies (NCRE). The modified IEEE 9-bar New England system is used as a case study, with a wind farm comprising 33 2.5 MW wind turbines and control systems validated according to international standards, such as the IEC60909-2016. A fault resistance value calculated using the Warrington method is considered. The proposed settings are simulated using the Digsilent Power Factory® software and a Siemens 7SA522 relay with quadrilateral characteristics. The methodology uses voltage and current data from the instrumentation transformers to calculate the line impedance up to the fault point. The proposed adaptive method demonstrates positive performance under different shortcircuit scenarios, where the fault location, fault resistance, and power fluctuations of generating park are varied. This indicates that the relay effectively operates in the appropriate protection zone.

**Keywords:** Distance protection, adaptive relay, adaptive quadrilateral characteristic, wind farm, fault resistance, inverter-based sources.

### Resumen

Este artículo propone una metodología para ajustar la protección de distancia (ANSI-21) en sistemas de potencia que integran energías renovables no convencionales (ERNC). Se utiliza el sistema New England de 9 barras IEEE modificado como caso de estudio, con un parque eólico compuesto por 33 aerogeneradores de 2.5 MW y sistemas de control validados según estándares internacionales, como el IEC60909-2016. Se considera un valor de resistencia de falla calculado mediante el método de Warrington. Los ajustes propuestos se simulan utilizando el software Digsilent Power Factory® y un relé Siemens 7SA522 con características cuadrilaterales. La metodología se basa en el uso de datos de voltaje y corriente de los transformadores de instrumentación para calcular la impedancia de la línea hasta el punto de falla. El método adaptativo propuesto demuestra un rendimiento positivo en distintos escenarios de cortocircuito, donde varían el lugar de la falla, la resistencia de la misma y las fluctuaciones de potencia del parque generador. Esto demuestra que el relé actúa en la zona de protección adecuada de manera efectiva.

**Palabras clave:** Protección de distancia, característica cuadrilateral adaptativa, parque eólico, relé adaptativo, resistencia de falla, fuentes basadas en inversores

<sup>1,\*</sup>Facultad de Ingeniería en Electricidad y Computación, Escuela Superior Politécnica del Litoral, Guayaquil, Ecuador  
Corresponding author ✉: mfvelasc@espol.edu.ec.

Suggested citation: Velasco, M. F. ; Maliza Paladines, G. y Vaca-Urbano, F. "Methodological Proposal for Distance Protection in Transmission Lines for Integration of Non-conventional Renewable Energies," *Ingenius, Revista de Ciencia y Tecnología*, N.º 30, pp. 106-119, 2023, DOI: <https://doi.org/10.17163/ings.n30.2023.09>.

## 1. Introduction

The integration of nonconventional renewable energies (NCRE) may compromise the reach of the protection zones of distance relays [1], mainly due to the stochastic nature of their resources [2]. Therefore, it is necessary to consider the modification, analysis and redesign of the protections so that they can adapt to the fault current variation produced by renewable energies [3].

The distance relay calculates the apparent impedance to the fault point through measurements of voltage and current, and compares this value with the impedance setting to determine the actuation zone. The difference between the conventional plants and the sources based on inverters lays on the current contribution in a fault scenario. In general, a conventional plant contributes with a current 5 to 6 times the nominal current, in contrast with renewables sources whose fault current is between 1.1 to 2 times the nominal current [3]; therefore, the sequence components are different between these two types of sources. Due to this difference, various authors have proposed possible solutions to avoid the problems of underreach and overreach of the distance protection.

Another point that should be considered when calculating a shortcircuit scenario is the fault resistance, which may cause underreach problems in distance relays. To improve the performance of the protection in this situation, it is proposed the use of new algorithms that incorporate the fault resistance in synchronous generation sources to estimate the line impedance [4]. In addition, the Mho characteristic is used in [5] to set the protection zone and address the problems associated to the relay operation in photovoltaic plants.

On the other hand, a setting methodology using the quadrilateral characteristic is proposed in [6], which results in a change of the relay actuation limit during the variation of the measured impedance, due to the insertion of the fault resistance.

The contributions of this paper include:

- Detailed modeling of the NCRE to verify the fault current contributions seen by the protection relay
- Development of a setting method based on the calculation of shortcircuit phase currents at 80 %

and 20 % of the length of the main and adjacent lines. This mathematical expression enables the independent variation of the resistance and reactance in the R-X plane, which addresses the relay underreach problem by considering the fault resistance.

- The performance of the proposed methodology has been verified using data from simulations of different types of faults and variable generation of the wind farm.

The rest of this document is organized as follows. Section 2 presents the basic concepts of distance protection with quadrilateral characteristic for the integration of NCRE, and provides a brief description of the electric scheme to be studied and the effects of the fault resistance in a shortcircuit event. Section 3 details the proposed methodology, and the results that evaluate its performance in different situations are presented in section 3.2. The discussion of the proposed methodology is supported in section 3.3 and, finally, the conclusions of the paper are explained in section 4.

## 2. Materials and methods

### 2.1. Electric protections of a power system for the integration of NCRE

The faults in a power system may produce damage to its elements, and thus it is essential to minimize their effect by means of a protection system that makes it more reliable and secure [7]. Since the transmission line is the most vulnerable element of the system, it has a primary protection (distance relay). The operation principles and features of such protection are presented in this section [8].

### 2.2. Description of the system

The IEEE 9-bus New England system [9] of 230 kV at 60 Hz, shown in Figure 1, is considered as a case study. The system is divided into two sectors: sector 1 is constituted by the gray buses, while sector 2 comprises the black elements.

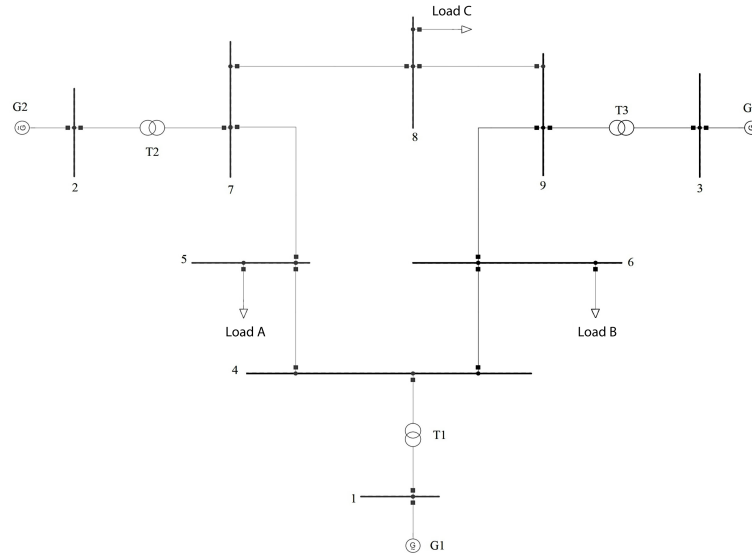


Figure 1. Case study: 9-bus IEEE system [9]

### 2.3. Equivalent circuit of the modified system

Sector 1 will be replaced by an equivalent circuit calculated using the REI (radial, equivalent and independent) method [10]. This method splits the system in active and passive sectors with the purpose of grouping the passive sectors to a common or equivalent bus,

which contains the values of three-phase and single-phase shortcircuit current and power at the common bus, as well as the constant of inertia of the system generators.

The characteristic parameters of the equivalent circuit connected to the system shown in Figure 2, are detailed in Table 1

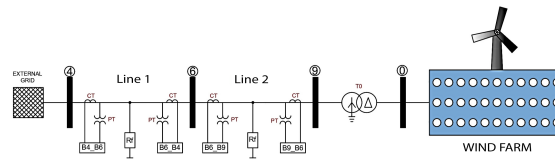


Figure 2. Equivalent circuit of the modified New England 9-bus system [9]

Table 1. Parameters of the equivalent circuit

External Grid	
Type of bus	Oscillation
Operating point	
Voltage magnitude ( $V_i$ )	1.025 [p.u.]
Bus angle ( $\delta_i$ )	147.783°
RMS data	
Constant of inertia ( $H_i$ )	5.892 [s]

To change the structure of the system, it is considered the insertion of a new bus (0) to integrate the wind farm constituted by 11 circuits, each with three 2.5 MW wind generators connected in parallel; this results in a total installed capacity of 82.5 MW for the farm.

The wind generators used belong to the Digsilent Power Factory® library; the wind generator is cou-

pled to the network through a voltage source converter (VSC) with a full-converter technology [11]. The input data of these controllers is detailed in Table 2.

For the subsequent analysis, the length of lines 1 and 2 is 100 km, and their electric parameters are shown in Table 3.

Table 2. Parameters of the full-converter wind generator

Current controller for EMT simulation	
Proportional gain d axis ( $k_d$ )	5
Integration time constant d axis ( $T_d$ )	0.01 [s]
Proportional gain q axis ( $k_q$ )	5
Integration time constant q axis time constant q axis ( $T_q$ )	0.01 [s]

**Table 3.** Electric parameters of the lines

Parameters	Line 1	Line 2
<i>Impedances</i> [ $\Omega/km$ ]		
Positive sequence $r_{1l} + jx_{1l} = r_{2l} + jx_{2l}$	0.2063 + j 0.8993	0.0899 + j 0.4887
Zero sequence $r_{0l} + jx_{0l}$	0.4126 + j 1.7980	0,1799 + j 0.9734
<i>Capacitances</i> [ $\mu F/km$ ]		
Positive sequence $C_{1l} = C_{2l}$	6.7675	2.9869
Zero sequence $C_{0l}$	3.3838	1.4935

The transformer has a nominal power of 150 MVA, 230/13.8 kV, YnD5 connection, the low voltage side leads the high voltage side by 150° and the shortcircuit reactance is 8.79 %.

### 2.4. Quadrilateral characteristic of the distance relay

The quadrilateral characteristic is more versatile within the distance protection, since it does not exhibit a reduction in its effective protection zone when there is fault resistance; the relay will operate correctly if the measured impedance is within the quadrilateral [12].

#### 2.4.1. Basic principle

The advantage of this type of relay is that the operation zone only depends on the impedance of the element to be protected, which practically remains constant, i.e., it does not depend on the voltage and current magnitudes [13] The quadrilateral characteristic is one of the most used methods. The horizontal axes of this protection depend only on the reactance “X”, while the vertical axes may be modified varying the resistance “R”. This is represented in the R-X plane (Figure 3), which results in a larger protection reach when inserting the fault resistance [14].

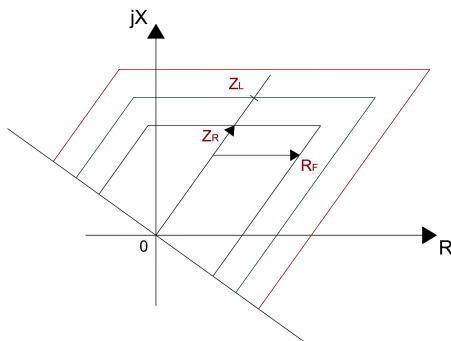


**Figure 3.** R-X diagram. Quadrilateral characteristic [14]

The quadrilateral characteristic operates if the impedance measured by the relay is within the posi-

tive and negative reactance of the right and left sides described in the previous figure.

Where:

- $Z_L$  = Line impedance
- $Z_R$  = Distance reach element
- $R_F$  = Setting of the resistive reach

#### 2.4.2. Relay protection zones

The protection of a transmission line cannot be implemented through a single zone because the instrumentation transformers must be very precise; backup protections are required [1]

The percentage assigned to every zone to be protected is analyzed according to the characteristic of the relay. In the case of the quadrilateral characteristic, the assignments operate as follows:

- Zone 1 is configured to protect between 80 % and 90 % of the line where the fault occurs. The response time of the relay is immediate,  $t_1 = 0$  seconds, because the distance protection should be activated before any other protection.
- On the other hand, zone 2 covers the entire line where the fault occurred plus 20 % of the adjacent line. The response time of the relay is  $t_2 = 0.4$  seconds.
- Zone 3 has a coordination time interval of  $t_3 = 0.8$  seconds, and is able to protect the entire line where the fault occurred plus the entire adjacent line [15].

#### 2.4.3. Effects of the fault resistance

The impedance of a transmission line is uniformly distributed along its length. This characteristic enables the distance relay to distinguish between internal and external faults, which might vary according to the fault resistance. This resistance may arise due to failures in the insulators or by the induction produced by lightning strikes; when this occurs, an electric arc is generated which should be taken into account when setting the relay operation [16].

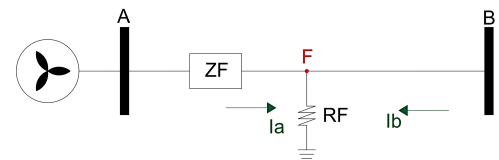


**Figure 4.** Diagram of a three-phase fault with fault resistance [16]

According to the diagram shown in Figure 4, the impedance seen by the relay considering the insertion of the system fault resistance is given by equation (1)

$$Z_m = \frac{V_F}{I_F} = Z_F + R_F + \left( \frac{I_a}{I_b} \right) \cdot R_F \quad (1)$$

Where:

- $Z_m$  = Impedance measured at buses A and B
- $Z_F$  = Fault impedance
- $R_F$  = Fault resistance
- $I_a$  = Current measured at bus A
- $I_b$  = Current measured at bus B

It may be seen in Figure 3 that in the quadrilateral characteristic the fault resistance is close to the relay triggering limit, and this causes that the fault is perceived farther than its real location, resulting in a more limited protection reach and wrong response times; for this reason it is necessary to modify the typical setting of the relay and use an adaptive approach [13] [16].

#### 2.4.4. Criteria for setting the distance relay

The relay impedance is estimated using the voltage and current measured by the potential (PT) and current transformers (CT), respectively. Such impedance is expressed as  $\Omega_{primary}$ . When using the conversion due to the ratio between the PT and the CT, the reading of the equipment is given as  $\Omega_{secondary}$ . The primary impedance may be converted into secondary impedance using the equation(2) [17].

$$\frac{V_{primary}}{I_{primary}} = Z_{primary} = \frac{V_{secondary} \cdot R_{TP}}{I_{secondary} \cdot R_{TC}} \quad (2)$$

For the SIEMENS 7SA522 [17] commercial relay, the protection settings are generally the ones indicated in Table 4.

**Table 4.** Reactances seen by the 7SA522 relay [17]

Reach of $X_{secondary} - Z_1$	$R_{TP}/R_{TC} \cdot 80\% \cdot X_{L1}$
Reach of $X_{secondary} - Z_2$	$R_{TP}/R_{TC} \cdot 120\% \cdot X_{L1}$
Reach of $X_{secondary} - Z_3$	$R_{TP}/R_{TC} (X_{L1} + X_{L2})$

The quadrilateral characteristic presents an important feature: the settings of the reactive and resistive reaches are independent. This feature is useful when there is a fault resistance in the system, because this is a parameter that makes difficult the correct measurement of the distance relay [15]. An arc is generated when a fault resistance occurs, and this arc has an electrical resistance that may be calculated using Warington formula given in equation (3) [18].

$$R_{arc} = \frac{28707(S + 2.046 \cdot v \cdot t)}{I^{1.4}} \quad (3)$$

Where:

- $S$  = Distance of phase-to-phase insulation [m]
- $I$  = Shortcircuit current [A]
- $v$  = Wind speed [m/s]
- $t$  = Duration time of the shortcircuit [s]

The addition of an arc resistance does not modify the values of line impedance; therefore, the protection continues measuring the direct reactance of the line. However, the resistance seen by the relay does consider this arc resistance [17] as indicated in Table 5.

**Table 5.** Resistances seen by the 7SA522 relay [17].

Reach of $R_{secondary} - Z_1$	$R_{TC}/R_{TP} \cdot R_{L1} + 0.5 \cdot R_{arc}$
Reach of $R_{secondary} - Z_2$	$R_{TC}/R_{TP} \cdot R_{L1} + 0.5 \cdot R_{arc}$
Reach of $R_{secondary} - Z_3$	$R_{TC}/R_{TP} \cdot R_{L1} + 0.5 \cdot R_{arc}$

## 3. Results and discussion

### 3.1. Application to the case study

This section presents a comparison between the protection systems of a synchronous generator and a wind generator with similar operation characteristics. The objective is to validate their correct performance in the stated scenarios.

#### 3.1.1. Shortcircuit calculation

For the analysis the shortcircuit calculation is carried out using the superposition method, which evaluates the fault current at a specific point of the network. Its main objective is to verify if the failure of the protection system is due to a wrong behavior of the relay or to its incorrect settings. To appropriately dimension the protection equipment, it is necessary to know two shortcircuit currents, the maximum one given by a three-phase fault (at the beginning of the line), which determines the triggering limits of the relays, and the minimum one due to a phase-to-neutral fault (at the end of the line), which is used to choose the triggering curve of the relay [19].

### 3.1.2. Fault current

Due to their topology, the electric systems powered by synchronous generators produce three-phase, two-phase and single-phase faults; this affects the normal flow of current through the transmission lines. On the other hand, due to their structure based on power electronics, the systems with NCRE sources (e.g. wind) do not have ground connections; hence, they do not have zero sequence.

In order to protect the control system of the wind generator, the fault current is in the range between 1.1 to 1.5 times its nominal current; in contrast, the contribution of the synchronous generator is 5 to 6 times its nominal current. This is shown in Table 6, which contains the current resulting from faults at different points of the line, when the system is powered by a synchronous generator and by a wind farm, thus confirming that the *fault current is lower* in a renewable generation system [20]. The  $R_1$  relay is connected to bus 9 that protects line 1, while relay  $R_2$  protects line 2 and is installed at bus 6 of the system.

**Table 6.** Comparison of the fault currents for a system powered by a synchronous generator and by a wind generator [kA]

Fault location [%]	Synchronous generator		Wind generator	
	Line 1 $R_1$	Line 2 $R_2$	Line 1 $R_1$	Line 2 $R_2$
0	1.18	0.67	0.23	0.20
10	1.09	0.65	0.23	0.20
20	1.02	0.63	0.22	0.19
30	0.95	0.62	0.22	0.19
40	0.89	0.60	0.21	0.19
50	0.84	0.59	0.21	0.19
60	0.80	0.58	0.21	0.19
70	0.75	0.56	0.20	0.18
80	0.71	0.55	0.20	0.18
90	0.68	0.55	0.20	0.18
100	0.65	0.55	0.19	0.18

### 3.1.3. Fault impedances

The basic principle of the distance protection is to measure the apparent impedance from the voltage to current ratio ( $V/I$ ). According to this ratio, in the occurrence of a fault, if the fault current increases the voltage drop will decrease to compensate this effect. Therefore, the impedance is slightly affected by the shortcircuit level, the type of fault or the source powering the system, thus demonstrating that the impedance will exhibit significant changes if the fault has a fault resistance [21]. Based on the above, Table 7 and Table 8 show that the impedance for a three-phase or a two-phase fault in a transmission line powered by a wind or synchronous generator is the same, as long as the fault resistance is zero.

**Table 7.** Three-phase fault impedance

Fault location [%]	Impedances [ $\Omega$ ]			
	Synchronous generator		Wind generator	
	Line 1 $R_1$	Line 2 $R_2$	Line 1 $R_1$	Line 2 $R_2$
0	0	0	0	0
10	9,229	4,950	9,229	4,950
20	18,476	9,901	18,476	9,901
30	27,756	14,857	27,756	14,857
40	37,087	19,820	37,087	19,820
50	46,487	24,791	46,487	24,791
60	55,973	29,773	55,973	29,773
70	65,564	34,768	65,564	34,768
80	75,278	39,779	75,278	39,779
90	85,137	44,806	85,137	44,806
100	95,159	49,854	95,159	49,854

**Table 8.** Two-phase fault impedance

Fault location [%]	Impedances [ $\Omega$ ]			
	Synchronous generator		Wind generator	
	Line 1 $R_1$	Line 2 $R_2$	Line 1 $R_1$	Line 2 $R_2$
0	0	0	0	0
10	9,229	4,950	9,229	4,950
20	18,476	9,901	18,476	9,901
30	27,756	14,857	27,756	14,857
40	37,087	19,820	37,087	19,820
50	46,487	24,791	46,487	24,791
60	55,973	29,773	55,973	29,773
70	65,564	34,768	65,564	34,768
80	75,278	39,779	75,278	39,779
90	85,137	44,806	85,137	44,806
100	95,159	49,854	95,159	49,854

### 3.1.4. Fluctuation of the generation

A wind farm consists of various units connected in parallel. It is possible that during the day not all units are in operation due to maintenance or to variability in climatic conditions, which results in a variation of the output power, i.e., the line will transport a varying power. These changes may produce a wrong behavior of the distance relay in case of a fault [22]. Figure 5 shows the active power generated by the wind farm along the day; two moments should be highlighted: at 16:00 the wind farm achieves its maximum daily generation of 47.91 MW and at 7:00 the generation achieves its minimum of 9.53 MW.

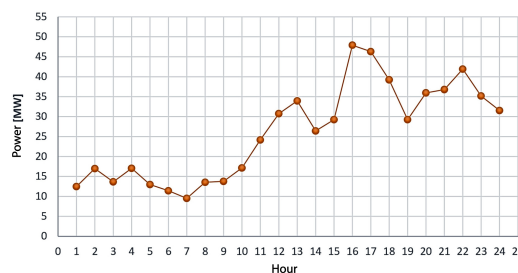


**Figure 5.** Generation of the wind farm per hour

When calculating the shortcircuit in the line for varying fault locations and for wind farm generation,

the fault impedances are evaluated for the power installed (82.50 MW), the maximum power during operation (47.91 MW) and the minimum power during operation (9.53 MW). Once again, it is evident that

the impedance seen by the relay is the same in the three operation scenarios with zero fault resistance. (see table 9)

**Table 9.** Fault impedance evaluated for a fluctuating generation of the wind farm with  $R_f=0$

Fault location [%]	Maximum operating power		Minimum operating power		Nominal power	
	Line 1 $R_1$	Line 2 $R_2$	Line 1 $R_1$	Line 2 $R_2$	Line 1 $R_1$	Line 2 $R_2$
0	0	0	0	0	0	0
10	9,229	4,950	9,229	4,950	9,229	4,950
20	18,476	9,901	18,476	9,901	18,476	9,901
30	27,756	14,857	27,756	14,857	27,756	14,857
40	37,087	19,820	37,087	19,820	37,087	19,820
50	46,487	24,791	46,487	24,791	46,487	24,791
60	55,973	29,773	55,973	29,773	55,973	29,773
70	65,564	34,768	65,564	34,768	65,564	34,768
80	75,278	39,779	75,278	39,779	75,278	39,779
90	85,137	44,806	85,137	44,806	85,137	44,806
100	95,159	49,854	95,159	49,854	95,159	49,854

### 3.1.5. Method for adaptive setting

Section 2 explained the influence of the fault resistance on the shortcircuit calculation in a transmission line: an underreach of the protection might produce wrong triggers of the relay. For this reason, the typical setting should be modified to an adaptive setting.

The quadrilateral adaptive setting method enables the individual variation of resistance and reactance in the R-X plane, resulting in extended production zones. This provides the system with more flexibility and precision que inserting the fault resistance.

The characteristic of the quadrilateral adaptive relay modified for zone 1 may be represented as: equation (4).

$$Z_{set}^{adap} = Z_{set} = 0.8Z_l = \frac{V_{cc\_80\%Z_m}}{I_{cc\_80\%Z_m}} \quad (4)$$

Where  $Z_{set}$  is the conventional impedance setting of the relay, which represents a shortcircuit occurring at 80 % of line 1, located at buses 9-6 (Figure 2). Regarding protection zones 2 and 3, it should be analyzed the adjacent line located at buses 6-4.

When a fault occurs and the fault resistance is zero, the impedance  $Z_m = xZ_{L1}$ , where  $x$  represents the percentage corresponding to the fault location. However, a fault resistance different than zero results in a change in  $\Delta Z$ , which produces an error in the measured impedance  $Z_m$  and in the fault impedance  $xZ_{L1}$ .

In order to avoid wrong measurements by the relay, Figure 6 represents the increase in the measured impedance  $Z_m$  in the R-X plane; the new impedance

is determined as  $Z_{set}^{adap}$ . This is the new setting of the protection when a fault occurs.

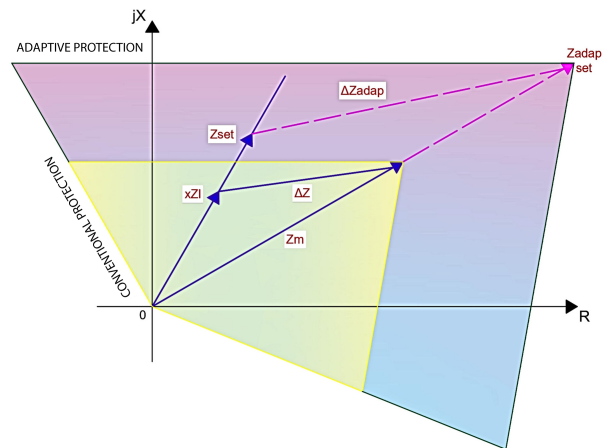


**Figure 6.** Basic principle of the adaptive quadrilateral characteristic for an internal fault

In order to implement the adaptive method in zone 2, the shortcircuit is calculated at 20 % of the adjacent line ( $L_2$ ) and for zone 3 a shortcircuit at 100 % of  $L_2$ . The adaptive setting of the relay is the following:

Zone 2: ecuación (5).

$$Z_{2set}^{adap} = \frac{V_{CC\_20\%L_2}}{I_{CC\_20\%L_2}} \quad (5)$$

Zone 3: ecuación (6).

$$Z_{3set}^{adap} = \frac{V_{CC\_100\%L_2}}{I_{CC\_100\%L_2}} \quad (6)$$

Where:

- $Z_{adap}$  = Adaptive impedance
- $V_{cc-80\%}$  = Shortcircuit voltage at 80 % of  $L_1$
- $I_{cc-80\%}$  = Shortcircuit current at 80 % of  $L_1$
- $V_{cc-20\%}$  = Shortcircuit voltage at 20 % of  $L_2$
- $I_{cc-20\%}$  = Shortcircuit current at 20 % of  $L_1$
- $V_{cc-100\%}$  = Shortcircuit voltage al 100 % of  $L_2$
- $I_{cc-100\%}$  = Shortcircuit current al 100 % of  $L_1$

### 3.1.6. Flow diagram

Figure 7 shows the flow diagram of the proposed method. For the application of this method, an equivalent model should be determined for the base system using the REI method. Then, the positive, negative and zero sequence parameters of the transmission lines are established, and subsequently the power values before the fault are entered; when connecting the wind farm, the parameters of the controller should be considered. Finally, a three-phase shortcircuit is calculated with fault resistances 0 and 25 Ω. When the fault resistance is 0, the conventional method explained in section 2 is employed. On the other hand, when a fault resistance different than zero is obtained by means of Warrington formula, it is necessary to apply the methodology proposed in this paper, where the voltage and current values measured by the transformers are used to calculate the adaptive impedance, considering the values previously established.

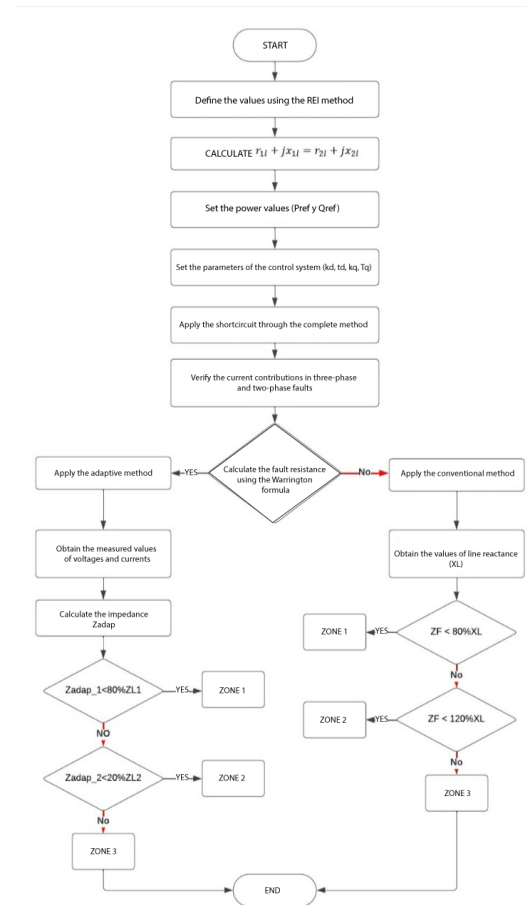


Figure 7. Flow diagram of the proposed adaptive quadrilateral setting

## 3.2. Results

For the subsequent analysis, the relay connected at buses 9-6 is denoted as  $R_1$ , while the protection device connected at buses 6-4 is denoted as  $R_2$ , as shown in Figure 2. Their performance has been evaluated for different fault situations, with two types of sources, the incorporation of the fault resistance and the variation in the power generated by the wind farm.

### 3.2.1. Fault resistance

With the purpose of verifying the optimal performance of the protection system, shortcircuit tests were conducted in lines  $L_1$  y  $L_2$  when connected to a synchronous generator and with fault resistances 0 and 25 Ω. It is seen in Table 10 that the conventional setting of the relay with  $R_f=0$  Ω does not exhibit errors in the response time. On the other hand, for  $R_f=25$  Ω the  $R_1$  relay shows a wrong operation at 80 and 90 % of the line length. (Table 10)

**Table 10.** Operation of the Siemens 7SA522 relay in conventional systems with fault resistance

Fault location %	$R_f = 0$		$R_f = 25$	
	Line 1	Line 2	Line 1	Line 2
	$R_1$	$R_2$	$R_1$	$R_2$
0	Zone 1	Zone 1	Zone 1	Zone 1
10	Zone 1	Zone 1	Zone 1	Zone 1
20	Zone 1	Zone 1	Zone 1	Zone 1
30	Zone 1	Zone 1	Zone 1	Zone 1
40	Zone 1	Zone 1	Zone 1	Zone 1
50	Zone 1	Zone 1	Zone 1	Zone 1
60	Zone 1	Zone 1	Zone 1	Zone 1
70	Zone 1	Zone 1	Zone 1	Zone 1
80	Zone 2	Zone 1	Not ok	Zone 1
90	Zone 2	Zone 2	Not ok	Zone 2
100	Zone 2	Zone 2	Zone 2	Zone 2

### 3.2.2. Fluctuating power from the wind farm generation

It is demonstrated in section 3 that when shortcircuit events are calculated in transmission lines powered by a wind farm with variable generation power and  $R_F = 0$ , the impedance seen by the protection remains fixed as the power varies.

In the following, the results obtained when calculating shortcircuit events for  $R_F = 25 \Omega$  with lines  $L_1$  and  $L_2$  affected by a fault are presented. The settings of relays  $R_1$  y  $R_2$  in the three generation scenarios have operation errors, with the line  $L_2$  being more affected, as shown in Table 11.

**Table 11.** Operation of the distance protection for a fluctuating power generated by the wind farm, with  $R_f = 25\Omega$ 

Fault location [%]	Maximum operating power		Minimum operating power		Nominal power	
	Line 1	Line 2	Line 1	Line 2	Line 1	Line 2
0	Zone 1	Not ok	Zone 1	Not ok	Zone 1	Not ok
10	Zone 1	Not ok	Zone 1	Not ok	Zone 1	Not ok
20	Zone 1	Not ok	Zone 1	Not ok	Zone 1	Not ok
30	Zone 1	Not ok	Zone 1	Not ok	Zone 1	Not ok
40	Zone 1	Not ok	Zone 1	Not ok	Zone 1	Not ok
50	Zone 1	Not ok	Zone 1	Not ok	Zone 1	Not ok
60	Zone 1	Not ok	Zone 1	Not ok	Zone 1	Not ok
70	Zone 1	Not ok	Not ok	Not ok	Zona 1	Not ok
80	Zone 1	Not ok	Zone 1	Not ok	Zone 1	Not ok
90	Not ok	Not ok	Zone 2	Not ok	Zone 2	Not ok
100	Not ok	Not ok	Zone 2	Not ok	Zone 2	Not ok

Figure 8 presents the distance-time diagram of the distance protection. For the  $R_1$  relay, zone 1 covers 80 % of the line length, zone 2 136 % and zone 3 covers the main and the adjacent lines. Considering what has been discussed in previous sections, there is an error in the reach of zone 2, since it normally covers only 120 % of the line length. The  $R_2$  relay also exhibits problems, since zone 2 only reaches 112 % of the pro-

tection, which is wrong as well.

It should be remembered that the response times of the distance protection were detailed in section 3 (relay protection zones). Based on this criterion, it has been determined that the conventional setting operates in wrong times for different locations of the faults in the lines; these values are highlighted in Table 12.

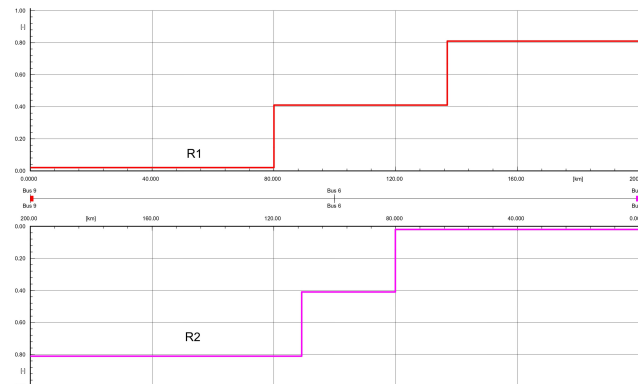
**Figure 8.** Projection of the protection zones for relays  $R_1$  and  $R_2$



Table 13 shows the effective performance of the proposed methodology for faults in lines connected to a wind farm.

The protection zones of the proposed methodology  $Z_{*set}^{adapt}$  ( $* = 1, 2, 3$ ) have been calculated with the impedance measured by each relay after a shortcircuit and considering the fault resistance, with the objective that the protection reach of  $R_1$  and  $R_2$  is correct.

Figure 10 shows the settings for relays  $R_1$  and  $R_2$ . The protection reach is obtained through equations (4), (5) and (6), where the maximum operation limit of the relay will be given by the impedance measured by the equipment after the fault. This is the difference between the conventional method and the new methodology, namely, the setting of the protection zones does not take into account the own reactance of the line,

but it now uses values of the impedance seen by the relay after the fault; this causes that the protections zones are extended to correct the improper operation of the relay

From an analysis of Table 12 it is identified that the relay  $R_1$  that protects line  $L_1$  operates incorrectly starting from 70 % of the line length, while relay  $R_2$  does not fulfill the task of protecting line  $L_2$  when the system considers a fault resistance. For this reason, it is essential to apply the proposed methodology. As shown in Figure 11, for a fault at 0 % of line  $L_2$  with a) maximum operating power, b) minimum operating power and c) nominal power, the protection operates in zone 1 at a response time of 0.02 s, in contrast with the conventional setting where the fault impedance was out of the zone.

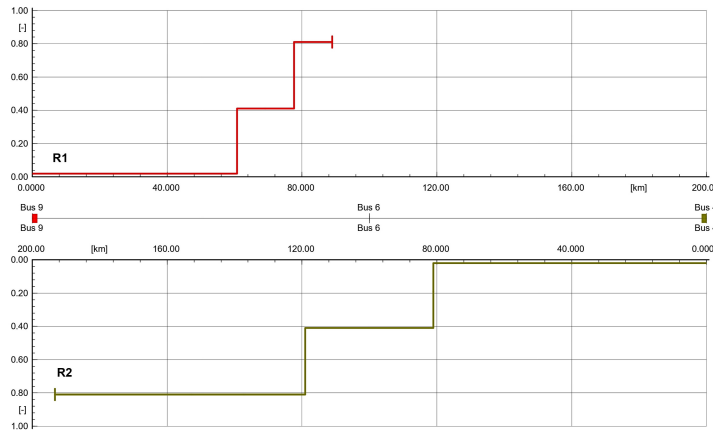


Figure 10. Coordination of the protection zones of the proposed system for maximum power

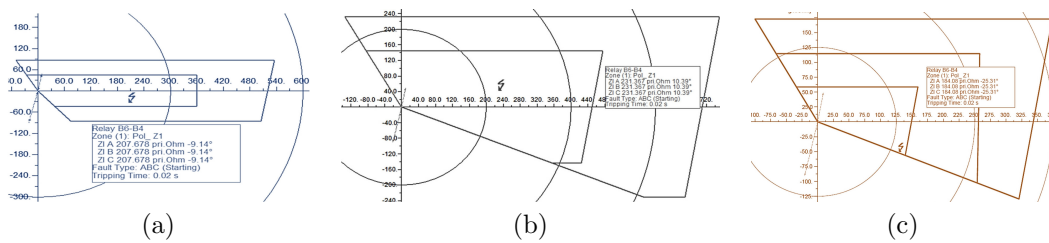


Figure 11. Shortcircuit in  $L_2$ , applying the method for adaptive quadrilateral setting with a) maximum operating power, b) minimum operating power and c) nominal power

The results of Table 14 show the performance of the proposed method for adaptive quadrilateral setting. In this case, the relays of both lines  $L_1$  and  $L_2$

correctly identify the faults with their precise location, and correct the wrong response times of the conventional relay.

**Table 14.** Response times for the adaptive setting for shortcircuits with minimum current

Fault location [%]	Maximum operating power		Minimum operating power		Nominal power	
	Line 1 [s]	Line 2 [s]	Line 1 [s]	Line 2 [s]	Line 1 [s]	Line 2 [s]
0	0.02	0.02	0.02	0.02	0.02	0.02
10	0.02	0.02	0.02	0.02	0.02	0.02
20	0.02	0.02	0.02	<b>0.02</b>	0.02	0.02
30	0.02	0.02	0.02	<b>0.02</b>	0.02	0.02
40	0.02	<b>0.02</b>	0.02	<b>0.02</b>	0.02	0.02
50	0.02	<b>0.02</b>	0.02	<b>0.02</b>	0.02	0.02
60	0.02	<b>0.02</b>	0.02	<b>0.02</b>	0.02	<b>0.02</b>
70	0.02	<b>0.02</b>	<b>0.02</b>	<b>0.02</b>	0.02	<b>0.02</b>
80	0.02	0.41	<b>0.41</b>	<b>0.41</b>	0.41	0.41
90	<b>0.41</b>	0.41	<b>0.41</b>	<b>0.41</b>	<b>0.41</b>	0.41
100	<b>0.41</b>	0.41	<b>0.41</b>	<b>0.41</b>	<b>0.41</b>	0.41

### 3.3. Discussion

When nonconventional renewable energies are integrated in the power system, the performance of the distance protection changes when there is a nonzero fault resistance. Due to this, it is possible to have a wrong operation of the relay, thus deteriorating the reliability of the power system. To address this issue, this paper proposes a protection of quadrilateral characteristic with adaptive setting. The results of simulations performed on the case study show that for internal faults, the aforementioned method corrects the response times of the relay. With respect to the traditional setting method, the proposed methodology exhibits advantages such as:

1. The consequences of the insertion of a fault resistance are considered and completely eliminated because the protection zone tends to be larger than usual.
2. The analysis of the behavior of faults in this paper is unique for a wind farm, and thus the proposed protection structure and methodology are applicable for the insertion of NCRE (wind farm).
3. The different protection zones of the proposed scheme are modified so that they get adapted to the variation of the additional impedance. This additional impedance ( $Z_{set}$ ) is due to the fault resistance, and causes a variation in the fault current.
4. The proposed scheme is designed for a unique network code, where it was considered a fault resistance of  $25 \Omega$  calculated by means of Warington formula.

5. Compared to the adaptive setting based on the Mho characteristic, the quadrilateral adaptive setting has more advantages because, depending on the location of the fault, the zone can be expanded only in the R axis, in the X axis or in both; in other words, it has a greater resistive reach because they do not depend on each other. This results in a higher reliability and security for the power system, even though this requires equipment with better technology and higher cost.
6. The methodology applied does not estimate the automatic detection of external faults of systems; for this purpose, the internal characteristics of the relay should be modified through its exclusive programming.

### 4. Conclusions

This work implements an adaptive setting for the IEEE 9-bus New England system, modified with the insertion of a wind farm constituted by 33 2.5 MW wind generators. The operation zones of the adaptive quadrilateral characteristic are set according to the fault that has occurred, to avoid errors in the operation of the SIEMENS 7SA522 relay. The following can be concluded in this work:

The distance relay with conventional quadrilateral setting operates incorrectly when there is a three-phase shortcircuit that considers the fault resistance. On the other hand, the adaptive quadrilateral setting correctly identifies the fault impedances shifted in the X axis due to the increase of the fault resistance.

The proposed adaptive method exhibits a favorable response for different shortcircuit scenarios, with variations in the fault point, fault resistance and oscil-

lation in the power generated by the wind farm, thus demonstrating that the relay operates in the correct protection zone.

The proposed method uses voltage and current data from the instrumentation transformers, and calculates the line impedance up to the fault point. The relay operates according to its protection setting. Specifically, if the fault is located at 80 % of the line length, zone 1 operates in  $t=0$  seconds. On the other hand, if the fault occurs at 20 % of the length of the line adjacent to the relay, zone 2 operates in  $t=0.4$  seconds. Finally, if the shortcircuit event occurs at 100 % of the line adjacent to the relay, zone 3 operates in  $t=0.8$  seconds.

## References

- [1] M. Singh and V. Telukunta, "Adaptive distance relaying scheme to tackle the under reach problem due renewable energy," in *2014 Eighteenth National Power Systems Conference (NPSC)*, 2014, pp. 1–6. [Online]. Available: <https://doi.org/10.1109/NPSC.2014.7103785>
- [2] H. Sadeghi, "A novel method for adaptive distance protection of transmission line connected to wind farms," *International Journal of Electrical Power & Energy Systems*, vol. 43, no. 1, pp. 1376–1382, 2012. [Online]. Available: <https://doi.org/10.1016/j.ijepes.2012.06.072>
- [3] V. Telukunta, J. Pradhan, A. Agrawal, M. Singh, and S. G. Srivani, "Protection challenges under bulk penetration of renewable energy resources in power systems: A review," *CSEE Journal of Power and Energy Systems*, vol. 3, no. 4, pp. 365–379, 2017. [Online]. Available: <https://doi.org/10.17775/CSEEJPES.2017.00030>
- [4] V. K. Gaur and B. R. Bhalja, "A new digital distance relaying scheme for three terminal transmission line," *2018 IEEE Power & Energy Society General Meeting (PESGM)*, pp. 1–5, 2018. [Online]. Available: <https://doi.org/10.1109/PESGM.2018.8586152>
- [5] Y. Liang, W. Li, and W. Zha, "Adaptive mho characteristic-based distance protection for lines emanating from photovoltaic power plants under unbalanced faults," *IEEE Systems Journal*, vol. 15, no. 3, pp. 3506–3516, 2021. [Online]. Available: <https://doi.org/10.1109/JSYST.2020.3015225>
- [6] R. Dubey, S. Samantaray, B. Panigrahi, and G. Venkoparao, "Adaptive distance relay setting for parallel transmission network connecting wind farms and UPFC," *International Journal of Electrical Power & Energy Systems*, vol. 65, pp. 113–123, 2015. [Online]. Available: <https://doi.org/10.1016/j.ijepes.2014.09.033>
- [7] Z. He, S. Lin, Y. Deng, X. Li, and Q. Qian, "A rough membership neural network approach for fault classification in transmission lines," *International Journal of Electrical Power & Energy Systems*, vol. 61, pp. 429–439, 2014. [Online]. Available: <https://doi.org/10.1016/j.ijepes.2014.03.027>
- [8] B. Kasztenny and D. Finney, "Fundamentals of distance protection," in *2008 61st Annual Conference for Protective Relay Engineers*, 2008, pp. 1–34. [Online]. Available: <https://doi.org/10.1109/CPRE.2008.4515045>
- [9] P. M. Anderson and A. A. Fouad, *Power system control and stability*. IEEE Press power engineering series, 2008. [Online]. Available: <https://bit.ly/43fa38M>
- [10] R. A. Espinoza San Martín, *Desarrollo de un equivalente reducido del SING para estudios de estabilidad transitoria de primera oscilación*. Tesis de grado. Universidad de Chile., 2012. [Online]. Available: <https://bit.ly/3MHi8MB>
- [11] DigSilent. (2023) Powerfactory application example wind farm base case 2 powerfactory project information. DigSilent. [Online]. Available: <https://bit.ly/45JuMDu>
- [12] S. H. Horowitz and A. G. Phadke, *Power System Relaying*. John Wiley & Sons, 2013. [Online]. Available: <https://bit.ly/3WmgcHd>
- [13] C. Merchán, P. Vintimilla, and P. Astudillo, *Análisis en estado estacionario y verificación del sistema de protecciones en las líneas de transmisión de las subestaciones adyacentes ante la incorporación del Parque Eólico Minas de Huascachaca al Sistema Nacional de Transmisión*. Tesis de Grado. Universidad de Cuenca., 2021. [Online]. Available: <https://bit.ly/42jpAmH>
- [14] J. A. Águila Ríos and J. F. Piña Tapia, *Análisis en laboratorio de respuesta de acción en Zona 1 de protección de IEDs de distancia*. Tesis de Grado. Universidad Politécnica Salesiana, 2021. [Online]. Available: <https://bit.ly/3N5DR1Y>
- [15] A. Chamorro, *Protecciones de distancia: guía de aplicación*. Areva T&D Ibérica, 2005. [Online]. Available: <https://bit.ly/42nBA6G>
- [16] M. Biswal, B. B. Pati, and A. K. Pradhan, "Adaptive distance relay setting for series compensated line," *International Journal of Electrical Power & Energy Systems*, vol. 52, pp. 198–206, 2013. [Online]. Available: <https://doi.org/10.1016/j.ijepes.2013.03.018>

- [17] SIEMENS, *Distance Protection 7SA522*. SIEMENS AG, 2011. [Online]. Available: <https://bit.ly/3C5cCOQ>
- [18] COESSINAC, *Requisitos mínimos para los sistemas de protección del SEIN*. Comité de operación económica del Sistema Interconectado Nacional, 2008. [Online]. Available: <https://bit.ly/3N7ORvX>
- [19] DigSilent. (2014) Powerfactory 15. DigSilent. [Online]. Available: <https://bit.ly/45EQfgK>
- [20] E. Muljadi, N. Samaan, V. Gevorgian, J. Li, and S. Pasupulati, "Short circuit current contribution for different wind turbine generator types," in *IEEE PES General Meeting*, 2010, pp. 1–8. [Online]. Available: <https://doi.org/10.1109/PES.2010.5589677>
- [21] L. He, C.-C. Liu, A. Pitto, and D. Cirio, "Distance protection of AC grid with HVDC-connected offshore wind generators," *IEEE Transactions on Power Delivery*, vol. 29, no. 2, pp. 493–501, 2014. [Online]. Available: <https://doi.org/10.1109/TPWRD.2013.2271761>
- [22] A. K. Pradhan and G. Joos, "Adaptive distance relay setting for lines connecting wind farms," *IEEE Transactions on Energy Conversion*, vol. 22, no. 1, pp. 206–213, 2007. [Online]. Available: <https://doi.org/10.1109/TEC.2006.889621>



# MONTE CARLO SIMULATION OF UNCONTROLLED ELECTRIC VEHICLE CHARGING IMPACT ON DISTRIBUTED GENERATION

## IMPACTO DE LA SIMULACIÓN MONTE CARLO DE CARGA NO CONTROLADA DE VEHÍCULOS ELÉCTRICOS EN LA GENERACIÓN DISTRIBUIDA

Villanueva-Machado, Carlos W.<sup>1,\*</sup> , Jaime E. Luyo<sup>1</sup> , Rios-Villacorta, Alberto<sup>2</sup> 

Received: 08-05-2023, Received after review: 31-05-2023, Accepted: 12-06-2023, Published: 01-07-2023

### Abstract

The uncontrolled charging of electric vehicles poses a great challenge for distribution network operators and power system planners. Instead of focusing on controlling this uncontrolled load, a model that uses contingency analysis variables to calculate the power capacity needed in the power system is proposed. The unserved power variable is used to evaluate the amount of uncovered load power at each bus of the system, followed by the calculation of the additional power capacity required using a photovoltaic and storage system and another constant generation alternative in the 14-bus IEEE power system with information on some electric vehicles and daily load in the power system of Peru. The results obtained in the power system with distributed generation, the absence of unserved power, corroborate the success of the methodology used. This model provides tools to both distribution network operators and power system planners, reducing the impact on the power system of electric vehicles and providing a methodology applicable to other electric distribution systems with uncontrolled loads.

**Keywords:** Electric Vehicles, Energy Storage Systems, Monte Carlo Simulation, Not Served Power, Optimal Power Flow, Renewable Energy Sources, Power System

### Resumen

La carga no controlada de vehículos eléctricos plantea un gran desafío para los operadores de redes de distribución y los planificadores de sistemas de potencia. En lugar de focalizarse en el control de esta carga no controlada, se propone un modelo que utiliza variables de análisis de contingencias para calcular la capacidad de potencia necesaria en el sistema de potencia. Se emplea la variable de potencia no servida para evaluar la cantidad de potencia de carga no cubierta en cada barra del sistema, seguido del cálculo de la capacidad de potencia adicional requerida utilizando un sistema fotovoltaico y de almacenamiento y otra alternativa de generación constante en el sistema de potencia IEEE de 14 barras con información sobre algunos vehículos eléctricos y la carga diaria en el sistema de potencia de Perú. Los resultados obtenidos en el sistema de potencia con generación distribuida muestran que no hay presencia de potencia no servida, corroborando el éxito de la metodología utilizada. Este modelo brinda herramientas tanto a los operadores de redes de distribución como a los planificadores de sistemas de potencia, reduciendo el impacto en el sistema de potencia de los vehículos eléctricos y aportando una metodología aplicable a otros sistemas de distribución eléctrica con cargas no controladas.

**Palabras clave:** Fuentes de Energía Renovable, Potencia no Servida, Sistema de Potencia, Sistemas de Almacenamiento de Energía, Simulación de Monte Carlo, Vehículos Eléctricos

<sup>1,\*</sup>Faculty of Mechanical Engineering, Universidad Nacional de Ingeniería, Perú.

Corresponding author ✉: [cwvillanuevam@uni.pe](mailto:cwvillanuevam@uni.pe).

<sup>2</sup> Faculty of Systems Electronics and Industrial Engineering, Universidad Técnica de Ambato, Ecuador.

Suggested citation: Villanueva-Machado, C. W.; Luyo, J. E. and Rios-Villacorta, A. "Monte Carlo simulation of uncontrolled Electric Vehicle charging impact on distributed generation," *Ingenius, Revista de Ciencia y Tecnología*, N.º 30, pp. 120-134, 2023, DOI: <https://doi.org/10.17163/ings.n30.2023.10>.

## 1. Introduction

Electric Vehicles (EVs) have become popular due to their low emissions, high efficiency, and lower operating costs [1]. However, the increase in EVs has created challenges for the electricity grid, including uncontrolled charging that strains distribution networks (DNs). This article proposes a system consisting of photovoltaic (PV) generation and battery energy storage (ES) that can be implemented to optimize the use of PV and battery systems, minimize the cost of EV charging, and reduce grid load [1, 2].

EVs present challenges to power grid capacity, charging infrastructure, and ES technology [3, 4]. Vehicle-to-Grid (V2G) and Distributed Generation (DG) have been proposed as supportive technologies to address these issues [1]. A model of the impact of local EV adoption on DNs is presented in [5], posing a challenge to Distribution Network Operators. Monte Carlo simulation (MCS) can assist operators in understanding the impact of their policies on system performance and identifying potential risks associated with certain decisions [6] as a way to address these issues.

According to a study by [7], MCS usage is a valuable tool for assessing the impact of uncertain factors on the performance of power systems (PSs). The operating condition of the electricity DN can be enhanced using MCS. The presence of the variable Not Served Power (NSP) shows energy-depleted or overloaded PSs operation conditions.

PV generation and ES technologies have been proposed as potential solutions for integrating EVs into the power grid, as suggested in [1], [6]. NSP optimization has been proposed as a method for monitoring PS performance. This method covers operational costs in contingencies, as NSP will be expelled from the load [8]. V2G technology is also a solution to the challenges of uncontrolled EV charging, since it can help mitigate negative aspects and improve sustainability [9]. MCS has been suggested as a potential tool for analyzing the impact of DG supplying surplus load required by EVs.

A description of complementary analysis examines the interaction with the EVs adoption. The interaction between the intermittency generated by renewable generators and the storage capacity allowed using the V2G charging process is described in [2]. A stochastic methodology associated with EVs smart charging process is considered in [4], focusing on battery degradation analysis. While [3] is focused on the interplay

between different variables required for a smart charging process. The Internet of Energy environment is adapted according to future smart grid operation required.

As proposed in [10], DG can help mitigate the negative impacts of uncontrolled EV charging and improve sustainability. DG can supply energy to the grid during peak hours and balance the load, reducing the impact of uncontrolled EV charging on the power grid. To determine appropriate energy policies, it is important to anticipate energy deficiencies. Reference [5] proposes a model that characterizes the geographic and travel patterns of EV owners' behavior. This provides insights into their travel behavior and energy demands.

The study proposed MCS usage to analyze the mid-term effects of uncontrolled EV charging. This contributes to establishing energy policies that meet the energy demands of EV owners. These measurements' implementation enhanced the stability and reliability of the electricity DN.

The method generates snapshots of potential scenarios based on global trends and Peru's EV transportation market, and it is valuable in optimizing the electricity DN using algebraic modeling. The study aims in developing policies that meet energy demands while ensuring stable and reliable electricity DN conditions. The need for future charging stations and DG strategies due to EV charging is highlighted in [6].

## 2. Materials and Methods

Different levels of EVs adoption will be analyzed to evaluate the impact on DN energy required, using worldwide and Peruvian information. The projection reviews Peruvian actual and historical vehicle fleet stratification.

The methodology presented in the article involves a loop that starts from EV model information and goes up to the stage of saving data, as illustrated in Figure 1. This loop is applied to all EV models and the three scenarios of EV adoption mentioned in the section "2.3 Multiple Scenarios." Table 1 shows the terminology employed in the current paper.

The resulting data is then processed through 2 separate processes. The MCS is the first process, reducing the amount of data. The DN analysis explained in section "2.8" is the second process. The information gathered from these processes is used to compare and evaluate the designed system that integrates PV generation and ES to tackle the surplus energy demand caused by uncontrolled charging of EVs on the DN.

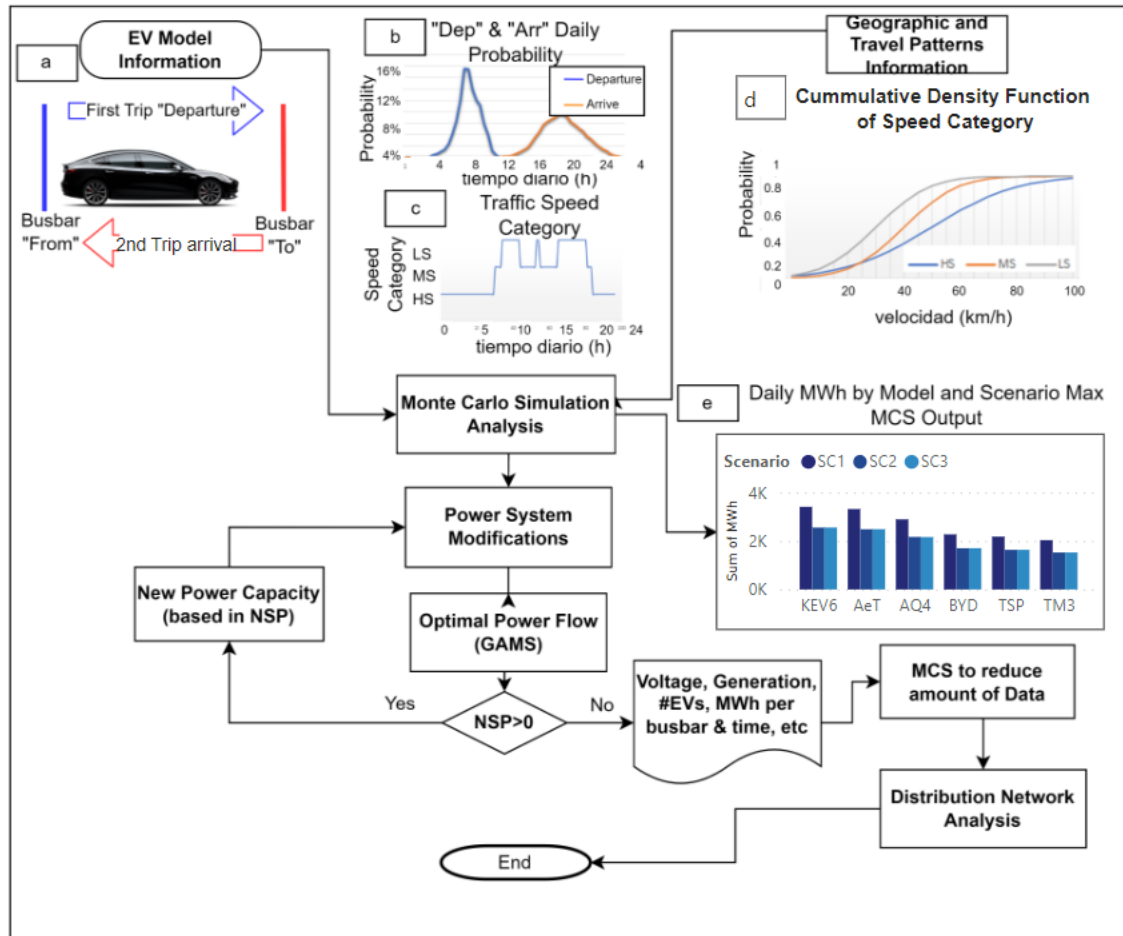


**Figure 1.** Methodology and input data: (a) Monte Carlo simulation input related to electric vehicle models, and explanations of daily travels (b) daily trip times probability density function (PDF) (c) daily traffic speed category (d) speed value cumulative density function per traffic speed category (e) results from Monte Carlo simulation, input for next steps

**Table 1.** Terminology employed in the current paper

Terminology	Description
PS	Power System
MCS	Maximum Continuous Service
V2G	Vehicle-to-Grid
GAMS	General Algebraic Modeling System
NSP	Not Served Power
EVs	Electric Vehicles
PC	Power Capacity
DG	Distributed Generation
DN	Distribution Network
PV	Photovoltaic
ES	Energy Storage
OPF	Optimal Power Flow
NSE	Not Served Energy

## 2.1. Uncontrolled charging projection description in Peru

Peruvian EV imports have been rising (as reported by the Economic Studies Department of AAP, 2019) since

2016. Until August 2019, there were 253 hybrid and 16 electric vehicles imported. The global number of yearly electric vehicles imported was 11 in 2016, 93 in 2017, and 165 in 2018. In total, 535 EVs were reported until August 2019. Peruvian government reported the number of vehicles on the road until 2018 of each category: cars, station wagons, and pickup trucks.

## 2.2. Uncontrolled charging projection process in Peru

The task projects the optimistic, pessimistic, and business-as-usual electric vehicle (EV) adoption rates in Peru. This estimates the controllable charging rate using market participation as a point of reference and calculating the uncontrollable charging rate. The uncontrollable charging rate is calculated as a complement of the controllable charging rate, which is assumed to vary yearly depending on regional and global EV adoption trends.

The assumptions for the pessimistic and optimistic projections are based on current trends. They may not

hold in the future. Electric vehicle sales are expected to continue increasing due to government incentives, reduced battery costs, and increased consumer awareness.

### 2.3. Multiple scenarios

This study examines the potential impact of EV adoption on energy demand in Peru's PS. Three growth scenarios for EV adoption are presented: low (15% per year), medium (25% per year), and high (40% per year). Three scenarios of 2000, 2500, and 3750 EVs estimate the number of uncontrolled charging EVs in the medium term. The scenarios were developed using Peruvian and worldwide data [11].

Based on the scenarios, the authors evaluated the potential impact of EV adoption on Peru's PS under different conditions. The selection criteria for the scenarios were based on realistic and varied growth rates, worst-case analysis, and historical and current data. A review of Peru's actual and historical vehicle fleet stratification is also provided.

As of August 2019, 253 hybrids and 16 EVs were imported into Peru. The Peruvian government reported the number of vehicles on the road until 2018 for each category [12]. For further details, refer to section 2.2.

### 2.4. Monte Carlo simulation analysis

Figure 1a shows how EVs depart from and arrive at different busbars, with departure and arrival times based on EV owner travel and geographic patterns [5]. The model uses  $Ns$  samples ( $s$ ),  $T$  time periods ( $t$ ), and  $NV$  EVs ( $v$ ) characterized with stochastic variables [13].

Figure 1b displays the stochastic variables [9],  $dep_{v,s}$  and  $arr_{v,s}$  that are fit into probabilistic distributions [2], with binary variables representing the states ( $deps_{t,v,s}$  and  $arrs_{t,v,s}$ ). Figure 1c and 1d depict probability characterizations of EV speed variable ( $sv_{t,v,s}$ ) and distance between buses corrected using  $tdcf_{v,s}$  and length  $L(Fr_{v,s} : To_{v,s})$ .

$$td_{v,s} = L(Fr_{v,s}; To_{v,s}) \times tdcf_{v,s} \quad (1)$$

Equation (1) combines stochastic parameters of EV location state  $Fr_{v,s}$  and  $To_{v,s}$ , with  $tdcf_{v,s}$  to determine the final travel distance  $td_{v,s}$ . Specific EV data is required for MCS analysis, such as Battery Capacity (BCES), Riding Specific Consumption ( $SC_{v,s}$ ), State of Charge ( $SoC_{min}$  and  $SoC_{max}$ ), maximum charging power ( $Pv_{max}$ ), charging and discharging efficiency ( $n_{chg}$  and  $n_{dsg}$ ), road consumption value ( $R_{t,v,s}$ ), and binary variable index ( $X_{t,v,s}$ ).

#### 2.4.1. Pseudo code – travel modeling

1. Define departure time or arrival time and temporal road distance travelled variable  $t = dep_{v,s}$  and on road distance travelled,  $rdt_{v,s} = 0$  for departure &  $t = arr_{v,s}$ ) and  $rdt_{v,s} = 0$  for arrival travel.
2. Start Loop to fill the road distance traveled until surpassing the travel distance, as in equations (2) and (3).

$$\text{while } rdt_{v,s} \leq td_{v,s} \{ \quad (2)$$

$$rdt_{v,s} = +sv_{v,s} \times 24/T \quad (3)$$

3. Conditional to check if the last stage of departure travel is reached as in equations (4) and (5).

$$\text{if } rdt_{v,s} \leq td_{v,s} \{ \quad (4)$$

$$R_{t,v,s} = sv_{v,s} \times SC_{v,s}/n_{dsg} \times 24/T \quad (5)$$

4. Assign a value to on-road consumption for non-last stages of departure travel as in equation (6).

$$\text{else} \{ R_{t,v,s} = (sv_{v,s} + td_{v,s} - rdt_{v,s}) \times SC_{v,s}/n_{dsg} \} \quad (6)$$

5. End loop assigning the value of departure end time or arrival start time and binary state of on-road as in equation (7)) for departure trip and equation (8) for arriving trip.

$$X_{t,v,s} = 1 \wedge t = +1 \} de_{v,s} = t \quad (7)$$

$$X_{t,v,s} = 1 \wedge t = -1 \} ai_{v,s} = t \quad (8)$$

Variables such as  $de_{v,s}$  and  $ai_{v,s}$  mark the end of the departure trip and the time when the EV is ready to begin the return trip, respectively.

The binary variable  $CS_{b,t,v,s}$  tracks the charging bus state for the EV allocated in bus  $b$ . Equations (9) and (10) enforce constraints related to the charging bus state.

$$CS_{Fr_{v,s},t,v,s} = 1 \forall arr_{v,s} < t < dep_{v,s} \quad (9)$$

$$CS_{To_{v,s},t,v,s} = 1 \forall de_{v,s} < t < ai_{v,s} \quad (10)$$

The variables  $ChR_{v,s}$  and  $CC$  are defined as the total energy required by the EV on the road and the complete charge, respectively. These variables are assigned in equations (11) and (12), respectively.

$$ChR_{v,s} = \sum_t R_{t,v,s} \quad (11)$$

$$CC = Pv_{max} \times 24/T \times n_{chg} \quad (12)$$

#### 2.4.2. Pseudo code – uncontrolled charging modeling

1. Set 0 value to  $tch_{v,s}$  as in equation (13).

$$tch_{v,s} = 0; \forall v \in NV \wedge s \in Ns \quad (13)$$

2. Set charging time: departure and arrival as in equation (14).

$$t = de_{v,s} \wedge t = arr_{v,s} + 1 \quad (14)$$

3. Increase and assign the value of uncontrolled vehicle charge  $UC_{b,t,v,s}$ , according to temporal charge  $tch_{v,s}$ , measuring uncontrolled charging in the corresponding bus, without reaching the energy required as in equations (15) and (16).

$$tch_{v,s} = +CC \quad (15)$$

$$if\ tch_{v,s} \leq ChR_{v,s} \{UC_{b,t,v,s} = CS_{b,t,v,s} \times CC\} \quad (16)$$

4. Assign uncontrolled charge to the time while reaching the energy required as in equation (17).

$$else\{UC_{b,t,v,s} = (ChR_{v,s} + CC - tch_{v,s}) \times CS_{b,t,v,s}\} \quad (17)$$

5. End loop as in equation (18).

$$t = +1\} \quad (18)$$

Equation (19) is used to obtain the information on the required Peak Load,  $PLR_s$ , which is reported as the final output of the MCS. The load of PS in bus b is represented by  $Pdps_{b,t}$ . Figure 1e provides a summary of this information, showing the daily cumulative energy required by the DN for all models and scenarios. Figure 1e compares only the maximum MCS outputs, which cause more DN load during peak hours. On the other hand, the minimum MCS output represents the minimum impact on the peak hour charging state.

$$PLR_s = \max \left( t, \sum_b \left( \sum_v UC_{b,t,v,s} + Pdps_{b,t} \right) \right) \quad (19)$$

#### 2.5. Interaction between MCS and optimal power flow

Equations (21) and (22) show how the outputs of MCS are chosen. The surplus charge is added to the PS load and denoted as  $Pd_{b,t,s}$ . The information obtained from MCS analysis (Equations (21) and (22)) is an important input for optimizing the operation of the electricity DN, specifically the transmission subsection, using algebraic modeling.

$$[PLR_{smax}, smax] = \max(s, PLR_s) \quad (20)$$

$$[PLR_{smin}, smin] = \min(s, PLR_s) \quad (21)$$

$$Pd_{b,t,s} = Pdps_{b,t,s} + \sum UC_{b,t,v,s} \quad (22)$$

#### 2.6. Optimal power flow analysis

The electric OPF is modeled in GAMS software, using CONOPT minimizing of from equation (24) for each of the 6 cases (3 scenarios, 2 MCS outputs). This process provides the amount of NSP required in each bus of the DN for each period analyzed, as in equation (25). GAMS optimization and MCS complementary analysis approaches could overcome the challenges of integrating EVs and DG into PSs [14].

##### 2.6.1. Objective function

The main output is the energy allocated to daily Not Served Energy (NSE) with half-hourly information. It involves evaluating equations for all  $t \in T \wedge s \in \{s_{min}, s_{max}\}$ . NSE is used to allocate the amount of NSP during this time period, as per equation (23).

NSP is used as a slack variable to identify areas and the amount of energy required for surplus EV charging, and it can also represent the amount of power required as surplus generation in its busbar to avoid PS failures [8].

The objective function (*of*) for the optimization of energy losses associated with network operation is expressed in equation (24), where the power generation at the slack bus  $Pg_{slack}$  is also evaluated. The penalty price of  $C_{pen} = \$6,000.00$  for NSE in Peru is mentioned according to reference [15]. Using NSP as a data source can help planners compare generation source alternatives, fit the energy required in time-space modeling, and dimension the DG conditions along the PS.

$$NSE_k = 24/T \times NSP_k \quad (23)$$

$$of = \sum (C_{pen} NSE_k) + Pg_{slack} \quad (24)$$

### 2.6.2. Optimal power flow constraints

The OPF constraints are the active and reactive power balance. Equations (25) and (26) define the power balance, where  $Pg_k$  and  $NsP_k$  denote generation power and non-spinning reserves, while  $Pd_k$  represents the required power load.

$$Pg_k + NsP_k = Pd_k + \sum P_{km} \quad (25)$$

$$Qg_k = Qd_k + Qsh_k + \sum Q_{km} \quad (26)$$

The variables  $Qg_k$ ,  $Qd_k$ , relate to reactive power generation and load in each bus. Equations (27) and (28) calculate the active and reactive power per line ( $P_{km}$  and  $Q_{km}$ ) and apparent power  $S_{km}$  in equation (29) controls the overcharge in the corresponding power line.

$$P_{km} = V_k V_m Y_{km} \cos(th_{km} + d_{km}) - V_k^2 \cos(t_{km}) \quad (27)$$

$$Q_{km} = -V_k V_m Y_{km} \sin(th_{km} + d_{km}) + V_k^2 \sin(t_{km}) \quad (28)$$

$$S_{km} = \sqrt{P_{km}^2 + Q_{km}^2} \leq S_{kmupper} \quad (29)$$

The variables  $V_i$ ,  $d_i$ ,  $Qg_i$ ,  $Pg_i$  have lower and upper bounds, denoted by  $x_{lower}$  and  $x_{upper}$  in equation (30). The section refers to [8] for details on voltage parameters ( $V$  and  $d$ ) and admittance matrix parameters ( $Y$  and  $t$ ).

$$x_{lower} \leq x \leq x_{upper} \quad (30)$$

### 2.7. New power system capacity to guarantee normal operation

Two alternative options were considered for the model developed to determine the failure time and bus. The first option involves a linear increase in Power Capacity (PC) in a specific bus. The second option is a combination of PV generation and an ES system.

Equation (31) describes the first option, which models new PC ( $PNg_{k,t}$ ) to operate throughout the day to recover the investment costs. The second option aims to minimize the objective function of over costs with suffix cost  $x_{cost}$  related to NSP calculated ( $NSPc_{k,t}$ ).

$$PNg_{k,t} = Pg_{k,t} + NSPc_{k,t} \quad (31)$$

Equations (32) to (34) describe the process of the second option, which covers the new PC required, including power dimension ( $PhPC_b$ ) and energy storage

( $SSEC_b$ ), and is adjusted to solar availability ( $Saf_t$ ) and States of Charge variation ( $SoCv_{k,t}$ ) to redistribute energy stored half hourly ( $Dt$ ). The source of surplus generation capacity is not analyzed due to its variety.

$$fo = PhPC_{cost} \times PhPC_k + SSEC_{cost} \times SSEC_k \quad (32)$$

$$PhPC_k \times Saf_t \geq NSPc_{k,t} + SoCv_{k,t} \quad (33)$$

$$SoC_{k,t} = SoC_{k,t-1} + SoCv_{k,t-1} \times Dt \quad (34)$$

### 2.8. Distribution network impact

Studies indicate that EVs have an impact on DN. The daily energy requirements are independent of the EV model. The voltage data and the energy required by EVs are collected and processed through data science, obtaining statistical information using MCS. The EVs charging can cause voltage drops and instability in the network, which can be addressed by using ES systems and smart charging strategies [2], [5].

### 2.9. Study Case

#### 2.9.1. Uncontrolled charging projection results in Peru

Assumptions and sources of information use market participation as a reference point for regional and global controllable charging rates. The cumulative EV sales are assumed as total on-road EVs, and EV sales are expected to continue increasing due to government incentives, reduced battery costs, and increased consumer awareness.

The optimistic projection assumes a yearly increase in EV sales of 25%, and the controllable charging rate is assumed to be 70%. The pessimistic projection assumes a yearly increase in EV sales of 10%, and the controllable charging rate is assumed to be 50%. These assumptions were used to project EV adoption in Peru.

Table 2 presents ranges of the projection of EV adoption in Peru from 2023 to 2031. This includes cumulative EV sales, controllable and uncontrollable charging rates, and the number of EVs on the road. The data is presented in ranges, from optimistic, pessimistic, and business-as-usual scenarios.

**Table 2.** Uncontrolled charging electric vehicles (projected data 2023 - 2031)

Year	Total Vehicles N°	Cumulative EV Sales N° EVs	Market Participation %	Uncontrollably Charging Rate %	Uncontrolled Charging EVs N° EVs
2023	366,900-372,700	2,450-2,930	6.67%-7.85%	85.30%-86.70%	2,120-2,490
2024	375,800-385,900	3,180-4,170	8.45%-10.81%	84.30%-85.80%	2,719-3,460
2025	384,000-399,800	4,200-5,750	10.94%-14.39%	83.30%-84.90%	3,606-4,880
2026	392,300-414,500	5,480-7,770	13.97%-18.74%	82.30%-84.00%	4,760-7,070
2027	400,800-430,000	7,190-10,350	17.95%-24.07%	81.30%-83.10%	6,455-9,060
2028	409,400-446,400	9,370-13,500	22.84%-30.21%	80.30%-82.20%	8,485-11,978
2029	418,200-463,700	12,030-17,350	28.73%-37.40%	79.30%-81.30%	10,963-16,652
2030	427,100-482,100	15,220-22,020	35.63%-45.65%	78.30%-80.40%	14,372-17,494
2031	436,100-501,600	18,920-27,650	43.31%-55.31%	77.30%-79.50%	15,390-24,768

### 2.9.2. Multiple scenarios

The article is based in three scenarios for the growth of EV sales in Peru: optimistic, business-as-usual, and pessimistic, with controllable charging rates estimated for each scenario. Based on this information and analysis of uncontrolled charging of EVs, the study projects that the number of EVs on the road in Peru for 2023

will range from 2450 to 2940. The article also compares the technical characteristics of different EV models and their effects on the DN, as shown in Table 3, with the KIA EV6 found to require the most energy among the EVs studied. However, the scenarios presented are based on broad assumptions and may not accurately reflect the specific conditions of the Peruvian market. More information is shown in Table 2.

**Table 3.** Electric vehicle models (2,021 data)

EV	BCES kWh	SCv,smin kWh/km	SCv,smax kWh/km	Pvmax kW	SoCmin %	SoCmax %
TSP	100	0.18	0.21	250	5	80
AQ4	82	0.181	0.181	125	15	95
KEV6	77.4	0.21	0.227	228	10	80
BHEV	76.9	0.164	0.207	360	30	80

### 2.9.3. Monte Carlo simulation analysis

The study analyzed three scenarios with stochastic micro scenarios. Scenario 1 had 2,000 EVs with 200 samples. Scenario 2 had 2,500 EVs with 120 samples. Scenario three 3 had 3,750 EVs with 80 samples. The analysis included  $1.0 \times 10^6$  uncertainty stochastic micro scenarios. In Section 2.4, the variables  $dep_{v,s}$  and  $arr_{v,s}$  were fitted to a normal distribution. Figure 1b illustrates significant differences between the probability distribution functions of departure and arrival times. The arrival time has a standard deviation encompassing after-work hours when individuals may attend to household duties or socialize after work, which does not occur similarly during morning hours before work.

According to [13], the Tesla Model 3 has a  $BCES$  of  $2.88 \times 10^{+8}$  J (80 kWh). The specific energy consumption for the vehicle falls within the range of  $SC_{v,s} \in < 684; 900 > J/m (< 0.19; 0.25 > kWh/Km)$ . The EVs

maximum charging power is approximately  $Pv_{max} = 1.5 \times 10^{+5}$  W with  $n_{chg} = 90\%$  and  $n_{dsg} = 90\%$ . To model EV batteries, the minimum State of Charge  $SoC_{min}$  is set to 15% of the battery capacity, while the maximum State of Charge  $SoC_{max}$  is set to 95% of battery capacity.

### 2.9.4. Interaction between MCS and OPF

Travel and geographic uncertainties characterization involves categorizing the number of EVs per bus as either "From" or "To" bus based on the departure trip. Figure 2 displays boxplots of the hourly total energy required by the DN, comparing the KIA EV6, which requires the greatest amount of energy, with the Tesla Model 3, which requires the least energy (as seen in Figure 1e). The values reported in Figure 2 show that the KIA EV6 is the model that consumes more energy, triggering a higher energy requirement for the DN.

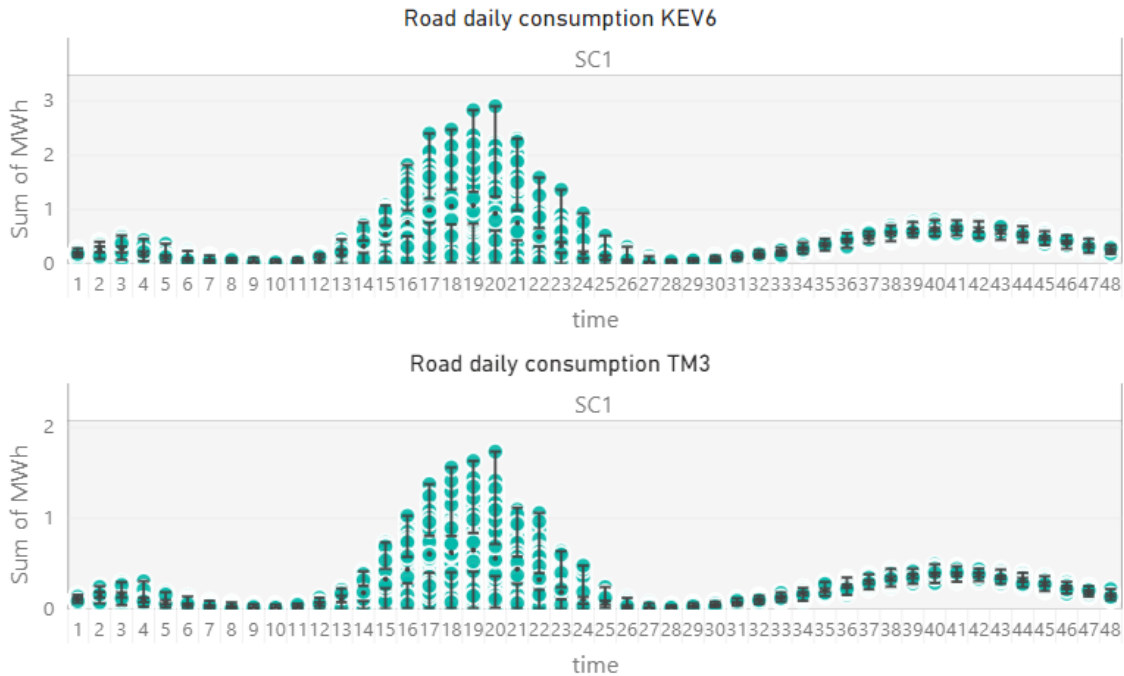


Figure 2. Road daily consumption needed per scenario and time

### 2.9.5. Optimal power flow usage

The IEEE 14 Power Bus System [16] represents the PS of socioeconomic class A in Peru with variations in power line length. The electric market load data from February 2020 serves as the daily load factor. The traffic categories effects of high, medium, and low speed are reported on [13]. Google Maps provided traffic history data for three categories represented by normal distributions. The first category is high speed, with a mean value of 13.89 m/s (50 km/h) and a standard deviation of 5.56 m/s (20 km/h). The second category is medium speed, with a mean value of 9.72 m/s (35 km/h) and a standard deviation of 4.17 m/s (15 km/h). The third category is low speed, with a mean value of 5.56 m/s (20 km/h) and a standard deviation of 2.78 m/s (10 km/h).

### 2.9.6. New power system capacity to guarantee normal operation

The first surplus PC option needs no additional data, but the PV generation with storage system option requires a solar availability factor, obtained from [17], with cost data from [18]. Subsection 2.7 presents constraints and the objective function of power interaction with NSP. Constraints (32) to (34) are complemented by equation (35), limiting the  $SoC_{k,t}$  variable to the bounds of 0 and the capacity of the storage system,  $SSEC_k$ .

$$0 \leq SoC_{k,t} \leq SSEC_k \quad (35)$$

The objective function variables in equation (33) include  $PhPC_{cost}$  at 1.30 \$/W for photovoltaic PC cost and  $SSEC_{cost}$  at  $1.11 \times 10^{-4}$  \$/J (400 \$/kWh) for storage system energy capacity.

### 2.9.7. Distribution network analysis

Two final syntheses that closely resemble the global data are obtained. The first one represented 4% of the occurrences. The other one collected 10% of the occurrences. These reductions are evaluated in a commonly used DN (IEEE 13 BUS power system) using Simulink from MATLAB software. The effect of all the simulations performed on the DN is reported in this section.

## 3. Results and discussion

### 3.1. Monte Carlo simulation analysis

Figure 3 shows the number of EVs in the PS and two figures for each scenario, illustrating the geographic and travel patterns of the EVs. Table 4 provides additional information on the number of EVs departing from and arriving at each bus on their first trip, along with geographic patterns uncertainty. The headers in Table 4 are classified as "Min MCS" and "Max MCS," representing the minimum and maximum scenarios of daily peak load reported from MCS outputs. These classifiers can help assess the potential impacts of EVs on the PS.

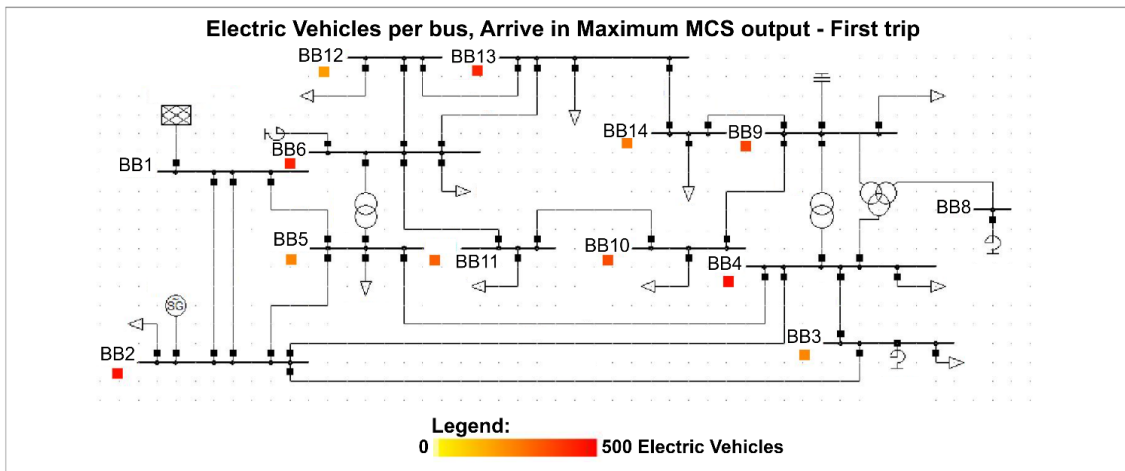


Figure 3. Amount of arriving electric vehicle in maximum Monte Carlo simulation output - scenario 1

Table 4. Number of electric vehicles from and to each bus per scenario for Monte Carlo simulation outputs

EVs Bus	Scenario 1		Scenario 2		Scenario 3		Scenario 1		Scenario 2		Scenario 3	
	Min Fr	Max To										
1	0	0	0	0	0	0	0	0	0	0	0	0
2	180	242	171	269	227	265	224	288	325	460	307	424
3	186	132	197	117	208	151	240	149	337	219	333	227
4	179	255	177	256	215	296	223	336	360	454	342	502
5	204	120	200	103	214	152	227	141	328	217	380	209
6	186	225	188	222	208	339	232	286	320	463	352	440
7	0	0	0	0	0	0	0	0	0	0	0	0
8	0	0	0	0	0	0	0	0	0	0	0	0
9	191	179	166	188	229	256	224	264	358	341	360	342
10	172	196	204	157	244	227	257	242	340	353	322	344
11	172	131	153	164	240	183	232	197	343	287	329	274
12	188	132	201	119	234	150	234	147	357	202	341	221
13	170	244	167	260	249	290	196	280	324	467	337	468
14	172	144	176	145	232	191	211	170	358	287	347	299

### 3.2. Interaction between MCS and OPF

Figure 4 compares the application for the Tesla Model 3, which has the lowest specific consumption. The first application is the  $PS_{MCS}$  which is in the right section. The values are also related to the Maximum output of MCS. Meanwhile, Table 5 presents the mean characteristics of daily load for different scenarios with

minimum and maximum MCS outputs.

The energy load  $Ed_s$  is computed using equation (36). The peak load  $Pd_{max,s}$  represents the maximum daily load supplied by the PS grid for each scenario analyzed, as expressed in equation (37). Finally, the load factor  $LF_s$  is determined by dividing the mean power load by the max power load, as shown in equation (38).

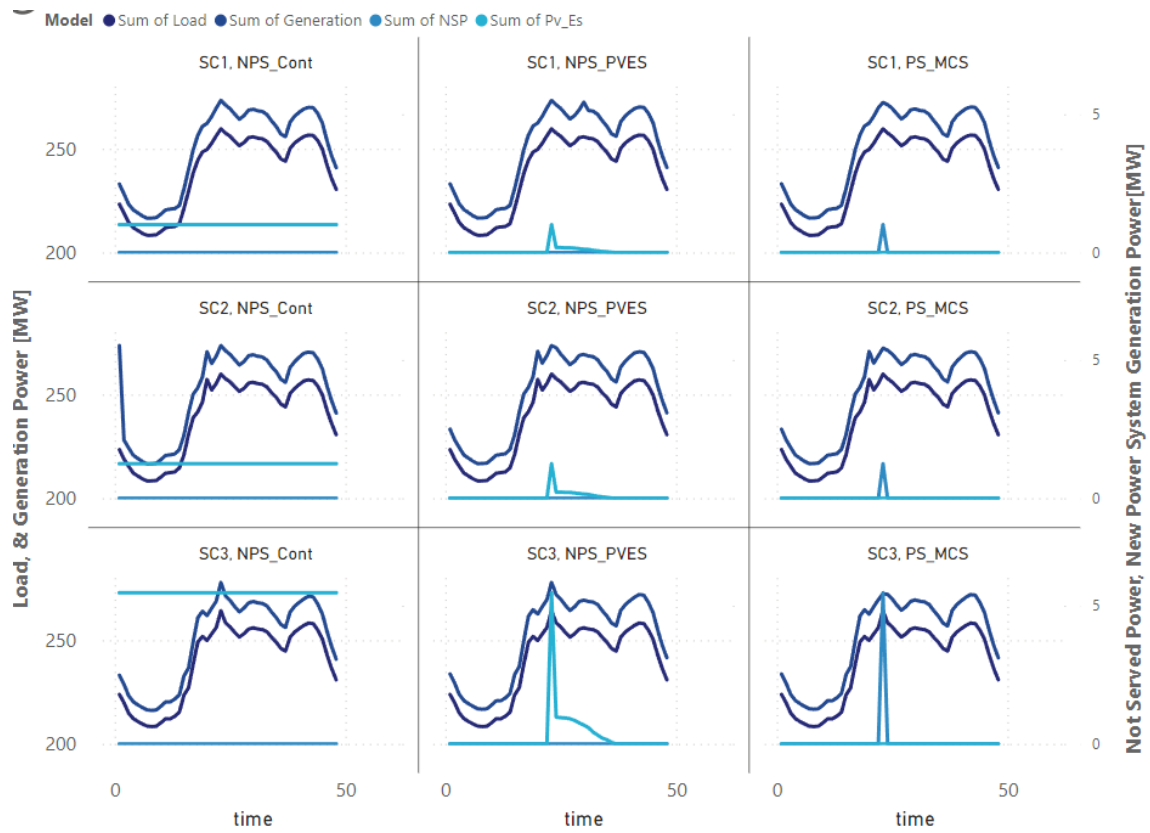


**Figure 4.** Power System Performance Comparison of Optimal Power Flow (PS\_MCS), Photovoltaic and Energy Storage (NPS\_PVES), and Continuous Generation (NPS\_Cont)

**Table 5.** Load data per scenarios for Tesla (2018) electric vehicle & Optimal Power Flow performance for all scenarios

Daily Load	BAU w/o EVs	Scenario 1		Scenario 2		Scenario 3	
		Min MCS	Max MCS	Min MCS	Max MCS	Min MCS	Max MCS
$Ed_s$ (MWh)	5,704.6	5710.58	5724.82	5711.51	5729.43	5715.56	5742.4
$Pd_{max,s}$ (MW)	257.2	257.25	259.66	257.31	259.91	257.51	264.23
$LF_s$	0.906	0.906	0.907	0.905	0.906	0.910	0.906
$Eg_s$ (MWh)	5,979.1	5985.82	6000.95	5986.67	6005.91	5991.1	6017.9
$Los_s$ (MWh)	274.5	275.24	276.12	275.17	276.48	275.54	275.5
NSE (MWh)			0.5		0.62		2.74
Max NSP (MW)			1.01		1.25		5.47
NSP bus			14		14		14

$$Ed_s = \sum \sum Pd_{b,t,s} \times 24/T; s = \{s_{min}, s_{max}\} \quad (36)$$

$$Pd_{max,s} = \max \left( \sum Pd_{b,t,s} \right); s = \{s_{min}, s_{max}\} \quad (37)$$

$$LF_s = \frac{\sum \sum \frac{Pd_{p,t,s}}{T}}{Pd_{max,s}}; s = \{s_{min}, s_{max}\} \quad (38)$$

The difference in peak load between the maximum and minimum MCS outputs was observed to be increasing, indicating the stochastic effect of the analysis. For Scenario 1, the gap between MCS outputs is  $2.41 \times 10^{+6} W$ . For Scenario 2, the difference in MCS outputs is  $2.60 \times 10^{+6} W$ . For Scenario 3, the gap between MCS outputs is  $6.72 \times 10^{+6} W$ . The difference in daily energy load between maximum and minimum MCS outputs is reported per scenario. Scenario 1 has a difference in daily energy of  $5.13 \times 10^{+10} J$  (14.24 MWh). Scenario 2 has a difference in daily energy of  $6.45 \times 10^{+10} J$  (17.92 MWh). Scenario 3 has a difference in daily energy of  $9.66 \times 10^{+10} J$  (26.84 MWh). The increment in the gap is explained due to the number of EVs in the tested scenarios.

### 3.3. Optimal power flow usage

The model commonly employs OPF to evaluate PS performance concerning different EV charging scenar-

ios. Figure 4 displays the performance of PS and NSP required to maintain normal operation, with the highest output of the Tesla Model 3 EV's MCS specified. Table 5 summarizes the optimized power flow findings, including variables such as  $Eg_s$  and  $Loss_s$  representing energy generated, energy gaps, and  $NSE_s$  allocating NSP for all buses during the day. Equations (39) to (41) define these variables.

$$Eg_s = \frac{\sum \sum Pg_{b,t,s} \times 24}{T}; s = \{s_{min}, s_{max}\} \quad (39)$$

$$Loss_s = Eg_s - Ed_s; s \in \{s_{min}, s_{max}\} \quad (40)$$

$$NSE_s = \frac{\sum \sum NSP_{b,t,s} \times 24}{T}; s = \{s_{min}, s_{max}\} \quad (41)$$

The tested model enables the identification of the bus bar that requires more capacity and whose option is best suited to supply it. The amount of NSP will determine the required capacity for new power plants. Table 6 reports the information for the Tesla Model 3 (2018).

The study found that the NSE was expelled at the last bus of the PS, which is located farthest from the generation buses (#14). The amount of NSE increased as the number of EVs in each scenario.

**Table 6.** New power system (NPS) capacity to guarantee normal operation as all day fixed value; with photovoltaic - storage system (PSS) option

OPF	Scenario 1			Scenario 2			Scenario 3		
	BAU w/o EVs	Min MCS	Max MCS	BAU w/o EVs	Min MCS	Max MCS	BAU w/o EVs	Min MCS	Max MCS
$Eg_{NPS}$ (MWh)	5975.91	5982.49	5998.33	5975.16	5982.75	6002.67	5962.67	5974.66	6004.41
$Loss_{NPS}$ (MWh)	271.36	271.91	273.51	270.62	271.25	273.25	258.12	259.1	262.01
Max $Pg_{NPS}$ (MW)	270.7	270.72	273.41	270.67	270.75	273.65	270.08	270.38	277.87
NPS Capacity (MW)		1.01			1.25			5.47	
$Eg_{PSS}$ (MWh)	5978.9	5985.49	6001.34	5978.86	5986.45	6007.05	5978.13	5990.15	6020.07
$Loss_{PSS}$ (MWh)	274.36	274.91	276.52	274.31	274.95	277.63	273.58	274.59	277.67
Max $Pg_{PSS}$ (MW)	270.82	270.83	273.41	270.82	270.84	273.65	270.71	270.72	277.87
PV Capacity (MW)		0.177687			0.219993			0.965943	
Storage System (MWh)		0.419278			0.519105			2.279288	
Busbar (#)		14			14			14	
PSS cost (\$)		345,397.68			427,634.56			1,877,658.44	

### 3.4. New power system capacity to guarantee normal operation

The PS requires additional generation capacity to address the identified problem. The methodology section offers options for obtaining extra generation capacity using: microturbines, internal combustion engines, PV generation mixed with a storage system, etc. Figure 4 displays the performance of the PS and the power supplied by the PV-storage system in Maximum MCS output for the Tesla Model 3. Table 5 provides information about the required capacity of the new power system (NPS). The cost of the PV-storage system is reported for each scenario in Figures 5a, 5b, and 5c, ranging from \$ 0 to  $7.40 \times 10^{+5}$  for Scenario 1, \$  $2.22 \times 10^{+5}$  to \$  $7.81 \times 10^{+5}$  for Scenario 2 and \$  $5.88 \times 10^{+5}$  to \$  $3.41 \times 10^{+6}$  for Scenario 3. The cost of the first option of adding capacity for an entire day is not assessed in this study, but its PC is set constant as NSP from PS OPF.

### 3.5. Distribution network results

Section 3.4 of the study examines the relationship between load and PS capacity. However, increasing the general load does not necessarily require more PS capacity or increase the cost of PV and ES. The study also shows that the load required by EV models does not result in more NSP. These findings suggest that the PS requirements and the EV model are independent.

Data reduction techniques are used to synthesize the large amount of information processed. Two reductions are performed on the data, with errors of 1.24% and 0.85% compared to the global data. The reduction of 4% of the data is used to process the data in MATLAB using the Simulink tool. The DN data is used to redistribute EVs into the feeders of the IEEE 13 bus Power System, and the resulting performance of the feeders is shown in Figure 6. The results indicate that the voltage values remain within range for all buses of the IEEE 13 bus Power System even under uncontrolled charging assumptions.

## 4. Conclusions

The effect of EVs' uncontrolled charging presence in electricity markets is shown in this study, as seen in Table 5 and Figure 2. The minimum and maximum outputs from the Monte Carlo Simulations depend on the specific consumption of the EV models, which values are reported in Table 3. The EV model that required more energy from the DN is the Kia EV6, while the EV model that required less energy from the DN is the Tesla Model 3, as shown in Figure 1 (e). The highest consumption of scenario 3 is for the Kia EV6 model with 31.8 MWh, while the lowest consumption of scenario 1 is for the Tesla Model 3 with 10.14 MW.

Even for the specific models of EVs that require more energy, the NSP variable is not guaranteed to be needed. Figure 5a shows that the models that did not have NSP are the Kia EV6 (which has the highest energy need) and Tesla S Plaid. Figure 5b and Figure 5c also reinforce this fact due to the intermittency of maximum and minimum NSP presented in the OPF executions.

On the other hand, the dependency noted in Figure 5 is the relationship between the costs of different dimensions of the PV generation – ES System and the amount of daily NSE presence in the OPF execution. This relationship is not strictly linear, but for similar NSE values, the cost of the system designed is close. For example, in scenario 3, the highest value of NSE is 6.84 MWh. The corresponding EV model is the Kia EV6. The cost related to this point is \$  $2.84 \times 10^{+6}$ . But the highest system designed cost is \$  $3.41 \times 10^{+6}$  with a not served energy value of 5.94 MWh.

The impact of the uncontrolled charging is not relevant in distribution, as shown by the voltage stability

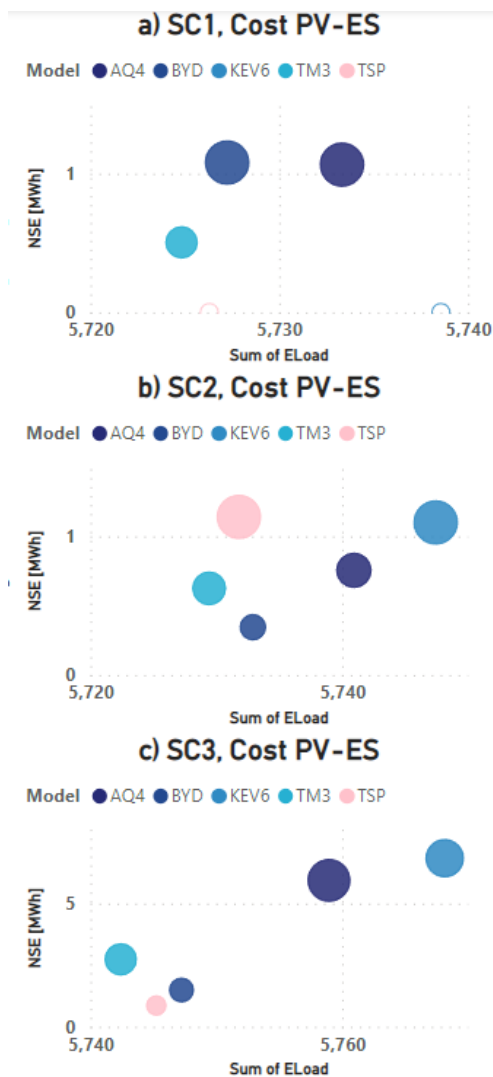


**Figure 5.** Not Served Energy Comparison and Photovoltaic-Energy Storage Costs for Three Scenarios: (a) for Scenario 1, (b) for Scenario 2 and (c) for Scenario 3

of the executed model. Even the further busbars have voltage values that achieve the Peruvian electric distribution policies' bounds. The busbars 632, 645, 646, and

633 have well-distributed voltage levels. The others also have values according to policies.

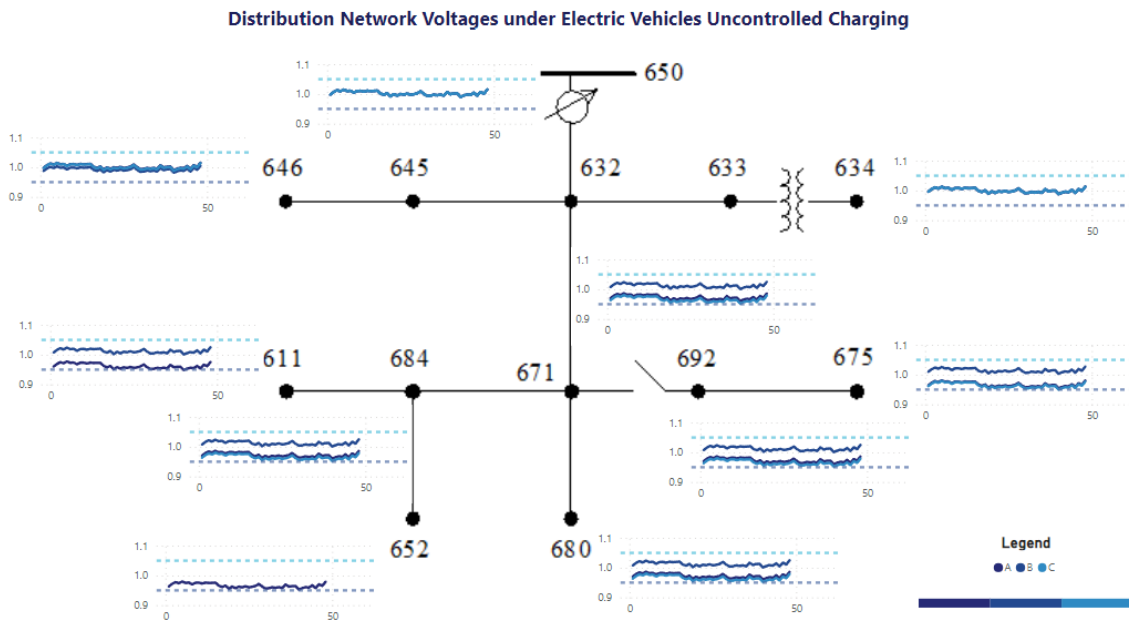


Figure 6. Distribution Network Daily Voltage for each phase

## Acknowledgments

A special thanks to the "Program of Doctorates in Peruvian Universities," promoted by the National Council of Science, Technology and Technological Innovation (CONCYTEC) through the National Fund for Scientific, Technological and Technological Innovation Development (FONDECYT).

## References

- [1] V. Vita and P. Koumides, "Electric vehicles and distribution networks: Analysis on vehicle to grid and renewable energy sources integration," in *2019 11th Electrical Engineering Faculty Conference (BulEF)*, 2019, pp. 1–4. [Online]. Available: <https://doi.org/10.1109/BulEF48056.2019.9030787>
- [2] L. Wang, S. Sharkh, and A. Chipperfield, "Optimal decentralized coordination of electric vehicles and renewable generators in a distribution network using a search," *International Journal of Electrical Power & Energy Systems*, vol. 98, pp. 474–487, 2018. [Online]. Available: <https://doi.org/10.1016/j.ijepes.2017.11.036>
- [3] K. Mahmud, G. E. Town, S. Morsalin, and M. Hossain, "Integration of electric vehicles and management in the internet of energy," *Renewable and Sustainable Energy Reviews*, vol. 82, pp. 4179–4203, 2018. [Online]. Available: <https://doi.org/10.1016/j.rser.2017.11.004>
- [4] A. Ahmadian, M. Sedghi, B. Mohammadi-ivatloo, A. Elkamel, M. Aliakbar Golkar, and M. Fowler, "Cost-benefit analysis of v2g implementation in distribution networks considering pevs battery degradation," *IEEE Transactions on Sustainable Energy*, vol. 9, no. 2, pp. 961–970, 2018. [Online]. Available: <https://doi.org/10.1109/TSTE.2017.2768437>
- [5] R. R. Desai, R. B. Chen, and W. Armington, "A pattern analysis of daily electric vehicle charging profiles: Operational efficiency and environmental impacts," *Journal of Advanced Transportation*, vol. 2018, p. 6930932, Jan 2018. [Online]. Available: <https://doi.org/10.1155/2018/6930932>
- [6] J. H. Angelim and C. de Mattos Affonso, "Probabilistic assessment of voltage quality on solar-powered electric vehicle charging station," *Electric Power Systems Research*, vol. 189, p. 106655, 2020. [Online]. Available: <https://doi.org/10.1016/j.epr.2020.106655>
- [7] S. Kumar, R. Saket, D. K. Dheer, J. B. Holm-Nielsen, and P. Sanjeevikumar, "Reli-

- ability enhancement of electrical power system including impacts of renewable energy sources: a comprehensive review,” *IET Generation, Transmission & Distribution*, vol. 14, no. 10, pp. 1799–1815, 2020. [Online]. Available: <https://doi.org/10.1049/iet-gtd.2019.1402>
- [8] C. W. Villanueva Machado, M. F. Bedriñana Aronés, and J. E. Luyo Kuong, *Planificación de expansión de transmisión bajo condiciones de máxima generación con recursos energéticos renovables*. Universidad Nacional de Ingeniería, 2018. [Online]. Available: <https://bit.ly/3XfQZ8b>
- [9] S. Pirouzi, J. Aghaei, T. Niknam, H. Farahmand, and M. Korpås, “Exploring prospective benefits of electric vehicles for optimal energy conditioning in distribution networks,” *Energy*, vol. 157, pp. 679–689, 2018. [Online]. Available: <https://doi.org/10.1016/j.energy.2018.05.195>
- [10] S. Lazarou, V. Vita, C. Christodoulou, and L. Ekonomou, “Calculating operational patterns for electric vehicle charging on a real distribution network based on renewables’ production,” *Energies*, vol. 11, no. 9, 2018. [Online]. Available: <https://doi.org/10.3390/en11092400>
- [11] D. Schmerler Vainstein, J. C. Velarde Sacio, and B. Rodríguez González, Abel Solís Sosa, *Electromovilidad. Conceptos, políticas y lecciones aprendidas para el Perú*. Osinergmin, 2019. [Online]. Available: <https://bit.ly/3NBY53W>
- [12] AAP, *Los Protagonistas de la nueva era automotriz: Vehículos eléctricos e híbridos en el Perú*. Asociación Automotriz del Perú, 2019. [Online]. Available: <https://bit.ly/465w2kl>
- [13] C. Villanueva, J. Luyo, and C. Delgado, A. Carbajal, “Electric vehicle aggregator participation in energy markets considering uncertainty travel patterns,” *International Journal of Innovative Technology and Exploring Engineering (IJITEE)*, vol. 8, no. 12, pp. 4994–4998, 2019. [Online]. Available: <https://doi.org/10.35940/ijitee.L3747.1081219>
- [14] R. Jing, M. Wang, Z. Zhang, X. Wang, N. Li, N. Shah, and Y. Zhao, “Distributed or centralized? designing district-level urban energy systems by a hierarchical approach considering demand uncertainties,” *Applied Energy*, vol. 252, p. 113424, 2019. [Online]. Available: <https://doi.org/10.1016/j.apenergy.2019.113424>
- [15] A. Dammert, R. García Carpio, and F. Molinelli, *Regulación y Supervisión del Sector Eléctrico*. Fondo Editorial Pontificia Universidad Católica del Perú, 2013. [Online]. Available: <https://bit.ly/3p7riQW>
- [16] PSCAD, *IEEE 14 Bus System*. Manitoba HVDC Research Centre, 2014. [Online]. Available: <https://bit.ly/3CxmAZt>
- [17] T. Khatib and W. Elmenreich, “A model for hourly solar radiation data generation from daily solar radiation data using a generalized regression artificial neural network,” *International Journal of Photoenergy*, vol. 2015, p. 968024, Oct 2015. [Online]. Available: <https://doi.org/10.1155/2015/968024>
- [18] A. Babajide and M. C. Brito, “Solar pv systems to eliminate or reduce the use of diesel generators at no additional cost: A case study of lagos, nigeria,” *Renewable Energy*, vol. 172, pp. 209–218, 2021. [Online]. Available: <https://doi.org/10.1016/j.renene.2021.02.088>



## GUIDELINES FOR PUBLICATION IN INGENIUS JOURNAL

### 1. General Information

INGENIUS is a scientific publication of the *Universidad Politécnica Salesiana* of Ecuador, published since January 2007, with a fixed biannual periodicity, specialized in Mechanical Engineering, Electrical Engineering, Electronics, Computer Science and its integration in what is now known as Mechatronics; these lines of action strengthen areas such as automation, control, robotics, among others..

It is a scientific journal, which uses the peer-review system, under double-blind review methodology, according to the publication standards of the Institute of Electrical and Electronics Engineers (IEEE). Compliance with this system allows authors to guarantee an objective, impartial and transparent review process, which facilitates the publication of their inclusion in reference databases, repositories and international indexing.

INGENIUS is indexed in the directory and selective catalog of the Regional Online Information System for Scientific Journals of Latin America, the Caribbean, Spain and Portugal (Latindex), in the Directory of Journals of Open Access DOAJ, In the Information Matrix for the Analysis of Journals, MIAR, In the Ibero-American Network of Innovation and Scientific Knowledge, REDIB and in repositories, libraries and specialized catalogs of Latin America.

The journal is published in a double version: printed (ISSN: 1390-650X) and digital (e-ISSN: 1390-860X), in Spanish, each work being identified with a DOI (Digital Object Identifier System). The articles sent to INGENIUS magazine must comply with the following criteria:

### 2. Scope and policy

#### 2.1. Theme

Original contributions in Mechanical Engineering, Electrical and Electronic Engineering, Computer Science and its integration in what is now known as Mechatronics, as well as related areas: Automation, Control, Domotics, Robotics in their different fields of action and all those related disciplines with the same central theme.

All the work carried out by national or foreign researchers may be published once they meet the required scientific quality criteria.

#### 2.2. Contributions

INGENIUS Journal preferably publishes articles related to empirical research, and also reports of technological development, proposals for models and innovations, products for the elaboration of graduate and postgraduate thesis that contribute to the field of science and technology, as well as select revisions of literature. (state-of-the-art).

- **Research:** 5,000 to 6,500 words of text, including title, abstracts, descriptors, charts and references.
- **Reports:** 5,000 to 6,500 words of text, including title, abstracts, charts and references.
- **Reviews:** 6,000 to 7,000 words of text, including charts and references. Current, selective and justified references, would be specially valued from among 40 works

The INGENIUS Journal publishes original and unpublished works written in Spanish and English, they may not have been published

through any printed or electronic media, nor be in the process of arbitration or publication.

Every article will be subjected to a rigorous arbitration process; the evaluation of the article will be made according to criteria of originality, relevance, relevance, contributions, scientific rigor and compliance with established editorial guidelines.

Being an arbitrated publication, the Editorial Board approves its publication based on the concept of specialized pairs. The reception of a document does not imply commitment of publication.

It is essential to present a letter of presentation and grant of rights which can be downloaded from: [urlhttps://goo.gl/ZNkMRD](https://goo.gl/ZNkMRD).

Contributions must be exclusively sent and through the OJS (Open Journal System) [urlhttps://goo.gl/JF7dWT](https://goo.gl/JF7dWT). In which all authors must previously register as a user. For any consultation of the procedure you should contact:

[revistaingenius@ups.edu.ec](mailto:revistaingenius@ups.edu.ec),  
[jcalles@ups.edu.ec](mailto:jcalles@ups.edu.ec) ó  
[mquinde@ups.edu.ec](mailto:mquinde@ups.edu.ec).

To promote diversity in publications, the author(s) may not publish more than one (1) article per issue, nor in consecutive issues. In order for the author(s) to submit their research again to Ingenius, a minimum of 3 published issues must have elapsed.

### 3. Presentation and structure of the manuscripts

For those works that are empirical investigations, the manuscripts will follow the IMRDC structure (Introduction, Materials and Methods, Results and Discussion and Conclusions), being optional the Notes and Supports. Those papers that, on the contrary, deal with reports, studies, proposals and reviews may be

more flexible in their epigraphs, particularly in material and methods, analysis, results, discussion and conclusions. In all typologies of works, references are mandatory.

Articles may be written on Microsoft Word (.doc or .docx) or L<sup>A</sup>T<sub>E</sub>X(.tex). The template to be used can be downloaded from the journal's website, a, [urlhttps://goo.gl/gtCg6m](https://goo.gl/gtCg6m), while for L<sup>A</sup>T<sub>E</sub>X in [urlhttps://goo.gl/hrHzzQ](https://goo.gl/hrHzzQ), it is necessary that the file be anonymised in Properties of File, so that the author(s) ID is not displayed.

Figures, Graphs and/or Illustrations, as well as Charts shall be numbered sequentially including an explanatory description for each. The equations included in the article must also be numbered; the figures, charts and equations must be cited in the text.

Use space after point, commas and question marks.

Use "enter" at the end of each paragraph and title heading. Do not use .<sup>enter</sup>anywhere else, let the word processor program automatically break the lines.

Do not center headings or subheadings as they should be aligned to the left.

Charts must be created in the same program used for the document body, but must be stored in a separate file. Use tabs, not spaces, to create columns. Remember that the final size of printed pages will be 21 x 28 cm, so the tables must be designed to fit the final print space.

#### 3.1. Structure of the manuscripts

##### 3.1.1. Presentation and cover letter

1. **Título (español) / Title (inglés):** Concise but informative, in Spanish on the front line and in English on the second, when the article is written in Spanish and vice versa if it is written in English.

2. **Authors and affiliations:** Full name and surname of each author, organized by order of priority and their institutional affiliation with reference to the end of the first sheet, where it must include: Dependency to which belongs within the institution, Institution to which he/she belongs, country, ORCID. A maximum of 5 authors will be accepted, although there may be exceptions justified by the complexity and extent of the topic.
  3. **Abstract (Spanish) / Abstract (English):** It will have a maximum extension of 230 words, first in Spanish and then in English. : 1) Justification of the topic; 2) Objectives; 3) Methodology and sample; 4) Main results; 5) Main conclusions.
  4. **Keywords (Spanish) / Keywords (English):** 6 descriptors must be presented for each language version directly related to the subject of the work. The use of the key words set out in UNESCO's Thesaurus will be positively valued.
  5. **Presentation (Cover Letter):** A statement that the manuscript is an original contribution, not submission or evaluation process in another journal, with the confirmation of the signatory authors, acceptance (if applicable) of formal changes in the manuscript according to the guidelines and partial assignment of rights to the publisher, according to the format established in: <<https://goo.gl/ZNkMRD>>
- ### 3.1.2. Manuscript
1. **Título (español) / Title (inglés):** Concise but informative, in Spanish on the front line and in English on the second, when the article is written in Spanish and vice versa if it is written in English.
  2. **Authors and affiliations:** Full name and surname of each author, organized by order of priority and their institutional affiliation with reference to the end of the first sheet, where it must include: Dependency to which belongs within the institution, Institution to which he/she belongs, country, ORCID. A maximum of 5 authors will be accepted, although there may be exceptions justified by the complexity and extent of the topic.
  3. **Abstract (Spanish) / Abstract (English):** It will have a maximum extension of 230 words, first in Spanish and then in English. : 1) Justification of the topic; 2) Objectives; 3) Methodology and sample; 4) Main results; 5) Main conclusions.
  4. **Keywords (Spanish) / Keywords (English):** 6 descriptors must be presented for each language version directly related to the subject of the work. The use of the key words set out in UNESCO's Thesaurus will be positively valued.
  5. **Introduction:** It should include the problem statement, context of the problem, justification, rationale and purpose of the study, using bibliographical citations, as well as the most significant and current literature on the topic at national and international level.
  6. **Material and methods:** It must be written so that the reader can easily understand the development of the research. If applicable, it will describe the methodology, the sample and the form of sampling, as well as the type of statistical analysis used. If it is an original methodology, it is necessary to explain the reasons that led to its use and to describe its possible limitations.
  7. **Analysis and results:** It will try to highlight the most important observations, describing, without making value judgments, the material and methods used. They will appear in a logical sequence

in the text and the essential charts and figures avoiding the duplication of data.

8. **Discussion and Conclusions:** It will summarize the most important findings, relating the observations themselves to relevant studies, indicating contributions and limitations, without adding data already mentioned in other sections. It should also include deductions and lines for future research.
9. **Supports and acknowledgments (optional):** The Council Science Editors recommends the author (s) to specify the source of funding for the research. Priority will be given to projects supported by national and international competitive projects.
10. **The notes (optional):** will go, only if necessary, at the end of the article (before the references). They must be manually annotated, since the system of footnotes or the end of Word is not recognized by the layout systems. The numbers of notes are placed in superscript, both in the text and in the final note. The numbers of notes are placed in superscript, both in the text and in the final note. No notes are allowed that collect simple bibliographic citations (without comments), as these should go in the references.
11. **References:** Bibliographical citations should be reviewed in the form of references to the text. Under no circumstances should references mentioned in the text not be included. Their number should be sufficient to contextualize the theoretical framework with current and important criteria. They will be presented sequentially in order of appearance, as appropriate following the format of the IEEE.

### 3.2. Guidelines for Bibliographical references

#### *Journal articles:*

- [1] J. Riess, J. J. Abbas, "Adaptive control of cyclic movements as muscles fatigue using functional neuromuscular stimulation". IEEE Trans. Neural Syst. Rehabil. Eng vol. 9, pp.326–330, 2001. [Online]. Available: <https://doi.org/10.1109/7333.948462>

#### *Books:*

- [1] G. O. Young, "Synthetic structure of industrial plastics" in *Plastics*, 2nd ed., vol. 3, J. Peters, Ed. New York: McGraw–Hill, 1964, pp. 15–64.

#### *Technical reports:*

- [1] M. A. Brusberg and E. N. Clark, "Installation, operation, and data evaluation of an oblique–incidence ionosphere sounder system," in "Radio Propagation Characteristics of the Washington–Honolulu Path," Stanford Res. Inst., Stanford, CA, Contract NOBSR–87615, Final Rep., Feb. 1995, vol. 1

#### *Articles presented in conferences (unpublished):*

- [1] Vázquez, Rolando, Presentación curso "Realidad Virtual". National Instruments. Colombia, 2009.

#### *Articles of memories of Conferences (Published):*

- [1] L. I. Ruiz, A. García, J. García, G. Tafoada. "Criterios para la optimización de sistemas eléctricos en refinerías de la industria petrolera: influencia y análisis en el equipo eléctrico," IEEE CONCAPAN XXVIII, Guatemala 2008.

#### *Thesis:*

- [1] L.M. Moreno, "Computación paralela y entornos heterogéneos," Tesis doctoral, Dep. Estadística, Investigación Operativa y Computación, Universidad de La Laguna, La Laguna, 2005.

#### *Guidelines:*

- [1] IEEE Guide for Application of Power Apparatus Bushings, IEEE Standard C57.19.100–1995, Aug. 1995.

*Patents:*

- [1] J. P. Wilkinson, “Nonlinear resonant circuit devices,” U.S. Patent 3 624 125, July 16, 1990.

*Manuals:*

- [1] Motorola Semiconductor Data Manual, Motorola Semiconductor Products Inc., Phoenix, AZ, 1989.

*Internet resources:*

- [1] E. H. Miller, “A note on reflector arrays” [Online]. Available. <https://goo.gl/4cJkCF>

### 3.3. Epigraphs, Figures and Charts

The epigraphs of the body of the article will be numbered in Arabic. They should go without a full box of capital letters, neither underlined nor bold. The numbering must be a maximum of three levels: 1. / 1.1. / 1.1.1. At the end of each numbered epigraph will be given an enter to continue with the corresponding paragraph.

The charts must be included in the text according to order of appearance, numbered in Arabic and subtitled with the description of the content, the subtitle should go at the top of the table justified to the left.

Figures can be linear drawings, maps or black and white halftone or color photographs in 300 dpi resolution. Do not combine photographs and line drawings in the same figure.

Design the figures so that they fit eventually to the final size of the journal 21 x 28 cm. Make sure inscriptions or details, as well as lines, are of appropriate size and thickness so that they are not illegible when they are reduced to their final size (numbers, letters and symbols must be reduced to at least 2.5 mm in height After the illustrations have

been reduced to fit the printed page). Ideally, the linear illustrations should be prepared at about a quarter of their final publication size.

Different elements in the same figure should be spelled a, b, c, etc.

Photographs should be recorded with high contrast and high resolution. Remember that photographs frequently lose contrast in the printing process. Line drawings and maps should be prepared in black.

The text of the figures and maps must be written in easily legible letters.

If the figures have been previously used, it is the responsibility of the author to obtain the corresponding permission to avoid subsequent problems related to copyright.

Each figure must be submitted in a separate file, either as bitmap (.jpg, .bmp, .gif, or .png) or as vector graphics (.ps, .eps, .pdf).

## 4. Submission process

The manuscript must be sent through the OJS system of the journal, <<https://goo.gl/JF7dWT>>, the manuscript should be uploaded as an original file in .pdf without author data and anonymized according to the above; In complementary files the complete manuscript must be loaded in .doc or .docx (Word file), that is to say with the data of the author (s) and its institutional ascription; Also the numbered figures should be uploaded in independent files according to the corresponding in the manuscript (as bitmap .jpg, .bmp, .gif, or .png or as vector graphics .ps, .eps, .pdf). It is also obligatory to upload the cover letter and grant of rights as an additional file.

All authors must enter the required information on the OJS platform and only one of the authors will be responsible for correspondence.

Once the contribution has been sent the system will automatically send the author for correspondence a confirmation email of receipt

of the contribution.

## 5. Editorial process

Once the manuscript has been received in OJS, a first check by the editorial team of the following points:

- The topic is in accordance with the criteria of the journal.
- Must have the IMRDC structure.
- Must be in the INGENIUS format.
- Must use the IEEE citation format.
- All references should be cited in the text of the manuscript as well as charts, figures and equations.
- The manuscript is original; for this, software is used to determine plagiarism.

The assessment described above can take up to 4 weeks.

If any of the above is not complete or there is inconsistency, an email will be sent to the author to make the requested corrections.

The author will make the corrections and resend the contribution through an email in response to the notification and will also upload the corrected manuscript into OJS supplementary files.

The editorial team will verify that the requested corrections have been incorporated, if it complies, the manuscript will start the second part of the process that may be followed by the author through OJS, otherwise the author will be notified and the manuscript will be archived.

The second phase of the process consists of the evaluation under the methodology of double-blind review, which includes national and foreign experts considering the following

steps:

- The editor assigns two or more reviewers for the article.
- After reviewing the article, the reviewers will submit the evaluation report with one of the following results.
  - Publishable
  - Publishable with suggested changes
  - Publishable with mandatory changes
  - Non publishable
- The editor once received the evaluation by the reviewers will analyze the results and determine if the article is accepted or denied.
- If the article is accepted, the author will be notified to make corrections if required and the corresponding editorial process will be continued.
- If the article is denied, the author will be notified and the manuscript will be archived.
- In the two previous cases the result of the evaluation of the reviewers and their respective recommendations will be sent.

The second phase of the process lasts at least 4 weeks, after which they will be notified to the author giving instructions to continue with the process.

## 6. Publication

The INGENIUS Journal publishes two issues per year, on January 1st and July 1st, so it is important to consider the dates for sending the articles and their corresponding publication. Articles received until October will be considered for the January publication and those received until April for the July publication.



**UNIVERSIDAD POLITÉCNICA SALESIANA DEL ECUADOR**

Juan Cárdenas Tapia, sdb,  
Rector

©Universidad Politécnica Salesiana  
Turuhuayco 3-69 y Calle Vieja  
Postal code 2074  
Cuenca, Ecuador  
Teléfono: (+593 7) 205 00 00  
Fax: (+593 7) 408 89 58  
Email: srector@ups.edu.ec

**Exchange**

Exchange with other periodicals is accepted.

Address:

Secretaría Técnica de Comunicación  
Universidad Politécnica Salesiana  
Turuhuayco 3-69 y Calle Vieja  
Postal code 2074  
Cuenca, Ecuador  
Phone: (+593 7) 205 00 00 Ext. 1182  
Fax: (+593 7) 408 89 58  
Email: rpublicas@ups.edu.ec  
www.ups.edu.ec  
Cuenca – Ecuador

INGENIUS, Journal Science of Technology,  
Issue 30  
july/december 2023  
John Calle Sigüencia, Editor in chief  
revistaingenius@ups.edu.ec

**Printed**

Centro Gráfico Salesiano: Antonio Vega Muñoz 10-68 y General Torres.  
Phone: (+593 7) 283 17 45  
Cuenca – Ecuador  
Email: centrograficosalesiano@lms.com.ec

**OTHER PERIODIC PUBLICATIONS OF THE UNIVERSITY**

**UNIVERSITAS**, Journal of Social and Human Sciences.

**LA GRANJA**, Journal of the Sciences.

**ALTERIDAD**, Journal of Education.

**RETOS**, Journal of Administration Sciences and Economics.

**UTOPIA**, University Youth Ministry Magazine.

**SOPHIA**, Collection of Philosophy of Education.



**ABYA  
YALA** | UNIVERSIDAD  
POLITÉCNICA  
SALESIANA

